Electrochemical oceanic carbon capture using bipolar membrane electrodialysis

sharifian, rezvan

DOI
10.4233/uuid:a897737d-9aa0-44e2-80d3-c4041691de0a

Publication date
2022

Document Version
Final published version

Citation (APA)
sharifian, R. (2022). *Electrochemical oceanic carbon capture: using bipolar membrane electrodialysis*. [Dissertation (TU Delft), Delft University of Technology]. https://doi.org/10.4233/uuid:a897737d-9aa0-44e2-80d3-c4041691de0a

ELECTROCHEMICAL OCEANIC CARBON CAPTURE

USING BIPOLAR MEMBRANE ELECTRODIALYSIS

ELECTROCHEMICAL OCEANIC CARBON CAPTURE

USING BIPOLAR MEMBRANE ELECTRODIALYSIS

Proefschrift

ter verkrijging van de graad van doctor
aan de Technische Universiteit Delft,
op gezag van de Rector Magnificus Prof. dr. ir. T.H.J.J. van der Hagen,
voorzitter van het College voor Promoties,
in het openbaar te verdedigen op Wednesday, 30 November 2022 om 15:00 uur

door

Rezvan SHARIFIAN

Master of Science in Petroleum Engineering,
Technische universiteit delft, Delft, The Netherlands,
geboren te Hamedan, Iran.

Dit proefschrift is goedgekeurd door de

promotor: Prof. dr. ir. C.R. Kleijn
copromotor: Dr. ir. D.A. Vermaas

Samenstelling promotiecommissie:

Rector Magnificus,	voorzitter
Prof. dr. ir. C.R. Kleijn	Technische Universiteit Delft, promotor
Dr. ir. D.A. Vermaas	Technische Universiteit Delft, copromotor
Onafhankelijke leden:	
Prof. T.A Hatton	Massachusetts Institute of Technology, USA
Prof. dr. ir. H.V.M. Hamelers	Wageningen University / Wetsus, NL
Prof. dr. ir. C.A. Ramirez	Technische Universiteit Delft, NL
Prof. dr. ir. J.B. van Lier	Technische Universiteit Delft, NL
Prof. dr. J.J.C. Geerlings	Technische Universiteit Delft, NL

This work is part of the research programme NWO-Wetsus Sustainable Water Technology with project number ALWET.2016.004, which is (partly) financed by the Netherlands Organization for Scientific Research (NWO).

Keywords: Bipolar membrane, carbon capture, electrochemistry

Printed by: Proefschriftspecialist

Front & Back: Designed by Chiel Van Hoeij (studiomoonshine.com)

ISBN/EAN: 978-94-6384-382-9

An electronic version of this dissertation is available at
http://repository.tudelft.nl/.

CONTENTS

1

General Introduction

Parts of this chapter is published as "Electrochemical methods for carbon dioxide separations", by K.M. Diederichsen*, R. Sharifian*, J. Kang, Y. Liu, S. Kim, B. Gallant, D. A. Vermaas, T. A. Hatton. Journal of Nature Reviews Methods Primers **2**, 68 (2022). [1] * These authors contributed equally.

1

1.1. Necessity of carbon capture

To mitigate the climate change, complying with the Paris Agreement, a global net zero greenhouse gasses (GHG) emission needs to be realized by 2050 [2]. In line with this ambition, to decarbonize the global economy, the "Net Zero by 2050" IEA-roadmap provides a pathway by setting out more than 400 milestones for all countries and policy makers (Figure 1.1) [2].

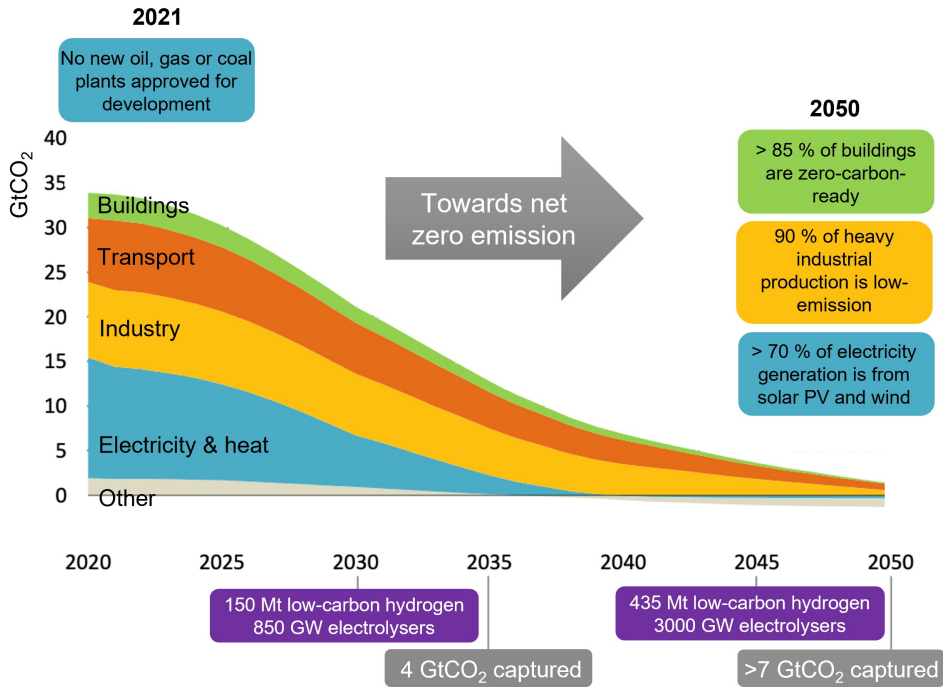

Figure 1.1: Few selected global milestones for policies, infrastructure, and technology deployment for achieving the net zero emission scenario by 2050 [2].

The global annual clean energy investments need to at least triple by 2030 (i.e., to around 4 trillion USD) to reach net zero emissions by 2050 [2]. Approximately 90 % of the global electricity generation in 2050 would need to come from renewable sources, including solar PV and wind together to account for more than 70%. Unfortunately, the current share of renewable electricity generation is less than 30 % [3]. For solar power, the required capacity-increase translates to a need to install the world's largest solar park every day [2]. The energy transition must also involve achieving 3000 GW electrolysers to produce low-carbon hydrogen in Mt scale (while the global installed electrolysers capacity in 2020 was only 0.3 GW [4]), Figure 1.1. It is an immense challenge to transition this fast, while also adressing the needs in transport and industry.

On the bright side, we can use extra tools to speed up the carbon neutrality challenge; removing carbon dioxide directly from the environment is such a tool. Even in the most optimistic scenario, if by 2050 the global energy sector transitions to renew-

able electricity, direct carbon removal from the environment is still inevitable to achieve the carbon neutrality goal (Figure 1.1). Particularly as many markets (e.g., long-distance transport, agriculture and industry that need carbon as a feedstock) are not able to transition to renewable sources in the short term. Therefore, carbon removal, directly from the air (DAC) or ocean (i.e., indirect air capture [5]), is necessary to compensate for hard-/ impossible-to-abate emissions [2].

By 2030, a capture capacity of 4 $GtCO_2$ per year must already be achieved. This is while, unfortunately, the current carbon capture, utilization, and storage (CCUS) facilities around the world have the capacity to capture only 0.04 $GtCO_2$ per year (and that mainly from flue gas) [6].

Annually, more than 35 Gt CO_2 is emitted. From the total emissions, at least 35 % is decentralized emission that cannot be addressed locally (see Chapter 2). All uncaptured emissions end up in the atmosphere which, subsequently, can settle an equilibrium with the dissolved CO_2 in the ocean through the carbonate equilibrium (see Chapter 2). While the carbon concentration in the atmosphere is small (ca. 400 ppm), the dissolved inorganic carbon in the ocean, converted to CO_2 gas, is more than 140× more concentrated by volume in seawater than is CO_2 gas in air [7]. Furthermore, thanks to the vast contact area of the ocean with the atmosphere, the air-ocean carbon exchange rate is fast, enabling indirect carbon capture from the air through oceanic carbon removal [5].

Extracting 1 Gton-CO_2 per year (i.e., ca. 2.7 % of the total global CO_2 emission) from the ocean surface layer (i.e., the upper ca. 100 m, also known as the ocean surface/ mixed layer) requires processing only a fraction of 0.00025 of this layer's volume [5]. From every 1 L of seawater, theoretically ca. 2.13 mM CO_2(g) or 2.078 mM $CaCO_3$(s) can be extracted (see Chapter 4). When the dissolved inorganic carbon (DIC) content is extracted from the ocean, the decarbonized stream can be directed back to the ocean where it can re-equilibrate with the atmosphere again through absorbing CO_2(g) from the atmosphere, allowing the cycle to be repeated. Assuming that the decarbonized sea/ ocean water is returned to the surface mixed layer of the ocean, the time scale for CO_2 re-absorption is approximated to be within one year [8].

1.2. ELECTROCHEMICAL CARBON CAPTURE

Electrochemistry is the science that deals with interaction between electrical energy and chemical changes [9]. The separation of carbon dioxide from a dilute feed driven by an electrochemical potential comprises a growing field of research that shows promise towards reducing the energy requirements of carbon capture processes. The importance of improving carbon capture processes has only grown as the climate crisis driven by anthropogenic CO_2 emissions worsens. Traditional methods of separating CO_2 from the flue gas of a power plant, industrial process, or from air rely on thermal or pressure-swings to modulate the affinity of a sorbent for CO_2. Such processes, including amine scrubbing [10], calcium looping [11], and solid supported sorbent [12] have been studied for decades, with several commercial processes now available, but still require significant improvements in cost and energetic penalty, required chemicals, and sustainability (see Chapter 2). While advances have been made with new chemistries that increase sorbent capacity and reduce the required change in temperature, methods involving electrochemistry show promise for revolutionary enhancements [13].

Electrochemical methods of separating CO_2 from a dilute feed gas were first studied in the early days of manned spacecraft as a means of cabin air filtration, using molten carbonate cells [14–17]. Since then, many other types of electrochemical processes have been described, comprising a wide range of potential applications with any concentration of feed CO_2 (see Chapter 2). Electrochemical methods may fall under two general classes of separations, depending on the type of influence on the sorbent; direct or indirect process.

In a direct process, electrochemistry acts directly on the sorbent, while indirect processes act on a secondary aspect of the system to modulate capacity. This includes adjustments to solution pH or addition and removal of a blocking species which may bind more strongly to the sorbent than CO_2. In either type of process, electrochemical methods show several potential advantages (see Chapter 2). Conventional (temperature-swing) capture processes often face difficulties related to operation at elevated temperatures, including accelerated sorbent degradation and equipment corrosion, high evaporative losses, and challenges in heat integration with existing plant designs; integration in renewable energy systems (which often do not rely on heat cycles) would be even more challenging. On the other hand, electrochemical processes can operate isothermally and without necessarily including heating or cooling, though some designs benefit from faster kinetics at elevated temperatures. Furthermore, electrochemical systems can be designed to couple to renewable power sources (such as wind and solar) directly, and quickly scale to different applications with highly modular units.

As elaborated in Chapter 2, electrochemical carbon capture can be done via (1) organic redox [13] (i.e., direct or indirect modification of a CO_2 sorbent using sorbent such as, bipyridines [18, 19], disulfides [20], copper/amine systems, the quinone species [21], quinone in salt-concentrated aqueous electrolytes [22], and ionic liquid [23]), (2) Transition metal (TM) Redox (e.g., Zn, Cu, and Ni compounds) [24], (3) pH-swing (leveraging the carbonate equilibrium via acid-alkaline pH-swing through electrolysis [25], bipolar membrane electrodialysis [5, 7, 26, 27], capacitive deionization [28], H^+ (de)intercalation [29], and proton-coupled electron transfer (PCET) of organic molecules) [30, 31], (4) high-temperature molten carbonate cells [32–35], and (5) hybrid methods (including electrochemical CO_2 capture and conversion combinations [36] and battery systems [37, 38]).

The performance of the carbon capture electrochemical process is determined by factors including the type of input feed (e.g., gaseous, aqueous) and its CO_2/ water/ impurity content, temperature, heat/steam availability, energy source, choice/ performance of the cell components (e.g., membrane, solvents, electrodes) and the cell design. Furthermore, the accuracy and availability of measurement techniques influence the obtained results and analysis.

This thesis focuses on the pH-swing method applied via a bipolar membrane electrodialysis (BPMED) cell for oceanic carbon capture. The BPMED cell consists of two end electrodes, charged membranes, and in-between-membranes flow paths (i.e., integrated gasket spacers) (Figure 1.2). The desired chemical reaction (in the case of oceanic carbon capture) is the conversion of bicarbonate ions to gaseous CO_2 or carbonate ion (and subsequently e.g., calcium carbonate $CaCO_3$(s)). Via electrochemistry, this reaction takes place under an electrical driving force supplied by a power supply or potentiostat/

galvanostat.

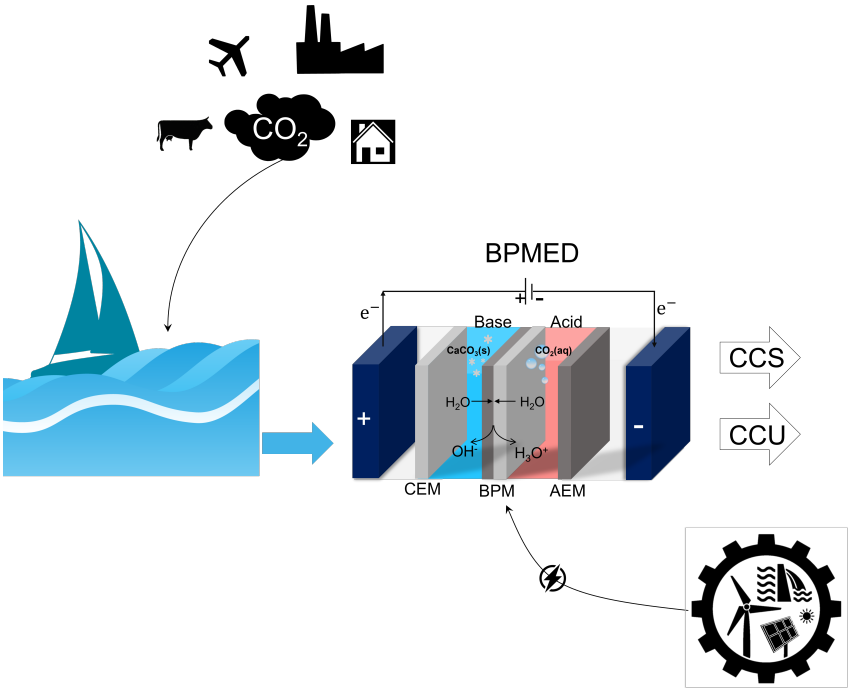

Figure 1.2: The electrochemical bipolar membrane electrodialysis (BPMED) stack technology for sustainable carbon capture from the ocean and the possible captured carbon fates of utilization (CCU) or storage (CCS). The BPMED cell consists of two end electrodes, cation/ anion exchange membranes (CEM, AEM) and the bipolar membrane (BPM, where the water dissociation reaction (WDR) takes place). Gaseous CO_2(g) and solid $CaCO_3$(s) are the captured products from the acid and base compartments, respectively that can be used or stored.

Unfortunately, the energy consumption of carbon capture is still high, particularly from diluted streams including the air and ocean, even using electrochemical methods [26, 39, 40], see Chapter 2 and 6. Furthermore, the TRL of these methods is still low (< 5), requiring further studies to be performed to explore the challenges in the technology upon practical deployment.

1.3. ENERGY CONSUMPTION OF THE ELECTROCHEMICAL CARBON CAPTURE

For measurements in electrochemical capture technologies, the most common figures of merits are the energy consumption, process rate (i.e., current density), product purity and long term/cycle stability. For the energy consumption, expressed in kJ per moles of captured CO_2, it is noteworthy that electrical energy is required (e.g., from renewable sources), opposed to traditional methods based on amines or calcium looping, which requires heat. Most publications report only the electrical energy consumption of the

electrochemical cell, ignoring the energy consumption for circulating the liquids or extracting/dissolving gases from the liquid. The electrical energy consumption of the electrochemical cell is defined as (see Chapter 4):

$$E = \int \frac{VI}{n_{CO_2(g)}} dt \tag{1.1}$$

In which E is the energy consumption ($kJ\,mol^{-1}CO_2$), V is the cell voltage (V), I is the current (A), t is the time (s) and $n_{CO_2(g)}$ is the number of moles CO_2 in the product stream. In the particular case of the bipolar membrane electrodialysis (BPMED) for pH-swing based carbon capture, in case of steady state, Equation 1.1 becomes:

$$E = V \times F \times n \tag{1.2}$$

In which F is the Faraday constant of 96485 $C\,mol^{-1}$, n the number of charges needed to go from (bi)carbonate to CO_2 (which depends on the Coulombic efficiency and the starting compound e.g., bicarbonate or carbonate), and V is the cell voltage (V). In BPMED, a very low current (I) deceases the Coulombic efficiency, thus increases n, while a high current increases the voltage V (i.e., due to ohmic losses), see Chapter 4. Hence, an optimum in energy efficiency occurs (for the electrochemical stack), which is currently at relatively low current density of $< 10\ mA\,cm^{-2}$ [41].

From an environmental point of view, the total required electrical energy for CO_2 capture should be lower than the amount of CO_2(g) emitted per unit of electricity used. As currently the average European emission factor from electricity is ca. 0.46 $kgCO_2$(eq) per kWh [42], it translates that the *total* capture energy consumption (incl. pumping, electrochemical reaction etc.) should not exceed 2.17 kWh per $kgCO_2$(eq) (i.e., ca. 344 $kJ\,mol^{-1}CO_2$). However, in countries where electricity is mainly generated from renewable sources such as Iceland or Denmark (i.e., electricity emission $< 0.05\ kgCO_2(eq)\,kWh^{-1}$), much higher values for energy consumption of the carbon capture can still be economically appealing. Thankfully, some (lab-scale) electrochemical CO_2(g) captures are demonstrated using even less than 121 $kJ\,mol^{-1}CO_2$ [22], proving the potential of electrochemically induced CO_2 capture.

In addition to the amount of required energy and its source, the footprint of the capture plant/ technology is also important. For instance, solar farms require 5-10 acres per MW; meaning that, for direct air capture (DAC) of all emissions at about 35 - 40 $Gt\,yr^{-1}$, one would need a solar farm 12 times the size of Rhode Island; meaning that the footprint of the solar panels is actually larger than the DAC unit itself [43], so optimising the energy consumption is also important to keep a small overall footprint.

While the energy consumption is the most reported figure of merit for (electrochemical) CO_2 capture methods, a stable process at high current density (allowing high throughput) and a high product purity is required for a practical relevant process. Commercially relevant current densities are typically in the order of 100 $mA\,cm^{-2}$, while the minimum energy consumption is typically at an order of magnitude lower current density [39]. The gas purity is often defined as the molar fraction of CO_2 in the product gas. In the case of capture from dilute CO_2 sources, such as water or air, the recovery rate (for example the fraction of the entering stream captured) is less relevant, and often not reported.

1.4. FATE OF THE CAPTURED CARBON

Once separated, the captured CO_2 can be e.g., (1) injected (typically in a supercritical state, in deep geologic formations e.g., in underground saline aquifers and empty oil/ gas reservoirs); (2) mineralized (e.g., by injection into suitable mineral-rich formations e.g., basalt, yielding magnesium or calcium carbonates); or (3) further utilized in downstream processes such as electrosynthesis of chemicals or fuels (CCU, Figure 1.2). It must be noted that carbon utilization as chemicals or fuels cannot achieve net carbon removal, but is necessary to meet the industrial carbon demand, especially when little/ no fossil fuels are produced anymore. Consequently, so far, the main argument for utilization has been to provide cost offsets for adoption of capital-intensive capture systems, helping industries to encourage their earlier-stage adoption.

1.5. ION EXCHANGE MEMBRANES

The electrochemical bipolar membrane electrodialysis (BPMED) stack (Figure 1.2) consists of charged dense ion exchange membranes (IEMs, Figure 1.3). IEMs include cation-exchange membranes (CEM, negatively charged), anion-exchange membranes (AEM, positively charged), and bipolar membranes (BPM, cation- and an anion-exchange membrane laminated/ electro-spun together with a water dissociation catalyst in between [44, 45]). The choice of the IEM determines the dominant ion carrier.

Ion exchange membranes operate under application of an electrical field. Additional type of membranes used in carbon capture may operate under partial pressure gradient of CO_2(g), including (1) micro-porous gas-liquid contactors (for non-dispersive absorption), (2) dense membranes for gas permeation, and (3) supported liquid membranes (also known as immobilized liquid membranes) in which selectivity is given by the affinity of CO_2 with the liquid [46].

In addition to IEMs cost and life-time, their (perm)selectivity, and electrical resistance are the main considerations for the use in industry [39, 40, 46, 47]. In the case of the bipolar membrane for the pH-swing capture, decreasing the required voltage for the water dissociation reaction (WDR) towards its thermodynamic value (instead of the currently high voltage of ca. 0.83 V [48]) can reduce the energy consumption of the process by a factor three [49] (see Chapter 3).

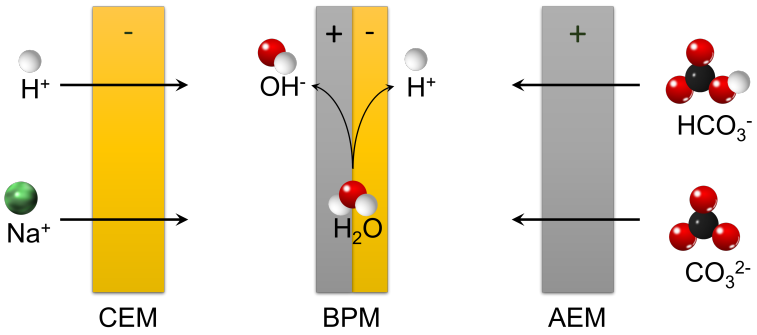

Figure 1.3: Three different types of ion exchange membranes (IEM), from right to left anion exchange membrane (AEM), which is selective for negatively charged (carbonic) species, bipolar membrane (BPM), which enables fast water dissociation, and cation exchange membrane (CEM), which is selective for positively charged ions.

1.6. THESIS OUTLINE AND RESEARCH QUESTIONS

Among capture technologies that remove CO_2 from the environment, the electrochemical methods already have proven their advantage over the traditional (thermal based) capture thanks to their sustainability, ease of retrofitting, higher efficiency, and especially their ability to capture CO_2 from diluted streams. Nevertheless, they are still much more expensive than the price of carbon in market (i.e., > 10×), particularly due to the amount and price of the required electricity. Aside from the price of electricity and carbon market, reducing the electrical energy consumption of the capture technology is the game changer for further capture developments. In pursuit of lowering the energy consumption of carbon capture, this work has investigated the *in-situ* oceanic carbon capture using bipolar membrane electrodialysis (BPMED).

The use of the bipolar membrane (BPM) in electrochemical cells is versatile; their ability to support charges via water dissociation allows to use them as a barrier between electrolytes and products in electrolysis, or to create a pH-swing in BPMED setups. The bipolar membrane has great potential in electrochemical energy applications and resource recovery [45]. However, current bipolar membranes are designed for production of high purity acid and base (i.e., large pH-swing of e.g., pH = 0 vs. pH = 14) and have not yet been optimized for other developing applications, such as resource recovery, carbon capture, and carbon conversion where a milder pH-swing is already acceptable [49]. While the BPM-selectivity is most important for acid/ base production, for the later applications (such as carbon capture), membrane ionic selectivity might be of less importance in comparison with e.g., the membrane resistance [49]. For the BPMED to be fully

deployed in these newer applications, further development and knowledge is required. Furthermore, despite its potential in offsetting excess atmospheric CO_2, data on oceanic carbon capture and particularly using electrochemical methods is very limited and (1) lacks guidelines to decrease the process energy consumption, (2) includes unknowns in operating at relatively low pH-differences, and (3) misses the opportunities for exploring the use of base stream in seawater CO_2 capture. In the framework of the necessary carbon capture, and the opportunities for electrochemical (ocean) CO_2 capture, the following research questions are addressed in the remainder of this thesis:

- What are current challenges, limitations, and advantages of implementing pH-swing based electrochemical carbon capture technologies on an industrial scale? (Chapter 2).
- What is the role of the pH-profile along the bipolar membrane (BPM) on its voltage when performing the water dissociation reaction? (Chapter 3).
- How to reduce the electrical energy consumption of the oceanic carbon capture performed via bipolar membrane-based *in-situ* mineralization? (Chapter 4).
- What is the most effective scaling management scenario when performing oceanic carbon capture using bipolar membrane-based *in-situ* mineralization? (Chapter 5).
- What are the large-scale impacts and costs of oceanic carbon capture technology performed via bipolar membrane electrodialysis (BPMED)? (Chapter 6).

A thorough literature review has been used for determining the current electrochemical technologies (Chapter 2) while a broader context for estimating the large-scale impacts and costs of oceanic carbon capture via BPMED is presented later (Chapter 6). An experimental approach is used for the findings in Chapter 3-5. Given the low TRL of the technology, both the acid route to isolate carbon species (as CO_2(g), Chapter 3) and the route of using base (to enable a product of $CaCO_3$(s), Chapter 4-5) are explored. Both synthetic seawater and real seawater are used to enable prototype demonstration in a relevant environment (Chapter 4), in order to increase the TRL of the technology to 5.

The findings in this work unlocks the potential for further upscaling and allows for subsequent research to process engineering of a practical carbon dioxide removal (CDR) plant from the ocean.

BIBLIOGRAPHY

[1] K. M. Diederichsen et al. “Electrochemical methods for carbon dioxide separations”. In: *Nature Reviews Methods Primers* 2.1 (2022), pp. 1–20.

[2] S. Bouckaert et al. “Net Zero by 2050: A Roadmap for the Global Energy Sector”. In: (2021).

[3] *IEA: Global Energy Review 2021*. https://www.iea.org/reports/global-energy-review-2021.

[4] *IEA: Global installed electrolyser capacity in 2020 and projects planned for commissioning 2021-2026*. https://www.iea.org/data-and-statistics/charts/global-installed-electrolyser-capacity-in-2020-and-projects-planned-for-commissioning-2021-2026.

[5] C. F. de Lannoy et al. “Indirect ocean capture of atmospheric CO2: Part I. Prototype of a negative emissions technology”. In: *Int. J. Greenh. Gas Control* 70 (May 2018), pp. 243–253.

[6] *IEA: About CCUS*. https://www.iea.org/reports/about-ccus. 2021.

[7] M. D. Eisaman et al. “Indirect ocean capture of atmospheric CO2: Part II. Understanding the cost of negative emissions”. In: *International Journal of Greenhouse Gas Control* 70 (2018), pp. 254–261.

[8] M. Roy-Barman et al. *Marine geochemistry: ocean circulation, carbon cycle and climate change*. Oxford University Press, 2016.

[9] A. J. Bard et al. “Electrochemical Methods: Fundamentals and Applications”. In: *Surface Technology* 20.1 (1983), pp. 91–92.

[10] G. Rochelle. “3 - Conventional amine scrubbing for CO2 capture”. In: *Absorption-Based Post-combustion Capture of Carbon Dioxide*. Ed. by P. H. Feron. Woodhead Publishing, 2016, pp. 35–67. ISBN: 978-0-08-100514-9.

[11] J. Blamey et al. “The calcium looping cycle for large-scale CO2 capture”. In: *Progress in Energy and Combustion Science* 36.2 (2010), pp. 260–279.

[12] A. Samanta et al. “Post-Combustion CO2 Capture Using Solid Sorbents: A Review”. In: *Industrial & Engineering Chemistry Research* 51.4 (2012), pp. 1438–1463.

[13] J. H. Rheinhardt et al. “Electrochemical capture and release of carbon dioxide”. In: *ACS Energy Lett* 2 (2 2017), pp. 454–461.

[14] R. Huebscher et al. “Electrochemical concentration and separation of carbon dioxide for advanced life support systems-carbonation cell system”. In: *SAE TRANSACTIONS*. Vol. 78. 1969, p. 151.

[15] M. P. Kang et al. “Concentration of carbon dioxide by a high-temperature electrochemical membrane cell”. In: *Journal of Applied Electrochemistry* 15.3 (1985), pp. 431–439.

[16] L. Walke et al. “Recovery of CO2 from flue gas using an electrochemical membrane”. In: *Gas Separation and Purification* 2.2 (1988), pp. 72–76.

[17] J. Winnick. “Electrochemical membrane gas separation”. In: 1990.

[18] H. Ishida et al. “Interaction between CO2 and Electrochemically Reduced Species”. In: *Chemistry Letters* 23.5 (1994), pp. 905–908.

[19] R. Ranjan et al. “Reversible electrochemical trapping of carbon dioxide using bipyridine that does not require thermal activation”. In: *The journal of physical chemistry letters* 6.24 (2015), pp. 4943–4946.

[20] P. Singh et al. “Electrochemical capture and release of carbon dioxide using a disulfide thiocarbonate redox cycle”. In: *Journal of the American Chemical Society* 139.3 (2017), pp. 1033–1036.

[21] C. Huang et al. “CO2 Capture from Flue Gas Using an Electrochemically Reversible Hydroquinone/Quinone Solution”. In: *Energy & Fuels* 33.4 (2019), pp. 3380–3389.

[22] Y. Liu et al. “Electrochemically mediated carbon dioxide separation with quinone chemistry in salt-concentrated aqueous media”. In: *Nature Communications* 11 (May 2020), p. 2278.

[23] B. Gurkan et al. “Quinone Reduction in Ionic Liquids for Electrochemical CO2 Separation”. In: *ACS Sustainable Chemistry & Engineering* 3.7 (2015), pp. 1394–1405.

[24] A. M. Appel et al. “Concentration of carbon dioxide by electrochemically modulated complexation with a binuclear copper complex”. In: *Inorganic chemistry* 44.9 (2005), pp. 3046–3056.

[25] S. Stucki et al. “Coupled CO2 recovery from the atmosphere and water electrolysis: Feasibility of a new process for hydrogen storage”. In: *International Journal of Hydrogen Energy* 20.8 (1995), pp. 653–663.

[26] I. A. Digdaya et al. “A direct coupled electrochemical system for capture and conversion of CO2 from oceanwater”. In: *Nature Communications* 11.1 (2020), pp. 1–10.

[27] M. D. Eisaman et al. “CO2 separation using bipolar membrane electrodialysis”. In: *Energy Environ. Sci.* 4 (4 2011), pp. 1319–1328.

[28] L. Legrand et al. “Solvent-Free CO2 Capture Using Membrane Capacitive Deionization”. In: *Environmental Science & Technology* 52.16 (2018). PMID: 29993236, pp. 9478–9485.

[29] M. Rahimi et al. “Bench-scale demonstration of CO2 capture with an electrochemically driven proton concentration process”. In: *RSC Adv.* 10 (29 2020), pp. 16832–16843.

[30] S. Jin et al. “pH swing cycle for CO2 capture electrochemically driven through proton-coupled electron transfer”. In: *Energy Environ. Sci.* 13 (10 2020), pp. 3706–3722.

[31] S. Jin et al. “Low energy carbon capture via electrochemically induced pH swing with electrochemical rebalancing”. In: *Nature communications* 13.1 (2022), pp. 1–11.

[32] D. Bove et al. “Process analysis of molten carbonate fuel cells in carbon capture applications”. In: *International Journal of Hydrogen Energy* 46.28 (2021), pp. 15032–15045.

[33] S. Campanari et al. “Economic analysis of CO2 capture from natural gas combined cycles using Molten Carbonate Fuel Cells”. In: *Applied energy* 130 (2014), pp. 562–573.

[34] J. Rosen et al. “Molten Carbonate Fuel Cell Performance for CO2 Capture from Natural Gas Combined Cycle Flue Gas”. In: *Journal of The Electrochemical Society* 167.6 (2020), p. 064505.

[35] L. Duan et al. “Study on coal-fired power plant with CO2 capture by integrating molten carbonate fuel cell system”. In: *Energy* 117 (2016), pp. 578–589.

[36] I. Sullivan et al. “Coupling electrochemical CO2 conversion with CO2 capture”. In: *Nature Catalysis* 4.11 (2021), pp. 952–958.

[37] A. Khurram et al. “Tailoring the Discharge Reaction in Li-CO2 Batteries through Incorporation of CO2 Capture Chemistry”. In: *Joule* 2.12 (2018), pp. 2649–2666.

[38] H. Bae et al. “Hybrid seawater desalination-carbon capture using modified seawater battery system”. In: *Journal of Power Sources* 410-411.July 2018 (2019), pp. 99–105.

[39] F. Sabatino et al. “Evaluation of a Direct Air Capture Process Combining Wet Scrubbing and Bipolar Membrane Electrodialysis”. In: *Industrial & Engineering Chemistry Research* 59.15 (2020), pp. 7007–7020.

[40] F. Sabatino et al. “A comparative energy and costs assessment and optimization for direct air capture technologies”. In: *Joule* 5.8 (2021), pp. 2047–2076.

[41] M. D. Eisaman et al. “CO2 extraction from seawater using bipolar membrane electrodialysis”. In: *Energy Environ. Sci.* 5 (6 2012), pp. 7346–7352.

[42] *European Environment Agency (EEA): Greenhouse gas emission intensity of electricity generation in Europe 2021*. https://www.eea.europa.eu/ims/greenhouse-gas-emission-intensity-of-1.

[43] W. A. Smith et al. “Pathways to Industrial-Scale Fuel Out of Thin Air from CO2 Electrolysis”. In: *Joule* 3.8 (2019), pp. 1822–1834.

[44] E. Al-Dhubhani et al. “Entanglement-Enhanced Water Dissociation in Bipolar Membranes with 3D Electrospun Junction and Polymeric Catalyst”. In: *ACS Appl. Energy Mater* (Mar. 2021).

[45] R. Parnamae et al. “Bipolar membranes: A review on principles, latest developments, and applications”. In: *Journal of Membrane Science* 617 (2021), p. 118538.

[46] P. Luis et al. “Recent developments in membrane-based technologies for CO2 capture”. In: *Progress in Energy and Combustion Science* 38.3 (2012), pp. 419–448.

[47] S. E. Renfrew et al. “Electrochemical Approaches toward CO2 Capture and Concentration”. In: *ACS Catalysis* 10.21 (2020), pp. 13058–13074.

[48] S. Z. Oener et al. “Accelerating water dissociation in bipolar membranes and for electrocatalysis”. In: *Science* (July 2020), p. 1487.

[49] M. A. Blommaert et al. “Insights and Challenges for Applying Bipolar Membranes in Advanced Electrochemical Energy Systems”. In: *ACS Energy Letters* 6.7 (2021). PMID: 34277948, pp. 2539–2548.

2

ELECTROCHEMICAL CARBON CAPTURE TO CLOSE THE CARBON CYCLE

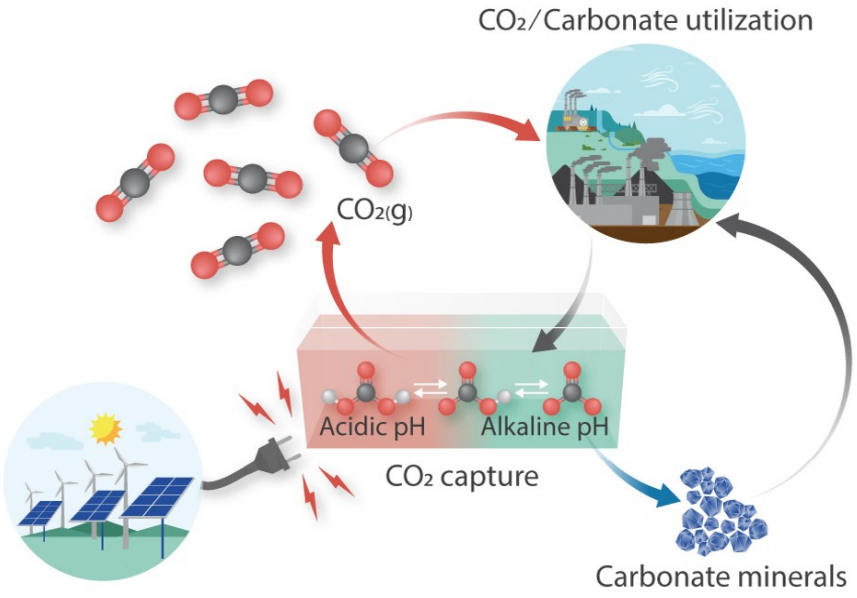

This chapter has been published as "Electrochemical carbon dioxide capture to close the carbon cycle", by R. Sharifian, R.M. Wagterveld, I. A. Digdaya, C. Xiang, D.A. Vermaas. Energy Environ. Sci. **14**, 781-814 (2021) [1].

Electrochemical CO_2 capture technologies are gaining attention due to their flexibility, their ability to address decentralized emissions (e.g., ocean and atmosphere) and their fit in an electrified industry. In the present work, recent progress made in electrochemical CO_2 capture is reviewed. The majority of these methods rely on the concept of "pH-swing" and the effect it has on the CO_2 hydration/ dehydration equilibrium. Through a pH-swing, CO_2 can be captured and recovered by shifting the pH of a working fluid between acidic and basic pH. Such swing can be applied electrochemically through electrolysis, bipolar membrane electrodialysis, reversible redox reactions and capacitive deionization. In this review, we summarize main parameters governing these electrochemical pH-swing processes and put the concept in the framework of available worldwide capture technologies. We analyse the energy efficiency and consumption of such systems, and provide recommendations for further improvements. Although electrochemical CO_2 capture technologies are rather costly compared to the amine based capture, they can be particularly interesting if more affordable renewable electricity and materials (e.g., electrode and membranes) become widely available. Furthermore, electrochemical methods have the ability to (directly) convert the captured CO_2 to value added chemicals and fuels, and hence prepare for a fully electrified circular carbon economy.

2.1. INTRODUCTION

To honour the Paris Agreement, a global *net* zero greenhouse gasses (GHG) emission needs to be realized by the end of this century [2–4]. Among all GHG's, CO_2(g) is accepted to be the main anthropogenic control knob on the climate and has been the focus of many studies [5, 6]. To achieve a net zero emission [7], reducing the total CO_2 emission obtains most impact in the short term [8]. The largest CO_2 emission is due to combustion of fossil fuels and thus can be reduced through fossil fuels phase out. However, although ultimately fossil fuels phase out might be possible for the power industry and transportation sector (through substitution with renewable energy), many sectors (e.g., steel/cement production, intercontinental air transport or non electrical trains) do not have a suitable alternative for carbon based fuels. In addition, due to the current agriculture techniques, the net global deforestation and the growing demand for carbon as a resource, CO_2 will be emitted due to many anthropogenic activities. Therefore, to achieve a net zero GHG's emission, in addition to emission reduction, CO_2 capture and utilization is required in the long term. Also, as the long term CO_2 emitters include decentralized emitters, direct capture from CO_2 sinks (e.g., atmosphere and ocean, see Figure 2.1 is necessary for effectively addressing the anthropogenic CO_2 emissions [9, 10].

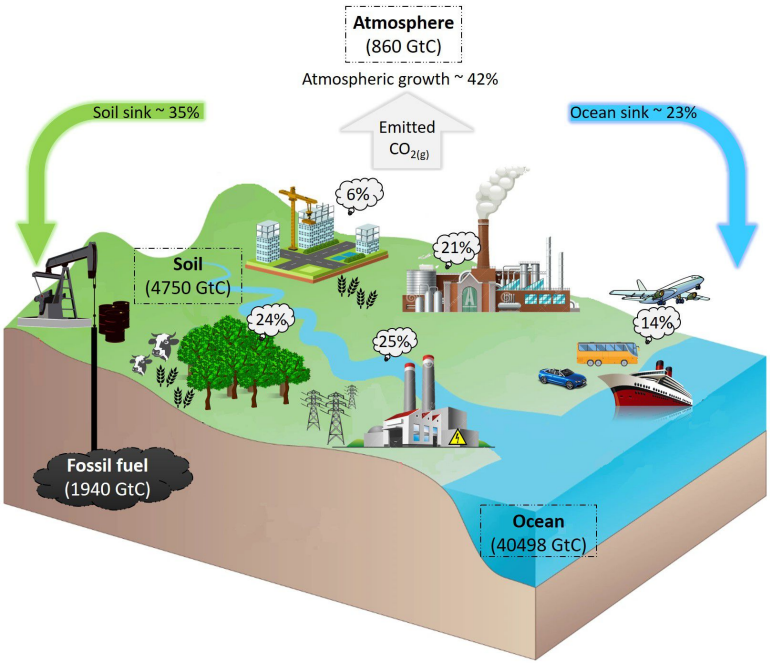

Figure 2.1: Schematic of the carbon cycle. The total carbon reserve is shown in gigatonnes of carbon (GtC). The global GHG emissions in CO_2(eq) by economic sectors: 25% Electricity and heat production, 24% Agriculture, forestry and land use, 6% Buildings, 14% Transportation, 21% industry and 10% other energy usages. Data extracted from [11–13].

The main challenge that currently available CO_2 capture methods face is a high energy consumption [14–16]. A few mature, non-electrochemical CO_2 capture technologies e.g., absorption, adsorption, membrane separation and cryogenic capture are already available in industrial scales [17–26], section (2.4). These methods often depend on the availability of thermal energy, which makes them less well suited for CO_2 capture from dilute sources e.g., air and ocean. Furthermore, the cost of direct air capture via traditional technologies has been estimated in the literature from $ 100 to $1000 per tonne of captured CO_2 [4, 27–29].

Electrochemical processes have the potential to be rather energy efficient as they can target molecules directly (instead of the medium surrounding them) [30, 31]. Using electrochemistry for CO_2 capture dates back to the late 1960s, when molten carbonates as electrolyte were used for CO_2 control in a manned spacecraft [32–35]. Nowadays, electrochemical CO_2 capture methods can be applied to all CO_2 containing streams with any concentration. Direct capture from air [36], ocean [9, 37] and flue gas [38–40] have been reported. Such capture units can be retrofitted as plug-and-play processes, allow small footprints and are geometrically flexible [40, 41]. They do not require external sources of heat or high pressures/ vacuum for operation, nor degradation of sorbent material is expected [41]. Although heat integration can be beneficial for power plants in reducing the need for energy, other industries (e.g., food and water sector) cannot integrate high heat, rising the need for technologies that can perform under low heat conditions from centralized emitters as well [15]. In electrochemical systems, the electric potential gradient is the main driving force which can be controlled precisely to drive chemical reactions isothermally [30, 31, 42]. A number of bench-scale capture demonstrations via electrochemical pH-swing have obtained CO_2 capture and release at the promising value of ~100 kJ mol^{-1} CO_2 [43, 44]. The added advantage of the electrochemical methods is their ability to integrate CO_2 capture and utilization [45] (section (2.5)). An example is the modular, sequential CO_2 capture and conversion system that uses the pH-swing concept to produce CO electrochemically [46, 47]. In addition, reactive CO_2 capture, in which the CO_2 capturing medium pre-concentrates the dilute feed and produces favorable local micro-environments, has become an emerging field for integrated CO_2 capture and conversion using electrochemical techniques [48, 49].

A wide variety of efforts to electrochemically capture CO_2 has been demonstrated in the past 50 years, with an intensification of research activities in the last two decades. In this work we give an overview of such advances. The center of our scope are the electrochemical methods that use a pH-swing concept, as shown in Figure 2.2 (a) and (b). The swing refers to (electrochemically) shifting the pH of a working fluid (continuously) between basic and acidic pH to influence the CO_2 equilibrium to capture and recover CO_2.

The pH-swing allows absorption and desorption at ambient temperature and does not require use of any special chemicals. Widely available, inexpensive, non toxic/ non corrosive/ non volatile salt solutions, such as NaCl, KCl, $KHCO_3$ or even seawater can be used for the process. The pH-swing can be applied electrochemically using electrolysis, bipolar membrane electrodialysis (BPMED), capacitive deionization and reversible PCET agents as demonstrated in Figure 2.3. In this work, after providing the required theoretical background in section (2.2), each pH-swing route is explained and the re-

search of this route is comprehensive reviewed in section (2.3). In addition to a pH-swing approach, other electrochemical technologies involve using redox-active carriers [50] (section (2.3.3)), molten carbonate cells and hybrid methods (section (2.3.4)) such as electrochemically enhanced absorption/ adsorption [30, 31]. To enable comparison, we also briefly describe the main conventional capture methods, their drawbacks and advantages, and opportunities to improve these technologies with electrochemical methods, in section (2.4). Finally, CO_2 utilization and storage is discussed briefly in section to close the carbon cycle (2.5).

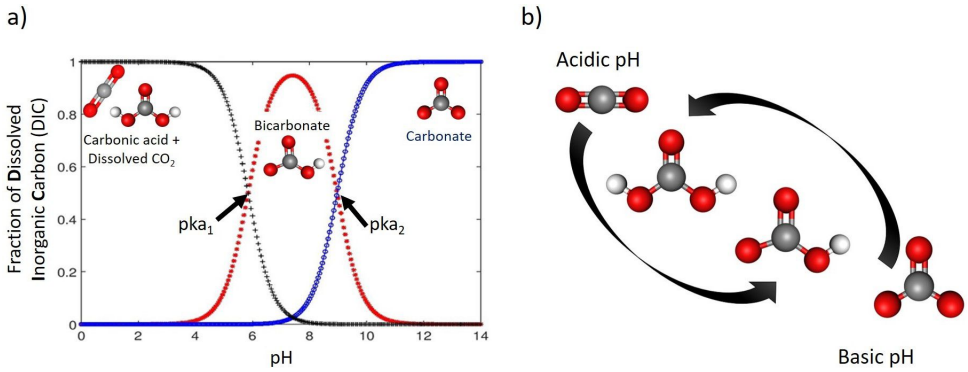

Figure 2.2: a) Effect of pH on the CO_2 equilibrium (for a closed system at temperature of 25 °C and salinity of 35 ppt). The solution is buffered around two pKa values. b) Schematic of the pH-swing concept.

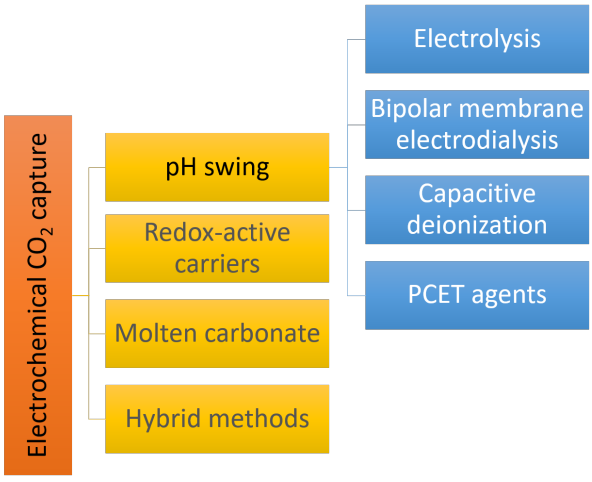

Figure 2.3: Summary of electrochemical CO_2 capture methods.

2.2. THEORY: PH-SWING CONCEPT AND INVOLVED REACTIONS

The concept of CO_2 capture via pH-swing leverages the responsiveness of the thermodynamic equilibrium of CO_2 to pH changes. A pH-swing is also used for other resource recovery applications than CO_2 capture, but the method is not always explicitly referred to as "pH-swing". For instance, pH-swing is employed to recover ammonia electrochemically from urine [51, 52] and to remove phosphate from waste water streams [53].

2.2.1. CARBONATE EQUILIBRIUM

The carbonate equilibrium can be described as open or closed based on the contact with an overlying gas and is explained in detail in [54–57]. In an open system, the total concentration of the dissolved inorganic carbon varies by changing in the pH; Acidification results in CO_2(g) out-gassing, while basification lead to more CO_2(g) absorption, increasing the DIC. In a closed system (e.g., inside of an electrochemical cell), the total DIC remains constant regardless of any pH changes. If so, the dominant carbonic species alter by changing the pH as demonstrated in Figure 2.2 (a). The equilibrium can be shown through reaction (2.1) to (2.4):

$$CO_2(g) \rightleftharpoons CO_2(aq) \tag{2.1}$$

$$CO_2(aq) + H_2O \rightleftharpoons H_2CO_3 \tag{2.2}$$

$$CO_2(aq) + OH^- \rightleftharpoons HCO_3^- \tag{2.3}$$

$$OH^- + H^+ \rightleftharpoons H_2O \tag{2.4}$$

Reaction (2.1) is dependent on the fugacity of CO_2(g) and often described through Henry's law (see section (2.2.3)). It is often assumed to be really fast (i.e., 10^{10} s^{-1} in both directions) in a well-mixed scenario (i.e., only mass-transport limited) [56, 58, 59]. For experimental values of reaction rates k_1, k_{-1} (Equations 2.2) and k_2, k_{-2} (Equations 2.3) see references [58, 60, 61]. As the pH increases, reaction (2.3) pushes the equilibrium towards HCO_3^-, and it predominates reaction (2.2) above pH 8.5 [60]. See section (2.2.2) for more discussion on the kinetics of the reactions. The total dissolved inorganic carbon, DIC, can be described as the summation of the concentration of all present carbonic species:

$$DIC = [H_2CO_3^*] + [HCO_3^-] + [CO_3^{2-}] \tag{2.5}$$

Where $H_2CO_3^* = H_2CO_3 + CO_2$(aq). In multi-ionic systems, additional carbonate species or complexes (e.g., $NaCO_3^-$ and $NaHCO_3$(aq)) are present in the definition of DIC, as well [62, 63].

2.2.2. REACTIONS KINETICS AND HOW TO IMPROVE IT

To capture and release CO_2(g) through a pH-swing, both thermodynamics and kinetics play a role [58, 60]. Assuming thermodynamic equilibrium, the equilibrium ratio of $\frac{[H_2CO_3^*]}{[HCO_3^-]}$ changes by a factor of more than 100 over when using a small pH-swing of only 2 pH-units, see Figure 2.2 (a). However, although such a narrow pH-swing is thermodynamically favourable and enables lower energy consumption, it suffers from slow

kinetics. At near neutral pH, the CO_2 hydration rate is $\simeq 2.9 \times 10^{-2}$ s^{-1} and the (HCO_3^-) dehydration rate is $\simeq 2 \times 10^{-4}$ s^{-1} [43, 61]. These reaction rates are a function of e.g. temperature and ionic strength of the system [64–66]. To overcome the slow kinetics, (1) a wider range of pH-swing or (2) a reaction catalyst need to be applied. As for a wider pH-swing range, the base promoted hydration rate of the CO_2/HCO_3^- system is reported to be $\simeq 6 \times 10^3$ $M^{-1}s^{-1}$ and the acid-promoted dehydration rate is increased to $\simeq 4.1 \times 10^4$ $M^{-1}s^{-1}$ [43, 60, 61, 66]. Alternatively, the use of a catalyst such as the Carbonic Anhydrase (CA) enzyme (CA, [67]) is suggested for improving the kinetics [43, 68, 69]. CA is reported to enhance both the CO_2 hydration and dehydration reaction kinetics; Hydration rate constant $\simeq 10^5$ s^{-1} and dehydration rate constant ~10^6 s^{-1} near a neutral pH of 7 are reported [67]. However, although initially effective, such enzyme is not stable, and is prone to enzyme loss, deactivation, or degradation. Investigation on improved catalysts is recommended, but until such catalysts are developed, to effectively capture and recover CO_2, a wider range of pH-swing ($pH < pKa_1$ and $pKa_2 < pH$) is needed for capture application.

2.2.3. INORGANIC CARBON SOLUBILITY

In equilibrium, the concentration of free CO_2 in water (i.e., [CO_2(aq)]) is proportional to its partial pressure in the gas phase; According to the Henry's law, $[CO_2(aq)] = K_0 \times f_{CO_2(g)}$ where K_0 (in $mol\,L^{-1}atm^{-1}$) is the solubility coefficient of CO_2(g) and $f_{CO_2(g)}$ stands for the gas fugacity (in atm), which is close to the partial pressure of CO_2(g) (within 1%). Figure 2.4 (a) shows the solubility of CO_2 as a function of temperature and CO_2 partial pressure. At elevated alkalinity, the total solubility of CO_2(g), and hence DIC (in Eq.2.5) increases due to reaction (2.3) route. Figure 2.4 (b) shows the solubility of DIC as a function of the water pH and the partial pressure of CO_2. See the supporting information for the used equations and references.

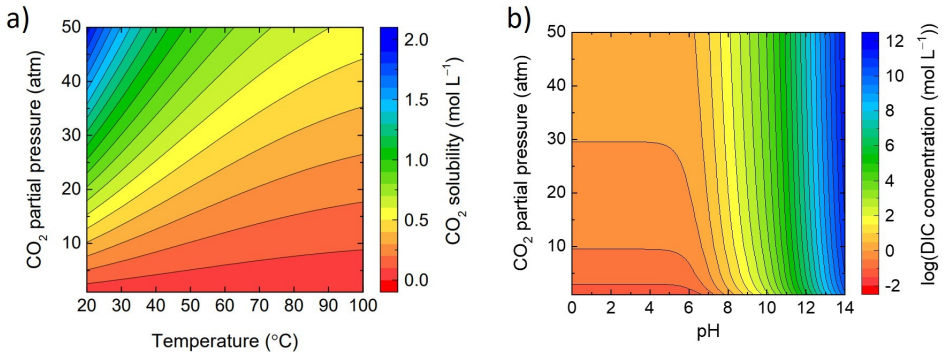

Figure 2.4: (a) CO_2 solubility in water as a function of the temperature and CO_2 partial pressure. (b) Logarithmic solubility of dissolved inorganic carbon (DIC) in water at 25 °C as a function of the water pH and CO_2 partial pressure.

2.2.4. INPUTS AND METRICS

Figure 2.5 demonstrates input parameters and the metrics of electrochemical CO_2 capture based on a pH-swing. The feed, cell, process and kinetics can be leveraged for the product/ output. The main challenge such capture technologies are facing is their (estimated) high Capex, resulted from a high energy consumption and the immaturity of the technology [4]. Data on Capex of electrochemical methods is still scarce, making the energy consumption (at high current density and capture efficiency) the most practical metric of comparison. Thankfully, despite the currently high energy consumption, optimization of the process and cell parameters can significantly decrease the energy loss involved in such processes as explained in section (2.3.2) and (2.3.5).

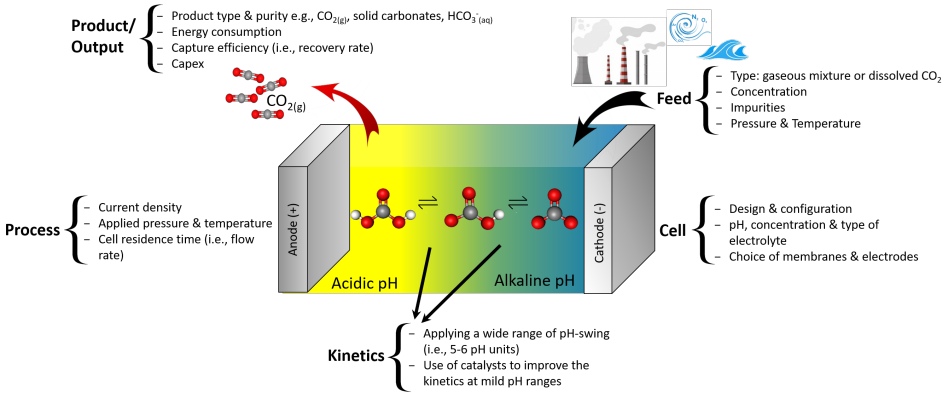

Figure 2.5: Input and metrics of electrochemical pH-swing based CO_2 capture and the overall process concept.

2.3. ELECTROCHEMICAL PH-SWING CONCEPTS

Electrochemically induced pH-swings for CO_2 capture have been demonstrated through (membrane) electrolysis, bipolar membrane electrodialysis, reversible redox couples, capacitive deionization and hybrid processes that combine two or more methods as shown previously in Figure 2.3. In this section we introduce each method separately and compare them in terms of feasibility, energy consumption, energy efficiency and technology readiness level (TRL).

2.3.1. ELECTROLYSIS

Electrolysis can enable the pH-swing in the vicinity of (two) electrodes as shown in Figure 2.6. (Membrane) electrolysis for CO_2 capture is used for alkali absorbent (re)generation [39, 70–74] or simultaneous H_2 production [37, 75–77]. H_2 production can (partially) offset the cost of CO_2 capture and is possible when water electrolysis takes place. In the earliest work done by Stucki *et al.*, CO_2 is absorbed from a flue gas in an KOH absorbent, the resulted (bi)carbonate solution is fed into the electrolyser (for alkaline regeneration), where CO_2 is recovered and H_2 is produced via the following reaction:

$$2H_2O + K_2CO_3(aq) \rightarrow 2KOH(aq) + CO_2(g) + H_2(g) + 0.5O_2(g) \tag{2.6}$$

The KOH can be used as absorbent for capturing CO_2, turning into $K_2CO_3(aq)$, which can be fed again to the electrolysis system.

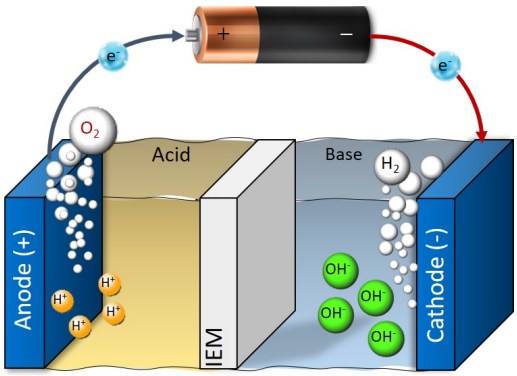

Figure 2.6: Schematic of water electrolysis. Depending on the catholyte/ anolyte (air, water etc.), applied voltage and the pH of the medium, different half reactions take place

One downside in such systems is that the cell voltage has, in addition to 1.23 V for water splitting, a contribution from the pH difference between the anolyte and the catholyte, represented by Nernstian potential of $\Phi = 0.059\Delta pH$ (in volts) at 25 °C, as shown in the Pourbaix diagram (Figure 2.7) [75]. When using an extreme pH gradient (pH 0 at anode, pH 14 at cathode), this would imply a 2.06 V for balancing the free enthalpy of the reaction.

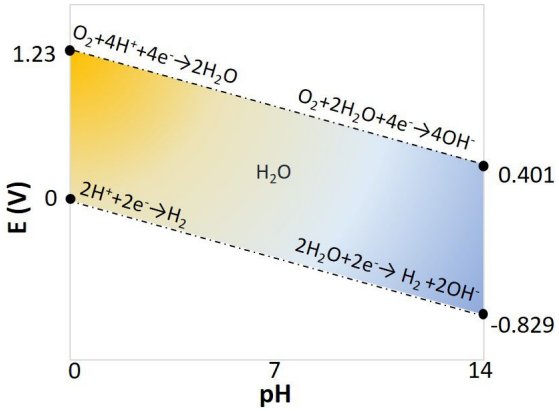

Figure 2.7: Pourbaix diagram of water electrolysis [78].

Using the pH-swing in electrolysis, the CO_2 can be either released as (purified) gas (e.g., via reaction (2.6)), or as (bi)carbonate products in the work of Rau and Park *et al.* [71, 72, 76, 79]. The latter has been demonstrated for $Ca(HCO_3)_2$(aq) (Figure 2.8 (a)) and [72, 76] solid carbonate mineral as shown in Figure 2.8 (b) [71]. Natural (mined and crushed) carbonate minerals are used to provide Ca^{2+} in Figure 2.8 (a). Through reaction (2.7), CO_2 can be removed from an overlying gas mixture (e.g., air or flue gas). The produced $Ca(HCO_3)_2$(aq) can be diluted and stored in the ocean, water reservoirs or underground:

$$2H_2O + CaCO_3(s) + CO_2(g) \rightarrow Ca(HCO_3)_2(aq) + H_2(g) + 0.5O_2(g) \tag{2.7}$$

Capture of 1 mole of CO_2(g) for each mole of $CaCO_3$ via reaction (2.7) is possible, while 22 tonnes of CO_2 can be captured per tonne H_2 generated (assuming a 1:1 molar ratio) [72]. This implies that, depending on CO_2 emission involved in the operation (e.g., for supplying electricity and for limestone/carbonate mining, crushing and transport), the system has the potential of producing carbon-negative hydrogen [80].

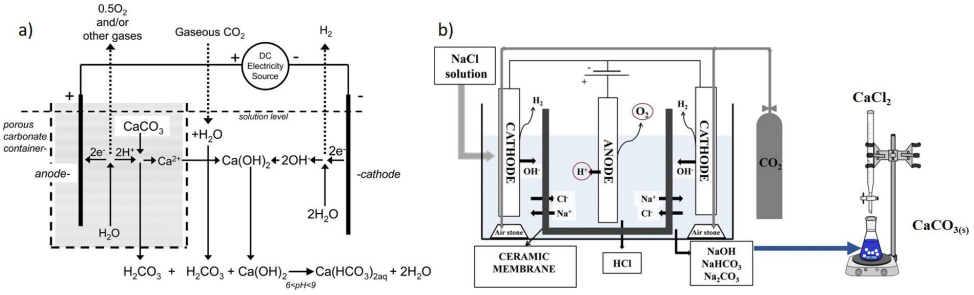

Figure 2.8: a) H^+ ions at the anode dissolve $CaCO_3$(s), the resulted Ca^{2+} ions move towards the cathode, forming $Ca(HCO_3)_2$(aq). Reprinted (adapted) with permission from [72]; Copyright (2008) American chemical society. b) NaCl electrolysis, where NaOH is used as the CO_2(g) absorbent and $CaCO_3$(s) is the final capture product, Figure from [71]. Both approaches use the concept of placing the anode inside of a porous container.

The process efficiency in Figure 2.8 (a) can be enhanced e.g., by:

- Improving the mass transfer between the overlying gas and the absorbent (to improve CO_2(g) dissolution).
- Introducing an ion selective membrane between the electrodes (to avoid unwanted secondary reactions).

Alternative to water electrolysis, salt electrolysis, such as NaCl [70] and KCl [39] can also be used for CO_2 capture. If so, only an alkaline pH (at the cathode) is enabled, because at the anode e.g., the reaction $2Cl^- \rightarrow Cl_2(g) + 2e^-$ takes place instead of the oxygen evolution reaction (OER) [71]. The produced alkalinity at the cathode can then be utilized to sequestrate CO_2 in the form of carbonate salts. When the capture product is $CaCO_3$(s), no CO_2(g) desorption step is required. Furthermore, $CaCO_3$ is easier to transport and store compared to CO_2(g). NaCl electrolysis for alkaline absorbent (re)generation follows reaction (2.8) [70]:

$$2H_2O + 2NaCl(aq) \rightarrow 2NaOH(aq) + Cl_2(g) + H_2(g) \tag{2.8}$$

Using salt electrolysis for CO_2 capture is especially interesting due to salt availability in the seawater, leveraging possible substitution of the electrolyte with abundant seawater [70]. The produced (toxic) Cl_2(g) at the anode can be treated by the produced NaOH solution using a scrubber, or can alternatively be utilized as a feedstock for the synthesis of HCl, Cl containing polymers and bleaching agents [70]. Alternatively, using water electrolysis and by inserting two ion exchange membranes (IEMs) between the electrodes (Figure 2.9), produces H_2 simultaneous acidifies seawater to recover CO_2(g) [37, 81, 82]. The use of two IEMs avoids the production of Cl_2(g) and electrode contamination.

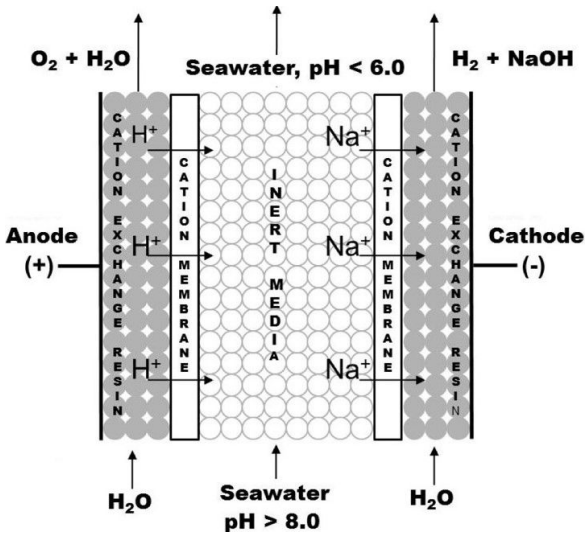

Figure 2.9: CO_2 capture and H_2 production via sea water acidification and water electrolysis. In the middle compartment, cation exchange resins are used. Reprinted (adapted) with permission from [82]; Copyright (2014) American chemical society.

When applying electrolysis using a reversible redox reaction - thus no net gas production - saves energy. For example, the production of O_2(g) (or Cl_2(g)) can be avoided by recirculating the produced H_2(g) from the cathode to the anode compartment [73, 74]. Alternatively, H_2 production can be avoided if O_2 reduction takes place on the cathode, instead of the H_2O reduction [83]. At the cathode, depending on availability of O_2 or H_2, two possible reactions may exist for OH^- production:

$$2H_2O + O_2 + 4e^- \rightarrow 4OH^- \qquad (E^0 = 0.401\,V \text{vs. SHE}) \tag{2.9}$$

$$4H_2O + 4e^- \rightarrow 2H_2(g) + 4OH^- \qquad (E^0 = -0.83\,V \text{vs. SHE}) \tag{2.10}$$

When sufficient O_2 is available at the cathode, or sufficient H_2 at the anode, the H^+/OH^- generation can take place in a practical cell voltage range of 1.3 V to 2.2 V through reaction (2.9). The supply of sufficient gas to the opposing electrode can be assisted by using gas diffusion electrodes [84]. Without recirculating the gaseous products, the cell voltage is typically > 2.2 V [83]. From a thermodynamic point of view, the use of (net) water electrolysis requires a significant thermodynamic minimum energy (1.23 V for water splitting), in addition to the potential required for generating a pH difference (see Figure 2.7) [78, 85]. Considering the necessity of a wide pH-swing to enhance the carbon equilibrium kinetics, and using pH 0 and 14 to favour electrolyte conductivity, a minimum of 2.06 V is required, corresponding to 199 kJ/mol CO_2. Furthermore, in almost all demonstrated devices/systems, the rate of CO_2 capture is locked with the rate of H_2 or O_2 generation, which sometimes may not be desirable and present additional challenges for multi-stack development of the system. These drawbacks can be addressed using bipolar membrane electrodialysis as explained in the following section.

2.3.2. BIPOLAR MEMBRANE ELECTRODIALYSIS (BPMED)

A Bipolar membrane (BPM) consists of an anion (AEL) and a cation (CEL) exchange layers, laminated together. When a sufficient electric field is applied, the BPM dissociates water into OH^- and H^+, producing a controllable ΔpH over the membrane as shown in Figure 2.10 (a) and b [86–91]. Using a bipolar membrane, the thermodynamic minimum voltage required for this water dissociation is 0.829 volts for a produced ΔpH = 14. That is 2.5× lower than that of water electrolysis at the same ΔpH = 14 (1.23 + 0.829 at minimum), as no gas evolution takes place using a bipolar membrane [86]. The thermodynamic voltages over the BPM are even lower for smaller ΔpH over the membrane [85, 89].

The feasibility of using bipolar membrane electrodialysis for pH-swing based CO_2 capture is shown in early studies in 1995 [92]; Alkaline KOH and acidic H_2SO_4 were regenerated in a two compartment BPMED cell, containing a BPM and a cation exchange membrane. After CO_2 from air is captured in KOH absorbent, it can be recovered through acidification. The produced K_2SO_4 is treated in the BPMED cell to regenerate the desired acid and base again. CO_2 capture via BPMED has been further explored by others, and these works are addressed in more details in next sections.

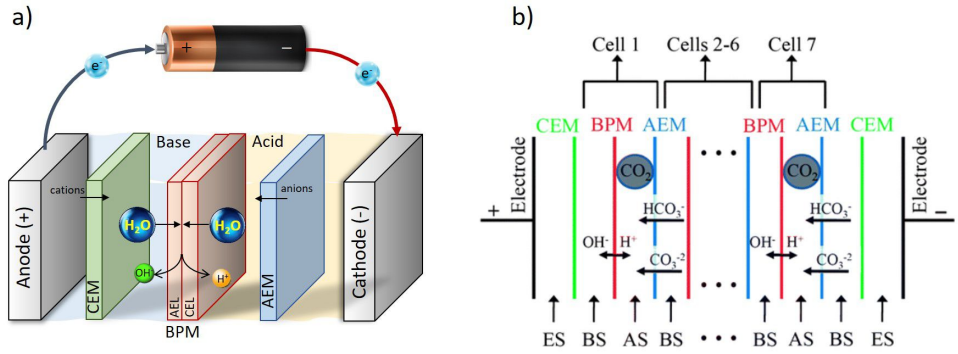

Figure 2.10: a) BPMED schematic. b) BPMED for CO_2 recovery in [93]. (ES) electrode solution = KOH, (AS) acid solution of KH_2PO_4 + H_3PO_4, (BS) base solution of six different mixtures of $KHCO_3$, K_2CO_3 and KOH. Figure adapted from [93].

ENERGY CONSUMPTION AND CAPTURE EFFICIENCY

In BPMED, a trade off between the energy consumption and the process rate, determined by the applied current density, exists. Operating at very low current densities is not effective due to the higher salt ion leakage through the BPM and hence the lower water dissociation rate [93]. On the other hand, at high current densities, the ohmic voltage losses increase, leading to an undesirable higher energy consumption (see supporting information).

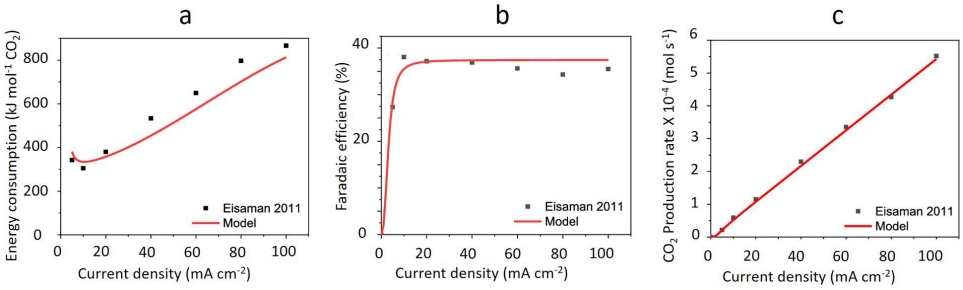

Figure 2.11: Trend of energy consumption, faradaic efficiency and CO_2 production rate vs. current density in CO_2(g) recovery from 0.125 M K_2CO_3-rich solution via BPMED. The black squares are experimentally measured data by [93] while the red lines show the calculated values performed by [4]. Reprinted (adapted) with permission from [4]; Copyright (2020) American chemical society.

Figure 2.11 (a) shows the minimum energy consumption for CO_2(g) recovery from 0.125 M K_2CO_3-rich solution via BPMED at a current density around 10 mA cm^{-2} [4]. However, although the energy consumption is the lowest at that current density, production rate favours higher current densities as shown in Figure 2.11 (c). The experimentally measured current efficiency (i.e., faradaic efficiency) in Figure 2.11 (b) shows - in addition to its low values at $i < 10$ mA cm^{-2} due to salt cross-over - a slight decreases at $i > 20$ mA cm^{-2}. It is hypothesized that current densities above the optimum value, reduce the

BPM's permselectivity [94] or enhance the water splitting reaction in the AEM's [95, 96], leading to a lower efficiency [93]. The current efficiency also decreases if the current is carried by an undesired ion through the membranes. For example, in Figure 2.10 (b), the (bi)carbonate ions are the desired current carriers. However, if (as a result of high pH) OH^- ions become the main charge carrier through the AEM, the current efficiency decreases. On the other hand, when capturing CO_2(g) from flue gas or in DAC, a high pH (i.e, high [OH^-]) is favoured in the outlet of the same compartment, because CO_2(g) absorption capacity and rate increase in a solution with high pH. Adopting monovalent-ion-selective AEM's that favour the transport of HCO_3^- ions over OH^- ions then could improve the efficiency when such process is intended [4, 97].

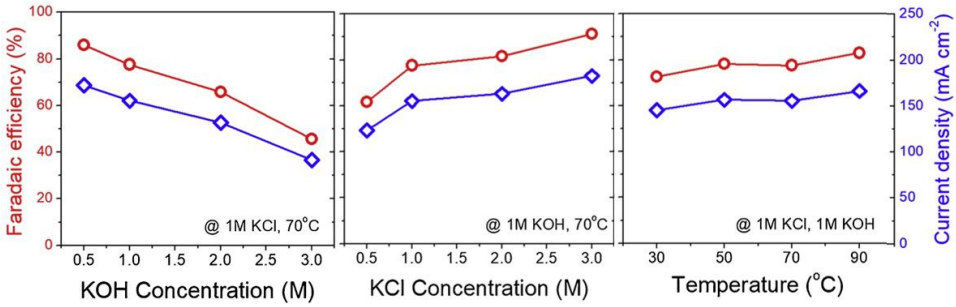

Figure 2.12: Change of the measured current density (blue diamond line) and faradaic efficiency (red circle line) with regards to the change in catholyte concentration, anolyte concentration and the applied temperature in an electrochemical KOH (absorbent) production via KCl electrolyser. Reprinted from [39], Copyright (2019), with permission from Elsevier.

As opposed to what is shown in Figure 2.11 (b), the current efficiency of BPMED can reach as high as 95% if e.g., a 0.5 M $KHCO_3$ is used instead of the 0.125 M K_2CO_3 for CO_2(g) recovery through acidification. In fact, both in BPMED and (membrane) electrolysis, in addition to the current density, the anolyte and catholyte concentrations and the operation temperature affect the current efficiency, as demonstrated in Figure 2.12 [39] and summarized in Table (2.1). The (slightly) positive effect of temperature on improving the faradaic efficiency of electrochemical methods has been reported [39, 70]. Higher temperatures improve the electrochemical reaction rates. In the case of BPMED, the kinetics of water dissociation in BPM is also enhanced at elevated temperatures [98, 99]. However, in addition to the extra energy needed for heating up the electrolytes, the thermal stability of the ion exchange membranes poses a limitation on high temperature processes. For instance, the commercial bipolar membranes are cannot withstand temperatures higher than 40-60 °C for a long duration [100]. Moreover, CO_2 solubility decrease at higher temperatures (up to 100 °C) [101–103]. This means that operating at high temperature is not yet practical. A breakdown of energy consumption and comparison for (membrane) electrolysis and BPMED is provided in section (2.3.5) and the supporting information.

CELL CONFIGURATION

The cell configuration defines the number of membranes, membrane cell pair arrangement, electrolyte flow path and the thickness of the compartment/ membrane. The design of the cell is the most important factor to minimize the cell resistance [75]. As opposed to the BPMED for traditional acid and base production (i.e., BPM-CEM-AEM-BPM), the pH-swing process for CO_2 capture allows a simplified membrane sequence due to the limited pH-range (i.e., pH 3-9 instead of 0-14).

In choosing the optimised configuration, the (co-)ionic leakage of the membranes is crucial. When using multi-ionic CO_2 feed, such as seawater, carbonic species should be rejected to obtain a maximum capture efficiency. Carbonic species are neutral (e.g., CO_2(aq) and H_2CO_3) or negatively charged and hence are rejected better by a CEM than by an AEM. In addition to higher selectivity, the use of CEM's instead of AEM's have proven to increase conductivity and mechanical stability in a BPMED cell for CO_2 capture [73, 104]. For further reducing co-ionic cross-over, a trade off between the permselectivity of IEM's and their resistance should be considered, which is controlled by the membrane thickness. In general, thicker membranes have higher resistivity but show a better selectivity [73]. Applying a reinforced structure to a thinner membrane can improve its selectivity while maintaining its resistivity to a certain extent [73, 105].

Depending on the charge carriers in the cell, the flow mode (i.e., one-way pass vs. batch mode) and feed concentration, each BPMED process asks for a different cell configuration. While BPM-CEM might be the choice of some researchers for CO_2 recovery from carbonate solutions [106, 107], others chose a BPM-AEM [44, 93] for the same purpose. That is while novel configurations as BPM-AEM-AEM are also emerging for minimizing BPM fouling when extracting $CaCO_3$ from seawater [108], see section (2.3.2).

HIGH PRESSURE BPMED

In a closed system (such as the one created inside of an electrochemical cell), acidification increases the concentration of dissolved CO_2. This concentration can lead to the formation of CO_2(g) bubbles inside of the cell. Theoretical models, suggest the trapped CO_2 in the acid solution dominate the cell resistance and increase the energy consumption [109]. Trapped gas bubbles lower the effective membrane surface area, cause high voltages and shorten the membrane lifetime (due to localized "hot spots" of high current density). To avoid gas production inside of the cell, Eisaman *et al.* [44] proposed a high pressure BPMED process using a similar cell as shown in Figure 2.10 (b) where the entire stack is kept at high pressure, i.e., there is no pressure difference *across* the membranes in the stack. The authors observed that by increasing the pressure, the total cell voltage decreases due to the avoided CO_2 gas bubbles production in the cell; the electrochemical energy required at 6 atm (333 kJ mol$CO_2{}^{-1}$) was seen to be 29% less than that of 1.5 atm (471 kJ mol$^{-1}CO_2$) at a current density of 139 mA cm^{-2}.

BPMED FOR CARBON CO_2 EXTRACTION FROM SEAWATER

The ocean is a massive sink for CO_2 [12, 110, 111]. The higher carbon content of the ocean compared to that of the atmosphere [9, 55, 112] makes the ocean an interesting source for CO_2 capture [110]. Moreover, as opposed to the separation of CO_2 from a gas mixture that involves *two* steps (i.e., capture and release), in CO_2 capture from seawater, a separate CO_2(g) adsorption/absorption step is not required, because the ocean already

acts as CO_2 absorbent leveraging its gigantic surface. The ocean contain DIC of ~2.3-2.5 mM, mainly in the form of HCO_3^- ions, in normal seawater of pH ~8.1. The product of seawater CO_2 capture can be (1) gaseous CO_2 [9], (2) solid carbonates [108], or (3) dissolved bicarbonates and carbonates ions (to be subsequently stored in the ocean) [72, 76, 79, 113].

To extract the CO_2 as gas, the bi-/ carbonate ions present in the seawater can be converted into $H_2CO_3^*$ in the acidic compartments adjacent to the BPM [114]. Subsequently, through vacuum stripping of the acidified stream using membrane contactors, CO_2(g) can then be produced [9, 114].

Alternatively, at alkaline pH > pKa_2, HCO_3^- converts to CO_3^{2-} and can subsequently precipitate through reaction with dissolved Mg^{2+} or Ca^{2+} [9, 108]. When the partial pressure of CO_2 remains unchanged, the pH determines which mineral is obtained e.g., the precipitation of $CaCO_3$ (in synthetic seawater) is favoured in 9.3 < pH < 9.6 [9, 115]. Considering that the Ca^{2+} and Mg^{2+} concentrations in seawater are respectively 4× and 25× higher than that of DIC, mineralization has the potential to remove all DIC, theoretically [116]. In addition, mineralization eliminates the expenses of using a membrane contactor [117, 118].

In the third option, converting CO_2 to dissolved alkaline bicarbonates and carbonates enables carbon sequestration. This is a long-term carbon storage which also helps against ocean acidification by increasing the ocean alkalinity [72, 76, 79, 113]. However, further research is required for understanding the full range and capacity of such approach.

The main bottlenecks in using *in-situ* BPMED for this mineral crystallization are the risk of membrane contamination (i.e., fouling) in the stack and the slow kinetics of the carbonate precipitation. To avoid the fouling, pure NaCl (instead of seawater) can be used in the BPMED for NaOH and HCl production [9]. The produced NaOH is then added to the seawater stream in a controlled crystallizer to initiate the precipitation. In order to improve the kinetics of the precipitation, use of a seeded crystallizer unit is suggested [108, 119]. Although seawater CO_2 capture through mineralization is shown feasible, debates on the environmental impacts of reducing Ca^{2+}/Mg^{2+} concentration of the ocean are in progress [116, 120].

ELECTRODEIONIZATION (EDI)

Electrodeionization (EDI) combines ion exchange membranes technology with ion exchange resins [121–126]. Ion exchange resins are solid cross-linked polymers that contain fixed charged groups typically based on acrylic or styrene monomers. When filling the flow compartments with beads or 3D structures of ion exchange resins, the polymer-electrolyte interface area is increased [127]. The combination can help overcome the concentration polarization losses associated with electrodialysis and electrolysis. The major application of electrodeionization (EDI) includes the removal/ recovery of heavy metals and organic acids for pure water production [128–132]. The combination of BPMED with resin wafer electrodeionization (RW-EDI) is demonstrated in the lab-scale, where porous, solid matrix of ion-exchange resin beads are incorporated in between of the CEM's and BPM's in the cell [43]. However, unfortunately, data on the energy consumption and current efficiency of the system is not reported. The combination of electrodeionization (EDI) with electrolysis is shown feasible as demonstrated in Figure 2.9

[77, 82]. However, as shown in Table (2.1), the process still requires further optimization (in terms of production of H_2(g) and cost/ stability of resins) to decrease its significant energy consumption. Furthermore, the (bio)fouling of the resin beads due to the contact with seawater decreases the overall efficiency of the method and needs yet to be addressed.

The pH-swing based EDI application for CO_2 capture has only been explored at a basic level [128]. More work has been done on the use of amine based ion exchange resins as adsorbent for CO_2 capture, through thermal swing. Such resins are reported to show good stability after repetitive adsorption-desorption cycles with only a small reduction in capture capacity, and require relatively mild desorption conditions [127, 133, 134]. Recently, wafer enhanced electrodeionization for conversion of CO_2 into HCO_3^- feed for algae cultured photobioreactors is reported [135]. Suggestions for further research on EDI technology are producing inexpensive ion exchange resins, reducing possibility of resin fouling (e.g., for the case of seawater feed [77]), and maintaining long-term resin stability [128].

2.3.3. REDOX-ACTIVE CARRIERS AND ELECTRODE REACTIONS

An alternative to BPMED and electrolysis for CO_2 capture, is the more classical electrochemical separation strategies that perform absorber/desorber cycles using specific redox-active sorbent carriers [40, 50]. These redox-active carriers can be used for separation of CO_2(g) from a gas mixture through (1) binding route Figure 2.13 (a) and (2) pH-swing route Figure 2.13 (b). Both routes have been demonstrated feasible in the lab-scale [136, 137]. As for the "binding route", the suitable carrier is activated at the cathode and can bind with the target species at its reduced state. The target species in this case is the CO_2 molecule. Subsequently, the captured CO_2 can be released at the anode through oxidation of the carrier while the carrier is regenerated. This process is also referred to as "electrochemical CO_2 pumping" [136, 138], see Figure 2.13 (a). The cycle can be broken down into four steps [42]:

1. Sorbent activation through oxidation or reduction
2. CO_2(g) capture on the activated sorbent
3. Sorbent deactivation through the reverse electrochemical process
4. CO_2(g) release

Alternatively, in order to decrease the required electrical energy, these steps could be integrated in a two or three-stage process [41, 42] by e.g., enabling CO_2 capture or release to be performed simultaneously with electrochemical reduction or oxidation of the carrier. In order to improve the kinetics of CO_2 capture and release, the "pH-swing route" can be integrated, where the chemistry of redox-active carriers are designed to undergo proton coupled electron transfer (PCET) reactions [136, 137, 139, 140], as shown in Figure 2.13 (b) [136, 137, 141]. If so, an "electrochemical H^+ pumping" takes place that enables an acidic and a basic pH on the anode and the cathode, respectively.

Although redox-active systems have yet to achieve industrial utility, they have the potential of producing pure CO_2 stream even from dilute gas mixtures e.g., air [142].

Among different classes of redox-active compounds that have been explored, such as bipyridines [143, 144], disulfides [50] and copper/amine systems [30, 31], the quinone species [142, 145–147] are of particular interest [41], owing their strong binding affinity for CO_2 in their reduced form compared to that of their neutral state [40, 148]. Quinones are organic compounds derived from aromatics, through conversion of an even number of -CH= groups into –C(=O)– groups [149]. Quinones have also gained great interest as potential ideal candidates for PCET mechanism [139, 140, 150–154] inspired by their role in biological systems [155]. These redox reactions are (ideally) reversible, and can operate within the water splitting window [136].

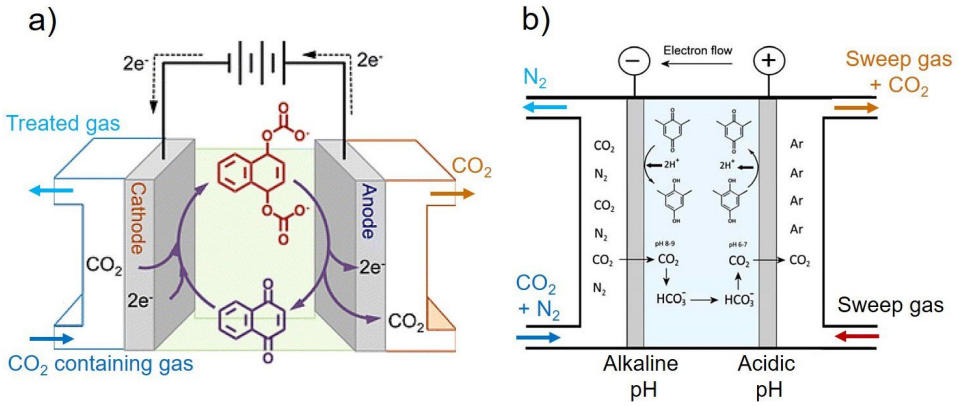

Figure 2.13: a) Electrochemical CO_2 separation using gas diffusion electrodes (GDE) through binding with quinone redox-active carrier (i.e., no pH-swing is created). Reprinted (adapted) with permission from [145]; Copyright (2015) American chemical society. b) Combination of pH-swing with the chemistry of redox active carriers through (PCET) reaction using mixture of hydroquinone, quinone, and sodium bicarbonate. Reprinted (adapted) with permission from [137]; Copyright (2015) American chemical society.

The choice of catalysts on the surface of the electrodes to facilitate the electron transfer together with the type and concentration of the electrolyte are important in determining the process efficiency in terms of capture, transport and release of CO_2, and kinetics [137]. Furthermore, the local pH shown in Figure 2.13 (b) is not the same as the bulk pH [156]. While the high pH at the cathode determines the CO_2 absorption and the lower pH at the anode drives CO_2 desorption, only the bulk pH can be controlled in a practical process. That makes the choice of an appropriate average pH that enhances both reactions, challenging. Alternatively, the local pH can be maintained by inserting (1) an anion-exchange membrane (AEM) or (2) an extra salt compartment sandwiched between an AEM and a cation-exchange membrane (CEM) between the electrodes [148].

Despite its progress in the lab-scale, CO_2 separation using redox active carriers is not practically implemented because of the limitation it faces in terms of both solvents and carriers. It is difficult to find a solvent that is inexpensive, safe, electrochemically stable and allows high solubility of the redox species [50, 148]. Possible improvements in terms of solvents can be achieved by using ionic liquids as electrolytes [40, 145] or using salt-concentrated aqueous electrolytes [148]. As for the carriers, the solubility, chemical stability and kinetics of the redox molecule can pose limitations on the process [50]. To

address these drawbacks, electrochemically mediated amine regeneration can be employed, using a similar concept, but by employing amines rather than quinones as described in section (2.4.1). Alternative to using dissolved carriers in an electrolyte-where the transport of both the electrolyte and the carrier molecules between the two electrodes is required-, the active carriers can be immobilized between the opposite electrodes [40]. The latter is explained further in section (2.4.2). Recently, solid polymerized quinone (formed into a composite with carbon nanotubes to confer electronic conductivity) is employed [40]. This so called "electro-swing" exhibits a high Faradaic efficiency and a low energy consumption (40–90 kJ mol^{-1} CO_2 captured) compared to the thermal or pressure swings for sorbent regeneration. However, it needs to be improved in terms of capacity and kinetics.

ELECTRODE INDUCED PH-SWING

Another electrochemical based CO_2 capture concept utilizing local pH near electrodes is the (membrane) capacitive deionization (MCDI) method [38, 157]. Capacitive deionization is mainly used for water treatment, but its application has recently expanded to energy harvesting and CO_2 capture [158–166]. The motivation to capture CO_2 via such system is that deionized water can be used without the need of any other chemicals, using inexpensive carbon based electrodes [38, 157]. MCDI cells consist of activated carbon electrodes and ion-exchange membranes. When a current is applied in the charging step of MCDI, HCO_3^- and H^+ ions are adsorbed into the porous electrodes inside of the cell (causing a local low pH at the cathode and increasing pH in the bulk). As the electrolyte is being depleted from ions, more CO_2(g) can be absorbed in the deionized water due to the shift in the CO_2 equilibrium, to make up for the depletion. It has been proposed to use a gas–liquid contactor spiral glass tube outside of the cell for *in-situ* absorption. When the current direction is reversed (i.e., discharging step), the subsequent desorption of H^+ and HCO_3^- (plus a small amount of CO_3^{2-}) ions from the carbon electrodes drives the chemical equilibrium in the opposite direction. As the concentration of $H_2CO_3^*$ will exceed the solubility, CO_2(g) is formed from the electrolyte. CO_2(g) absorption and desorption can be controlled through shifting the current direction. CDI can also be used in combination with NH_3-based CO_2 capture [167].

In addition to the carbon based capacitive electrodes, other metals can also be used. For example, CO_2 can be captured through intercalation/ deintercalation of protons on the manganese dioxide (MnO_2) based electrodes. The electrodes can host protons (i.e., intercalation) during reduction and release them (i.e., deintercalation) during oxidation, creating the required pH-swing for CO_2 absorption and desorption, respectively [168]. In such methods, periodic electrode polarity and the switching fluid flows ensure a continuous process.

2.3.4. MOLTEN CARBONATE CELLS AND HYBRID ELECTROCHEMICAL CAPTURE METHODS

Electrochemical methods can benefit from a pH-swing approach but are not limited to it. Examples are using (high temperature) molten carbonate cells or the hybrid methods that integrate CO_2 capture and conversion. High-temperature molten carbonate cells are early electrochemical CO_2 capture examples [33, 169]. In such process, a CO_2 con-

taining (flue) gas is fed to the cathode side of an electrochemical cell, where electricity is used to drive CO_2 and O_2 (in form of CO_3^{2-}) across a molten carbonate salts electrolyte (sandwiched between ceramic membranes in contact with the electrodes). At the anode, carbonate ion will be reduced to CO_2 and O_2 again. An alternative design enables a molten carbonate fuel cell, where CO_2 is captured while H_2 is produced [170–172]. Involved challenges are difficult operating conditions due to the high temperatures, corrosion and sensitivity to the presence of SO_x in the gaseous mixture [21, 25, 173]. Research for developing dense molten carbonate CO_2 selective membranes at high temperatures (> 723 K) is still in progress [174–176]. Examples of electrochemical hybrid capture and utilization is the electrochemical seawater battery system [177], the alkali metal-based CO_2 batteries (e.g., lithium-CO_2 batteries [178, 179]) and electrochemical CO_2 capture and conversion combinations [26, 180–184]. The absence of pH-swings, and the lack of further development of these proposed electrochemical capture routes, categorizes these concepts beyond the scope of this review. The broader context in terms of CO_2 utilization is discussed in section (2.5).

2.3.5. WHICH ELECTROCHEMICAL METHOD TO USE?

A comparison of the metrics of electrochemical pH-swing based CO_2 capture methods is given in Table (2.1). These capture methods have often energy consumption > 300 kJ mol^{-1} CO_2. As a comparison with conventional methods, the energy consumption of CO_2 capture (from flue gas) via aqueous monoethanolamine (MEA) using a thermal swing, currently the most mature capture method, is between ~170-300 kJ mol^{-1}CO_2 [185–191]. Approximately ~80% of this energy is the contribution of the thermal regeneration [14], included in the reboiler heat duty [192]. Most conventional and electrochemical captures are energy intensive, when compared to the combustion energy of various fuels and the emitted CO_2 per mole of the fuel. From an economic point of view, CO_2 capture is only interesting if the energy consumption of the capture is <66 kJ mol^{-1} CO_2 [43, 193]. Renewable sources would be preferred over fossil fuels for driving electrochemical CO_2 capture to 1) maximize the reduction in net carbon emission and 2) leverage the advantage of electrifying the CO_2 capture process. At the same time, the absence of flue gas from power plants in renewable sources would make diffused CO_2 sources (e.g., atmosphere and seawater) the most logical feed for electrochemical CO_2 capture technologies. This is also reflected in Table (2.1), where most research has focused on capture from air, seawater or (low concentrated) bi(carbonate) solutions.

Table 2.1: Electrochemical CO_2 capture

Capture method	Feed	Energy-consumption[1] ($kJ\,mol^{-1}$ CO_2)	Current-efficiency	Product	Current-density ($mA\,cm^{-2}$)	Remarks
Fuel-cell [36]	air + H_2	350	23%	CO_2(g)	0.5	Upscaling unfeasible (low current-density)
Electrolysis [75]	air	290-350 ($kJ\,mol^{-1}$ KOH)	>95% [2]	CO_2(g)+H_2(g)	100	KOH/ K_2CO_3 electrolysis at 70 °C
Electrolysis [72]	air + mined $CaCO_3$(s)	1267200 [3]	Not reported	H_2(g)+CO_2(g)	Not reported	Water electrolysis. Figure 2.8 (a)
Electrolysis [39]	synthetic flue gas + cement kiln dust	> 634-1276 ($kJ\,mol^{-1}$ $CaCO_3$) [4]	60-90% [2]	$CaCO_3$(s)	100-200	KCl electrolysis. Figure 2.12
BPMED [92]	K_2SO_4	~308	Not reported	CO_2(g)	50	produces KOH + H_2SO_4
BPMED [107]	$NaHCO_3$ / NaOH	160-500	65-80%	CO_2(g)	5-20	
BPMED [93]	$KHCO_3$ / K_2CO_3	100-450 [5]	95% ($KHCO_3$), 50% (K_2CO_3)	CO_2(g)	5-100	Figure 2.10 (b) for cell design & Figure 2.11 for cell performance
BPMED [44]	$KHCO_3$	200-500	70-90%	CO_2(g)	22-139	High pressure BPMED enables 30% energy win. See section (2.3.2)
BPMED [114]	artificial seawater	250-400	<70%	CO_2(g)	1-3	59% of DIC from seawater was removed using ca. 242 $kJ\,mol^{-1}$ CO_2
BPMED [9]	artificial seawater+NaCl	390-640	60-95% [6]	CO_2(g) or $CaCO_3$(s)	100	Cost of membrane contactors is avoided via the base route

[1] Only for the electrochemical step, defined as $\frac{I \times V}{\text{recovered } CO_2}$.

[2] For KOH electrochemical regeneration.

[3] Although the theoretical work requirement for the reaction is only 266 $kJ\,mol^{-1}$ CO_2.

[4] Calculated from data on energy consumption for KOH production, assuming 2 moles KOH delivers 1 mole $CaCO_3$.

[5] Plus 200 for CO_2(g) capture into hydroxide solutions [194].

[6] Only for the production of HCl and NaOH, not for CO_2 capture and recovery.

BPMED [108]	artificial seawater+CO_2(g)	1080-2880 (kJ mol^{-1} $CaCO_3$)	Not reported	$CaCO_3$(s)	Not reported	CO_2(g) absorption in basified seawater followed by crystallization
EDI+BPMED [43]	synthetic flue gas	Not reported	Not reported	CO_2(g)	2-16	At near neutral pH, the slow kinetics can be enhanced using CA enzyme
EDI+electrolysis [37, 77, 82, 195]	natural seawater	2775-6940 [1]	Not reported	CO_2(g)/ H_2(g)	20-61	Figure 2.9
MCDI [157]	synthetic flue gas	40-50	60-80 %	CO_2(g)	0.02-0.06	Using IEM's improve efficiency [38]
Redox-active carriers+pH-swing [141]	synthetic flue gas	106 [2]	90%	CO_2(g)	18	Aqueous tiron (Na_2Q) is used as pH mediator/ active carrier to capture CO_2
Redox-active carriers [148]	synthetic flue gas	56	>75%	CO_2(g)	0.5	

[1] Calculated based on data from [77]: R = 0.5-1.8 Ω, i=20.4-61.2 mA cm^{-2} and recovered CO_2 rate of 0.004 mol min^{-1}.
[2] Only for the CO_2 desorption step.

At present, (membrane) electrolysis and BPMED are the most studied electrochemical capture approaches. Figure 2.14 (a) shows the estimated energy consumption of both methods (see supporting information for calculations). This electrical energy consumption, E (in kJ mol^{-1} CO_2), is calculated via:

$$E = \frac{i \cdot A \cdot V}{r_{CO_2(g)}} \tag{2.11}$$

Where i is the current density (A m^{-2}), A is effective area of the electrodes (m^2), V is the total cell voltage (volts) and $r_{CO_2(g)}$ is the recovery rate of the captured CO_2(g) in mol s^{-1}. To put the energy consumption of Figure 2.14 (a) in perspective, the energy produced per mole of fuel (through combustion) and the associated emitted CO_2 are shown in Figure 2.14 (b). This emphasizes the energy-intensive nature of the capture process: capturing 1 mole of CO_2 via BPMED consumes 25-60% of the energy obtained from combustion of hydrocarbon fuel per mole of CO_2, dependent on the fuel type. For conventional methods and electrochemical capture via electrolysis, this figure is even larger.

a)

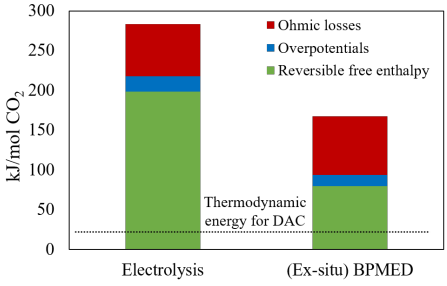

b)

Fuel type	Combustion energy (kJ/ mol fuel)	Energy vs. emission (kJ/ mol $CO_{2(g)}$)
CO	283	283
H_2	286	0
Coal (100% on Cs)	393	393
Methane (CH_4)	890	890
Ethanol (C_2H_5OH)	1367	683.5
Gasoline (octane)	5450	681.25

Figure 2.14: a) Electrical energy consumption for direct air capture (DAC) through (membrane) electrolysis. Current density of 20 mA cm^{-2} and ΔpH=14 is assumed for both cases. See supporting information for detailed calculations. The thermodynamic work required for DAC (assuming 400 ppm CO_2(g)) is 20 kJ mol^{-1} CO_2 [16]. b) The combustion heat of common fuels and their CO_2(g) emission, obtained from reference [196] and stoichiometric combustion reactions.

Figure 2.14 (a) shows that the ohmic losses cover a significant part of the energy

losses ([78]), and bring in a lever to reduce E. In electrochemical cells, such losses can appear as e.g., heat and/or unwanted chemical byproducts. For example, losses caused by product recombination, such as recombination of produced H^+ and OH^- in BPMED or the recombination of O_2(g) and H_2(g) in water electrolysis to form water again. Membrane co-ion leakage is another common loss often involved in membrane based electrochemical processes [94]. The limitations and areas of improvements of each electrochemical CO_2 capture method can be summarized as:

1. It is obvious from Figure 2.14 (a) that the energy consumption for BPMED is lower than that of electrolysis when targeting CO_2 capture. In case hydrogen is an aimed product as well, the energy difference between these two methods (which is equivalent to 1.23V) can be justified, and can be lower than the energy for two separate systems making acid/base and hydrogen. However, in more detail, the combination of these two products in electrolysis complicates the optimal current density, which is not necessarily the same for hydrogen and acid/base production. Moreover, most hydrogen catalysts are geared towards acidic environments, and earth abundant oxygen catalyst are available for alkaline environments, while the opposite environments are present in the combined electrolysis/acid-base production [197]. That limits the options for electrocatalytic material (e.g., platinum and ruthenium), which can pose resource limitations as a relatively large electrode area is required. On the contrary, up scaling can be done easily for BPMED capture method by repeating multiple cell pairs within a single electrode pair.

2. When using BPMED, despite its uncomplicated up scaling, the typical energy consumption in Table (2.1) is still 2-3 times more than theoretically expected in Figure 2.14 (a). These losses are due to the involved non-idealities in charged membranes (e.g., high resistivity, co-ion leakage, low chemical stability), the high over potential of water dissociation in BPM, or carbonate feed (requiring 2 H^+ per molecule to acidify to H_2CO_3) instead of bicarbonate. Thankfully, achieving a lower energy consumption is possible both through process optimization and material engineering. Process optimizations can be done by e.g., controlling the applied current density (i), feed flow rate (residence time in the cell), electrolyte conductivity/ pH, cell configuration, flow path/ mode, and operation pressure/ temperature, while water dissociation can be improved through material engineering [198, 199]. The current minimum economic cost of BPMED is at least twice of the cost of the wet-scrubbing rival [4]. However, the cost can significantly decrease if improvements in the cost of renewable energies, cost and availability of ion exchange membrane, membrane life time and membrane selectivity is achieved. Finally, the total capture cost does not only depend on the method, but also on the source of the capture. For example, depending on the pumping facilities and plant location, indirect ocean capture (IOC) can be economically favored relative to direct air capture (DAC), or vice versa [200].

3. The reversible free enthalpy in Figure 2.14 (a) is based on a ΔpH=14. Using lower ΔpH, a lower reversible free enthalpy is involved [85]. Although it is theoretically possible to perform a pH-swing between pH 4-7, potentially reducing the energy

consumption to values close to the thermodynamic limits, this low energy consumption is not obtained in practical BPMED at medium to high current density.

4. Membrane capacitive deionization (MCDI) is recently demonstrated to capture CO_2 from a CO_2(g)+N_2(g) mixture, using only demineralized water [38, 157] with the lowest capture energy among other methods (~40-50 kJ mol^{-1} CO_2), see Table (2.1). However, the obtained current density is extremely low (~0.02-0.06 mA cm^{-2}) and there is a long way to go before (M)CDI becomes a competitive means of CO_2 capture as the stability and performance of the large-scale CDI applications are yet unknown. Future work is suggested to investigate the physical and chemical effects of weak electrolyte solutions in CDI [157].

5. Only a few works on CO_2 capture through electrodeionization (EDI) show lab scale feasibility [77, 122, 201] as summarized in Table (2.1). However, no data on the energy consumption of those systems is available. CO_2 capture through EDI is limited due to the cost of ion exchange resins, their poor stability and their sensitivity to fouling [128].

6. Electrochemical methods that use redox-active carriers are shown to be less energy intensive (~100 kJ mol^{-1} CO_2). However, these results have been only obtained using synthetic flue gas. Quinones, used as binding agents for CO_2, are highly sensitive to water and oxygen, making the applications for real flue gas (or direct air capture) impractical. Moreover, most redox carriers need organic solvents electrolytes that suffer from a low ionic conductivity which limit the current density. When using quinones as carriers, the total CO_2 carrying capacity is limited by the solubility of quinone in the solvent, the applied electrode potentials, evaporative solvent losses and consequent drying of the electrodes [145]. Luckily, the efficiency of the CO_2 absorption and desorption in such systems can be increased by combining a pH-swing through electrochemical reactions [137], where proton coupled electron transfer (PCET) takes place. However, the practicality of this approach still awaits the improvement of electrochemical redox kinetics. The low solubility of PCET organics limits its capture capacity [136]. Furthermore, PCET carriers are also very sensitive to gasses such as O_2 and sulfur, posing again challenges for (real) gas CO_2 capture application [136]. Upscaling can be done by using a larger electrode surface area.

All electrochemical CO_2 capture methods are still under development (TRL 5 to 6), although they enable high CO_2 recovery rate (>80%). In order to provide a framework of comparison between these methods and the conventional (non-electrochemical) processes- which have already been commercialized- the conventional processes are described further in the next section.

2.4. COMBINING ELECTROCHEMICAL METHODS WITH CONVENTIONAL CAPTURE TECHNOLOGIES

Conventionally, the capture industry only targeted CO_2 capture from centralized CO_2 emitters such as fossil fueled power plants, iron, steel, and cement industries. However,

this approach is impotent to achieve a *net* zero CO_2 emission because, as shown in Table (2.2), decentralized sources still constitute a large part of the total emission (total GHG emission of 55 Gt $CO_{2\,eq}$ in 2019 [202]). Therefore, currently DAC and IOC are gaining attention (Table (2.3)). For achieving climate targets, CO_2 removal within a gigaton order of magnitude is needed [203, 204].

Table 2.2: Thermodynamically required energy, properties and the scale of main capture feeds

Source	Thermodynamic properties & required energy	Emission & capture scale
Centralized	• Flue gas: – 150<T<1200°C, p_{CO_2}~0.03-0.15 atm [205, 206] – 7 kJ mol^{-1} CO_2 for 13% flue gas [207]	• >58% of total emission, see Figure 2.1 • Current post-combustion capture >2.4 Mt CO_2/year [208]
Decentralized	• Direct Air Capture (DAC): – Ambient T, p_{CO_2}~0.0004 atm (~400ppm) – 20 kJ mol^{-1} CO_2 [16, 207, 209] • Indirect Ocean Capture (IOC): – 5<T<35°C, p_{CO_2}~0.072 atm (~2.5mM DIC) – Same thermodynamically required energy as DAC [200]	• <42% of total emission, see Figure 2.1 • Current DAC capture shown in Table (2.3), but no large scale IOC, yet [210]

Table 2.3: Large scale DAC companies

Company	Process mechanism	Capacity (tonne CO_2/year)
Carbon Engineering [211]	(KOH) absorption + high temperature calcination	1,000,000
Global Thermostat [212]	(Amine based) adsorption + thermal & pressure swing regeneration	4,000
Climeworks [213, 214]	(Amine based) adsorption + thermal swing regeneration	900

The (centralized) capture technologies are often grouped in main categories of [19]; (1) Oxy-fuel combustion, (2) Pre-combustion, (3) Post-combustion and (4) Chemical looping (combustion) as discussed in Table (2.4). In addition, capture by algae [215–221], biochar [222–227] and charcoal [228] are recently demonstrated. While there are many CO_2 capture methods, introducing all of them are out of scope of this work and we refer the reader to various available literature on this topic [14, 18–26, 229, 230]. For an overview of the current state-of-the-art of CO_2 capture, transport, utilisation and storage

see reference [231]. Among the available methods, most research focus has been given to the post-combustion methods as they can be retrofitted more easily to the existing industrial units, compared to the Oxy-fuel and Pre-combustion methods [230]. Traditional post-combustion capture methods are absorption [19, 20, 232–237], adsorption [14, 19, 238–240], membrane gas separation [241–247], calcium looping [20, 248–250] and mineral carbonation [111, 251–261], see Table (2.4). These methods are combined with thermal swing, pressure swing or vacuum swing for CO_2 desorption.

Table 2.4: Dominant non-electrochemical capture methods

Capture method	Process mechanism	Challenges
Oxy-fuel [262–264]	Instead of air, pure O_2(g) or a CO_2(g)/O_2(g) mixture is used for fuel combustion. 75–80% CO_2 is produced as opposed to combustion in normal air where 3-15% CO_2 is produced	• High oxygen production energy costs (ca. 200–220 kWh per tonne of oxygen generated by cryogenic air separation [264]) • High sensitivity to air leakage into the system • Although an efficient capture method ([265]), difficult to retrofit compared to Post-combustion method • Special materials are needed to resist the high flame temperature (ca. 3500 °C). Although, the recycled CO_2 can be used to moderate this temperature [19]
Pre-combustion [266–269]	CO_2 is separated from H_2- rich fuel before combustion. For example, synthetic gas is produced from fossil fuel by adding steam or pure oxygen at high temperature and pressure (1400 °C and 25–55 atm) and a subsequent water-gas shift reaction.	• Retrofit to existing plants is costly and more difficult compared to Oxy-fuel and Post-combustion • Reaction CO + steam ↔ CO_2 + H_2 produces 15–40% CO_2 at 14–40 atm. The produced H_2 can be used for power generation, but CO_2 needs to be removed using a subsequent separation technique
Post-combustion:		

(*table continues*)

Table 2.4: Dominant non-electrochemical CO_2 capture methods (continued)

Capture method	Process mechanism	Challenges
Absorption [19, 20, 232–237]	CO_2(g) (from flue gas or air) is absorbed (i.e., chemically or physically) in an absorbent. Pure CO_2(g) is subsequently recovered through temperature swing desorption while the absorbent will be regenerated. Currently, amine based capture is the most mature method for CO_2 capture	• Limited CO_2 absorbing capacity resulted from the reaction stoichiometry and dependent on the absorbent type (e.g., low capacity as 0.4 kg CO_2/kg-MEA or higher as 1.2 kg CO_2/kg-NH_3 [19, 270]) • High absorbent regeneration (i.e., CO_2 desorption) energy • Solvent losses caused by volatility or thermal/chemical degradation, the subsequent equipment corrosion & negative environmental impacts of solvent emissions • High sensitivity to flue gas temperature, pressure and presence of impurities, such as NOx, SOx and oxygen (i.e., oxidative degradation) [271]
Adsorption [14, 19, 238–240]	CO_2(g) is adsorbed on solid materials and will be recovered through temperature, pressure or vacuum swing desorption	• When used for flue gas, pretreatments to remove impurities, such as NOx, SOx and H_2O and to decrease gas temperature are needed • Possible loss in the adsorption capacity of the adsorbent after desorption step (e.g., 4–9% loss for amine immobilized onto solid silica) • Sorbent degradation in cyclic operation

(*table continues*)

Table 2.4: Dominant non-electrochemical CO_2 capture methods (continued)

Capture method	Process mechanism	Challenges
Membrane gas separation [14, 241, 242, 245, 247, 272, 273]	Process is driven by partial pressure difference of the gas molecules to be separated. Gas molecules permeate according to their size, diffusivity, or solubility through the membrane.	• Not feasible for streams with low CO_2 partial pressure and concentration • To accommodate the high flow rate of industrial flue gas, high membrane surface area is required • Sensitivity to presence of moisture (i.e., lower selectivity) • On-going research on new membranes with high selectivity and permeability [274–276]
Calcium looping [14, 249, 277]	A variant of chemical looping (combustion) that involves carbonation and calcination. Metal oxides e.g., CuO, Mn_2O_3, NiO, and Fe_2O_3 are used instead of O_2(g) in Oxy-fuel combustion	• Rapid decrease in the limestone (i.e., sorbent) capacity after a number of cycles of reaction with CO_2 • Environmental concerns caused by limestone mining, the waste from Ca-looping (i.e., the spent CaO) and the need for high temperatures for the operation • Need for air separation unit to obtain pure O_2 for calcination

The conventional absorption and adsorption based captures can be combined with electrochemical methods to decrease (or eliminate) the required thermal energy for the regeneration step as discussed in section (2.4.1) and (2.4.2). No available work have been found on electrochemical enhancement of the other conventional methods.

2.4.1. ABSORPTION (WET SCRUBBING)

CO_2 is a weak acid. Therefore, substrates that contain basic moieties such as amine groups (e.g., alkanolamines) are efficient absorbents for CO_2 capture [278]. Amines are derivatives of ammonia (NH_3), containing a basic nitrogen atom, where one ($R-NH_2$) or more hydrogen atoms have been replaced by a substituent. Amines act as a nucleophiles (i.e., electron pair donors also known as Lewis bases), reacting with CO_2 at the electrophilic (i.e., electron pair acceptor) carbon center to form a carbamate (derivatives of carbamic acid H_2NCOOH where one or more hydrogens are replaced by other organic functional groups) [50, 168, 279]. Although the amine capture processes are extensively studied, the reaction mechanism is not yet fully understood. For a detailed description see [280]. The post-combustion CO_2 capture is dominated by amine-based absorption, using aqueous solutions of mono-, di-, tri-ethanolamine or hindered amines to absorb CO_2 in gas form [233, 279, 281–284]. Aqueous solutions are often used in order to control

the density, viscosity, surface tension, and the thermal expansion coefficient of the pure amines [285–287]. This is while. the energy consumption for solvent regeneration decreases substantially with increasing the amine concentration (due to an improved CO_2 reaction rate and absorption capacity [288]). However, such high concentrations also increase the degradation rate, viscosity and the involved environmental concerns, posing challenges on the overall capture process [286, 288].

In addition to aqueous solutions, both non- and low-aqueous solvents (i.e, water-lean solvent) are viable [285, 289, 290]. These alternatives are not well studied yet although they have gained interests recently. All currently assessed water-lean solvents have shown lower CO_2 solubilities than aqueous monoethanolamine (MEA). However, because the heat of absorption is not much affected, solvents with the lower volatility than water could potentially offer opportunities for processes with overall less reboiler heat duties than that of ordinary aqueous MEA [285].

Amines have been used for CO_2 capture since 1930 [279]. Monoethanolamine (MEA) scrubbing technology is seen as a benchmark technology for CO_2 capture from flue gas of large-scale power plants [188, 191, 291, 292]. In this method, CO_2(g) is chemically absorbed at low temperatures (~40 to 60°C) in the absorbent and is extracted in a desorber column later, generally via a temperature swing at high temperatures (~120°C), where the absorbent is also regenerated [187, 293]. The energy consumption of CO_2 capture (from flue gas) via aqueous monoethanolamine (MEA) thermal swing is between ~170-300 $kJ\,mol^{-1}CO_2$ [185–191]. To address the drawbacks discussed in Table (2.4), for CO_2 capture via chemical absorption, other inorganic solvents, such as aqueous potassium and sodium carbonate ([168]), ammonia solution and alkali hydroxide solution have been investigated [294, 295]. When using alkaline or carbonate based solution, hydration of CO_2 takes place rather than carbamate formation [168]. However, CO_2 absorption in carbonate is very slow compared to that of amines [271]. Increasing the absorbent pH (i.e., applying a wide range pH-swing), can enhance the kinetics substantially.

pH-SWING VS. THERMAL SWING

All available large-scale CO_2 capture processes rely on heating or using a combination of heat and vacuum to release the captured CO_2 [28, 295]. Given the initial focus was to capture CO_2 from flue gas of fossil fuel power stations, heat integration is relatively straightforward. However, as an alternative to this thermal swing, an (electrochemical) pH-swing approach can be applied for CO_2 recovery and absorbent regeneration [4]. In a thermal swing absorption process, the energy performance is dominated by (1) absorbent absorption capacity, (2) absorption rate, (3) heat of absorption and (4) thermal degradation [271]. The required thermal energy is often exacerbated due to use of aqueous solutions in which the capturing agent is contained (e.g., water for the case of MEA [271]) [50]. Furthermore, the required heat is normally generated from combustion of fossil fuels, decreasing the net captured CO_2 in the conventional processes [109]. Alternatively a pH-swing can be used, to absorb and desorb CO_2. The cost of absorbent regeneration through pH-swing via BPMED in wet scrubbing (using KOH absorbent) is estimated to be ~773 $ per tonne CO_2. That is more than three times of the cost of the thermal swing rival. However, the cost can significantly decrease if the cost of renewable energy decreases (e.g., from 0.06 to 0.018 $/kWh), cost of membrane decreases (to lower

than 100 $\$m^{-2}$), membrane life time increases from around 3 years [296] to 15 years and the process is optimized [4].

PHYSICAL ABSORPTION

The advantage of the physical absorption to chemical absorption explained above is its lower heat consumption in the solvent regeneration step [22, 23]. Solvents, such as methanol, poly(ethylene glycol) and dimethyl ether can be used to absorb CO_2(g) physically. Recently, ionic liquids have been proposed as alternatives to the conventional absorption solvents [297–299]. Ionic liquids are molten salts that exist as liquids near room temperature, often composed of an organic cation with an inorganic or organic anion and featuring polar properties [26]. Ionic liquids are referred to as green solvents due to their low volatility, exceptional thermal stability, non-flammability and environmentally benign character [300]. The capture using ionic liquids is often based on physisorption although some ionic liquids react with CO_2 in a chemisorption mechanism [23].

ELECTROCHEMICAL ENHANCEMENT OF AMINE BASED ABSORPTION

Electrochemical methods provide alternative routes to the conventional thermal regeneration step in absorption based capture. Such electrochemical enhancements are shown feasible through (1) pre-concentrating the CO_2 rich amine stream, (2) substituting CO_2 with suitable metallic species or (3) pH-swing. These three routes are explained here.

For pre-concentrating the CO_2 rich amine stream, a capacitive deionization unit (CDI) can be used. Inside the CDI cell, when current is applied, ionic species (i.e., $MEAH^+$ and $MEACOO^-$ in case of monoethanolamine absorption) are adsorbed at the electrodes, creating an ion-free solution (mainly water [271]) that can be sent back to the absorber column without the need to undergo the thermal desorption step. Subsequently, when power is switched off or reversed, the adsorbed ions will be released back from the porous electrodes, creating a carbon rich stream that can then be sent to the stripper column. When applying thermal regeneration, the concentrated solution from the CDI unit then requires 50% lower solvent regeneration heat energy because of its high CO_2 loading [301]. As an alternative approach, the conventional temperature swing step in the amine absorption process can be replaced by metal ion substitution in an electrochemical cell [30, 31, 302]. Such a cell consists of multiple anode and cathode chambers made of copper. At the anode, Cu^{2+} reacts with the amines, displacing the CO_2 as shown in Figure 2.15. CO_2 is subsequently removed in flash tanks after the anode chambers and the amines are regenerated by subsequent reduction of the Cu^{2+} to Cu in the cathodes. The process allows for higher CO_2 desorption pressures, smaller absorber columns and lower energy demands.

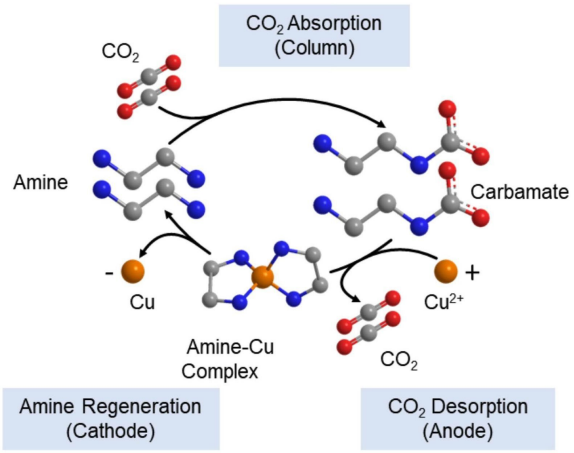

Figure 2.15: Electrochemically-mediated amine regeneration (EMAR) using copper. Reprinted from [303], Copyright (2019), with permission from Elsevier. The conventional thermal swing is replaced with an electrochemical step. In addition to Cu/Cu^{2+}, many possible chemistries can be utilized in such separation processes as discussed further in [30, 31, 302].

There are few works available on using a pH-swing to regenerate amine based absorbents; The early work of Zabolotskii *et al.* shows the feasibility of a low-temperature BPMED for regeneration of aqueous monoethanolamine (MEA) sorbent [304]. Huang *et al.* demonstrated a pH-swing for amine based absorbents, doing so electrochemically (for flue gas desulfurization) [305] and Feng *et al.* by simply adding a (weak) acid to the rich amine stream (for CO_2 capture) [237]. Such addition of acid is reported to have the potential to increase the volume of the released CO_2 and to decrease the absorbent regeneration heat energy. Both contributing to a higher energy efficiency [237].

2.4.2. ADSORPTION

CO_2 can be adsorbed on solid porous materials, where CO_2(g) is subsequently recovered and the adsorbent is regenerated through a temperature, pressure [306], vacuum [307–316] or electric swing desorption [317]. Previous work has shown CO_2 adsorption on metal–organic frameworks (MOF's), silica, zeolites, immobilized amine, alumina, polymeric resins, molecular sieves and activated carbon. Adsorption is possible through both physical (e.g., on zeolite, graphene, MOF's, silica) and chemical (e.g., amine and calcium based materials) bonding with CO_2.

An advantage of adsorption based capture is that using solid adsorbents (instead of the mature aqueous monoethanolamine (MEA) technology) in capturing systems reduce the regeneration heat (due to the much lower heat capacity of solid adsorbents and the avoidance of water evaporation in the regenerator) [188]. The (calculated) regeneration heat for polyethyleneimine (PEI)/silica adsorbent based capture is reported to be around 2.46 GJ/tonne CO_2, which is much lower than the value of 3.3-3.9 GJ/tonne CO_2 for a typical aqueous MEA system [188]. In general, adsorption also has higher CO_2 adsorption capacity compared to that of absorption e.g., ca. 88–176 kgCO_2/kg adsorbent

[306] vs. 0.4-1.2 kgCO_2/kg absorbent [19, 270, 318].

ELECTROCHEMICAL ENHANCEMENT OF ADSORPTION

Similar to absorbents, the CO_2 capture and recovery of recent adsorbents has been assessed via electrochemical swings instead of the conventional pressure or temperature swings [40, 319]. As an example, the redox active carriers described in section (2.3.3) can be employed as solid adsorbents, immobilized on surface of electrodes. Such electro-swing systems normally operate in charge/ discharge cycles where changing the cell polarity regulates the activation and deactivation of the carrier [40]. The significant advantage of the electro-swing process with respect to pressure swing adsorption (PSA) and temperature swing adsorption (TSA) is that the CO_2 capacity of these solid adsorbents does not depend on the feed concentration, making them suitable for CO_2 capture even from very dilute streams [40]. Moreover, up-scaling is easily achievable in electro-swing adsorption by using multiple anode and cathode chambers repeating within one cell. Alternative to the electrochemical elctro swing approach described above and in [40], the electrochemical process can induce a temperature swing. In that case, a low voltage passes through a conductor to change the sorbent temperature via Joule heating (i.e., resistance turning electric energy into heat) [319–323].

2.5. CARBON DIOXIDE UTILIZATION

After CO_2 is captured, it can be stored or utilized, see Figure 2.16. CO_2 is an inexpensive, non-toxic, renewable commodity [324, 325]. The market for CO_2 use is projected to grow from 0.23 gigatonnes (Gt) per year today to 7 Gt/year by 2030 [326].

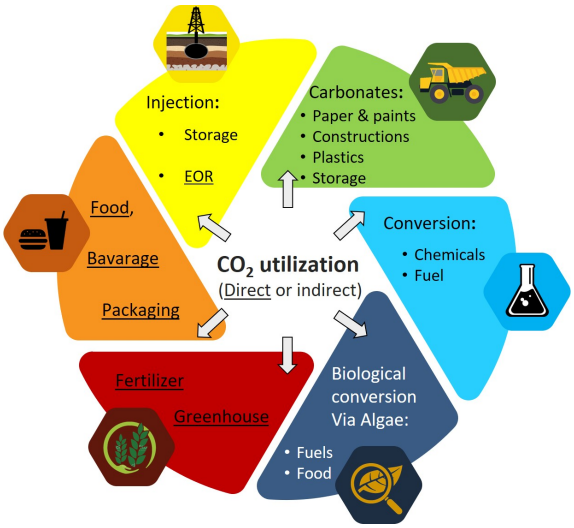

Figure 2.16: Schematic of direct and indirect (i.e., via conversion) utilization of CO_2. Alternative to gaseous CO_2, carbonate minerals (e.g., $CaCO_3$) can be utilized [327] in paper industry, coating, plastics [328], paints, adhesive/sealants, rubber, cement and construction materials [329].

In addition to fuels, chemicals such as ethylene, alcohols, formic acid (or formate), syngas, urea and other organic materials can be produced from CO_2, electrochemically, thermo-chemically or by other approaches [324, 330–338]. Such organic chemicals are often more expensive than fuels and may offer advantages in the techno-economic analysis. However, the global demand for them are much lower than fuels as shown in Figure 2.17. For instance, the global demand for one of the largest chemical markets, ethylene, is 184 Mt/year [339]. Ethylene manufacture also stands as the prime contributor for CO_2 emissions among carbon-based chemicals, with a CO_2 emissions rate of 184.3 - 213 Mt in 2015, which could reach 1.34 Gt/year by 2030 [340].

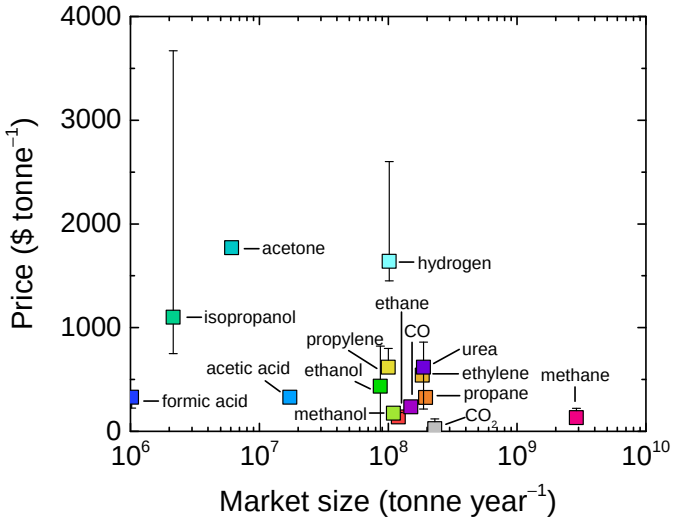

Figure 2.17: Average price of CO_2 utilization products as a function of their market size. Error bars indicate anomalies in some regions (see the supporting information Table 1 for values). CO_2 and H_2 are included for reference.

Production of synthetic hydrocarbon fuels and chemicals often requires high purity CO_2 feeds. Many CO_2 capture facilities using centralized sources simultaneously capture sulfur containing compounds, such as hydrogen sulfide (H_2S) that must be removed upstream to avoid catalyst poisoning [341]. The process of desulfurization typically involves liquid phase oxidation to promote H_2S oxidation to sulfur, followed by sulfur separation from the gas stream [342]. Chemical adsorption using high surface area ZnO-based adsorbents may be used in sequence to further eliminate H_2S prior to pipeline transmission [343, 344]. Alternatively, CO_2 conversion can take place via biocatalytic routes with both natural and engineered microorganisms [345, 346] that generally have higher tolerance for impurities [347]. CO_2 capture from dilute sources, such as from air and seawater, usually contains non-negligible amount of O_2 and N_2 [29, 46]. While N_2 is an inert gas and may not negatively impact the CO_2 conversion, a trace amount of O_2 may lower the catalytic turnover through the unwanted reaction with hydrogen in the thermochemical process [348], or through the preferential reaction of oxygen reduction in the electrochemical process [46]. Strategies for O_2 removal from CO_2 stream include

catalytic oxidation of hydrogen [349] or methane [350] on noble metal catalysts such as Pt or Pd [351], chemical adsorption of O_2 on Cu surfaces at elevated temperatures [349], and electrochemical reduction of O_2 on Ag catalysts [46].

A pressurized CO_2(aq) stream is beneficial for a subsequent CO_2 conversion step. In a CO_2 electrolyser for methanol production, when the produced CO_2 remains dissolved due to an applied pressure, the avoided typical gas regeneration step and CO(g) compression step save more than 150 kJ mol^{-1}CO_2 [47]. High pressure electrolyser (up to 40 bar) is also reported to increase the current efficiency of CO_2 reduction to formic acid/formate [352, 353]. Moreover, a high pressure CO_2(g) is required for the transportation in the pipes, enhanced oil recovery or geological CO_2 sequestration for underground injection. Supercritical CO_2 (above its critical temperature 31.0 °C and pressure 72.8 atm) with its low density and viscosity plays a significant role in the extraction of oil [354–356]. Furthermore, supercritical CO_2 can be used in the enhanced geothermal system for heat exchange [248, 357].

The electrochemical CO_2 conversion lacks studies that demonstrate the capability of the technology at scales large enough for industrial implementation [358]. As an alternative, CO_2 can be converted biologically to organic carbon in plants or microalgae, through photosynthesis, resulting in various products, such as biofuel or animal feed [359, 360]. Gaseous CO_2 can be stored (i.e., sequestrated) in deep geological layers or in the ocean [20, 361–363]. In 2019, from the 19 in operation large-scale carbon capture & storage (CCS) facilities, 33.2 Mt/year of CO_2 were captured and stored [364] (i.e., less than 0.1% of the total global emissions) [365]. By addition of the already in constructions facilities, this value is estimated to be doubled, within the coming years. Most of this storage is done through enhanced oil recovery (EOR) application (i.e., over 260 Mt of anthropogenic CO_2 by 2019) [364]. As an alternative to sequestration of gaseous CO_2, CO_2(g) can first be converted to bicarbonate ion and, subsequently, be stored as already abundant forms of ocean alkalinity, through electrogeochemistry [72, 76, 79, 113]. There are social concerns associated with the gas sequestration including fear of CO_2 leakages, lack of suitable locations, required site monitoring, unknown impacts on living organisms and limitations involved with CO_2 transportation and injection to storage sites. Alternatively, solid (carbonates) storage can be used. Such mineral carbonate sequestration is permanent, safe, has a large worldwide storage capacity and is less subject to social opposition [329, 366, 367].

2.6. CONCLUSIONS

Electrochemical CO_2 capture methods are undergoing a renaissance as their applications expand due to their higher energy efficiency, flexibility and sustainability compared to the conventional approaches. Electrochemical CO_2 capture is classified into four categories; (1) methods that apply a pH-swing to capture and recover the CO_2, (2) methods that rely on the binding affinity of CO_2 molecules to redox-active species, (3) molten carbonate cells and (4) hybrid electrochemical processes that combine CO_2 capture and e.g., direct conversion. Among the electrochemical capture methods, pH-swing based approaches, leveraging the carbonate equilibrium, are most widely studied, due to their straightforward operation and the absence of toxic or expensive chemicals. In theory, a mild pH-swing over ca. 2-3 pH units would allow to capture >98% of the CO_2.

However, in practice, to improve the slow kinetics associated with such a mild swing, either a wider pH range (ca. 5-6 pH units) or catalytic enzymes (e.g., carbonic anhydrase) need to be applied. An electrochemical pH-swing is induced via electrolysis, bipolar membrane electrodialysis (BPMED), redox active molecules that undergo proton coupled electron transfer (PCET) or capacitive deionization. Among all, electrolysis is the earliest method (used for alkaline absorbent regeneration), but is still rather energy intensive due to the intrinsic irreversibility of the gas evolution redox reactions. However, the produced H_2(g) (through water electrolysis) can be used to offset the total energy consumption. Capture via PCET active agents enable high current efficiencies, but are at the moment limited by slow electrode kinetics, low solubility of PCET organics and the sensitivity of the process to impurities in the flue gas such as O_2, water and sulfur. Using (membrane) capacitive deionization (MCDI) enables capture with an electrical energy consumption as low as 40 kJ mol^{-1} using only deionized water. However, (M)CDI capture is so far only applied at very low current densities, is still in the very early stage of the lab-scale research (TRL of 3) and its large scale applications await more performance studies. All electrochemical capture methods can be used easily as plug-and-play units. Among the four technology for electrochemical pH-swing, BPMED has the advantage of keeping a small footprint upon up scaling. At present, the cost of using BPMED for CO_2 desorption and alkaline (re)generation in alkaline wet scrubbing is estimated to be 2-3 times more than the conventional thermal swing desorption rival. However, the cost can significantly decrease if improvements in the cost of renewable energies and ion exchange membranes, membrane life time and their permselectivity and resistivity are achieved. Despite of the successful lab-scale demonstrations, both CO_2 capture via electrolysis and BPMED have achieved TRL of 5-6 and are not yet commercialized. This is while, the conventional post-combustion CO_2 capture methods, such as absorption, adsorption, membrane separation and chemical looping have found their way to industrial applications. As opposed to the electrochemical captures, conventional methods are mainly designed to capture CO_2 from centralized emitters such as fossil fueled power plants. These methods have a larger footprint and are not geared for efficient decentralised emitted CO_2. However, in the last decade, to benefit from the high efficiency and selectivity of the electrochemical processes, conventional methods are also promoted to be combined with electrochemical process. Substituting the temperature or pressure swings with an electrochemical swing in an amine based absorption capture is shown to halve the energy consumption of the CO_2 desorption step while decreasing the footprint of the unit. The framework established in this paper can be the basis for future studies on the energetics of electrochemical CO_2 capture processes, not only for flue gas separations, but also for a range of other applications, such as seawater CO_2 capture and direct air capture.

2.7. SUPPORTING INFORMATION

2.7.1. SOLUBILITY OF GASEOUS CARBON DIOXIDE AND CARBONATE MINERALS

Values of the solubility product (i.e., K_{sp}) of the three main forms of calcium carbonate minerals and the effect of temperature and pH on K_{sp} are provided.

SOLUBILITY OF GASEOUS CARBON DIOXIDE: EFFECT OF THE TEMPERATURE, SALINITY, AND PRESSURE

The temperature (T, in K) dependent CO_2 solubility coefficient (mol L^{-1} atm^{-1}) and carbonic acid dissociation constants (K_1 and K_2) in water at 1 atm are given by :[368]

$$\log K_0 = 108.3865 + 0.01985076T - 6919.53/T - 40.45154 \log T + 669365/T^2$$

$$\log K_1 = -356.3094 - 0.06091964T + 21834.37/T + 126.8339 \log T - 1684915/T^2$$

$$\log K_2 = -107.8871 - 0.03252849T + 5151.79/T + 38.92561 \log T - 1684915/T^2$$

In seawater, K_0 depends on the salinity (S, in %) and temperature (T, in K), as expressed by: [369]

$$\ln K_0 = -58.0931 + 90.5069(100/T) + 22.2940 \ln(T/100) + S\,[0.027766 - 0.025888(T/100) + 0.0050578(T/100)^2]$$

The carbonic dissociation constants (K_1 and K_2) in seawater at 1 atm are represented by the following equations:[370]

$$\log K_1 = 43.6977 + 0.0129037S - 1.364 \times 10^{-4} S^2 - 2885.378/T - 7.045159 \ln T$$

$$\log K_2 = 452.0940 - 13.142162S + 8.101 \times 10^{-4} S^2 - 21263.61/T - 68.483143 \ln T - (581.4428S + 0.259601S^2)/T - 1.967035S \ln T$$

where S is the salinity (in %). At an average seawater S = 34.8 %, the pressure dependent K_1 and K_2 of carbonic acid is given by:

$$\log ({K_1}^P/\ {K_1}^1) = 0.013 + 1.319 \times 10^{-3} P - 3.061 \times 10^{-6} PT - 0.161 \times 10^{-6} T^2 - 0.02 \times 10^{-6} P^2$$

$$\log ({K_2}^P/\ {K_2}^1) = -0.015 + 0.839 \times 10^{-3} P - 1.908 \times 10^{-6} PT + 0.182 \times 10^{-6} T^2$$

where ${K_1}^1$ and ${K_2}^1$ are K_1 and K_2 at 1 atm, and ${K_1}^P$ and ${K_2}^P$ at P atm. These equations are valid for temperature range between 2 °C and 22 °C and pressures up to 1000 atm.

SOLUBILITY OF CARBONATE MINERALS: EFFECT OF THE TEMPERATURE AND PH

Uptake and release of carbon at alkaline pH usually involve precipitation of carbonate mineral through the reaction of ${CO_3}^{2-}$ with divalent cation such as Ca^{2+} (i.e., $CaCO_3$). The solubility of $CaCO_3$ depends on the pH due to the hydrolysis of ${CO_3}^{2-}$. At 25 °C and 1 atm the Solubility product (K_{sp}) is 3.31×10^{-9} for calcite, 4.61×10^{-9} for aragonite, and 1.22×10^{-8} for vaterite. Figure S1 (a) and (b) show the K_{sp} of various $CaCO_3$ crystal forms at temperature range between 0 and 90 °C and the calcite solubility as a function of pH and temperature, respectively.

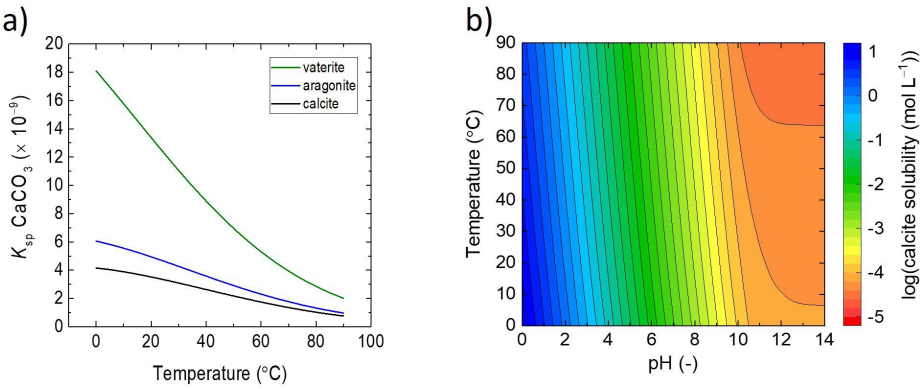

Figure S1: (a) Solubility product (K_{sp}) of three different crystal forms of $CaCO_3$ as a function of temperature. (b) Logarithmic calcite solubility in water as a function of the water pH and temperature.

The solubility products of calcite ($K_{\text{sp, calcite}}$), aragonite ($K_{\text{sp, aragonite}}$), and vaterite ($K_{\text{sp, vaterite}}$) at temperature range between 0 and 90 °C are given by: [368]

$\log K_{\text{sp, calcite}} = -171.9065 - 0.0077993T + 2839.319/T + 71.595 \log T$

$\log K_{\text{sp, aragonite}} = -171.9773 - 0.0077993T + 2903.293/T + 71.595 \log T$

$\log K_{\text{sp, vaterite}} = -172.1295 - 0.0077993T + 3074.688/T + 71.595 \log T$

In seawater, at salinity range between 27 and 43 % and temperature range between 2 and 25 °C, $K_{\text{sp, calcite}}$ is given by:[371]

$K_{\text{sp}} = [-34.452 - 39.866S^{1/3} + 110.21 \log S - 7.5752 \times 10^{-6} T^2] \times 10^{-7}$

The values of $K_{\text{sp, calcite}}$ as a function of pressure (P, in atm) in seawater is expressed by:[372]

$\ln ({K_{\text{sp, calcite}}}^{P} / {K_{\text{sp, calcite}}}^{1}) = 0.071320 + 0.0080412P - 2.2544 \times 10^{-5}\, PT$

where ${K_{\text{sp, calcite}}}^{1}$ is the solubility product of calcite at 1 atm and ${K_{\text{sp, calcite}}}^{P}$ is the solubility product of calcite at elevated pressure.

2.7.2. ELECTRICAL ENERGY CONSUMPTION FOR CARBON DIOXIDE CAPTURE

In this section, the underlying assumptions and calculations for obtaining Figure 2.14 are provided. The aim here is to compare the electrical energy required for the $CO_{2(g)}$ capture and recovery using a pH-swing generated via (membrane) electrolysis and BPMED.

As an example, the magnitude of pH-swing here is considered to be $\Delta pH = 14$. The required voltage (hence the energy consumption) of both methods depends strongly on the magnitude of the applied ΔpH. Note that a milder ΔpH can enable lower energy consumption.

Using both electrolysis and BPMED, 1 mole of OH^- and 1 mole of H^+ per mole of electron can be produced (assuming 100 % Coulombic efficiency). Assuming the following reactions, each produced OH^- (or H^+) ion, contributes to 1 mole of CO_2(g) being captured (or recovered):

$CO_{2(g)} + OH^- \leftrightarrow HCO_3^-$ at pH > 8.5 for the capture step

$HCO_3^- + H^+ \leftrightarrow CO_{2(g)}$ at lower pH for the recovery step

According to the Faraday's law, the electric quantity (Q) to produce 1 mole $CO_{2(g)}$ is 1 Faraday constant (F = 96485 $Cmol^{-1}$). The energy consumption per mole of capture $CO_{2(g)}$ can then be calculated via:

$$\text{Energy consumption} = V \times F$$

The required voltage (V, in volts) for (membrane) electrolysis can be written as [373]:

$$U_{electrolysis} = E^0_{anode} - E^0_{cathode} + i\sum R = E^0_{cell} + \eta_{H_2/O_2} + i\sum R_{tot} \quad \text{(S1)}$$

Where E^0_{anode} is the standard anode potential for oxygen evolution reaction (OER), $E^0_{cathode}$ is the standard cathode potential for hydrogen evolution reaction (HER), i is the applied current density, R_{tot} is the total ohmic resistivity, η_{H_2/O_2} is the over potential at the anode and cathode for OER and HER (i.e., the Tafel plot), and E^0_{cell} the standard cell potential. The estimated value for each term is given in Table S1.

Similarly, the required voltage for BPMED can be written as [89, 198, 374]:

$$U_{BPMED} = 0.059\Delta pH + \eta_{WDR} + i\sum R_{tot} \quad \text{(S2)}$$

Where ΔpH is the difference of the pH over the BPM, $0.059\Delta pH$ is the Nernstian potential based on the reversible free enthalpy (see chapter 3 for elaboration) and η_{WDR} is the over potential associated with the water dissociation reaction in the junction layer of the BPM. The estimated value for each term is given in Table S2.

For the calculations, electrochemical cells as shown in Figure S2 are assumed. For BPMED, the effect of the end electrodes is neglected as multiple cell pair (CEM-AEM-BPM) can be stacked up in one unit, overruling the electrodes over potential. In electrolysis stacking is not possible and the process is strongly dependent on the electrode reactions.

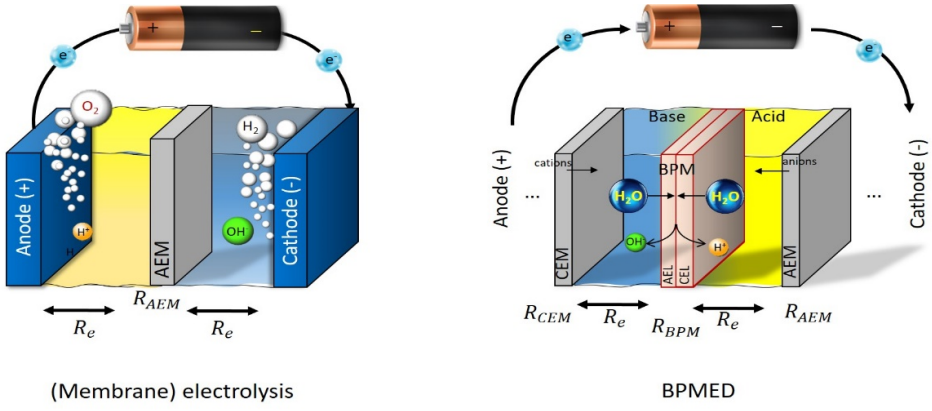

Figure S2: Schematic of the (membrane) electrolysis cell (left) and the BPMED cell (right) used for calculation of the electrical energy consumption of the electrochemical CO_2(g) capture and recovery.

Table S1: Summary of the ohmic resistance and the subsequent voltage losses in (membrane) electrolysis. R_e is calculated assuming a 0.5 M NaCl electrolyte with a conductivity of 47 mS cm^{-1} and a cell total thickness of $0.5 \times 2 = 1$ cm, while R_m is estimated assuming ion exchange membranes from Fumasep B.V.

R_e (electrolyte resistance) for 0.5 M NaCl	20 Ω cm^2
R_m (membrane resistance)	4 Ω cm^2
R_c (circuit resistance)	neglected
$i \times R_b$ (H_2(g) and O_2(g) bubble ohmic losses)	0.2 V
Assuming i= 20 mA cm^{-2}: $i(R_e + R_m + R_b)$ =	**0.68 V**

Table S2: Summary of the ohmic resistance and the subsequent voltage losses in Bipolar membrane electrodialysis (BPMED). R_e is calculated assuming a 0.5 M NaCl electrolyte with a conductivity of 47 mS cm^{-1} and a cell total thickness of $0.5 \times 2 = 1$ cm, while R_m is calculated assuming ion exchange membranes from Fumasep B.V.

R_e (electrolyte resistance) for 0.5 M NaCl	20 Ω cm^2
$R_m = R_{BPM} + R_{CEM} + R_{AEM}$	$4 + 10 + 4 = 18$ Ω cm^2
R_c (circuit resistance)	neglected
Assuming i= 20 mA cm^{-2}: $i(R_e + R_m)$ =	**0.76 V**

1. **(Membrane) electrolysis :$E^0_{cell}+\eta_{H2/O2}+i\sum R_{tot}$**

   (a) The standard cell potential, E^0_{cell} according for the water redox is as follow:

   - Cathode: $2H_2O + 2e^- \rightarrow H_{2(g)} + 2OH^-$, $E^0_{cathode} = -0.829V\ vs.SHE\ at\ pH{=}14$
   - Anode: $2H_2O \rightarrow 4e^- + O_{2(g)} + 4H^+$, $E^0_{anode} = 1.23V\ vs.SHE\ at\ pH{=}0$

   It follows that $E^0_{cell} = E^0_{anode} - E^0_{cathode} = 1.23 - (-0.829) = 2.059V$ for creating a ΔpH =14 using water electrolysis.

   (b) $\eta_{H2/O2}$ is approximately $2 \times 0.1 = 0.2V$ at current density $i = 20$mA cm^{-2} (based on the Tafel plot for HER and OER).

   (c) The ohmic voltage drop is $i\sum R_{tot}$, where $R_{tot} = R_e + R_m + R_b + R_c$ as shown in Table S1.

2. ***Ex-situ* BPMED: $0.059\Delta pH+\eta_{WDR}+i\sum R_{tot}$** *Ex-situ* here means that a neutral salt stream (e.g., NaCl) is used to produce high purity NaOH and HCl in BPMED. The produced acid and base are then used for CO_2(g) capture and recovery in external gas absorption and desorption steps.

   (a) The reversible Nernstian voltage based on the free enthalpy for creating a ΔpH =14 over the BPM is $0.059 \times 14 = 0.826V$ [374].

   (b) η_{WDR}: reaction over potential is estimated at 0.15 V [375].

   (c) $i\sum R$: The ohmic voltage losses can be estimated as shown in Table S2.

2.7.3. THE MARKET SIZE AND PRICE OF CARBON DIOXIDE UTILIZATION PRODUCTS

Table S3 gives the values associated with Figure 2.17, showing the market size and price of CO_2 utilization products in various regions between 2018 and first quarter of 2020 (unless otherwise noted). CO_2 and H_2 market size and price are included for reference.

Table S3: CCU products market size and price

Products	Market size ($Mtyr^{-1}$)	Price ($\$tonne^{-1}$)	References
Methane [1]	2894	86 – 173	[376–378]
Ethane	120.27	139 – 180	[379–382]
Propane	195[2]	317 – 374	[383–387]
Ethylene	184	474 – 609	[388–390]
Propylene	100	551 – 800	[391–394]
Methanol	98.9	174 – 235	[395–397]
Ethanol	86.8	45 – 1026	[398–401]
Isopropanol	2.15	750 – 3670	[402–404]
Acetone	6.1	906 – 1770 [3]	[405, 406]
Acetic acid	17.28	330[3]	[407, 408]
Formic acid	1.02	225 – 332[3]	[409, 410]
Urea	187.8	214 – 860	[411–414]
Carbon monoxide	150	236[4]	[415]
Carbon dioxide	230	15 – 120	[416]
Hydrogen	102	1640 – 2500	[417–419]

[1] assumes natural gas market size and price.
[2] 2016 market size.
[3] Chinese spot price.
[4] 2014-2018 average price in United States.

BIBLIOGRAPHY

[1] R. Sharifian et al. “Electrochemical carbon dioxide capture to close the carbon cycle”. In: *Energy Environ. Sci.* 14 (2 2021), pp. 781–814.

[2] M. Fajardy et al. *BECCS-deployment-: a-reality-check*. Dec. 2018.

[3] J. P. Mulligan. *Carbon Dioxide Emissions*. Nova Science.

[4] F. Sabatino et al. “Evaluation of a Direct Air Capture Process Combining Wet Scrubbing and Bipolar Membrane Electrodialysis”. In: *Industrial & Engineering Chemistry Research* 59.15 (2020), pp. 7007–7020.

[5] S. Nanda et al. “The progressive routes for carbon capture and sequestration”. In: *Energy Science & Engineering* 4.2 (2016), pp. 99–122.

[6] IPCC. *Summary for Policymakers*. Ed. by T. Stocker et al. Cambridge, United Kingdom and New York, NY, USA: Cambridge University Press, 2013. Chap. SPM, pp. 1–30. ISBN: ISBN 978-1-107-66182-0.

[7] C. Fernández-Dacosta et al. “Closing carbon cycles: Evaluating the performance of multi-product CO2 utilisation and storage configurations in a refinery”. In: *Journal of CO2 Utilization* 23 (2018), pp. 128–142.

[8] A. T. Fane. “A grand challenge for membrane desalination: More water, less carbon”. In: *Desalination* 426 (2018), pp. 155–163.

[9] C. F. de Lannoy et al. “Indirect ocean capture of atmospheric CO2: Part I. Prototype of a negative emissions technology”. In: *International Journal of Greenhouse Gas Control* 70 (2018), pp. 243–253.

[10] S. E. Tanzer et al. “When are negative emissions negative emissions?” In: *Energy Environ. Sci.* 12 (4 2019), pp. 1210–1218.

[11] O. Edenhofer. *Climate change 2014: mitigation of climate change*. Vol. 3. Cambridge University Press, 2015.

[12] “Global Carbon Budget 2018”. In: *Earth System Science Data* 10.4 (2018), pp. 2141–2194.

[13] A. Alonso et al. “Critical review of existing nanomaterial adsorbents to capture carbon dioxide and methane”. In: *Science of the total environment* 595 (2017), pp. 51–62.

[14] C. Song et al. “Alternative pathways for efficient CO2 capture by hybrid processes—A review”. In: *Renewable and Sustainable Energy Reviews* 82 (2018), pp. 215–231.

[15] A. Al-Mamoori et al. “Carbon Capture and Utilization Update”. In: *Energy Technology* 5.6 (2017), pp. 834–849.

[16] K. Z. House et al. “Economic and energetic analysis of capturing CO2 from ambient air”. In: *Proceedings of the National Academy of Sciences* 108.51 (2011), pp. 20428–20433.

[17] J. Míguez et al. “Evolution of CO2 capture technology between 2007 and 2017 through the study of patent activity”. In: *Applied Energy* 211 (2018), pp. 1282–1296.

[18] R. S. Haszeldine. “Carbon Capture and Storage: How Green Can Black Be?” In: *Science* 325.5948 (2009), pp. 1647–1652.

[19] B. P. Spigarelli et al. “Opportunities and challenges in carbon dioxide capture”. In: *Journal of CO2 Utilization* 1 (2013), pp. 69–87.

[20] D. Y. Leung et al. “An overview of current status of carbon dioxide capture and storage technologies”. In: *Renewable and Sustainable Energy Reviews* 39 (2014), pp. 426–443.

[21] E. J. Granite et al. “Review of novel methods for carbon dioxide separation from flue and fuel gases”. In: 2005.

[22] M. M. Abu-Khader. “Recent Progress in CO2 Capture/Sequestration: A Review”. In: *Energy Sources, Part A: Recovery, Utilization, and Environmental Effects* 28.14 (2006), pp. 1261–1279.

[23] D. M. D’Alessandro et al. “Carbon Dioxide Capture: Prospects for New Materials”. In: *Angewandte Chemie International Edition* 49.35 (2010), pp. 6058–6082.

[24] R. Surampalli et al. *Carbon capture and storage : physical, chemical, and biological methods*. English. Reston, Virginia : American Society of Civil Engineers, 2015.

[25] M. Songolzadeh et al. “Carbon Dioxide Separation from Flue Gases: A Technological Review Emphasizing Reduction in Greenhouse Gas Emissions”. In: *The Scientific World Journal* 2014 (2014), pp. 1–34.

[26] A. S. R. Machado et al. “CO2 capture and electrochemical conversion”. In: *Current Opinion in Green and Sustainable Chemistry* 11 (2018). Pharmaceuticals / Green Processes and Technologies, pp. 86–90.

[27] Y. Ishimoto et al. “Putting Costs of Direct Air Capture in Context”. In: *SSRN Electronic Journal* (June 2017).

[28] E. National Academies of Sciences et al. *Negative Emissions Technologies and Reliable Sequestration: A Research Agenda*. Washington, DC: The National Academies Press, 2019. ISBN: 978-0-309-48452-7.

[29] D. W. Keith et al. “A Process for Capturing CO2 from the Atmosphere”. In: *Joule* 2.8 (2018), pp. 1573–1594.

[30] M. C. Stern et al. “Post-combustion carbon dioxide capture using electrochemically mediated amine regeneration”. In: *Energy Environ. Sci.* 6 (8 2013), pp. 2505–2517.

[31] M. Wang et al. “CO2 Capture Using Electrochemically Mediated Amine Regeneration”. In: *Industrial & Engineering Chemistry Research* 59.15 (2020), pp. 7087–7096.

[32] R. Huebscher et al. “Electrochemical concentration and separation of carbon dioxide for advanced life support systems-carbonation cell system”. In: *SAE TRANSACTIONS*. Vol. 78. 1969, p. 151.

[33] M. P. Kang et al. “Concentration of carbon dioxide by a high-temperature electrochemical membrane cell”. In: *Journal of Applied Electrochemistry* 15.3 (1985), pp. 431–439.

[34] L. Walke et al. “Recovery of CO2 from flue gas using an electrochemical membrane”. In: *Gas Separation and Purification* 2.2 (1988), pp. 72–76.

[35] J. Winnick. “Electrochemical membrane gas separation”. In: 1990.

[36] M. Eisaman et al. “Energy-efficient electrochemical CO2 capture from the atmosphere”. In: *Technical Proceedings of the 2009 NSTI Nanotechnology Conference and Expo, NSTI-Nanotech 2009* 3 (Jan. 2009).

[37] F. Dimascio et al. “Extraction of Carbon Dioxide from Seawater by an Electrochemical Acidification Cell. Part 1 - Initial Feasibility Studies”. In: (July 2010), p. 25.

[38] L. Legrand et al. “Solvent-Free CO2 Capture Using Membrane Capacitive Deionization”. In: *Environmental Science & Technology* 52.16 (2018). PMID: 29993236, pp. 9478–9485.

[39] M. H. Youn et al. “Carbon dioxide sequestration process for the cement industry”. In: *Journal of CO2 Utilization* 34 (2019), pp. 325–334.

[40] S. Voskian et al. “Faradaic electro-swing reactive adsorption for CO2 capture”. In: *Energy Environ. Sci.* 12 (12 2019), pp. 3530–3547.

[41] R. A. Shaw et al. “Electrochemical CO2 capture thermodynamics”. In: *International Journal of Greenhouse Gas Control* 95 (2020), p. 102878.

[42] M. C. Stern et al. “Electrochemically mediated separation for carbon capture”. In: *Energy Procedia* 4 (2011). 10th International Conference on Greenhouse Gas Control Technologies, pp. 860–867.

[43] S. Datta et al. “Electrochemical CO2 Capture Using Resin-Wafer Electrodeionization”. In: *Industrial & Engineering Chemistry Research* 52.43 (2013), pp. 15177–15186.

[44] M. D. Eisaman et al. “CO2 desorption using high-pressure bipolar membrane electrodialysis”. In: *Energy Environ. Sci.* 4 (10 2011), pp. 4031–4037.

[45] B. De Mot et al. “Influence of flow and pressure distribution inside a gas diffusion electrode on the performance of a flow-by CO2 electrolyzer”. In: *Chemical Engineering Journal* 378 (2019), p. 122224.

[46] I. A. Digdaya et al. “A direct coupled electrochemical system for capture and conversion of CO2 from oceanwater”. In: *Nature Communications* 11.1 (2020), pp. 1–10.

[47] W. A. Smith et al. “Pathways to Industrial-Scale Fuel Out of Thin Air from CO2 Electrolysis”. In: *Joule* 3.8 (2019), pp. 1822–1834.

[48] T. Li et al. “Electrolytic Conversion of Bicarbonate into CO in a Flow Cell”. In: *Joule* 3.6 (2019), pp. 1487–1497.

[49] E. W. Lees et al. “Electrodes Designed for Converting Bicarbonate into CO”. In: *ACS Energy Letters* 5.7 (2020), pp. 2165–2173.

[50] J. H. Rheinhardt et al. “Electrochemical Capture and Release of Carbon Dioxide”. In: *ACS Energy Letters* 2.2 (2017), pp. 454–461.

[51] P. Kuntke et al. “Hydrogen Gas Recycling for Energy Efficient Ammonia Recovery in Electrochemical Systems”. In: *Environmental Science & Technology* 51.5 (2017), pp. 3110–3116.

[52] P. Kuntke et al. “Energy-Efficient Ammonia Recovery in an Up-Scaled Hydrogen Gas Recycling Electrochemical System”. In: *ACS Sustainable Chemistry & Engineering* 6.6 (2018), pp. 7638–7644.

[53] Y. Lei et al. “Calcium Carbonate Packed Electrochemical Precipitation Column: New Concept of Phosphate Removal and Recovery”. In: *Environmental Science & Technology* 53.18 (2019), pp. 10774–10780.

[54] V. L. Snoeyink et al. *Water chemistry*. John Wiley & Sons, Ltd, 1980.

[55] J. Butler. “Carbon dioxide equilibria and their applications”. In: (Jan. 1982).

[56] J. J. Morgan et al. *Aquatic chemistry: chemical equilibria and rates in natural waters*. Wiley, 1996.

[57] J. W. Murray. “Ocean Carbonate Chemistry: The Aquatic Chemistry Fundamentals”. In: *The Ocean Carbon Cycle and Climate*. Ed. by M. Follows et al. Dordrecht: Springer Netherlands, 2004, pp. 1–29.

[58] J. M. Mark et al. “A model of carbon dioxide dissolution and mineral carbonation kinetics”. In: *Proceedings: Mathematical, Physical and Engineering Sciences* 466.2117 (2010), pp. 1265–1290.

[59] C. A. Rochelle et al. “The impact of chemical reactions on CO2 storage in geological formations: a brief review”. In: *Geological Society, London, Special Publications* 233.1 (2004), pp. 87–106.

[60] X. Wang et al. “Comprehensive study of the hydration and dehydration reactions of carbon dioxide in aqueous solution”. In: *The Journal of Physical Chemistry A* 114.4 (2010), pp. 1734–1740.

[61] Y. Pocker et al. “Stopped-Flow Studies of Carbon Dioxide Hydration and Bicarbonate Dehydration in H2O and D2O. Acid-Base and Metal Ion Catalysis”. In: *Journal of the American Chemical Society* 99.20 (1977), pp. 6537–6543.

[62] A. G. Dickson et al. *Guide to best practices for ocean CO2 measurements*. North Pacific Marine Science Organization, 2007.

[63] R. E. Zeebe et al. *CO2 in seawater: equilibrium, kinetics, isotopes*. 65. Gulf Professional Publishing, 2001.

[64] F. J. Millero. “The thermodynamics of the carbonate system in seawater”. In: *Geochimica et Cosmochimica Acta* 43.10 (1979), pp. 1651–1661.

[65] A. Dickson et al. “The estimation of acid dissociation constants in seawater media from potentionmetric titrations with strong base. I. The ionic product of water — Kw”. In: *Marine Chemistry* 7.2 (1979), pp. 89–99.

[66] K. Schulz et al. “Determination of the rate constants for the carbon dioxide to bicarbonate inter-conversion in pH-buffered seawater systems”. In: *Marine Chemistry* 100.1 (2006), pp. 53–65.

[67] S. Lindskog. “The catalytic mechanism of carbonic anhydrase”. In: *Inorganica Chimica Acta* 79 (1983), p. 36.

[68] J. da Costa Ores et al. “Purification of carbonic anhydrase from bovine erythrocytes and its application in the enzymic capture of carbon dioxide.” In: *Chemosphere* 88 2 (2012), pp. 255–9.

[69] I. M. Power et al. “Carbon sequestration via carbonic anhydrase facilitated magnesium carbonate precipitation”. In: *International Journal of Greenhouse Gas Control* 16 (2013), pp. 145–155.

[70] H. Yun et al. “Simultaneous Sodium Hydroxide Production by Membrane Electrolysis and Carbon Dioxide Capture”. In: *Chemical Engineering & Technology* 40.12 (2017), pp. 2204–2211.

[71] H. Park et al. “CO2 Fixation by Membrane Separated NaCl Electrolysis”. In: *Energies* 8 (Aug. 2015), pp. 8704–8715.

[72] G. H. Rau. “Electrochemical Splitting of Calcium Carbonate to Increase Solution Alkalinity: Implications for Mitigation of Carbon Dioxide and Ocean Acidity”. In: *Environmental Science & Technology* 42.23 (2008). PMID: 19192821, pp. 8935–8940.

[73] A. Mehmood et al. “A novel high performance configuration of electrochemical cell to produce alkali for sequestration of carbon dioxide”. In: *Electrochimica Acta* 219 (2016), pp. 655–663.

[74] J. Way et al. “Low-Voltage Electrochemical Process for Direct Carbon Dioxide Sequestration”. In: *Journal of The Electrochemical Society* 159 (Jan. 2012), B627–B628.

[75] S. Stucki et al. “Coupled CO2 recovery from the atmosphere and water electrolysis: Feasibility of a new process for hydrogen storage”. In: *International Journal of Hydrogen Energy* 20.8 (1995), pp. 653–663.

[76] G. H. Rau. “Electrochemical CO2 capture and storage with hydrogen generation”. In: *Energy Procedia* 1.1 (2009). Greenhouse Gas Control Technologies 9, pp. 823–828.

[77] H. D. Willauer et al. *Extraction of Carbon Dioxide and Hydrogen from Seawater By an Electrolytic Cation Exchange Module (E-CEM) Part 5: E-CEM Effluent Discharge Composition as a Function of Electrode Water Composition*. Tech. rep. NAVAL RESEARCH LAB WASHINGTON DC WASHINGTON United States, 2017.

[78] A. Bard et al. *Electrochemical Methods: Fundamentals and Applications, 2nd Edition*. Wiley Textbooks, 2000. ISBN: 9781118312803.

[79] G. H. Rau. “CO2 Mitigation via Capture and Chemical Conversion in Seawater”. In: *Environmental Science & Technology* 45.3 (2011). PMID: 21189009, pp. 1088–1092.

[80] N. R. Council et al. *The Hydrogen Economy: Opportunities, Costs, Barriers, and R&D Needs*. Washington, DC: The National Academies Press, 2004. ISBN: 978-0-309-09163-3.

[81] H. D. Willauer et al. “Development of an Electrochemical Acidification Cell for the Recovery of CO2 and H2 from Seawater II. Evaluation of the Cell by Natural Seawater”. In: *Industrial & Engineering Chemistry Research* 51.34 (2012), pp. 11254–11260.

[82] H. D. Willauer et al. “Feasibility of CO2 Extraction from Seawater and Simultaneous Hydrogen Gas Generation Using a Novel and Robust Electrolytic Cation Exchange Module Based on Continuous Electrodeionization Technology”. In: *Industrial & Engineering Chemistry Research* 53.31 (2014), pp. 12192–12200.

[83] C. Wang et al. “Importance of Ambient O2 for Electrochemical Enrichment of Atmospheric CO2”. In: *Industrial & Engineering Chemistry Research* 52.7 (2013), pp. 2470–2476.

[84] H. W. Pennline et al. “Separation of CO2 from flue gas using electrochemical cells”. In: *Fuel* 89.6 (2010). Advanced Fossil Energy Utilization, pp. 1307–1314.

[85] S. Z. Oener et al. “Ionic Processes in Water Electrolysis: The Role of Ion-Selective Membranes”. In: *ACS Energy Letters* 2.11 (2017), pp. 2625–2634.

[86] H. Strathmann et al. “Limiting current density and water dissociation in bipolar membranes”. In: *Journal of Membrane Science* 125.1 (1997), pp. 123–142.

[87] T. Xu et al. “Water dissociation phenomena in a bipolar membrane”. In: *Science in China Series B: Chemistry* 42.6 (1999), pp. 589–598.

[88] D. A. Vermaas et al. “Synergistic electrochemical CO2 reduction and water oxidation with a bipolar membrane”. In: *ACS Energy Letters* 1.6 (2016), pp. 1143–1148.

[89] D. A. Vermaas et al. “Ion transport mechanisms in bipolar membranes for (photo) electrochemical water splitting”. In: *Sustain. Energy Fuels* 2 (9 2018), pp. 2006–2015.

[90] W. J. van Egmond et al. “Performance of an environmentally benign acid base flow battery at high energy density”. In: *International Journal of Energy Research* 42.4 (2018), pp. 1524–1535.

[91] J. Han et al. “Reverse electrodialysis (RED) using a bipolar membrane to suppress inorganic fouling around the cathode”. In: *Water Research* (2019), p. 115078.

[92] A. Bandi et al. “CO2 recycling for hydrogen storage and transportation —Electrochemical CO2 removal and fixation”. In: *Energy Conversion and Management* 36.6 (1995). Proceedings of the Second International Conference on Carbon Dioxide Removal, pp. 899–902.

[93] M. D. Eisaman et al. “CO2 separation using bipolar membrane electrodialysis”. In: *Energy Environ. Sci.* 4 (4 2011), pp. 1319–1328.

[94] R. E. Moussaoui et al. “Co-ion leakage through bipolar membranes Influence on I–V responses and water-splitting efficiency”. In: *Journal of Membrane Science* 90.3 (1994), pp. 283–292.

[95] Y. Tanaka. “Acceleration of water dissociation generated in an ion exchange membrane”. In: *Journal of Membrane Science* 303.1 (2007), pp. 234–243.

[96] Y. Tanaka. “Water dissociation reaction generated in an ion exchange membrane”. In: *Journal of Membrane Science* 350.1 (2010), pp. 347–360.

[97] T. Luo et al. “Selectivity of ion exchange membranes: A review”. In: *Journal of Membrane Science* 555 (2018), pp. 429–454.

[98] A. Alcaraz et al. “Conductive and Capacitive Properties of the Bipolar Membrane Junction Studied by AC Impedance Spectroscopy”. In: *The Journal of Physical Chemistry B* 105 (Nov. 2001), p. 11669.

[99] P. Ramírez et al. “Effects of temperature and ion transport on water splitting in bipolar membranes”. In: *Journal of Membrane Science* 73.2 (1992), pp. 191–201.

[100] R. Parnamae et al. “Bipolar membranes: A review on principles, latest developments, and applications”. In: *Journal of Membrane Science* 617 (2021), p. 118538.

[101] R. Wiebe et al. “The Solubility of Carbon Dioxide in Water at Various Temperatures from 12 to 40° and at Pressures to 500 Atmospheres. Critical Phenomena*”. In: *Journal of the American Chemical Society* 62.4 (1940), pp. 815–817.

[102] L. Diamond et al. “Solubility of CO2 in water from -1.5 to 100°C and from 0.1 to 100 MPa: Evaluation of literature data and thermodynamic modelling”. In: *Fluid Phase Equilibria* 208 (June 2003), pp. 265–290.

[103] S. Hangx. “Behaviour of the CO2-H2O system and preliminary mineralisation model and experiments”. In: *CATO Workpackage WP* 4.1 (2005), pp. 1–43.

[104] M. Vandiver et al. “Mechanical Characterization of Anion Exchange Membranes by Extensional Rheology under Controlled Hydration”. In: *Journal of the Electrochemical Society* 161 (June 2014), H677–H683.

[105] J. Peron et al. “Properties of Nafion® NR-211 membranes for PEMFCs”. In: *Journal of Membrane Science* 356.1 (2010), pp. 44–51.

[106] H. Nagasawa et al. “A New Recovery Process of Carbon Dioxide from Alkaline Carbonate Solution via Electrodialysis”. In: *AIChE Journal* 55 (Dec. 2009), pp. 3286–3293.

[107] A. Iizuka et al. “Carbon dioxide recovery from carbonate solutions using bipolar membrane electrodialysis”. In: *Separation and purification technology* 101 (2012), pp. 49–59.

[108] Y. Zhao et al. “A novel technology of carbon dioxide adsorption and mineralization via seawater decalcification by bipolar membrane electrodialysis system with a crystallizer”. In: *Chemical Engineering Journal* 381 (2020), p. 122542.

[109] C. Jiang et al. “Mathematical modelling and experimental investigation of CO2 absorber recovery using an electro-acidification method”. In: *Chemical Engineering Journal* 360 (2019), pp. 654–664.

[110] H. Li et al. “Study of CO2 capture by seawater and its reinforcement”. In: *Energy* 164 (2018), pp. 1135–1144.

[111] S. A. Rackley. “10 - Mineral carbonation”. In: *Carbon Capture and Storage (Second Edition)*. Ed. by S. A. Rackley. Second Edition. Boston: Butterworth-Heinemann, 2017, pp. 253–282. ISBN: 978-0-12-812041-5.

[112] T. Coffey et al. “Hydrogen as a Fuel for DOD”. In: *Defense Horizons* (2003), p. 1.

[113] G. H. Rau et al. “The global potential for converting renewable electricity to negative-CO 2-emissions hydrogen”. In: *Nature Climate Change* 8.7 (2018), pp. 621–625.

[114] M. D. Eisaman et al. “CO2 extraction from seawater using bipolar membrane electrodialysis”. In: *Energy Environ. Sci.* 5 (6 2012), pp. 7346–7352.

[115] M. L. Druckenmiller et al. “Carbon sequestration using brine of adjusted pH to form mineral carbonates”. In: *Fuel Processing Technology* 86.14-15 (2005), pp. 1599–1614.

[116] W. Wang et al. “CO2 Fixation in Ca2+-/Mg2+-Rich Aqueous Solutions through Enhanced Carbonate Precipitation”. In: *Industrial & Engineering Chemistry Research* 50.13 (2011), pp. 8333–8339.

[117] D. Desai et al. “Electrochemical Desalination of Seawater and Hypersaline Brines with Coupled Electricity Storage”. In: *ACS Energy Letters* 3.2 (2018), pp. 375–379.

[118] M. D. Eisaman et al. “Indirect ocean capture of atmospheric CO2: Part II. Understanding the cost of negative emissions”. In: *International Journal of Greenhouse Gas Control* 70 (2018), pp. 254–261.

[119] W. Omar et al. “Application of seeded batch crystallization methods for reduction of the scaling tendency of seawater–A study of growth kinetics of calcium carbonate in seawater”. In: *Crystal Research and Technology: Journal of Experimental and Industrial Crystallography* 44.5 (2009), pp. 469–476.

[120] A. Kirchofer et al. “Impact of alkalinity sources on the life-cycle energy efficiency of mineral carbonation technologies”. In: *Energy Environ. Sci.* 5 (9 2012), pp. 8631–8641.

[121] G. C. Ganzi et al. “Water purification and recycling using the CDI process”. In: *Environmental Progress* 11.1 (1992), pp. 49–53.

[122] R. Datta et al. “Electrodeionization substrate, and device for electrodeionization treatment”. In: (Jan. 2002).

[123] Y. J. Lin et al. “Electronically and ionically conductive porous material and method for manufacture of resin wafers therefrom”. In: (July 2011).

[124] S.-Y. Pan et al. “Development of a Resin Wafer Electrodeionization Process for Impaired Water Desalination with High Energy Efficiency and Productivity”. In: *ACS Sustainable Chemistry & Engineering* 5.4 (2017), pp. 2942–2948.

[125] I. N. Widiasa et al. “Performance of a novel electrodeionization technique during citric acid recovery”. In: 2004.

[126] L. Alvarado et al. “Electrodeionization: Principles, Strategies and Applications”. In: *Electrochimica Acta* 132 (2014), pp. 583–597.

[127] M. Parvazinia et al. “CO2 capture by ion exchange resins as amine functionalised adsorbents”. In: *Chemical Engineering Journal* 331 (2018), pp. 335–342.

[128] G. Zeng et al. “Application of Electrodeionization Process for Bioproduct Recovery and CO2 Capture and Storage”. In: *Current Organic Chemistry* 20 (May 2016), pp. 1–1.

[129] J. Wang et al. “A study of the electrodeionization process — high-purity water production with a RO/EDI system”. In: *Desalination* 132.1 (2000). Membranes in Drinking and Industrial Water Production, pp. 349–352.

[130] K. H. Yeon et al. “Electrochemical Characterization of Ion-Exchange Resin Beds and Removal of Cobalt by Electrodeionization for High Purity Water Production”. In: *Separation Science and Technology* 38.2 (2003), pp. 443–462.

[131] Ö. Arar et al. “Various applications of electrodeionization (EDI) method for water treatment—A short review”. In: *Desalination* 342 (2014). Special Issue: Electromembrane Processes for Desalination, pp. 16–22.

[132] R. N. Gurram et al. “Removal of enzymatic and fermentation inhibitory compounds from biomass slurries for enhanced biorefinery process efficiencies”. In: *Bioresource Technology* 102.17 (2011), pp. 7850–7859.

[133] W. R. Alesi et al. “Evaluation of a Primary Amine-Functionalized Ion-Exchange Resin for CO2 Capture”. In: *Industrial & Engineering Chemistry Research* 51.19 (2012), pp. 6907–6915.

[134] R. Veneman et al. “Adsorption of H2O and CO2 on supported amine sorbents”. In: *International Journal of Greenhouse Gas Control* 41 (2015), pp. 268–275.

[135] K. Afrasiabi. “Wafer Enhanced Electrodeionization for Conversion of CO2 into Bicarbonate Feed for Algae Cultured Photobioreactors”. In: (2018).

[136] H. Xie et al. “Low-energy-consumption electrochemical CO2 capture driven by biomimetic phenazine derivatives redox medium”. In: *Applied Energy* 259 (2020), p. 114119.

[137] J. D. Watkins et al. “Redox-Mediated Separation of Carbon Dioxide from Flue Gas”. In: *Energy & Fuels* 29.11 (2015), pp. 7508–7515.

[138] B. P. Sullivan et al. *Electrochemical and electrocatalytic reactions of carbon dioxide*. Elsevier, 2012.

[139] M. Robert. “Proton-coupled electron transfer”. In: *Energy Environ. Sci.* 5 (7 2012), pp. 7695–7695.

[140] C. Costentin. “Electrochemical Approach to the Mechanistic Study of Proton-Coupled Electron Transfer”. In: *Chemical Reviews* 108.7 (2008), pp. 2145–2179.

[141] C. Huang et al. “CO2 Capture from Flue Gas Using an Electrochemically Reversible Hydroquinone/Quinone Solution”. In: *Energy & Fuels* 33.4 (2019), pp. 3380–3389.

[142] P. Scovazzo et al. “Electrochemical Separation and Concentration of Carbon Dioxide from Nitrogen”. In: *Journal of The Electrochemical Society* 150.5 (2003), p. D91.

[143] H. Ishida et al. “Interaction between CO2 and Electrochemically Reduced Species”. In: *Chemistry Letters* 23.5 (1994), pp. 905–908.

[144] R. Ranjan et al. “Reversible electrochemical trapping of carbon dioxide using bipyridine that does not require thermal activation”. In: *The journal of physical chemistry letters* 6.24 (2015), pp. 4943–4946.

[145] B. Gurkan et al. “Quinone Reduction in Ionic Liquids for Electrochemical CO2 Separation”. In: *ACS Sustainable Chemistry & Engineering* 3.7 (2015), pp. 1394–1405.

[146] D. H. Apaydin et al. “Direct Electrochemical Capture and Release of Carbon Dioxide Using an Industrial Organic Pigment: Quinacridone”. In: *Angewandte Chemie International Edition* 53.26 (2014), pp. 6819–6822.

[147] M. Mizen et al. “Reductive Addition of CO2 to Phenanthrenequinone”. In: *J. Electrochem. Soc.* 136 (1989), p. 941.

[148] Y. Liu et al. “Electrochemically mediated carbon dioxide separation with quinone chemistry in salt-concentrated aqueous media”. In: *Nature Communications* 11 (May 2020), p. 2278.

[149] G. P. Moss et al. “Glossary of class names of organic compounds and reactivity intermediates based on structure (IUPAC Recommendations 1995)”. In: *Pure and Applied Chemistry* 67.8-9 (1995), pp. 1307–1375.

[150] P. S. Guin et al. “Electrochemical Reduction of Quinones in Different Media: A Review”. In: *International Journal of Electrochemistry* 2011 (2011).

[151] L. F. Fieser. “THE TAUTOMERISM OF HYDROXY QUINONES”. In: *Journal of the American Chemical Society* 50.2 (1928), pp. 439–465.

[152] E. Laviron. “Electrochemical reactions with protonations at equilibrium”. In: *Journal of Electroanalytical Chemistry and Interfacial Electrochemistry* 169.1 (1984), pp. 29–46.

[153] M. Quan et al. “Voltammetry of Quinones in Unbuffered Aqueous Solution: Reassessing the Roles of Proton Transfer and Hydrogen Bonding in the Aqueous Electrochemistry of Quinones”. In: *Journal of the American Chemical Society* 129.42 (2007), pp. 12847–12856.

[154] D. R. Weinberg et al. “Proton-Coupled Electron Transfer”. In: *Chemical Reviews* 112.7 (2012), pp. 4016–4093.

[155] B. Trumpower. “The protonmotive Q cycle. Energy transduction by coupling of proton translocation to electron transfer by the cytochrome bc1 complex.” In: *Journal of Biological Chemistry* 265.20 (1990), pp. 11409–11412.

[156] Y. Lei et al. “Electrochemical Induced Calcium Phosphate Precipitation: Importance of Local pH”. In: *Environmental Science & Technology* 51.19 (2017). PMID: 28872838, pp. 11156–11164.

[157] L. Legrand et al. “Role of ion exchange membranes and capacitive electrodes in membrane capacitive deionization (MCDI) for CO2 capture”. In: *Journal of Colloid and Interface Science* 564 (2020), pp. 478–490.

[158] W. Xing et al. “Versatile applications of capacitive deionization (CDI)-based technologies”. In: *Desalination* 482 (2020), p. 114390.

[159] D. Vermaas et al. “Capacitive Electrodes for Energy Generation by Reverse Electrodialysis”. In: *Procedia Engineering* 44 (2012). Euromembrane Conference 2012, pp. 496–497.

[160] Z. H. Huang et al. “Carbon electrodes for capacitive deionization”. In: *J. Mater. Chem. A* 5 (2 2017), pp. 470–496.

[161] P. Ratajczak et al. “Carbon electrodes for capacitive technologies”. In: *Energy Storage Materials* 16 (2019), pp. 126–145.

[162] K. Singh et al. “Nickel hexacyanoferrate electrodes for high mono/divalent ion-selectivity in capacitive deionization”. In: *Desalination* 481 (2020), p. 114346.

[163] P. Biesheuvel et al. “Theory of membrane capacitive deionization including the effect of the electrode pore space”. In: *Journal of Colloid and Interface Science* 360.1 (2011), pp. 239–248.

[164] R. Zhao et al. “Energy consumption and constant current operation in membrane capacitive deionization”. In: *Energy Environ. Sci.* 5 (11 2012), pp. 9520–9527.

[165] P. Długołecki et al. “Energy Recovery in Membrane Capacitive Deionization”. In: *Environmental Science & Technology* 47.9 (2013). PMID: 23477563, pp. 4904–4910.

[166] S. Porada et al. “Review on the science and technology of water desalination by capacitive deionization”. In: *Progress in Materials Science* 58.8 (2013), pp. 1388–1442.

[167] A. Ullah et al. “Performance and energy cost evaluation of an integrated NH3-based CO2 capture-capacitive deionization process”. In: *International Journal of Greenhouse Gas Control* 66 (2017), pp. 85–96.

[168] M. Rahimi et al. “Carbon Dioxide Capture Using an Electrochemically Driven Proton Concentration Process”. In: *Cell Reports Physical Science* (2020), p. 100033.

[169] J. Winnick et al. “Carbon dioxide concentration for manned spacecraft using a molten carbonate electrochemical cell”. In: *AIChE Journal* 28.1 (1982), pp. 103–111.

[170] J. Rosen et al. “Molten Carbonate Fuel Cell Performance for CO2 Capture from Natural Gas Combined Cycle Flue Gas”. In: *Journal of The Electrochemical Society* 167.6 (2020), p. 064505.

[171] M. Spinelli et al. “Assessing the potential of molten carbonate fuel cell-based schemes for carbon capture in natural gas-fired combined cycle power plants”. In: *Journal of Power Sources* 448 (2020), p. 227223.

[172] P. Greppi et al. “Membranes and Molten Carbonate Fuel Cells to Capture CO2 and Increase Energy Production in Natural Gas Power Plants”. In: *Industrial & Engineering Chemistry Research* 52.26 (2013), pp. 8755–8764.

[173] K. Sugiura et al. “The carbon dioxide concentrator by using MCFC”. In: *Journal of Power Sources* 118.1 (2003). Scientific Advances in Fuel Cell Systems, pp. 218–227.

[174] D. Shekhawat et al. “A Review of Carbon Dioxide Selective Membranes: A Topical Report”. In: (Jan. 2003).

[175] Z. Rui et al. “Modeling and analysis of carbon dioxide permeation through ceramic-carbonate dual-phase membranes”. In: *Journal of Membrane Science* 345.1 (2009), pp. 110–118.

[176] Z. Rui et al. “Modeling and analysis of ceramic–carbonate dual-phase membrane reactor for carbon dioxide reforming with methane”. In: *International Journal of Hydrogen Energy* 36.14 (2011). 4th Asian Bio-Hydrogen Symposium, pp. 8292–8300.

[177] H. Bae et al. “Hybrid seawater desalination-carbon capture using modified seawater battery system”. In: *Journal of Power Sources* 410-411.July 2018 (2019), pp. 99–105.

[178] A. Khurram et al. “Tailoring the Discharge Reaction in Li-CO2 Batteries through Incorporation of CO2 Capture Chemistry”. In: *Joule* 2.12 (2018), pp. 2649–2666.

[179] Y. Li et al. “A High-Capacity Lithium–Gas Battery Based on Sulfur Fluoride Conversion”. In: *The Journal of Physical Chemistry C* 122.13 (2018), pp. 7128–7138.

[180] H. Yin et al. “Capture and electrochemical conversion of CO2 to value-added carbon and oxygen by molten salt electrolysis”. In: *Energy Environ. Sci.* 6 (5 2013), pp. 1538–1545.

[181] N. Hollingsworth et al. “CO2 capture and electrochemical conversion using superbasic [P66614][124Triz]”. In: *Faraday Discuss.* 183 (0 2015), pp. 389–400.

[182] S. Kar et al. “Integrated CO2 Capture and Conversion to Formate and Methanol: Connecting Two Threads”. In: *Accounts of Chemical Research* 52.10 (2019). PMID: 31487145, pp. 2892–2903.

[183] P. Zhang et al. “Electrochemical CO2 Capture and Conversion”. In: *Materials and Processes for CO2 Capture, Conversion, and Sequestration*. John Wiley and Sons, Ltd, 2018. Chap. 5, pp. 213–266. ISBN: 9781119231059.

[184] N. Li et al. “Understanding of Electrochemical Mechanisms for CO2 Capture and Conversion into Hydrocarbon Fuels in Transition-Metal Carbides (MXenes)”. In: *ACS Nano* 11.11 (2017). PMID: 28892617, pp. 10825–10833.

[185] J. Choi et al. “Process design and optimization of MEA-based CO2 capture processes for non-power industries”. In: *Energy* 185 (2019), pp. 971–980.

[186] R. Notz et al. “Post combustion CO2 capture by reactive absorption: Pilot plant description and results of systematic studies with MEA”. In: *International Journal of Greenhouse Gas Control* 6 (2012), pp. 84–112.

[187] T. Yokoyama. “Analysis of reboiler heat duty in MEA process for CO2 capture using equilibrium-staged model”. In: *Separation and Purification Technology* 94 (2012). CO2 Capture and Storage, pp. 97–103.

[188] W. Zhang et al. “Parametric study on the regeneration heat requirement of an amine-based solid adsorbent process for post-combustion carbon capture”. In: *Applied Energy* 168 (2016), pp. 394–405.

[189] H. P. Mangalapally et al. “Pilot plant experimental studies of post combustion CO2 capture by reactive absorption with MEA and new solvents”. In: *Energy Procedia* 1.1 (2009), pp. 963–970.

[190] S.-Y. Oh et al. “Energy minimization of MEA-based CO2 capture process”. In: *Applied Energy* 169 (2016), pp. 353–362.

[191] M. R. Abu-Zahra et al. “CO2 capture from power plants: Part I. A parametric study of the technical performance based on monoethanolamine”. In: *International Journal of Greenhouse gas control* 1.1 (2007), pp. 37–46.

[192] J. Thomas et al. “The evolution of performance solvents for gas treating”. In: *Petroenergy Conference, October*. Vol. 24. 1989, p. 1989.

[193] M. Clausse et al. “Numerical parametric study on CO2 capture by indirect thermal swing adsorption”. In: *International Journal of Greenhouse Gas Control* 5.5 (2011), pp. 1206–1213.

[194] J. K. Stolaroff et al. “Carbon Dioxide Capture from Atmospheric Air Using Sodium Hydroxide Spray”. In: *Environmental Science & Technology* 42.8 (2008), pp. 2728–2735.

[195] H. D. Willauer et al. “Development of an electrochemical acidification cell for the recovery of CO2 and H2 from seawater”. In: *Industrial and Engineering Chemistry Research* 50.17 (2011), pp. 9876–9882.

[196] E. ToolBox. *Heat of combustion [online]*. https://www.engineeringtoolbox.com/standard-heat-of-combustion-energy-content-d_1987.html. 2017.

[197] C. C. L. McCrory et al. “Benchmarking Hydrogen Evolving Reaction and Oxygen Evolving Reaction Electrocatalysts for Solar Water Splitting Devices”. In: *Journal of the American Chemical Society* 137.13 (2015). PMID: 25668483, pp. 4347–4357.

[198] S. Z. Oener et al. “Accelerating water dissociation in bipolar membranes and for electrocatalysis”. In: *Science* (2020).

[199] M. L. Jordan et al. “Promoting water-splitting in Janus bipolar ion-exchange resin wafers for electrodeionization”. In: *Mol. Syst. Des. Eng.* 5 (5 2020), pp. 922–935.

[200] M. D. Eisaman. “Negative Emissions Technologies: The Tradeoffs of Air-Capture Economics”. In: *Joule* 4.3 (2020), pp. 516–520.

[201] M. L. Jordan et al. “Promoting water-splitting in Janus bipolar ion-exchange resin wafers for electrodeionization”. In: *Mol. Syst. Des. Eng.* (2020).

[202] Olivier et al. “Trends in global CO2 and total greenhouse gas emissions 2019 Report”. In: *PBL Netherlands Environmental Assessment Agency* (2020).

[203] G. Realmonte et al. “An inter-model assessment of the role of direct air capture in deep mitigation pathways”. In: *Nature communications* 10.1 (2019), pp. 1–12.

[204] C. Beuttler et al. “The Role of Direct Air Capture in Mitigation of Anthropogenic Greenhouse Gas Emissions”. In: *Frontiers in Climate* 1 (2019), p. 10.

[205] G. Reiter et al. “Evaluating CO2 sources for power-to-gas applications–A case study for Austria”. In: *Journal of CO2 Utilization* 10 (2015), pp. 40–49.

[206] E. I. Koytsoumpa et al. “The CO2 economy: Review of CO2 capture and reuse technologies”. In: *The Journal of Supercritical Fluids* 132 (2018). SI: EMSF 2016, pp. 3–16.

[207] K. S. Lackner. “The thermodynamics of direct air capture of carbon dioxide”. In: *Energy* 50 (2013), pp. 38–46.

[208] Z. Zhongming et al. *The role of CCUS in low-carbon power systems*. 2020.

[209] C. Pritchard et al. “Thermodynamics, economics and systems thinking: What role for air capture of CO2?” In: *Process Safety and Environmental Protection* 94 (2015), pp. 188–195.

[210] IEA-Paris. *Direct Air Capture*. 2020.

[211] K. Heidel et al. “Process design and costing of an air-contactor for air-capture”. In: *Energy Procedia* 4 (2011). 10th International Conference on Greenhouse Gas Control Technologies, pp. 2861–2868.

[212] *Global Thermostat*. 2018.

[213] J. Wurzbacher. “Capturing CO2 from air”. In: *Internationaler Motorenkongress 2017*. Springer, 2017, pp. 499–511.

[214] A. Kiani et al. “Techno-Economic Assessment for CO2 Capture From Air Using a Conventional Liquid-Based Absorption Process”. In: *Frontiers in Energy Research* 8 (2020), p. 92.

[215] D. Moreira et al. “Atmospheric CO2 capture by algae: negative carbon dioxide emission path”. In: *Bioresource technology* 215 (2016), pp. 371–379.

[216] D. Tsai et al. “The potential of carbon dioxide capture and sequestration with algae”. In: *Ecological engineering* 98 (2017), pp. 17–23.

[217] M. K. Lam et al. “Current status and challenges on microalgae-based carbon capture”. In: *International Journal of Greenhouse Gas Control* 10 (2012), pp. 456–469.

[218] A. Ghorbani et al. “A review of carbon capture and sequestration in Iran: microalgal biofixation potential in Iran”. In: *Renewable and Sustainable Energy Reviews* 35 (2014), pp. 73–100.

[219] A. Ghosh et al. “Carbon concentration in algae: reducing CO2 from exhaust gas”. In: *Trends in biotechnology* 35.9 (2017), pp. 806–808.

[220] W. Zhou et al. “Bio-mitigation of carbon dioxide using microalgal systems: advances and perspectives”. In: *Renewable and Sustainable Energy Reviews* 76 (2017), pp. 1163–1175.

[221] K. Zhou et al. “Alternative materials in technologies for Biogas upgrading via CO2 capture”. In: *Renewable and Sustainable Energy Reviews* 79 (2017), pp. 1414–1441.

[222] M. Waqas et al. “Development of biochar as fuel and catalyst in energy recovery technologies”. In: *Journal of cleaner production* 188 (2018), pp. 477–488.

[223] X. f. Tan et al. “Biochar-based nano-composites for the decontamination of wastewater: a review”. In: *Bioresource technology* 212 (2016), pp. 318–333.

[224] N. A. Qambrani et al. “Biochar properties and eco-friendly applications for climate change mitigation, waste management, and wastewater treatment: A review”. In: *Renewable and Sustainable Energy Reviews* 79 (2017), pp. 255–273.

[225] A. E. Creamer et al. “Carbon dioxide capture using various metal oxyhydroxide–biochar composites”. In: *Chemical Engineering Journal* 283 (2016), pp. 826–832.

[226] S. P. Galinato et al. “The economic value of biochar in crop production and carbon sequestration”. In: *Energy Policy* 39.10 (2011), pp. 6344–6350.

[227] S. Gupta et al. “Use of biochar as carbon sequestering additive in cement mortar”. In: *Cement and concrete composites* 87 (2018), pp. 110–129.

[228] P. H. Huang et al. “Adsorption of carbon dioxide onto activated carbon prepared from coconut shells”. In: *Journal of Chemistry* 2015 (2015).

[229] M. Asif et al. “Post-combustion CO2 capture with chemical absorption and hybrid system: current status and challenges”. In: *Greenhouse Gases: Science and Technology* 8.6 (2018), pp. 998–1031.

[230] B. Dutcher et al. “Amine-Based CO2 Capture Technology Development from the Beginning of 2013—A Review”. In: *ACS Applied Materials & Interfaces* 7.4 (2015), pp. 2137–2148.

[231] M. Bui et al. “Carbon capture and storage (CCS): the way forward”. In: *Energy Environ. Sci.* 11 (5 2018), pp. 1062–1176.

[232] I. Sreedhar et al. “Carbon capture by absorption–path covered and ahead”. In: *Renewable and Sustainable Energy Reviews* 76 (2017), pp. 1080–1107.

[233] J. T. Yeh et al. “Study of CO2 Absorption and Desorption in a Packed Column”. In: *Energy & Fuels* 15.2 (2001), pp. 274–278.

[234] V. Nikulshina et al. “CO2 capture from air and co-production of H2 via the Ca(OH)2–CaCO3 cycle using concentrated solar power–Thermodynamic analysis”. In: *Energy* 31.12 (2006), pp. 1715–1725.

[235] V. Nikulshina et al. “Kinetic analysis of the carbonation reactions for the capture of CO2 from air via the Ca(OH)2–CaCO3–CaO solar thermochemical cycle”. In: *Chemical Engineering Journal* 129.1 (2007), pp. 75–83.

[236] V. Nikulshina et al. “Feasibility of Na-based thermochemical cycles for the capture of CO2 from air—Thermodynamic and thermogravimetric analyses”. In: *Chemical Engineering Journal* 140.1 (2008), pp. 62–70.

[237] B. Feng et al. “Reduction of Energy Requirement of CO2 Desorption by Adding Acid into CO2-Loaded Solvent”. In: *Energy & Fuels* 24.1 (2010), pp. 213–219.

[238] A. Samanta et al. “Post-Combustion CO2 Capture Using Solid Sorbents: A Review”. In: *Industrial & Engineering Chemistry Research* 51.4 (2012), pp. 1438–1463.

[239] Q. Cen et al. “Thermodynamics and regeneration studies of CO2 adsorption on activated carbon”. In: *Greenhouse Gases: Science and Technology* 6.6 (2016), pp. 787–796.

[240] S. Choi et al. “Adsorbent Materials for Carbon Dioxide Capture from Large Anthropogenic Point Sources”. In: *ChemSusChem* 2.9 (2009), pp. 796–854.

[241] P. Pandey et al. “Membranes for gas separation”. In: *Progress in Polymer Science* 26.6 (2001), pp. 853–893.

[242] P. Bernardo et al. “Membrane Gas Separation: A Review/State of the Art”. In: *Industrial & Engineering Chemistry Research* 48.10 (2009), pp. 4638–4663.

[243] T. C. Merkel et al. “Power plant post-combustion carbon dioxide capture: An opportunity for membranes”. In: *Journal of Membrane Science* 359.1 (2010). Membranes and CO2 Separation, pp. 126–139.

[244] T. C. Merkel et al. “Selective Exhaust Gas Recycle with Membranes for CO2 Capture from Natural Gas Combined Cycle Power Plants”. In: *Industrial & Engineering Chemistry Research* 52.3 (2013), pp. 1150–1159.

[245] G. Russo et al. “Selective-exhaust gas recirculation for CO2 capture using membrane technology”. In: *Journal of Membrane Science* 549 (2018), pp. 649–659.

[246] X. Feng et al. “Development of hollow fiber membrane systems for nitrogen generation from combustion exhaust gas: Part I. Effects of module configurations”. In: *Journal of Membrane Science* 176.2 (2000), pp. 197–207.

[247] U. W. Siagian et al. “Membrane-based carbon capture technologies: Membrane gas separation vs. membrane contactor”. In: *Journal of Natural Gas Science and Engineering* 67 (2019), pp. 172–195.

[248] M. Anwar et al. “CO2 capture and storage: A way forward for sustainable environment”. In: *Journal of Environmental Management* 226 (2018), pp. 131–144.

[249] J. Blamey et al. “The calcium looping cycle for large-scale CO2 capture”. In: *Progress in Energy and Combustion Science* 36.2 (2010), pp. 260–279.

[250] M. Erans et al. “Calcium looping sorbents for CO2 capture”. In: *Applied Energy* 180 (2016), pp. 722–742.

[251] P. R. Jeon et al. “Sorption equilibrium and kinetics of CO2 on clay minerals from subcritical to supercritical conditions: CO2 sequestration at nanoscale interfaces”. In: *Chemical Engineering Journal* 255 (2014), pp. 705–715.

[252] A. A. Olajire. “A review of mineral carbonation technology in sequestration of CO2”. In: *Journal of Petroleum Science and Engineering* 109 (2013), pp. 364–392.

[253] A.-H. A. Park et al. “CO2 mineral sequestration: physically activated dissolution of serpentine and pH swing process”. In: *Chemical Engineering Science* 59.22 (2004). ISCRE18, pp. 5241–5247.

[254] S. Kodama et al. “Development of a new pH-swing CO2 mineralization process with a recyclable reaction solution”. In: *Energy* 33.5 (2008), pp. 776–784.

[255] S. Eloneva et al. “Preliminary assessment of a method utilizing carbon dioxide and steelmaking slags to produce precipitated calcium carbonate”. In: *Applied Energy* 90.1 (2012). Energy Solutions for a Sustainable World, Special Issue of International Conference of Applied Energy, ICA2010, April 21-23, 2010, Singapore, pp. 329–334.

[256] A. Sanna et al. “Carbon dioxide capture and storage by pH swing aqueous mineralisation using a mixture of ammonium salts and antigorite source”. In: *Fuel* 114 (2013), pp. 153–161.

[257] A. Azdarpour et al. “A review on carbon dioxide mineral carbonation through pH-swing process”. In: *Chemical Engineering Journal* 279 (2015), pp. 615–630.

[258] V. Prigiobbe et al. “Mineral carbonation process for CO2 sequestration”. In: *Energy Procedia* 1.1 (2009). Greenhouse Gas Control Technologies 9, pp. 4885–4890.

[259] S. J. Gerdemann et al. “Ex Situ Aqueous Mineral Carbonation”. In: *Environmental Science & Technology* 41.7 (2007), pp. 2587–2593.

[260] A. Azdarpour et al. “Mineral carbonation of red gypsum via pH-swing process: Effect of CO2 pressure on the efficiency and products characteristics”. In: *Chemical Engineering Journal* 264 (2015), pp. 425–436.

[261] G. L. A. A. Ferrufino et al. “CO2 sequestration by pH-swing mineral carbonation based on HCl/NH4OH system using iron-rich lizardite 1T”. In: *Journal of CO2 Utilization* 24 (2018), pp. 164–173.

[262] R. Stanger et al. “Oxyfuel combustion for CO2 capture in power plants”. In: *International Journal of Greenhouse Gas Control* 40 (2015). Special Issue commemorating the 10th year anniversary of the publication of the Intergovernmental Panel on Climate Change Special Report on CO2 Capture and Storage, pp. 55–125.

[263] G. Scheffknecht et al. “Oxy-fuel coal combustion—A review of the current state-of-the-art”. In: *International Journal of Greenhouse Gas Control* 5 (2011). Oxyfuel Combustion Technology - Working Toward Demonstration and Commercialisation, S16–S35.

[264] L. Zheng. “1 - Overview of oxy-fuel combustion technology for carbon dioxide (CO2) capture”. In: *Oxy-Fuel Combustion for Power Generation and Carbon Dioxide (CO2) Capture*. Ed. by L. Zheng. Woodhead Publishing Series in Energy. Woodhead Publishing, 2011, pp. 1–13. ISBN: 978-1-84569-671-9.

[265] B. Metz et al. *IPCC special report on carbon dioxide capture and storage*. Tech. rep. Intergovernmental Panel on Climate Change, Geneva (Switzerland). Working . . ., 2005.

[266] C. F. Song et al. “Evaluation of Stirling cooler system for cryogenic CO2 capture”. In: *Applied energy* 98 (2012), pp. 491–501.

[267] T. F. Wall. “Combustion processes for carbon capture”. In: *Proceedings of the combustion institute* 31.1 (2007), pp. 31–47.

[268] R. Pardemann et al. “Pre-Combustion Carbon Capture”. In: *Handbook of Clean Energy Systems*. American Cancer Society, 2015. ISBN: 9781118991978.

[269] O. d. Q. F. Araujo et al. “Carbon capture and storage technologies: present scenario and drivers of innovation”. In: *Current Opinion in Chemical Engineering* 17 (2017), pp. 22–34.

[270] A. C. Yeh et al. “Comparison of ammonia and monoethanolamine solvents to reduce CO2 greenhouse gas emissions”. In: *Science of The Total Environment* 228.2 (1999), pp. 121–133.

[271] G. Rochelle. “3 - Conventional amine scrubbing for CO2 capture”. In: *Absorption-Based Post-combustion Capture of Carbon Dioxide*. Ed. by P. H. Feron. Woodhead Publishing, 2016, pp. 35–67. ISBN: 978-0-08-100514-9.

[272] M. Ho et al. “Reducing the Cost of CO 2 Capture from Flue Gases Using Membrane Technology”. In: *Industrial and Engineering Chemistry Research - IND ENG CHEM RES* 47 (Feb. 2008).

[273] C. E. Powell et al. “Polymeric CO2/N2 gas separation membranes for the capture of carbon dioxide from power plant flue gases”. In: *Journal of Membrane Science* 279.1 (2006), pp. 1–49.

[274] Y. Peng et al. “Two Dimensional Metal–Organic Framework Nanosheets for Membrane-Based Gas Separation”. In: *Angewandte Chemie International Edition* 56.33 (2017), pp. 9757–9761.

[275] X. Zou et al. “Microporous Organic Materials for Membrane-Based Gas Separation”. In: *Advanced Materials* 30.3 (2018), p. 1700750.

[276] J. Wang et al. “Recent development of ionic liquid membranes”. In: *Green Energy and Environment* 1.1 (2016), pp. 43–61.

[277] A. Perejón et al. “The Calcium-Looping technology for CO2 capture: On the important roles of energy integration and sorbent behavior”. In: *Applied Energy* 162 (2016), pp. 787–807.

[278] C. Verma et al. “Ionic liquid-mediated functionalization of graphene-based materials for versatile applications: a review”. In: *Graphene Technology* (Dec. 2018).

[279] G. T. Rochelle. “Amine Scrubbing for CO2 Capture”. In: *Science* 325.5948 (2009), pp. 1652–1654.

[280] S. Kim et al. “CO2 absorption mechanism in amine solvents and enhancement of CO2 capture capability in blended amine solvent”. In: *International Journal of Greenhouse Gas Control* 45 (2016), pp. 181–188.

[281] G. Sartori et al. “Sterically hindered amines for carbon dioxide removal from gases”. In: *Industrial & Engineering Chemistry Fundamentals* 22.2 (1983), pp. 239–249.

[282] A. Dibenedetto et al. “Reaction of silylalkylmono- and silylalkyldi-amines with carbon dioxide: evidence of formation of inter- and intra-molecular ammonium carbamates and their conversion into organic carbamates of industrial interest under carbon dioxide catalysis”. In: *Green Chem.* 4 (5 2002), pp. 439–443.

[283] G. Puxty et al. “Carbon Dioxide Postcombustion Capture: A Novel Screening Study of the Carbon Dioxide Absorption Performance of 76 Amines”. In: *Environmental Science & Technology* 43.16 (2009), pp. 6427–6433.

[284] H. Ahn et al. “Process configuration studies of the amine capture process for coal-fired power plants”. In: *International Journal of Greenhouse Gas Control* 16 (2013), pp. 29–40.

[285] R. R. Wanderley et al. “Investigating opportunities for water-lean solvents in CO2 capture: VLE and heat of absorption in water-lean solvents containing MEA”. In: *Separation and Purification Technology* 231 (2020), p. 115883.

[286] H. Karunarathne et al. “Physical Properties of MEA + Water + CO 2 Mixtures in Postcombustion CO 2 Capture: A Review of Correlations and Experimental Studies”. In: *Journal of Engineering* 2020 (Mar. 2020), pp. 1–17.

[287] P. Luis. “Use of monoethanolamine (MEA) for CO2 capture in a global scenario: Consequences and alternatives”. In: *Desalination* 380 (2016), pp. 93–99.

[288] K. Li et al. “Systematic study of aqueous monoethanolamine-based CO2 capture process: model development and process improvement”. In: *Energy Science & Engineering* 4.1 (2016), pp. 23–39.

[289] I. M. Bernhardsen et al. “A review of potential amine solvents for CO2 absorption process: Absorption capacity, cyclic capacity and pKa”. In: *International Journal of Greenhouse Gas Control* 61 (2017), pp. 27–48.

[290] S. Singto et al. “The effect of chemical structure of newly synthesized tertiary amines used for the post combustion capture process on carbon dioxide (CO2): Kinetics of CO2 absorption using the stopped-flow apparatus and regeneration, and heat input of CO2 regeneration”. In: *Energy Procedia* 114 (2017), pp. 852–859.

[291] M. K. Mondal et al. “Progress and trends in CO2 capture/separation technologies: a review”. In: *Energy* 46.1 (2012), pp. 431–441.

[292] C. Han et al. “Simulation of the Energy Consumption of CO2 Capture by Aqueous Monoethanolamine in Pilot Plant”. In: *Energy and Environment Research* 1.1 (2011), p. 67.

[293] F. A. Chowdhury et al. “CO2 Capture by Tertiary Amine Absorbents: A Performance Comparison Study”. In: *Industrial & Engineering Chemistry Research* 52.24 (2013), pp. 8323–8331.

[294] M. Mahmoudkhani et al. “Low-energy sodium hydroxide recovery for CO2 capture from atmospheric air—Thermodynamic analysis”. In: *International Journal of Greenhouse Gas Control* 3.4 (2009), pp. 376–384.

[295] F. Zeman. “Energy and Material Balance of CO2 Capture from Ambient Air”. In: *Environmental Science & Technology* 41.21 (2007), pp. 7558–7563.

[296] Y. Tanaka. “17 - Bipolar Membrane Electrodialysis”. In: *Ion Exchange Membranes (Second Edition)*. Ed. by Y. Tanaka. Second Edition. Amsterdam: Elsevier, 2015, pp. 369–392. ISBN: 978-0-444-63319-4.

[297] E. D. Bates et al. “CO2 Capture by a Task-Specific Ionic Liquid”. In: *Journal of the American Chemical Society* 124.6 (2002). PMID: 11829599, pp. 926–927.

[298] M. Ramdin et al. “State-of-the-Art of CO2 Capture with Ionic Liquids”. In: *Industrial & Engineering Chemistry Research* 51.24 (2012), pp. 8149–8177.

[299] K. Huang et al. “Ionic liquid–formulated hybrid solvents for CO2 capture”. In: *Current Opinion in Green and Sustainable Chemistry* 5 (2017). 5 Green Solvents 2017, pp. 67–73.

[300] M. Smiglak et al. “The Second Evolution of Ionic Liquids: From Solvents and Separations to Advanced Materials—Energetic Examples from the Ionic Liquid Cookbook”. In: *Accounts of Chemical Research* 40.11 (2007). PMID: 17979252, pp. 1182–1192.

[301] Y. A. C. Jande et al. “Energy minimization in monoethanolamine-based CO2 capture using capacitive deionization”. In: *International Journal of Energy Research* 38.12 (2014), pp. 1531–1540.

[302] M. C. Stern et al. “An Electrochemically-mediated Gas Separation Process for Carbon Abatement”. In: *Energy Procedia* 37 (2013). GHGT-11 Proceedings of the 11th International Conference on Greenhouse Gas Control Technologies, 18-22 November 2012, Kyoto, Japan, pp. 1172–1179.

[303] M. Wang et al. “Flue gas CO2 capture via electrochemically mediated amine regeneration: System design and performance”. In: *Applied Energy* 255 (2019), p. 113879.

[304] V. Zabolotskii et al. “Regeneration of monoethanolamine-based sorbents of carbon dioxide by electrodialysis with bipolar membranes”. In: *J. Appl. Chem. USSR (Engl. Transl.);(United States)* 58.10 PT 2 (1986).

[305] C. Huang et al. “Regenerating Fuel-Gas Desulfurizing Agents by Using Bipolar Membrane Electrodialysis (BMED):Effect of Molecular Structure of Alkanolamines on the Regeneration Performance”. In: *Environmental Science & Technology* 41.3 (2007), pp. 984–989.

[306] M. T. Ho et al. “Reducing the Cost of CO2 Capture from Flue Gases Using Pressure Swing Adsorption”. In: *Industrial & Engineering Chemistry Research* 47.14 (2008), pp. 4883–4890.

[307] R. T. Yang. “CHAPTER 6 - Cyclic Gas Separation Processes”. In: *Gas Separation by Adsorption Processes*. Ed. by R. T. Yang. Butterworth-Heinemann, 1987, pp. 201–235. ISBN: 978-0-409-90004-0.

[308] E. S. Kikkinides et al. “Concentration and Recovery of CO2 from Flue Gas by Pressure Swing Adsorption (PSA)”. In: *Ind. Eng. Chem. Res.* 32 (1993), p. 2714.

[309] K. T. Chue et al. “Comparison of Activated Carbon and Zeolite 13X for CO2 Recovery from Flue Gas by Pressure Swing Adsorption”. In: *Ind. Eng. Chem. Res.* 34 (1995), p. 591.

[310] S. J. Doong et al. “Bulk Separation of Multicomponent Gas Mixtures by Pressure Swing Adsorption: Pore Surface Diffusion and Equilibrium Models”. In: *AIChE J.* 32 (1986), p. 397.

[311] D. Ko et al. “Optimization of Pressure Swing Adsorption and Fractionated Vacuum Pressure Swing Adsorption Processes for CO2 Sequestration”. In: *Ind. Eng. Chem. Res.* 44 (2005), p. 8084.

[312] D. Ko et al. “Optimization of Pressure Swing Adsorption Process Using Zeolite 13X for CO2 Sequestration”. In: *Ind. Eng. Chem. Res.* 42 (2003), p. 339.

[313] C. Chou et al. “Carbon Dioxide Recovery by Vacuum Swing Adsorption”. In: *J. Chin. Inst. Chem. Eng.* 34 (2003), p. 135.

[314] W. K. Choi et al. “Optimal Operation of the Pressure Swing Adsorption Process for CO2 Recovery”. In: *Korean J. Chem. Eng.* 20 (2003), p. 617.

[315] J. Zhang et al. “Effect of Process Parameters on the Power Requirements of Vacuum Swing Adsorption Technology for CO2 Capture from Flue Gas”. In: *Energy Conv. Manage.* 49 (2008), p. 346.

[316] A. Kapoor et al. “Kinetic Separation of Methane Carbon Dioxide Mixture by Adsorption on Molecular Sieve Carbon”. In: *Chem. Eng. Sci.* 44 (1989), p. 1723.

[317] C.-H. Yu et al. “A Review of CO2 Capture by Absorption and Adsorption”. In: *Aerosol and Air Quality Research* 12 (Oct. 2012).

[318] J. Huertas et al. “CO2 Absorbing Capacity of MEA”. In: *Journal of Chemistry* 2015 (Aug. 2015), pp. 1–7.

[319] C. A. Grande et al. “Electric Swing Adsorption for CO2 removal from flue gases”. In: *International Journal of Greenhouse Gas Control* 2.2 (2008), pp. 194–202.

[320] H. An et al. “CO2 capture by electrothermal swing adsorption with activated carbon fibre materials”. In: *International Journal of Greenhouse Gas Control* 5.1 (2011), pp. 16–25.

[321] N. Tlili et al. “Electrical Swing Adsorption Using New Mixed Matrix Adsorbents for CO2 Capture and Recovery: Experiments and Modeling”. In: *Industrial & Engineering Chemistry Research* 51.48 (2012), pp. 15729–15737.

[322] M. Petkovska et al. “Temperature-Swing Gas Separation with Electrothermal Desorption Step”. In: *Separation Science and Technology* 26.3 (1991), pp. 425–444.

[323] M. Rahimi et al. “CO2 Adsorption on Charged Carbon Nanotube Arrays: A Possible Functional Material for Electric Swing Adsorption”. In: *The Journal of Physical Chemistry C* 119.27 (2015), pp. 15232–15239.

[324] R. M. Cuéllar-Franca et al. “Carbon capture, storage and utilisation technologies: A critical analysis and comparison of their life cycle environmental impacts”. In: *Journal of CO2 Utilization* 9 (2015), pp. 82–102.

[325] K. M. K. Yu et al. “Recent Advances in CO2 Capture and Utilization”. In: *ChemSusChem* 1.11 (2008), pp. 893–899.

[326] IEA-Paris. *Putting CO2 to use – Creating value from emissions*. 2019.

[327] C. M. Woodall et al. “Utilization of mineral carbonation products: current state and potential”. In: *Greenhouse Gases: Science and Technology* 9.6 (2019), pp. 1096–1113.

[328] J. van Heek et al. “Reduce, reuse, recycle: Acceptance of CO2-utilization for plastic products”. In: *Energy Policy* 105 (2017), pp. 53–66.

[329] R. Chang et al. “Calcium Carbonate Precipitation for CO2 Storage and Utilization: A Review of the Carbonate Crystallization and Polymorphism”. In: *Frontiers in Energy Research* 5 (2017), p. 17.

[330] M. Ramdin et al. “High Pressure Electrochemical Reduction of CO2 to Formic Acid/Formate: A Comparison between Bipolar Membranes and Cation Exchange Membranes”. In: *Industrial & Engineering Chemistry Research* 58.5 (2019), pp. 1834–1847.

[331] A. Adamu et al. “Process intensification technologies for CO2 capture and conversion – a review”. In: *BMC Chemical Engineering* 2 (Dec. 2020).

[332] H. Hashiba et al. “Effects of Electrolyte Buffer Capacity on Surface Reactant Species and the Reaction Rate of CO2 in Electrochemical CO2 Reduction”. In: *The Journal of Physical Chemistry C* 122.7 (2018), pp. 3719–3726.

[333] Y. Hori et al. “Production of CO and CH4 in electrochemical reduction of CO2 at metal electrodes in aqueous hydrogencarbonate solution”. In: *Chemistry Letters - CHEM LETT* 14 (Jan. 1985), pp. 1695–1698.

[334] K. P. Kuhl et al. “New insights into the electrochemical reduction of carbon dioxide on metallic copper surfaces”. In: *Energy Environ. Sci.* 5 (5 2012), pp. 7050–7059.

[335] Y. Song et al. “High-Selectivity Electrochemical Conversion of CO2 to Ethanol using a Copper Nanoparticle/N-Doped Graphene Electrode”. In: *ChemistrySelect* 1.19 (2016), pp. 6055–6061.

[336] Y. C. Li et al. “CO2 Electroreduction from Carbonate Electrolyte”. In: *ACS Energy Letters* 4.6 (2019), pp. 1427–1431.

[337] J. Lee et al. “Electrochemical CO2 reduction using alkaline membrane electrode assembly on various metal electrodes”. In: *Journal of CO2 Utilization* 31 (2019), pp. 244–250.

[338] J. Qiao et al. *Electrochemical reduction of carbon dioxide : fundamentals and technologies*. Boca Raton : CRC Press, 2016.

[339] D. Knuth. *Rapid changes in the ethylene capacity world order*. 2019. URL: https://www.woodmac.com/news/opinion/rapid-changes-in-the-ethylene-capacity-world-order/. (August 2020).

[340] L. A. Hamilton et al. “Plastic & Climate: The Hidden Costs of a Plastic Planet”. In: *Center for International Environmental Law (CIEL)* (2019).

[341] D. Mendez-Mateos et al. “A study of deactivation by H 2 S and regeneration of a Ni catalyst supported on Al 2 O 3, during methanation of CO 2. Effect of the promoters Co, Cr, Fe and Mo”. In: *RSC Advances* 10.28 (2020), pp. 16551–16564.

[342] X. Zhang et al. “H2S-selective catalytic oxidation: catalysts and processes”. In: *ACS catalysis* 5.2 (2015), pp. 1053–1067.

[343] J. M. Davidson et al. “Kinetics of the absorption of hydrogen sulfide by high purity and doped high surface area zinc oxide”. In: *Industrial & Engineering Chemistry Research* 34.9 (1995), pp. 2981–2989.

[344] P. Spath et al. *Biomass to hydrogen production detailed design and economics utilizing the Battelle Columbus Laboratory indirectly-heated gasifier*. Tech. rep. National Renewable Energy Lab., Golden, CO (US), 2005.

[345] J. C. Liao et al. “Fuelling the future: microbial engineering for the production of sustainable biofuels”. In: *Nature Reviews Microbiology* 14.5 (2016), pp. 288–304.

[346] T. Haas et al. “Technical photosynthesis involving CO 2 electrolysis and fermentation”. In: *Nature Catalysis* 1.1 (2018), pp. 32–39.

[347] M. Gotz et al. “Renewable Power-to-Gas: A technological and economic review”. In: *Renewable energy* 85 (2016), pp. 1371–1390.

[348] K. Muller et al. “Sabatier based CO2-methanation of flue gas emitted by conventional power plants”. In: *Energy Procedia* 40 (2013), pp. 240–248.

[349] Z. Abbas et al. “Evaluation of CO2 purification requirements and the selection of processes for impurities deep removal from the CO2 product stream”. In: *Energy Procedia* 37 (2013), pp. 2389–2396.

[350] Q. Zheng et al. “Oxygen removal from oxy-combustion flue gas for CO2 purification via catalytic methane oxidation”. In: *Industrial & Engineering Chemistry Research* 57.6 (2018), pp. 1954–1960.

[351] N. Chambron et al. *Method and unit for removing oxygen from a gas flow comprising co2*. US Patent App. 14/438,309. 2015.

[352] M. Ramdin et al. “High-Pressure Electrochemical Reduction of CO2 to Formic Acid/Formate: Effect of pH on the Downstream Separation Process and Economics”. In: *Industrial & Engineering Chemistry Research* 58.51 (2019), pp. 22718–22740.

[353] M. Ramdin et al. “High Pressure Electrochemical Reduction of CO2 to Formic Acid/Formate: A Comparison between Bipolar Membranes and Cation Exchange Membranes”. In: *Industrial & Engineering Chemistry Research* 58.5 (2019), pp. 1834–1847.

[354] Z. Zhang et al. “Carbon dioxide storage schemes: technology, assessment and deployment”. In: *Journal of Cleaner Production* 142 (2017), pp. 1055–1064.

[355] R. C. Ferguson et al. “Storing CO2 with enhanced oil recovery”. In: *Energy Procedia* 1.1 (2009). Greenhouse Gas Control Technologies 9, pp. 1989–1996.

[356] S. Lee et al. “Chapter 2 - Enhanced Oil Recovery by Using CO2 Foams: Fundamentals and Field Applications”. In: *Enhanced Oil Recovery Field Case Studies*. Ed. by J. J. Sheng. Boston: Gulf Professional Publishing, 2013, pp. 23–61. ISBN: 978-0-12-386545-8.

[357] C. Xu et al. “Carbon sequestration potential of the Habanero reservoir when carbon dioxide is used as the heat exchange fluid”. In: *Journal of Rock Mechanics and Geotechnical Engineering* 8.1 (2016), pp. 50–59.

[358] J. Durst et al. “Electrochemical CO2 reduction–a critical view on fundamentals, materials and applications”. In: *CHIMIA International Journal for Chemistry* 69.12 (2015), pp. 769–776.

[359] L. Brennan et al. “Biofuels from microalgae—A review of technologies for production, processing, and extractions of biofuels and co-products”. In: *Renewable and Sustainable Energy Reviews* 14.2 (2010), pp. 557–577.

[360] P. Styring et al. *Carbon Capture and Utilisation in the green economy*. Centre for Low Carbon Futures New York, 2011.

[361] K. Michael et al. “Geological storage of CO2 in saline aquifers–A review of the experience from existing storage operations”. In: *International Journal of Greenhouse Gas Control* In Press, Corrected Proof (July 2010).

[362] F. Yang et al. “Characteristics of CO2 sequestration in saline aquifers”. In: *Petroleum Science* 7.1 (2010), pp. 83–92.

[363] K. Asghari et al. “Effect of Operational Parameters on Carbon Dioxide Storage Capacity in a Heterogeneous Oil Reservoir:A Case Study”. In: *Industrial & Engineering Chemistry Research* 45.8 (2006), pp. 2452–2456.

[364] *Global status of CCS 2019*. 2019.

[365] R. G. Grim et al. “Transforming the carbon economy: challenges and opportunities in the convergence of low-cost electricity and reductive CO 2 utilization”. In: *Energy & Environmental Science* 13.2 (2020), pp. 472–494.

[366] A. Sanna et al. “A review of mineral carbonation technologies to sequester CO2”. In: *Chem. Soc. Rev.* 43 (23 2014), pp. 8049–8080.

[367] B. Smit et al. *Introduction to Carbon Capture and Sequestration*. IMPERIAL COLLEGE PRESS, 2014.

[368] L. N. Plummer et al. “The solubilities of calcite, aragonite and vaterite in CO2-H2O solutions between 0 and 90 C, and an evaluation of the aqueous model for the system CaCO3-CO2-H2O”. In: *Geochimica et cosmochimica acta* 46.6 (1982), pp. 1011–1040.

[369] W. R. “Carbon dioxide in water and seawater: the solubility of a non-ideal gas”. In: *Mar. Chem* 2 (3 Nov. 1974), pp. 203–215.

[370] F. J. Millero et al. “Dissociation constants for carbonic acid determined from field measurements”. In: *Deep Sea Res. Part I Oceanogr. Res. Pap* 49 (10 Oct. 2002), pp. 1705–1723.

[371] S. Ingle. “Solubility of calcite in the ocean”. In: *Marine Chemistry* 3.4 (1975), pp. 301–319.

[372] D. C. Plath et al. “The solubility of calcite — probably containing magnesium — in seawater”. In: *Marine Chemistry* 10.1 (1980), pp. 9–29.

[373] M. Wang et al. “The intensification technologies to water electrolysis for hydrogen production -A review”. In: *Renew. Sustain. Energy Rev* 29 (2014), pp. 573–588.

[374] H. Strathmann et al. “Theoretical and practical aspects of preparing bipolar membranes”. In: *Desalination* 90 (1-3 1993), pp. 303–323.

[375] S. Z. Oener et al. “Accelerating water dissociation in bipolar membranes and for electrocatalysis”. In: *Science* (July 2020), p. 1487.

[376] “Natural gas production”. In: *International Energy Agency (IEA)* (2018).

[377] “Short-term energy outlook -Natural gas”. In: *U.S. Energy Information Administration (EIA)* (2020).

[378] S. Mohanty et al. “Analysis: Low gas prices not enough for Asia to move away from coal”. In: *S&P Global Platts* (2020).

[379] “Will the world have enough ethane?” In: *Strata Advisors* (2018).

[380] “US ethane price to rise in 2021 on declining availability, rising demand”. In: *Chemical Week* (2020).

[381] CME-group. *Mont Belvieu Ethane (OPIS) Average Price Option Quotes*. 2020.

[382] "US petrochemical feedstock volatility could last through 2020: LyondellBasell CEO". In: *S&P Global Platts* (2020).

[383] grandviewresearch. *Propane Market Size Worth $ 106.9 Billion By 2025 | CAGR: 3.5%*. 2017.

[384] "Petroleum & Other Liquids Weekly Heating Oil and Propane Prices". In: *U.S. Energy Information Administration (EIA)* (Mar. 2020).

[385] "Asia faces costlier LPG as low US oil price prompts NGL estimate cuts". In: *S&P Global Platts* (2020).

[386] CMEgroup. *Mont Belvieu LDH Propane (OPIS) Futures Quotes*.

[387] CMEgroup. *European Propane CIF ARA (Argus) Futures Quotes*.

[388] D. Knuth. *Rapid changes in the ethylene capacity world order*. 2019. URL: https://www.woodmac.com/news/opinion/rapid-changes-in-the-ethylene-capacity-world-order/. (August 2020).

[389] CMEgroup. *Mont Belvieu Ethylene (PCW) Financial Futures Quotes*.

[390] "European ethylene oversupply intensifies amid lockdowns, price at 11-year low". In: *S&P Global Platts* (2020).

[391] "Propylene Global Supply Demand Analytics Service". In: *Wood Mackenzie* (2018).

[392] "US propylene contracts see first price increase in nine months: sources". In: *S&P Global Platts* (2020).

[393] "European propylene prices move higher, supported by stronger feedstocks". In: *S&P Global Platts* (2020).

[394] "Asia-Pacific propylene prices fall from 11-week high". In: *ArgusMedia* (2020).

[395] "The methanol industry". In: *Methanol Institute* (2020).

[396] "Platts Asia Methanol Assessments". In: *S&P Global Platts* (2020).

[397] "Methanol price and supply/demand". In: *Methanol Institute* (2020).

[398] "Annual fuel ethanol production -U.S. and world ethanol production". In: *RFA* (2019).

[399] "T2 ethanol price at pre-coronavirus levels on strong demand, tight undenatured supply". In: *S&P Global Platts* (2020).

[400] "US ethanol crush margin rebounds on higher prices, lower corn". In: *S&P Global Platts* (2020).

[401] "Ethanol market and pricing data". In: *U.S. Grains Council* (Aug. 2020).

[402] "Global Isopropyl Alcohol Market to Reach a Volume of 2.48 Million Tons by 2025". In: *Expert Market Research* (2021).

[403] "European IPA at record high as production of sanitary products ramps up". In: *S&P Global Platts* (2020).

[404] K. Y. "Southeast Asia IPA prices hit six-year high, market warns of peak". In: *Independent Commodity Inteligence Services (ICIS)* (2020).

[405] "An incisive, in-depth analysis on the acetone market". In: *Future Market Insights* (2016).

[406] *China's acetone prices triple on import duties, demand*. 2020.

[407] "Global Acetic Acid Market to Reach 24.51 Million Tons by 2025". In: *Expert Market Research* (2019).

[408] *China CN: Market Price: Monthly Avg, Organic Chemical Material: Acetic Acid*. 2020.

[409] *Worldwide Formic Acid Market Size to Reach USD 119.86 Million by 2026*. 2020.

[410] *China CN: Market Price: Monthly Avg: Organic Chemical Material, Formic acid 94 %*. 2020.

[411] *Global Urea Market*. 2015. URL: https://www.expertmarketresearch.com/reports/urea-market.

[412] *DTN Fertilizer Trends, Urea, Anhydrous Lead Retail Fertilizer Prices Lower*. 2020.

[413] "World Bank Commodities Price Data (The Pink Sheet)". In: *World Bank* (2020).

[414] *China's prilled urea sellers await return of India*. 2020. URL: https://www.argusmedia.com/en/news/2097202-chinas-prilled-urea-sellers-await-return-of-india.

[415] R. G. Grim et al. "Transforming the carbon economy: challenges and opportunities in the convergence of low-cost electricity and reductive CO 2 utilization". In: *Energy & Environmental Science* 13.2 (2020), pp. 472–494.

[416] "Putting CO2 to use -Creating value from emissions". In: *International Energy Agency (IEA)* (Sept. 2019).

[417] *U.S. Department of Energy (DOE) Hydrogen and Fuel Cells Program Record*. 2019.

[418] H. Council. *Path to hydrogen competitiveness: a cost perspective*. 2020. URL: https://hydrogencouncil.com/en/path-to-hydrogen-competitiveness-a-cost-perspective/.

[419] *The future of hydrogen, Seizing today opportunities*. Aug. 2020. URL: https://www.iea.org/reports/the-future-of-hydrogen.

3

INTRINSIC BPM CHARACTERISTICS DOMINATE EFFECTS OF FLOW ORIENTATION AND PH ON ITS VOLTAGE

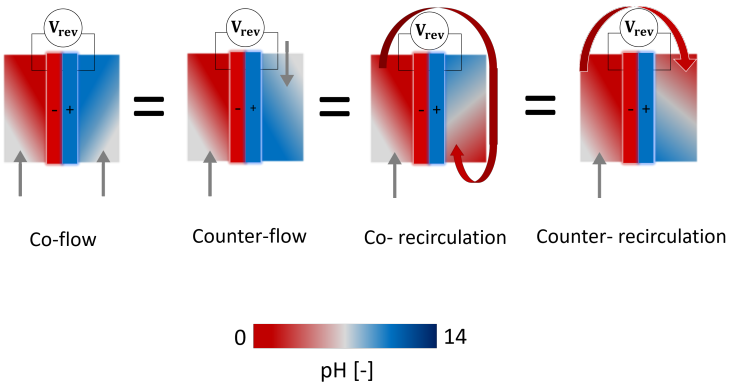

This chapter has been published as "Intrinsic bipolar membrane (BPM) characteristics dominate the effects of flow orientation and external pH-profile on the membrane voltage, by R. Sharifian, M.A. Blommaert, M. Bremer, R.M. Wagterveld, D.A. Vermaas. Journal of Membrane Science **638**, 119686 (2021) [1].

The practical energy required for water dissociation reaction in bipolar membrane (BPM) is still substantially higher compared to the thermodynamic equivalent. This required energy is determined by the bipolar membrane voltage, consisting of (1) thermodynamic potential and (2) undesired voltage losses. Since the pH gradient over the BPM affects both voltage components, in this work, pH gradient is leveraged to decrease the BPM-voltage. We investigate the effect of four flow orientations: 1) co-flow, 2) counter-flow, 3) co-recirculation, and 4) counter-recirculation, on the pH gradient and BPM-voltage, using an analytical model and chronopotentiometry experiments. The analytical model predicts the experimentally obtained pH accurately and confirms the importance of the flow orientation in determining the longitudinal pH gradient profile over the BPM in the bulk solution. However, in contrast to the simulated results, our observations show the effect of flow orientations on the BPM-voltage to be insignificant under practical operating conditions. When the water dissociation reaction in the BPM is dominant, the internal local pH inside of the membrane determines its final voltage, shadowing the effect of the external pH-gradient in the bulk solution. Therefore, although changing the flow orientation affects the bulk pH, it does not influence the local pH at the BPM junction layer and hence the BPM-voltage. Instead, opportunities for reducing the membrane voltage are in the realm of improved catalysts and ion exchange layers of the BPM.

3.1. INTRODUCTION

As industry and society is transitioning to sustainable electrified technologies, electrochemical methods are becoming more and more attractive. Bipolar membranes (BPM) have been successfully utilized in (emerging) electrochemical systems to create, and sustain, different pH at either sides of the membrane. The BPM-facilitated applications range from concentrated acid/base production [2], organic synthesis, biotechnology/ food industry [3, 4], production of value-added products [5–11], energy storage/ conversion [12, 13], resource recovery [14] (like CO_2 capture [15–20] and ammonia recovery [21–23]), and electrolysers [24–26]. A bipolar membrane consists of an anion and a cation exchange layer (AEL and CEL) laminated together. Upon application of an electrical current, inside of the BPM, water dissociation reaction (WDR) takes place in a "reverse bias mode" (i.e., CEL facing the cathode). The BPM provides, ideally, an impermeable barrier for salt ions from the electrolyte to cross the bipolar membrane (BPM). Instead, through the water dissociation reaction, the BPM produces H^+ and OH^- ions. The water dissociation reaction enables a pH gradient over the bipolar membrane (ΔpH_{BPM}) without the necessity of forming (gaseous) by-products.

Despite the advances made in BPMs, the energy consumption in BPM-facilitated applications, for water dissociation, is still high. The thermodynamic contribution of the BPM-voltage (i.e., reversible voltage, V_{rev}) is proportional to the pH difference and is only 0-0.83 V for pH-gradient between 0-14. However, the actual BPM-voltage is often measured beyond 1 V at any industrially relevant current density [6], [25], [27], [28]. In addition to thermodynamics, kinetics of water splitting, determined by its catalyst, is crucial in determining the actual BPM-voltage [29]. Manufacturing a properly catalyzed BPM, with highly perm-selective ion-exchange layers (i.e., perfect co-ion exclusion) and with optimum (layers/catalyst) thickness is the most direct way to minimize energy losses [28]. Additionally, as the thermodynamic reversible voltage (V_{rev}) is only dependent on the magnitude of ΔpH over the BPM, controlling the pH difference over the membrane is a potential lever to control the total BPM-voltage (V_{BPM}) independent of the membrane manufacturing. The effect of various feed pH on V_{BPM} has been demonstrated previously for cells that have a uniform pH in the feed compartment along the flow direction [6, 28, 30]. It has also been numerically shown that the external pH gradient (i.e., ΔpH_{BPM} of the feed solutions) over the BPM affects the ion concentration profile inside the BPM [28].

According to the mass balance, changing the hydrodynamic factors such as the flow orientation along the BPM affects the pH gradient profile over the BPM, which suggests that the flow orientation impacts the BPM voltage. However, the effect of flow orientations on the pH gradient profile along the BPM, and its subsequent impact on the BPM-voltage are still missing. Although the effect of different flow modes in bipolar membrane applications is missing in the literature, the performance of co-flow and counter-flow modes is studied before in electrodialysis (ED) and reverse electrodialysis (RED) cells containing mono-polar membranes [31], [32]. In RED, simulations demonstrate that counter-flow allows almost twice higher efficiencies in electricity production compared to the co-flow, due to lower ohmic losses and less untapped energy [32]. In comparison with RED and ED, the flow orientation has potentially even more impact in BPM-based processes when using solutions with initially mild pH, because the concentration

difference of H^+ (and OH^-) ions over the membrane is easily multiple orders of magnitude larger at the outflow of the cell compartments compared to the inflow. The co-flow and counter-flow orientations can be applied in all BPM-based applications. The recirculation modes are suitable for resource recovery e.g., CO_2 capture [33], ammonia and phosphorous recovery [23], [34], where after the extraction step, the acidic stream can be recirculated in the base compartment, enabling a neutral outflow.

This work represents BPM-facilitated technologies that deal with a mild pH, since the pH (and thus the theoretical V_{rev}) is insensitive to flow orientation at extreme pH. The targeted setup covers typical circumstances for e.g., electrochemical CO_2 capture/ conversion and resource recovery. We investigate the effect of different flow orientations on the reversible voltage (V_{rev}) and irreversible losses (V_{irr}) in bipolar membrane electrodialysis (BPMED), aiming to decrease the energy required by the BPM. First, a theoretical model is used to calculate the pH profile and V_{rev} over the BPM, using the mass balance and Visual MINTEQ ver. 3.1 chemical equilibrium software. Subsequently, BPM-voltage and its components are measured through chronopotentiometry experiments in a six-compartment BPMED cell. Finally, we share understanding of the involved losses in the system and give guidelines to reduce the currently high energy consumption in BPM-facilitated applications through membrane manufacturing.

3.2. THEORY

3.2.1. BPM-VOLTAGE

The BPM-voltage consists of two main components:

1. The thermodynamic (reversible) voltage required for the BPM-water dissociation
2. The undesired membrane voltage losses

When the current density is sufficiently high for water dissociation reaction to be the main charge carrier across the BPM, the reversible voltage can be defined using the Nernst equation [6], [27], [35], [36]:

$$V_{rev} = \frac{\Delta G}{nF} = 0.059 \Delta pH_{BPM} \tag{3.1}$$

Where ΔG is the Gibbs free energy that is required for acid and base production in an ideal bipolar membrane (i.e., complete exclusion of any ions except H^+ and OH^- ions) at ambient temperature and pressure (in J). V_{rev} is the thermodynamic reversible voltage across the BPM (V), F Faraday constant ($C\,mol^{-1}$), n number moles of electrons transferred in the reaction, and ΔpH_{BPM} the pH-difference between the AEL-electrolyte and CEL-electrolyte interfaces of the BPM. The losses can be approximated as [29, 35–37]:

$$V_{irr}^{BPM} \approx iR_M + \eta_{WDR} \tag{3.2}$$

Where R_M (= $R_{layers,stat}$) represents the membrane Ohmic area resistivity in $\Omega\ cm^2$ in the steady state, η_{WDR} the over potential of the water dissociation reaction in V [37–40], and i the applied current density in $A\,cm^{-2}$ [37]. Additional voltage losses, such as the water transport limitations from the electrolyte towards the BPM junction layer (JL) are neglected in Equation 3.2 [29, 41, 42].

3.2.2. GRADIENT OF PH IN Z-AXIS OVER THE BPM

The longitudinal pH-gradient can be obtained via the mass balance equation [35]. Assuming the AEM and the CEM are impermeable to co-ions, the mass balance can be written as (see also illustration of fluxes in in Figure 3.1 (A):

$$C^{H^+}_{outflow} = C^{H^+}_{inflow} + J_{H^+}\frac{A_m}{q} \tag{3.3}$$

$$J_{H^+} = \frac{i}{z_{H^+}F} \tag{3.4}$$

$$C^{H^+}_{outflow} = C^{H^+}_{inflow} + \left(\frac{i}{z_{H^+}F}\frac{t_r}{d}\right) \tag{3.5}$$

Where subscripts inflow (i.e., at z = 0) and outflow (i.e., at z = L = length of the cell) indicate the solution that flows in and out of the cell compartment, respectively. $C^{H^+}_{inflow}$ and $C^{H^+}_{outflow}$ (mol m^{-3}) represent the total acidity, meaning that they include (1) the free H^+ ions, plus (2) the protons present in complexes (the latter only in case of a buffered solution). A_m is the active area of the bipolar membrane (m^2), i the applied current density (A m^{-2}), J_{H^+} the flux of produced H^+ ions from the BPM (mol m^{-2} s^{-1}), z_{H^+} the electrochemical valence (=1 for H^+ ion), d the compartment thickness (m) and q the flow rate (m^3 s^{-1}), where $q = \frac{V_{acid}}{t_r} = \frac{A_m d}{t_r}$ with V_{acid} (excluding the effect of any spacer-mesh porosity ε, see Chapter 5) being the acidic compartment volume in m^3 (here, $V_{acid} = V_{base}$) and t_r the cell residence time (s) (note that the cell residence time differs if the compartment is filled with netted spacers according to the porosity of the spacer-mesh ε, see Chapter 5). The term $\frac{i}{z_{H^+}F}\frac{t_r}{d}$ (in mol m^{-3}) quantifies the produced moles of H^+ ions from the water dissociation reaction, per volume of the acidic compartment (if 100% Coulombic efficiency is assumed). To calculate the pH from $C^{H^+}_{inflow}$ and $C^{H^+}_{outflow}$, in an *unbuffered* solution:

$$C^{H^+}_{inflow} = 10^{-pH_{inflow}}, C^{H^+}_{outflow} = 10^{-pH_{outflow}} \tag{3.6}$$

However, depending on the buffer capacity, part of the produced H^+ ions from the water dissociation reaction neutralize with buffer compounds and, hence, will not contribute to a pH change. For example, in the phosphate buffer system:

$$10^{-pH} = C^{H^+} - \left([HPO_4{}^{2-}] + 2[H_2PO_4{}^{-}] + 3[H_3PO_4]\right) \tag{3.7}$$

Using Equation 3.5-3.7, the acidic and basic $pH_{outflow}$ can be calculated at each current density (i), compartment thickness (d), and cell residence time (t_r). Alternatively, by keeping i, d and t_r constant and by varying in z-axis between 0 and L, the full pH profile inside of the cell, in the direction of the flow, is obtainable through a step-wise mass balance at each position along the flow direction (z-axis), for $0 < z_i \leq L$:

$$C_{l_i}{}^{H^+} = C_{l_{i-1}}{}^{H^+} + \frac{z_i - z_{i-1}}{L}\left(\frac{i\,t_r}{Fd}\right) \tag{3.8}$$

L is the total length of the cell in the direction of the flow (z-axis in Figure 3.1). In Equation 3.8 *subscript* i indicates the ith length step chosen for the step-wise mass balance. This should not be confused with *i* that shows the current density in the equation.

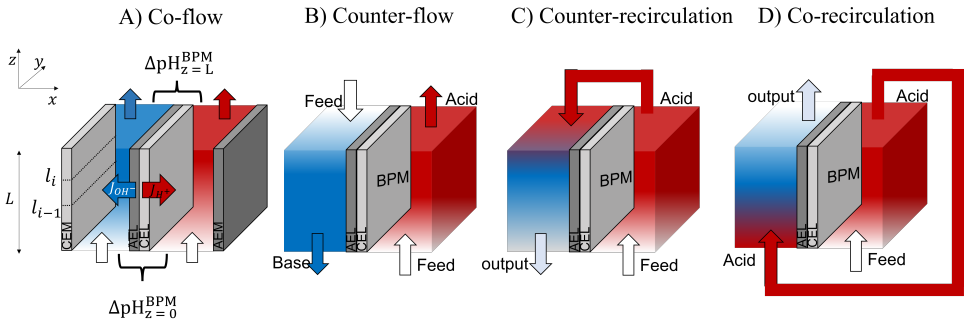

Figure 3.1: Schematic of the four flow orientation modes and H^+ ion mass balance. L represents the compartment length in z-axis.

3.3. MATERIALS AND METHODS

Three solutions of (1) 0.5 M NaCl, (2) 0.5 M NaCl + 2.5 mM $NaHCO_3$, and (3) 0.45 M NaCl + 50 mM Na_2HPO_4 Were used in four flow orientations according to Figure 3.1 (A-D). The chosen solutions mimic (1) an unbuffered reference case, (2) seawater (to represent the oceanic CO_2 capture application of BPMED), and (3) industrial water, respectively. The choice for the concentration of the phosphate (and NaCl) is to ensure similar neutral initial pH (and ionic conductivity) for all the three solutions. The buffer capacity and the underlying equilibrium that control the concentration of total and free H^+ ions are calculated using Equation 3.5-3.8 and with Visual MINTEQ ver. 3.1 as explained in supporting information 3.6.

3.3.1. BPMED SETUP

A single cell (i.e., one repeating unit) BPMED setup was assembled (Figure S1), using six compartments to avoid interference between electrodes and acid/base compartments. The setup comprised 22 cm^2 FBM-130, FKB-PK-130 and FAB-PK-130 (FuMATech B.V) as the BPM, CEM and AEM membranes, respectively. The compartment thickness (i.e., dis-

tance between the membranes) was d = 1 cm, and the cell length (in z-direction) was L = 11 cm. Prior to each run, all membranes used were equilibrated for several hours with 0.5 M NaCl and the cell was washed with demineralized water. All salts were acquired from VWR (purity of > 99.7%). To avoid CO_2(g) bubbles upon acidification of 0.5M NaCl + 2.5 mM $NaHCO_3$ [43], a membrane contactor (3M^{TM}Liqui-Cel^{TM} MM Series 8.75 inch) was placed after the outflow (z = L) of the acidic compartment [20] and before recirculation to the base compartment in both recirculation modes. No gas bubbles were visibly trapped during any of the experiments (for any of the three tested solutions).

The feed solutions were pumped through the cell at flow rate of 30 ml min^{-1} (i.e., flow velocity of v = 0.25 cm s^{-1}, t_r = 44 s) by peristaltic pumps (Cole-Parmer, Masterflex L/S Digital drive).

3.3.2. APPLIED TECHNIQUES

Chronopotentiometry experiments were performed using an Ivium Potentiostat (Ivium Technologies B.V.) in a four-electrode setup, measuring the BPM-voltage through two leak-free Ag-AgCl (sat. KCl) reference electrodes (Innovative Instruments, Inc.), placed *in-situ* at two sides of the membrane (at the length of z = 0.5L). The distance between the reference electrodes was approximately 1 cm, and the BPM was placed exactly between these electrodes. The pH and temperatures (always 23 ± 2 ^{o}C) were monitored in line with Orbisint CPS11D-7BA21 pH probes connected to a Liquiline CM444, both from Endress + Hauser (Germany).

Current densities of 5, 12.5, and 25 mA cm^{-2} were applied for 20 minutes at a recording interval of 2 seconds. After applying the current, the BPM- voltage (V_{BPM}) stabilized for all series within couple of minutes (< 200 s). The steady-state values of V_{BPM} (at z = 0.5 L) and the outflow acidic and basic pH (at z = L), averaged over the last (stable) 5 minutes of the constant current interval, were used for processing. However, the pH of the base output for 0.5 M NaCl co-recirculation and counter-recirculation fluctuated in all repetitions, Figure S9 (C-D). This is while the BPM-voltage reached steady-state within couple of seconds after applying the current. As the mentioned pH-fluctuations were not progressing with time, same averaging interval was applied for these cases.

3.3.3. MEASURING REVERSIBLE AND IRREVERSIBLE VOLTAGES

The reversible and irreversible voltage contributions of the BPM-voltage can be obtained through chronopotentiometry (Figure 3.2) [44]. When the current is switched on (at t_{on}), both the solution (between the two sides of the membrane and the tips of the reference electrodes) and the membrane layers resistances contribute to the initially measured electric potential drop (V_{ohm} in Figure S2) [44]:

$$V_{ohm} = V_{sol} + V_{mem,ini} = I(R_{sol} + R_{mem,ini}) \tag{3.9}$$

Where R_{sol} and $R_{mem,ini}$ represent the solution and the initial BPM-layers ohmic resistances (Ω), see supporting information 3.6.

The irreversible voltage contributions (V_{irr}) can be derived from the sudden drop in voltage directly after turning off the constant current (at t_{off}). The membrane resistance in steady state (Equation 3.2), will differ from the initial resistance ($R_{mem,ini}$ in Equation 3.9) because of the difference in the concentration profiles and additional ionic species

in the membrane layers due to the current application [44]. The reversible potential (V_{rev}) is the electrical potential remaining after switching off the power supply (Figure 3.2) [40]. V_{rev} relates to the water dissociation reaction in the membrane and the concentration differences over the BPM-layers [44]. For current densities above the limiting current density, when the water dissociation reaction in the BPM is dominant over the salt ion-crossover, V_{rev} can be represented based on the concentration differences of H^+ and OH^- over the BPM junction and membrane-electrolyte interfaces, which is described in Equation 3.1 for an ideal BPM. This potential diminishes as the ions in the membrane equilibrate with the electrolyte (which is the same at either side at open circuit).

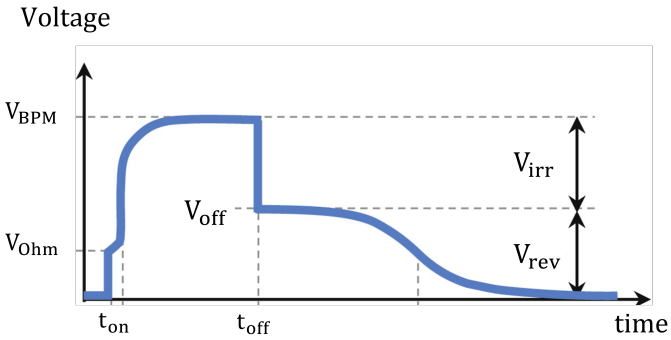

Figure 3.2: Schematic representation of a typical chronopotentiometry curve when the water dissociation reaction is dominant. The t_{on} and t_{off} mark the period of constant current application. The total steady state BPM-voltage (V_{BPM}) is the summation of the reversible voltage and irreversible voltage losses : $V_{BPM} = V_{rev} + V_{irr}$.

3.4. RESULTS AND DISCUSSIONS

3.4.1. SIMULATED PH PROFILE FOR DIFFERENT FLOW ORIENTATIONS

The H^+ ion concentration profile along the BPM is first obtained through a stepwise mass balance (Equation 3.8, and then it is converted to the corresponding pH values using Visual MINTEQ, as explained in the SI 3.6. The pH profiles at $i = 200$ mA cm^{-2} and 25 mA cm^{-2} for each flow orientation along the z-axis and the maximum ΔpH_{BPM} ($= pH_{Base} - pH_{Acid}$) are shown in Figure 3.3 and Figure S2, respectively.

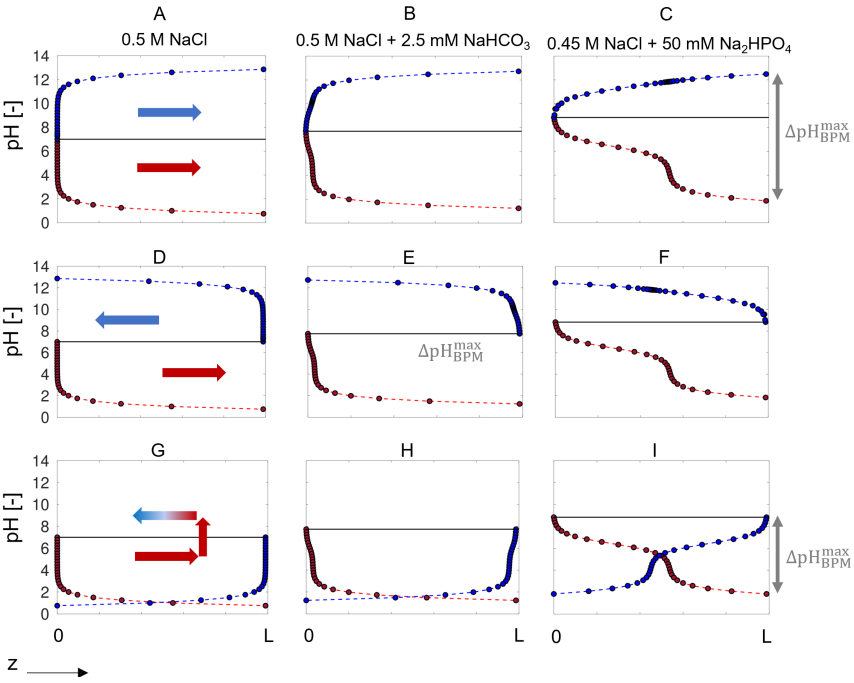

Figure 3.3: The simulated pH profile along the z-axis, for the co-flow (A, B, C), counter-flow (D, E, F), and co-recirculation (G, H, I), under assumption of a uniform current density of 200 mA cm^{-2} and t_r = 44 s (i.e., flow rate of 30 ml min^{-1}). The black horizontal line shows the initial solution pH. Blue and red arrows show flow orientations. This figure shows the pH profiles for $\frac{it_r}{d}$ = 8800 mC cm^{-3} = 0.091 mol$_{eq}$ L^{-1}. The counter-recirculation flow is not shown, since, theoretically, it creates $\Delta pH_{BPM} = 0$ for $0 \leq z \leq L$.

In the co-flow mode (Figure 3.3 (A-C)), $\Delta pH_{z=0}^{BPM}$ is equal to zero because the same feed solutions are used at both sides of the BPM. The ΔpH_{BPM} increases along the z-axis for co-flow mode, and reaches its maximum at z = L. The co-flow mode also creates a higher $\Delta pH_{z=L}^{BPM}$ than the other flow modes, because in single pass co-flow, the highest pH (i.e., alkaline) and lowest pH (i.e., acidic) at either side of the BPM coincide at z = L.

However, for the counter-flow (Figure 3.3 (D-F)), ΔpH_{BPM}at z= 0 is never zero when a current is applied, and ΔpH_{BPM} at z = L is smaller than that of the co-flow mode. One more important difference between the co-flow (Figure 3.3 (A-C)) and counter-flow (Figure 3.3 (D-F)) modes is the position of ΔpH_{BPM}^{max}; while in the co-flow mode, ΔpH_{BPM}^{max} always takes place at z = L, in the counter-flow it can occur near the middle of the cell (depending on the applied current density and solution type). This is particularly visible in poorly buffered solutions (Figure 3.3 (D)).

In buffered solutions such as the phosphate and bicarbonate case, the buffering ions partly neutralize the produced protons and hydroxides. For the phosphate solution, this neutralization is occurring in reactions at three pK_a values:

$$H_3PO_4 \leftrightarrow H^+ + H_2PO_4^-, pK_{a1} \sim 2.3$$

$$H_2PO_4^- \leftrightarrow H^+ + HPO_4^{2-}, pK_{a2} \sim 7.2$$

$$HPO_4^{2-} \leftrightarrow H^+ + PO_4^{3-}, pK_{a3} \sim 12.4$$

The effect of the $pK_{a1} - pK_{a3}$ is reflected in the mild slopes (i.e., almost horizontal) when the pH is near one of the pK_a in Figure 3.3 (C, F, I).

In the bicarbonate solution, upon acidification, a similar neutralization reaction takes place: $HCO_3^- + H^+ \leftrightarrow CO_2(aq) + H_2O$ However, the buffer effect is less visible in Figure 3.3 (B, E, H), due to the lower buffering capacity of the bicarbonate solution compared to the phosphate solution in this study (i.e., 2.5 mM vs. 50 mM).

Under a constant current density, the lowest values of ΔpH_{BPM} can be achieved by recirculating the acidic stream of the BPM to the adjacent base compartment, over the bipolar membrane (Figure 3.1 C, D). Re-circulation can be useful for resource recovery applications e.g., BPMED CO_2 capture/conversion and ammonia recovery.

The co-recirculation mode creates a smaller ΔpH_{BPM} compared to the co-flow and counter-flow as seen in Figure 3.3 (G-I). At the extreme, the counter-recirculation flow can even create $\Delta pH_{BPM} = 0$ on every position along the z-axis when no product is extracted in the process.

Flow orientations affect the pH-profile along the BPM and the magnitude of the maximum ΔpH_{BPM} (Figure 3.3); for the co-flow (A, B, C), $\Delta pH_{BPM}^{\max}$ is at z = L, while for the co-recirculation (G, H, I), $\Delta pH_{BPM}^{\max}$ is much smaller and located at z = 0 and L. For the counter-flow mode (D, E, F), $\Delta pH_{BPM}^{\max}$ is at the inside of the cell, and for the counter-recirculation flow mode, $\Delta pH_{BPM}^{\max}$ is zero on every position along the z-axis in these idealized conditions.

3.4.2. EFFECT OF FLOW ORIENTATION ON THE SIMULATED REVERSIBLE VOLTAGE

To obtain the thermodynamic voltage (V_{rev}) that is required to drive the water dissociation reaction (WDR) in the BPM, the maximum pH difference ($\Delta pH_{BPM}^{\max}$) must be considered in Equation 3.1 because the voltage must be sufficient to still drive WDR at this ΔpH. This result follows directly from having a single set of electrodes (i.e., a single stage), and implies that the minimum applied cell voltage is no longer a local variable but is equal for the whole cell and depends on the single position in the cell with the highest ΔpH_{BPM}. If this cell voltage is applied, that voltage is also adequate to enable any lower ΔpH along the whole normalized length. In reality, the current density may not be uniform, which would alter the exact shape of the curves in Figure 3.3, but still yield the same $\Delta pH_{BPM}^{\max}$ and thus the same reversible cell voltage.

Hence, the simulated reversible voltage for each flow mode is obtained using $\Delta pH_{BPM}^{\max}$ in Equation 3.1, and presented in Figure 3.4. To ensure applicability of Equation 3.1, in the simulation, only current densities higher than the limiting current density of Fumatech BPM are considered ($i_{\text{lim}} \sim 2.5\ \text{mA cm}^{-2}$, Figure S3).

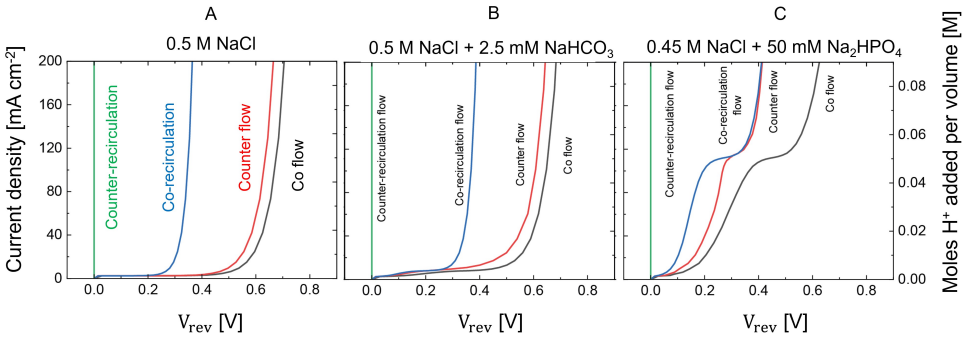

Figure 3.4: The reversible Nernstian voltage (V_{rev}) required to drive the water dissociation reaction at the BPM junction layer at steady state vs. current densities ($i > i_{lim}$) and the corresponding moles of H^+ ions added per volume of the solution. Here, "Moles H^+ added per volume" represents the produced $[H^+]$ from WDR (see Equation 3.5). The simulated $\Delta pH_{BPM}{}^{max}$ has the exact same trend as V_{rev} because $V_{rev} = 0.059\Delta pH_{BPM}{}^{max}$. In the simulation, same as in the experiments, $t_r = 44s$ (i.e., flow rate of 30 ml min^{-1} is used).

In Figure 3.4, the simulated V_{rev} increases as the current density increases because, as expected, a higher current density enables higher $\Delta pH^{\max}_{BPM}$. For co-flow, V_{rev} requires a cell voltage between ca. 0.6 - 0.7 V for all solutions to achieve i = 200 mA cm^{-2}.

V_{rev} decreases by an increase in the buffer capacity (Figure 3.4 from A to C), in particular for low current density (< 5 mA cm^{-2} for bicarbonate and < 100 mA cm^{-2} for phosphate, all at flow rate of 30 ml min^{-1}). These lower reversible membrane voltages are related to the lower $\Delta pH^{\max}_{BPM}$ that are obtained at these current densities in a buffered solution.

Finally, the flow orientation strongly affects simulated $\Delta pH^{\max}_{BPM}$ and, hence, simulated V_{rev} in these calculations; while the co-flow mode enables the highest V_{rev}, the voltage is almost half of that when co-recirculation is used. Assuming no buffer extraction upon recirculating, V_{rev} in the counter-recirculation is equal to zero regardless of the used solutions, at all current densities (green vertical line in Figure 3.4).

The difference in simulated V_{rev} between the co-flow and counter-flow is minor for low current densities for unbuffered or poorly buffered solutions (< 50 mV difference in Figure 3.4 (A, B), but increases at $i > 100$ mA cm^{-2} for buffered phosphate solution (Figure 3.4 (C)). The increased difference for 50 mM phosphate solution is reflected in the

pH profile along the z-axis (Figure 3.3) and follows from the balance between the moles H^+ added (max 88 mM, Figure 3.4) and the buffer capacity in the acidic compartment.

3.4.3. EFFECT OF FLOW ORIENTATION ON EXPERIMENTAL PH-GRADIENT AND BPM-VOLTAGE

The pH-gradient over the BPM at $z = 0$ and $z = L$, and the BPM-voltage (at $z = 0.5$L) were measured in the six-compartment electrochemical cell. Figure 3.5 compares the simulated pH-gradients with the measured ones, at the outflow of the alkaline stream. The individual ΔpH_{BPM} measurements at each current density are shown in Figure S4.

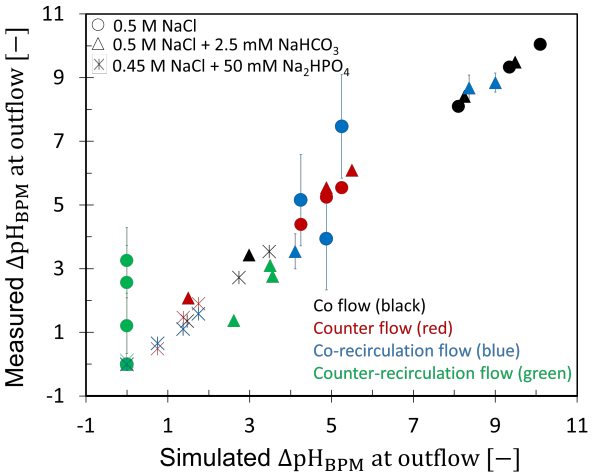

Figure 3.5: Comparison of the measured and simulated ΔpH_{BPM} for the three solutions and four flow orientations, at the outflow of the base compartment. For the co-flow and co-recirculation, the "outflow" refers to z = L, while for the counter-flow and counter-recirculation, outflow is at z = 0. All measurements are done at compartment residence time t_r = 44 s (i.e., flow rate of 30 ml min^{-1}). Error bars indicate the standard error. Not indicated error bars are smaller than the symbols. For 0.5 M NaCl, from lowest to highest current density, ΔpH measurements of counter-recirculation and co-recirculation modes fluctuate within ranges of (0.1 - 2.4), (1.6 - 4), (1.1 - 4.5) for counter-recirculation and (2.7 - 7.7), (2.1 - 6.5), (3.3 - 9.2), for co-recirculation modes, respectively.

As expected through the simulations, the co-flow mode creates the highest experimentally obtained ΔpH_{BPM}^{max} while the counter-recirculation generates the smallest one for all tested solutions (see Figure S4 for grouping per solution). The values for the counter-flow and co-recirculation orientations are positioned between those of the co-flow and counter-recirculation.

The data points for co-flow, counter-flow and co-recirculation flow are all very close to the 1:1 line. An exception is the simulated vs. measured ΔpH_{BPM} for 0.5 M NaCl counter-recirculation flow. There, at base outflow (z = 0), the simulations predict a zero-pH difference, while the experiments show a ΔpH_{BPM} at the outflow of 1 - 3 pH units (depending on current density) as illustrated in Figure 3.5 by the green circles. This is explained from the sensitivity of unbuffered solutions to pH change around neutral pH. Although a pH difference of ~ 3 units might seem significant, around pH = 7, it trans-

lates into an H^+ ion concentration difference of less than 1 μM. Since in the counter-recirculation mode, the highly acidic stream will come adjacent to a CEM upon recirculation to the base compartment, the H^+ ion can exchange with Na^+ ion over the CEM due to its concentration gradient toward the adjacent cell (Figure S9 and S8). A H^+ ion transport in the order of 1 - 2% already can shift the output base pH from 7 to 10, justifying the discrepancy in Figure 3.5- green circles. The unstable base outflow pH measurements for recirculation flow modes of 0.5 M NaCl (Figure S9 (C-D)) are another sign of such hydrogen ions transport taking place, reflected in relatively large error bars for the counter- and co-recirculation of NaCl (blue and green circles in Figure 3.5).

This discrepancy for counter-recirculation disappears when a buffer is present; the experimentally obtained ΔpH_{BPM} is (as simulated) very close to zero for the phosphate buffered solution. For the bicarbonate solution in Figure 3.5, CO_2(aq) extraction from the acidic compartment is done (via a membrane contactor) prior to recirculation to the base compartment in experiments as well as in simulations. Upon such degassing, the buffer capacity decreases.

The close agreement between the simulated and experimental values in Figure 3.5 shows that the theoretical framework in Equation 3.3-3.8 is adequate for defining the pH profile. Furthermore, with most data points so close to the 1:1 diagonal, the actual BPM-coulombic efficiency is close to 100% (as assumed in the simulations) for our cases, regardless of the flow orientation. The experiments results, also, confirm that the pH difference over the BPM is indeed heavily dependent on the flow orientation.

Following the theoretical framework, we expect to see a reversible membrane voltage that is proportional to the ΔpH_{BPM}. However, the experimentally measured reversible membrane voltage V_{rev}, determined according to the current interrupt method, is not affected at all by the flow orientation for any of the tested solutions (Figure 3.6 (B)). In more detail, as the applied current density increases, V_{rev} increases but reaches a plateau (< 0.8 V) already at (or below) 5 mA cm^{-2}, while V_{irr} keeps increasing (NaCl example in Figure 3.6 (A) and other solutions in Figure S5, S6 and Table S2). Hence, even though a clear difference in $\Delta pH^{\max}_{BPM}$ is measured between the cases (Figure 3.5), the reversible voltage (V_{rev}) and the irreversible losses (V_{irr}) are virtually independent of the flow orientation, for all current densities ≥ 5 mA cm^{-2} and for all solutions (Table S2). This absence of any impact of the flow orientation on V_{rev} is remarkable, because, theoretically, when the water dissociation reaction is the dominant, a difference of ~ 6 pH units in $\Delta pH^{\max}_{BPM}$ should enable a 6×0.059 = 354 mV difference in V_{rev}. However, that is not observed in the experimental results (Figure 3.6 (B)).

Instead, from Figure 3.6 (and Table S2), we see that the experimentally obtained reversible voltage (V_{rev}) are:

1. Higher than simulated values (up to six times),
2. Lower than 0.83 V, with values between ca. 0.59 - 0.74 V depending on the applied current density and feed solution.

The insignificant effect of flow orientation on the reversible voltage implies that, when the water dissociation reaction in the BPM is at substantial rate (i.e., i ≥ 5 mA cm^{-2} and higher), the effect of the solution-pH gradient on BPM-voltage is dwarfed. Furthermore, because all cases have similar V_{rev} values regardless of the difference in solutions and

flow orientations, the origin of this similarity in V_{rev} must come from one thing that is kept the same among the cases: the bipolar membrane itself.

Since the reversible voltage for extreme pH gradient (14 units) is ca. 0.826 V, and the obtained voltages are between 0.59 - 0.74 V, there is some pH-jump at the membrane-electrolyte interface, or there is a pH gradient over the CEL-AEL interface that is smaller than 14 units. When a pH-jump at the membrane-electrolyte interface would occur, e.g. a higher proton concentration in the CEL than in the electrolyte facing the CEL, the Donnan potential at this interface partly counteracts the water dissociation voltage [6]. Keeping the local solution pH near-neutral (e.g. minimizing concentration polarization), and keeping the CEL-pH low / AEL-pH high, would further exploit this effect. This would require a bipolar membrane that is prone to internal concentration polarization (e.g. having very thin layers or high affinity to protons and hydroxides over other ions) and flow geometries to keep the local pH close to the bulk pH.

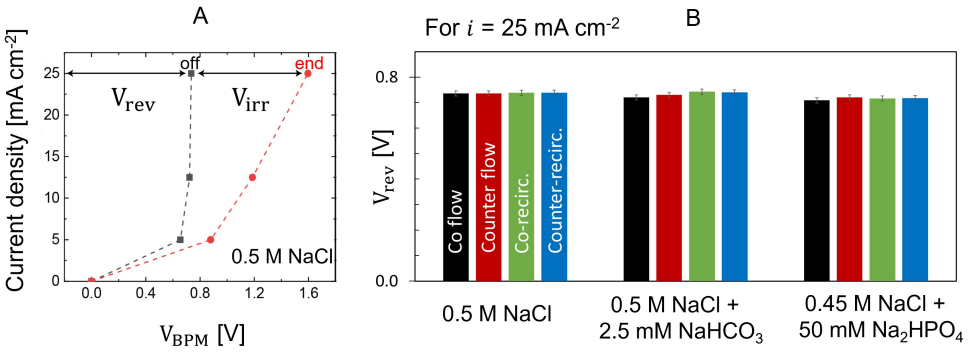

Figure 3.6: A) Characteristic current–voltage curves from chronopotentiometry, showing the measured steady state BPM-voltage vs. the applied current density for the co-flow in 0.5 M NaCl. V_{rev} and V_{irr} are gathered from "Switch-off" potential after constant current for 20 min with indicated current densities (Figure S5). Here, V_{irr} include both the BPM and solution resistances. B) The measured reversible voltage for all solutions (at 25 mA cm^{-2}) using flow rate of 30 ml min^{-1} ($t_r = 44s$).

The situation of a mild pH gradient over the CEL-AEL interface is more complex. As for internal properties of the BPM that affect its voltage for WDR, the type and thickness of the BPM-catalyst layer is reported to be crucial [27–29, 45]. It is shown that the local pH in the junction layer of the BPM affects the activity of the catalyst [29], but that,

unfortunately, the currently developed catalysts are only activated at high (local) pH-gradient. Furthermore, the internal ion concentration profiles in the BPM layers show a large gradient (i.e., internal concentration polarization), especially under high applied current [28].This internal concentration polarization increases the pH gradient at the BPM catalyst layer and thereby the catalytic WDR, but also increases the thermodynamically required potential to dissociate water. If new catalysts with ability to perform at close to neutral pH are developed, a decrease in the internal pH-gradient can decrease the WDR-voltage. In addition, thin catalyst layers (i.e., ~100 - 200 nm) are expected to decrease the BPM-voltage under WDR-dominated regime [29].

3.4.4. IRREVERSIBLE LOSSES

The irreversible voltage losses, V_{irr}, are compared for all flow orientations and for all solutions. Also, here, the total V_{irr} increases with the applied current density for all solutions (Figure 3.7), but no significant difference is observed in the magnitude of V_{irr} between the different flow orientations (Table S2). The different solutions have, however, a slight impact on V_{irr}, as demonstrated in Figure 3.7.

Figure 3.7 shows that V_{irr} increases with the buffering capacity of the solution. The solution resistivity (R_{sol}) is similar for all the tested solutions (ca. 0.95-0.98 Ω, Table S1 and Equation S1, S2), and it remains unchanged for 2 < pH < 12. Therefore, the BPM-contribution to the irreversible losses (V_{irr}^{BPM}) can be calculated (Figure 3.7, dashed lines).

In the BPM, the initial equilibrium resistance ($R_{mem,ini}$ in Equation 3.9) is different than the steady state (i.e., transport-state) resistance (R_M in Equation 3.2-Table S3) [44]. Both resistances change with current density, membrane history and electrolyte solutions. In this work, the membrane transport-state resistivity R_M is measured to be ca. 13 - 31 Ω cm^2. R_M decreases with current density, while increases with buffer capacity (Figure S7). The latter is probably because of the lower conductivity of AEL and CEL layers due to the presence of buffer in them.

At applied current density of 25 mA cm^{-2}, V_{irr}^{BPM} contributes to ~ 37 % (for 0.5 M NaCl), 39% (for 0.5 M NaCl + 2.5 mM $NaHCO_3$), and 47 % (for 0.45 M NaCl + 50 mM Na_2HPO_4) of the total measured irreversible voltage (V_{irr}^{tot}), respectively (Figure 3.7). The remaining contribution is mainly due to the solution resistivity between the reference electrodes and the membrane (Equation S1, S2), which unfortunately, even using the micro-reference electrodes, is rather high compared to the membrane resistivity.

In addition to the higher R_M, η_{WDR} can also play a role in justifying the slightly higher V_{irr}^{BPM} of the phosphate solution compared to 0.5 M NaCl (Equation 3.2). It is recently shown that η_{WDR} strongly depends on the local pH in the BPM junction layer (JL) [29], [41]. The existence of the phosphate buffer inside the BPM layers can change the local pH at the JL, affecting the WDR catalyst activity compared to the unbuffered 0.5 M NaCl solution. Unfortunately, the WDR catalyst properties of the used Fumasep BPM are unknown, and, thus, further investigations on the effect of local pH on activity of the WDR catalyst is beyond the scope of this work.

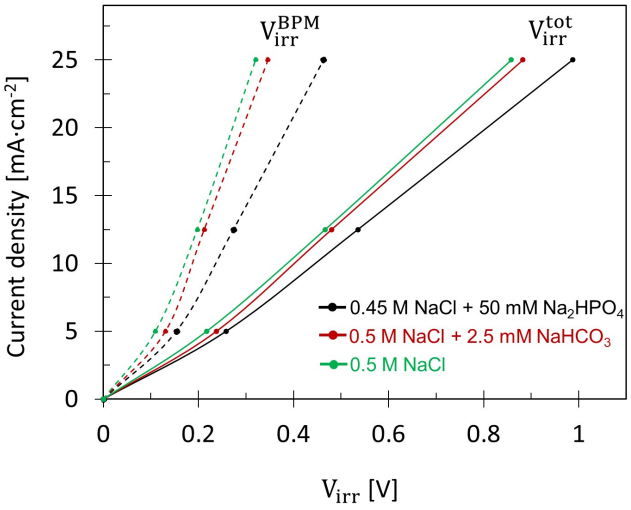

Figure 3.7: The total irreversible voltage (V_{irr}^{tot}) vs. the applied current density (solid lines). Tested solutions are 0.5 M NaCl (green), 0.5 M NaCl + 2.5 mM $NaHCO_3$ (red), and 0.45 M NaCl + 50 mM Na_2HPO_4 (black). A cell residence time of $t_r = 44s$ is applied for all cases. By correcting for the solution resistivity (V_{irr}^{sol}, between the two sides of the membrane and the tips of the reference electrodes : Equation S1, S2), values of V_{irr}^{BPM} can be obtained as $V_{irr}^{tot} \sim V_{irr}^{BPM} + V_{irr}^{sol}$.

3.5. CONCLUSION

In this work, with the aim of decreasing the energy consumption of bipolar membrane (BPM) based applications, the effect of pH gradient (ΔpH_{BPM}) on the reversible and irreversible voltage components associated with the BPM is investigated. The pH dependency is studied through an analytical model and is also measured experimentally, for four flow orientations using buffered and unbuffered electrolytes. First, using the analytical model, the pH profile along the BPM (i.e., in the flow direction) is obtained for each flow orientation. The simulated results fit the experimentally obtained ΔpH_{BPM} at the outflow very well. Second, based on the simulated pH profile, for each flow orientations, the reversible voltage (V_{rev}) is modeled. Surprisingly, except for the co-flow mode, the experimentally measured V_{rev} were higher (up to six times) than what was simulated. The origin of this discrepancy is the difference between the bulk and local pH; the local pH at the BPM-electrolyte interface and BPM junction layer (JL) determines the measured V_{rev}. However, the (measured) bulk pH is not representative of this local pH. Our results show that, although changing the flow orientations alters ΔpH_{BPM}, it does not affect V_{rev}, V_{irr}, and V_{BPM}. It seems that, when the water dissociation reaction (WDR) dominates, the membrane internal properties overshadow the effect of the bulk ΔpH_{BPM}. Therefore, to decrease the BPM-voltage (thus its energy consumption) under WDR regime, focus must be shifted towards tuning the membrane properties (e.g., WDR catalyst and thickness) rather than the external pH profile along the membrane.

3.6. SUPPORTING INFORMATION

3.6.1. THE ELECTROCHEMICAL CELL

The following six-compartment cell was used for applying the chronopotentiometry experiments.

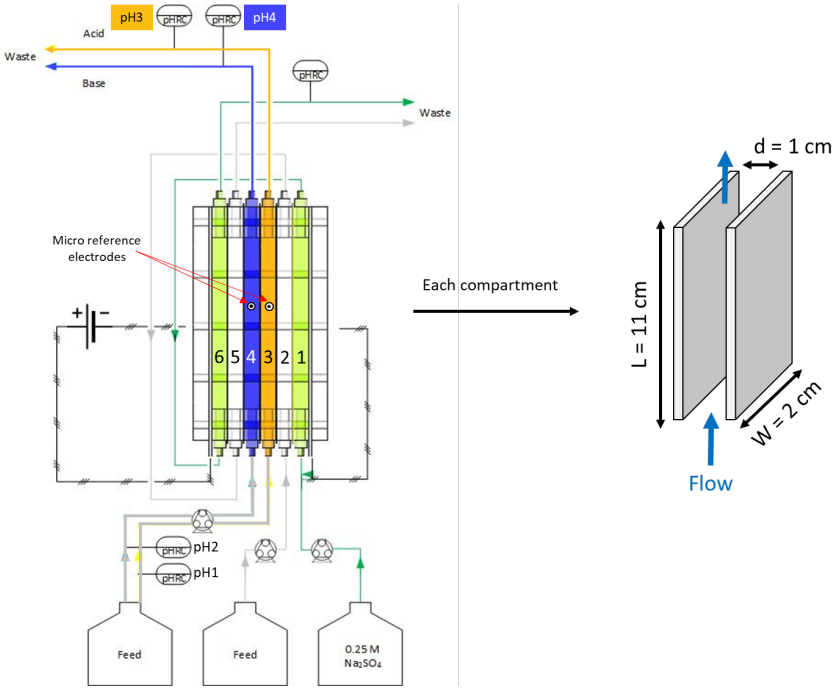

Figure S1: Schematic of the six-compartment cell. The compartments volume and configuration plus the position of the micro-reference electrodes are shown.

The volume of each cell compartment was $1^{cm}_{(d)} \times 2^{cm}_{(w)} \times 11^{cm}_{(L)} = 22$ cm^3. For each experiment, solutions in the following arrangement were used:

- Compartments 1 and 6: Electrode rinsing solution consisting of 0.25 M Na_2SO_4, in contact with two in-house made electrodes made of titanium coated with platinum. At the electrodes H_2(g) and O_2(g) production reaction takes place.
- Compartments 2 and 5: “Separation" compartments, containing the same solution as compartments 3 and 4, to eliminate the effect of electrode reactions on BPM-voltage measurements.
- Compartments 3 and 4: The base and acid production compartments, with three distinct feed solutions of 0.5 M NaCl, 0.5 M NaCl + 2.5 mM $NaHCO_3$ and 0.45 M NaCl + 50 mM Na_2HPO_4.

The open circuit voltage (OCV) was not zero, and it was measured to be 109 ± 8 mV. This is due to the non-ideality of the BPM that allows salt-ions cross over. The values of OCV

were not dependent on the tested solutions, and has been corrected for, in calculating V_{rev} from V_{irr}.

3.6.2. PH-SWEEP USING VISUAL MINTEQ

A pH sweep (-0.25 pH unit in 30 or 35 sweep steps) is applied on three different solutions, while assuming a closed carbonate system for the pH calculations in MINTEQ. Afterwards, the amount of added H^+ (in M) at each pH sweep step is calculated by subtracting the total H^+ concentration (i.e., free ions + in the buffer compound) in that step and the initial H^+ concentration of the start solution. Assuming the BPM produces the same amount of OH^- as H^+ (in M), the total concentration of H^+ for each pH sweep step in the base compartment is then calculated. Eventually, by running a sweep on the total concentration of H^+ in the base side of BPM, pH of the base side is estimated using Visual MINTEQ (choosing the option of being calculated from mass balance). In a buffered solution like 0.45 M NaCl + 50 mM Na_2HPO_4, the total concentration of H^+ must be considered; this includes the hydrogen atoms that are in a compound. For the phosphate solution, the following set of equation hold:

$$\text{Total } H^+ \text{ concentration} = \text{free } H^+ \text{ concentration} + \left([HPO_4{}^{2-}] + 2[H_2PO_4{}^-] + 3[H_3PO_4]\right)$$

$$\text{Total buffer concentration} = [PO_4{}^{3-}] + [HPO_4{}^{2-}] + [H_2PO_4{}^-] + [H_3PO_4]$$

$$[H_3PO_4] = \frac{[H^+]^3[PO_4{}^{3-}]}{K_1K_2K_3}, [H_2PO_4{}^-] = \frac{[H^+]^2[PO_4{}^{3-}]}{K_2K_3}, [HPO_4{}^{2-}] = \frac{[H^+][PO_4{}^{3-}]}{K_3}$$

Where K_i represent the known equilibrium constants for the phosphate buffer. As an example, the simulated acidic and basic pH profiles at current density of ~ 25 mA cm^{-2} are shown for each flow orientation and solution along the z-axis in Figure S2.

3.6.3. DETERMINING RESISTIVITY

The solution (i.e., electrolyte) concentrations in every compartment were chosen in such a way to enable same conductivities for all tested solutions (measured with Metrohm conductometer). The solution resistivity (R_{sol} in Ω) can be calculated using Equation S1, based on the conductivity of the solution (σ in S cm^{-1}), the distance filled with the solution (d in cm), and the compartment (i.e., membrane) area (A in cm^2):

$$R_{sol} = \frac{1}{\sigma} \times \frac{d}{A} \tag{S1}$$

Table S1 summarizes the values for solution conductivity and the corresponding R_{sol}. When using the Ohm law to define the voltage drop (V in volts) due to the electrolyte, at current density of i (in mA cm^{-2}), we get:

$$V_{irr}^{sol} = iAR_{sol} \tag{S2}$$

Table S1: Summary of the solution resistivity.

Solution	Solution conductivity (Ω cm^{-1})		Ω	Ω cm^2
	Measured values	Theoretical values using OLI Studio software	R_{sol}	$A \times R_{sol}$
0.5 M NaCl	0.047 ± 0.001	0.0465	0.98	21.51
0.5 M NaCl + 2.5 mM $NaHCO_3$	0.0455 ± 0.001	0.0466	0.98	21.46
0.5 M NaCl + 50 mM Na_2HPO_4	0.045 ± 0.001	0.0477	0.95	20.96

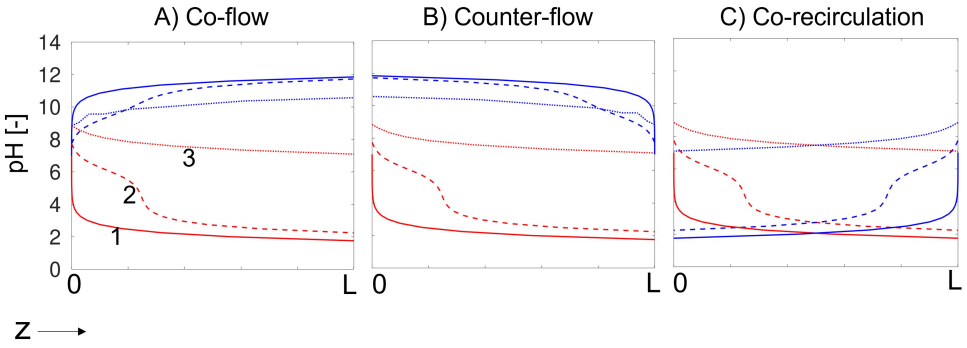

Figure S2: The simulated pH profile along the z-axis, for (A) co-flow, (B) counter-flow, and (C) co-recirculation flow orientations, under assumption of a uniform current density of ~25 mA cm^{-2} and flow rate of 30 ml min^{-1}. Solutions are indicated by (1) solid line : 0.5 M NaCl, (2) dashed line : 0.5 M NaCl + 2.5 mM $NaHCO_3$, and (3) dotted line : 0.45 M NaCl + 50 mM Na_2HPO_4. Blue and red indicate the pH-profile in the base and acid compartments, respectively. The counter-recirculation flow is not shown, but it creates $\Delta pH_{BPM} = 0$ for $0 \leq z \leq L$.

3.6.4. DETERMINING THE BPM-LIMITING CURRENT DENSITY

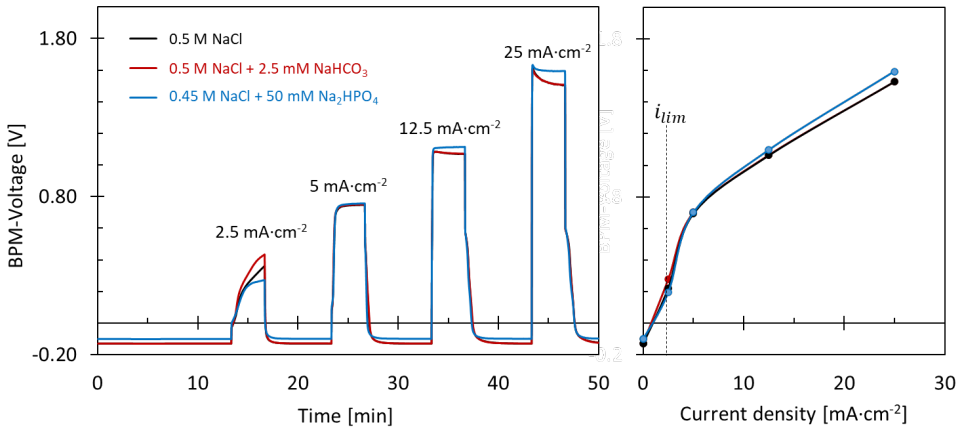

Figure S3: Chronopotentiometry experiments using setup in Figure S1 (using 30 ml min^{-1} flow rate). (A) the current is increased stepwise while BPM-voltage is measured using micro-reference electrodes. (B) the BPM current-voltage curve for each solution, to identify the limiting current density.

To determine the region where the water dissociation reaction (WDR) is dominant over the salt ion crossover in the BPM (i.e., where Equation 3.1 is valid), the limiting current density of the BPM in all three solutions was measured prior to the experiments through short chronopotentiometry experiment (Figure S3). The constant current period was 200 s, followed with 400 s intervals of zero current in between. The shape of the voltage graph in Figure S3 (A) and the vertical jump in Figure S3 (B) at $i = 2.5$ mA cm^{-2}, mark the limiting current density and the start of dominant WDR region.

3.6.5. EXPERIMENTALLY MEASURED PH-GRADIENT AND VOLTAGES

The maximum of the $\Delta pH^{BPM}_{z=0}$ and $\Delta pH^{BPM}_{z=L}$ is chosen and shown at each current density in Figure S4. Note that, for the counter-flow, particularly for unbuffered solutions, ΔpH^{max}_{BPM} can take place inside of the cell at e.g., $z \sim 0.5L$ (Figure S2). This means that values reported for the counter-flow (red line) in Figure S4 (A, B), are underestimated by 3 – 4 pH units, depending on the current density. The real values lie closer to the co-flow (black line). Unfortunately, in our work, due to the large size of the pH sensors, *in-situ* pH measurements at $z \sim 0.5L$ (or any other $0 < z < L$) were not possible.

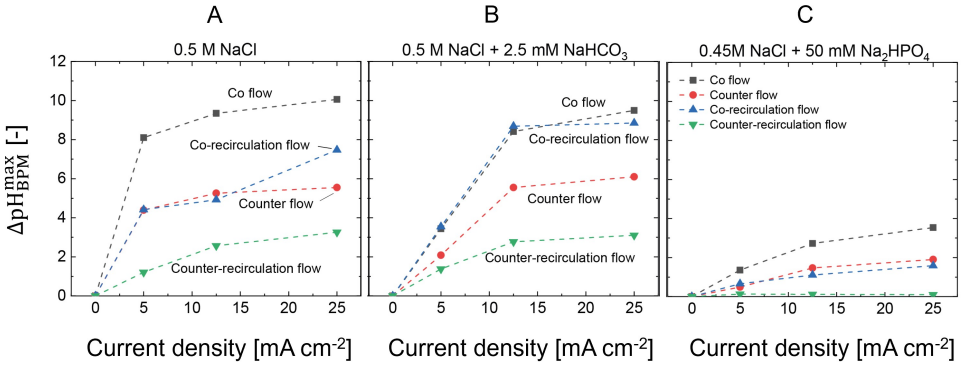

Figure S4: The experimentally measured ΔpH_{BPM}^{max} vs. the applied current densities. In all experiments, $t_r = 44$ s (i.e., flow rate of 30 mA cm^{-2}) is used.

3.6.6. EXPERIMENTALLY MEASURED VOLTAGES

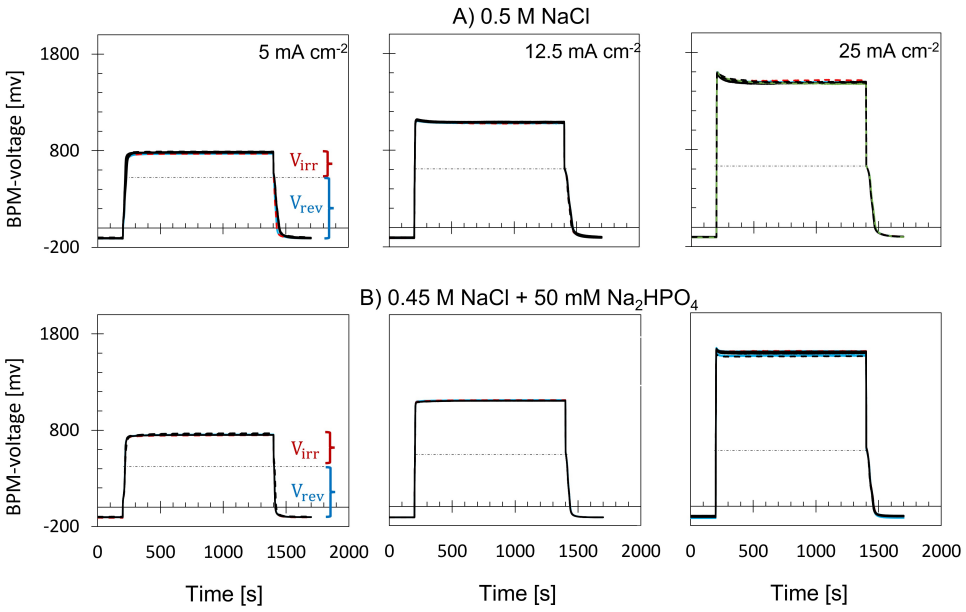

Figure S5: Chronopotentiometric curves for A) 0.5 M NaCl and B) 0.45 M NaCl + 50 mM Na_2HPO_4 solutions. The applied current density increases from left to right as shown. All experiments have been done using 30 mlmin^{-1} flow rate. The curves for the bicarbonate solution are not shown but the values are reported in Table S2. The expected Open circuit voltage (OCV) is zero, but due to the offset of the micro-reference electrodes, values around -100 mV are measured in all the tested cases. When obtaining the reversible and irreversible voltage, the values are corrected for the OCV, as shown in red and blue braces.

The experimental reversible and irreversible voltages are read from current interrupt curves (Figure S5). No significant difference was observed in the magnitude of V_{rev} and V_{irr} between the different flow orientations and solutions (Figure S3 and Table S2).

Table S2: Experimental values of the measured reversible and irreversible voltage in volts vs. applied current densities (i) for a flow rate of 30 ml min^{-1} ($t_r = 44s$) for co flow (1), counter flow (2), co-recirculation (3) and counter-recirculation (4), respectively.

Voltages	i	**0.5 M NaCl**				**0.5 M NaCl + 2.5 mM $NaHCO_3$**				**0.5 M NaCl + 50 mM Na_2HPO_4**			
[V]	(mA cm^{-2})	Co	Counter	Co-re	Counter-re	Co	Counter	Co-re	Counter-re	Co	Counter	Co-re	Counter-re
V_{irr}	0	0.00	0.00	0.00	0.00	0.00	0.00	0.00	0.00	0.00	0.00	0.00	0.00
	5	0.224	0.222	0.211	0.212	0.234	0.236	0.234	0.247	0.263	0.260	0.261	0.250
	12.5	0.464	0.464	0.472	0.466	0.485	0.491	0.472	0.473	0.539	0.538	0.533	0.532
	25	0.862	0.866	0.851	0.854	0.889	0.919	0.880	0.843	0.985	0.997	0.987	0.980
V_{rev}	0	0.00	0.00	0.00	0.00	0.00	0.00	0.00	0.00	0.00	0.00	0.00	0.00
	5	0.656	0.658	0.678	0.677	0.636	0.636	0.644	0.616	0.597	0.590	0.593	0.617
	12.5	0.723	0.724	0.723	0.726	0.701	0.701	0.719	0.709	0.685	0.685	0.683	0.685
	25	0.735	0.737	0.738	0.739	0.720	0.730	0.742	0.740	0.708	0.721	0.716	0.718

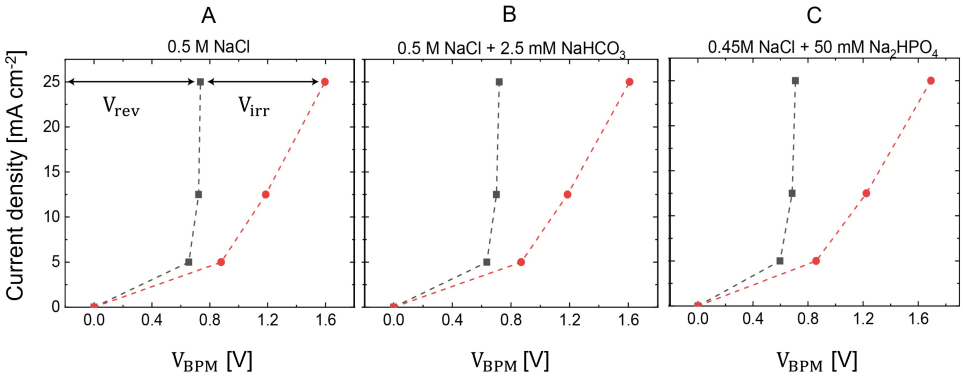

Figure S6: The measured steady state V_{BPM} vs. the applied current density for the co-flow in the three tested solutions, using flow rate of 30 ml min^{-1} ($t_r = 44s$).

Table S3: The total BPM membrane layers ohmic resistance in the steady-state calculated through Equation S3 and depicted in Figure S7.

Ω cm^2	i in mA cm^{-2}	0.5 M NaCl	0.5M NaCl+2.5mM $NaHCO_3$	0.45M NaCl+ 50 mM Na_2HPO_4
$R_m = R_{layers,stat}$	0	0	0	0
	0.005	21.9	26.1	30.7
	0.0125	15.8	17	21.9
	0.025	12.8	13.8	18.5

3.6.7. DETERMINING THE BPM MEMBRANE LAYERS OHMIC RESISTANCE

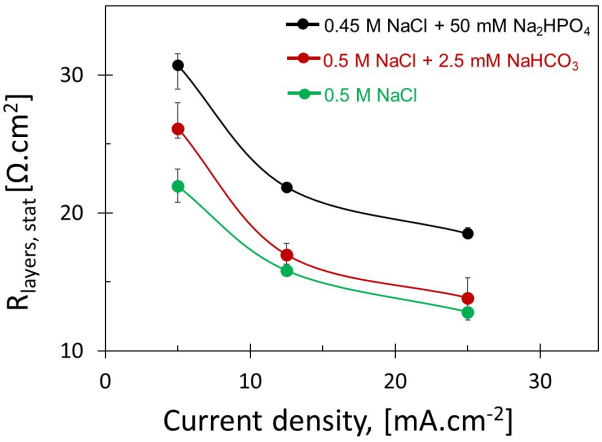

Figure S7: The total BPM membrane layers ohmic resistance in the steady state (i.e., transport state) for 0.5 M NaCl (green), 0.5 M NaCl + 2.5 mM $NaHCO_3$ (red), and 0.45 M NaCl + 50 mM Na_2HPO_4 (black).

To obtain the total BPM membrane layers ohmic resistance in the steady state, Equation S3 can be used. The values for V_{irr}^{tot} and $A \times R_{sol}$ are shown in Table S2 and Table S1, respectively:

$$R_{layers,stat} = \frac{V_{irr}^{tot}}{i} - A \times R_{sol} \tag{S3}$$

3.6.8. EXPERIMENTALLY MEASURED PH FOR THE SODIUM CHLORIDE CASE

The experimentally measured pH for the sodium chloride case (0.5 M NaCl) are shown in Figure S9 while the (possible) proton leakage as explained in the chapter is depicted in Figure S8.

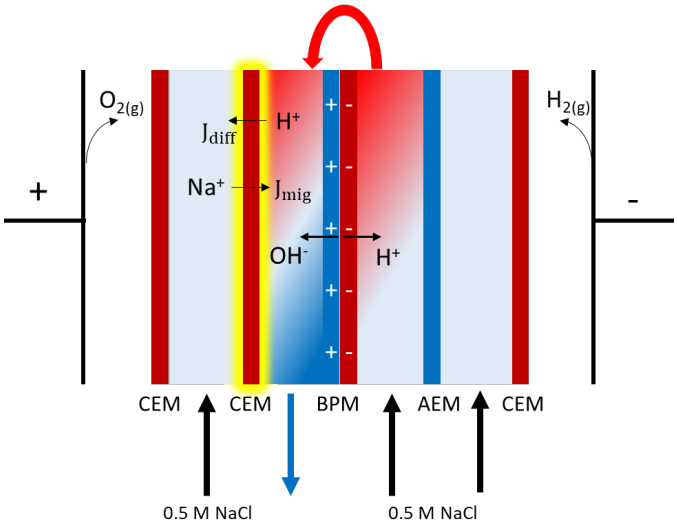

Figure S8: In the six-compartment cell, the acid recirculation creates a high H^+ ions concentration gradient over the highlighted CEM. The subsequent H^+ ion diffusion away from the base compartment (balanced out by Na^+ ions migration) plus the original OH^- ion production via the BPM, creates an alkaline outflow-pH in the base compartment, instead of the expected (neutral) pH.

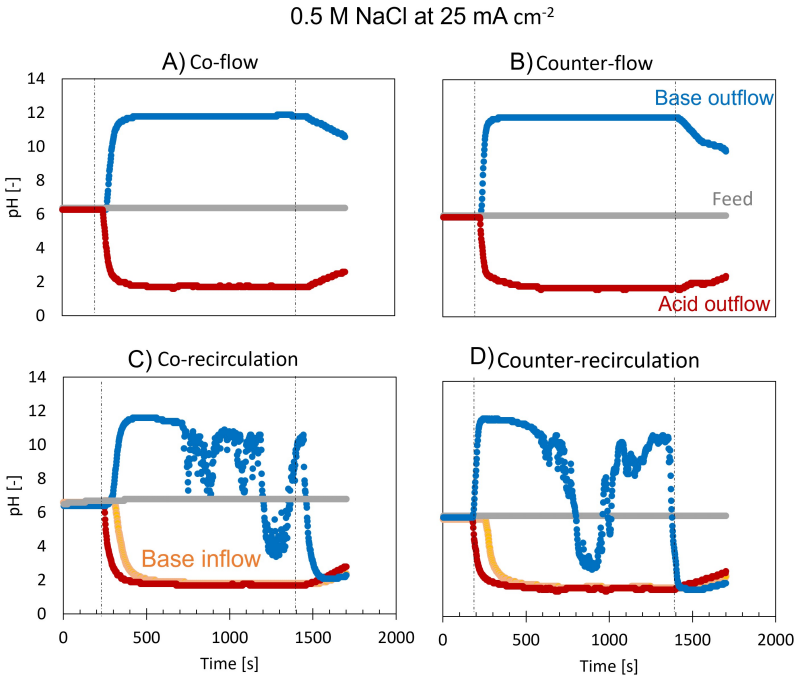

Figure S9: The measured pH values versus time for the 0.5 M NaCl solution, under applied current density of 25 mA cm^{-2}. For the recirculation modes, the Base-outflow-pH did not stabilize during the experiments, due to proton transport away from the base compartment. However, same as all the other cases, the average of data over the last 5 minutes of the constant current interval (i.e., 1100 -1400 s), is used for defining this pH. Constant current is applied for 20 min, between Time 200 – 1400 s, as shown with dashed vertical black lines.

BIBLIOGRAPHY

[1] R. Sharifian et al. “Intrinsic bipolar membrane characteristics dominate the effects of flow orientation and external pH-profile on the membrane voltage”. In: *Journal of Membrane Science* 638 (2021), p. 119686.

[2] M. B. Ali et al. “Coupling of bipolar membrane electrodialysis and ammonia stripping for direct treatment of wastewaters containing ammonium nitrate”. In: *Journal of membrane science* 244.1-2 (2004), pp. 89–96.

[3] J. Balster et al. “Electrochemical acidification of milk by whey desalination”. In: *Journal of membrane science* 303.1-2 (2007), pp. 213–220.

[4] L. Bazinet et al. “Bipolar-membrane electrodialysis: Applications of electrodialysis in the food industry”. In: *Trends in food science & technology* 9.3 (1998), pp. 107–113.

[5] D. A. Vermaas et al. “Synergistic electrochemical CO2 reduction and water oxidation with a bipolar membrane”. In: *ACS Energy Letters* 1.6 (2016), pp. 1143–1148.

[6] D. A. Vermaas et al. “Ion transport mechanisms in bipolar membranes for (photo) electrochemical water splitting”. In: *Sustain. Energy Fuels* 2 (9 2018), pp. 2006–2015.

[7] M. B. McDonald et al. “Graphene oxide as a water dissociation catalyst in the bipolar membrane interfacial layer”. In: *ACS applied materials & interfaces* 6.16 (2014), pp. 13790–13797.

[8] N. Vargas-Barbosa et al. “Assessing the Utility of Bipolar Membranes for use in Photoelectrochemical Water-Splitting Cells”. In: *ChemSusChem* 7 (11 Nov. 2014), pp. 3017–3020.

[9] J. Luo et al. “Bipolar Membrane-Assisted Solar Water Splitting in Optimal pH”. In: *Adv. Energy Mater* 6 (13 July 2016), p. 1600100.

[10] D. Vermaas et al. “Photo-assisted water splitting with bipolar membrane induced pH gradients for practical solar fuel devices”. In: *J. Mater. Chem. A* 3 (38 2015), pp. 19556–19562.

[11] D. Vermaas et al. “Chapter 8 Applications of Bipolar Membranes for Electrochemical and Photoelectrochemical Water Splitting”. In: *Advances in Photoelectrochemical Water Splitting: Theory, Experiment and Systems Analysis* (2018), pp. 208–238.

[12] A. Emren et al. “Energy storage in a fuel cell with bipolar membranes burning acid and hydroxide”. In: *Energy* 8 (4 1983), pp. 277–282.

[13] W. Van Egmond et al. “Performance of an environmentally benign acid base flow battery at high energy density”. In: ().

[14] F. Ilhan et al. “Evaluation of treatment and recovery of leachate by bipolar membrane electrodialysis process”. In: *Chem. Eng. Process. Process Intensif* 75 (2014), pp. 67–74.

[15] M. Eisaman et al. “CO 2 separation using bipolar membrane electrodialysis”. In: *Energy Environ. Sci* 4 (4 2011), pp. 1319–1328.

[16] S. Datta et al. “Electrochemical CO2 Capture Using Resin-Wafer Electrodeionization”. In: *Ind. Eng. Chem. Res* 52 (43 2013), pp. 15177–15186.

[17] A. Iizuka et al. “Carbon dioxide recovery from carbonate solutions using bipolar membrane electrodialysis”. In: *Sep. Purif. Technol* 101 (2012), pp. 49–59.

[18] M. Shuangchen et al. “Experimental study on desorption of simulated solution after ammonia carbon capture using bipolar membrane electrodialysis”. In: *Int. J. Greenh. Gas Control* 42 (2015), pp. 690–698.

[19] M. Eisaman et al. “Energy-efficient electrochemical CO2 capture from the atmosphere”. In: *Technical Proceedings of the 2009 NSTI Nanotechnology Conference and Expo, NSTI-Nanotech 2009* 3 (Jan. 2009).

[20] C. F. de Lannoy et al. “Indirect ocean capture of atmospheric CO2: Part I. Prototype of a negative emissions technology”. In: *Int. J. Greenh. Gas Control* 70 (May 2018), pp. 243–253.

[21] Y. Zhang et al. “Recovery of ammonia and sulfate from waste streams and bioenergy production via bipolar bioelectrodialysis”. In: *Water Res* 85 (2015), pp. 177–184.

[22] E. Koivisto et al. “Energy use of flux salt recovery using bipolar membrane electrodialysis for a CO2 mineralisation process”. In: *Entropy* 21 (4 2019).

[23] N. Van Linden et al. “Bipolar membrane electrodialysis for energetically competitive ammonium removal and dissolved ammonia production”. In: *J. Clean. Prod* 259 (2020), p. 120788.

[24] M. Mcdonald et al. “Corrigendum: Use of Bipolar Membranes for Maintaining Steady-State pH Gradients in Membrane-Supported, Solar-Driven Water Splitting”. In: *ChemSusChem* 8 (1 Jan. 2015), p. 14.

[25] S. Z. Oener et al. In: *Ionic Processes in Water Electrolysis: The Role of Ion-Selective Membranes* 2 (Nov. 2017), pp. 2625–2634.

[26] M. Lin et al. “An Experimental-and Simulation-Based Evaluation of the CO2 Utilization Efficiency of Aqueous-Based Electrochemical CO2”. In: ().

[27] R. Parnamae et al. “Bipolar membranes: A review on principles, latest developments, and applications”. In: *J. Memb. Sci* 617 (2021), p. 118538.

[28] J. Bui et al. “Understanding Multi-Ion Transport Mechanisms in Bipolar Membranes”. In: *ACS Appl. Mater. Interfaces* 12 (47 Nov. 2020), pp. 52509–52526.

[29] S. Z. Oener et al. “Accelerating water dissociation in bipolar membranes and for electrocatalysis”. In: *Science* (July 2020), p. 1487.

[30] P. Ramirez et al. “Membrane potential of bipolar membranes”. In: *J. Electroanal. Chem* 404 (2 1996), pp. 187–193.

[31] J. Veerman et al. “Electrical power from sea and river water by reverse electrodialysis: A first step from the laboratory to a real power plant”. In: *Environ. Sci. Technol* 44 (23 2010), pp. 9207–9212.

[32] D. Vermaas et al. “High Efficiency in Energy Generation from Salinity Gradients with Reverse Electrodialysis”. In: *ACS Sustain. Chem. Eng* 1 (10 Oct. 2013), pp. 1295–1302.

[33] R. Sharifian et al. “Electrochemical carbon dioxide capture to close the carbon cycle”. In: *Energy Environ. Sci* (2021).

[34] L. Shi et al. “Nutrient recovery from animal manure using bipolar membrane electrodialysis: Study on product purity and energy efficiency”. In: *Water Cycle* 1 (2020), pp. 54–62.

[35] H. Strathmann et al. “Theoretical and practical aspects of preparing bipolar membranes”. In: *Desalination* 90 (1-3 1993), pp. 303–323.

[36] K. Sun et al. “A Stabilized, Intrinsically Safe, 10% Efficient, Solar-Driven Water-Splitting Cell Incorporating Earth-Abundant Electrocatalysts with Steady-State pH Gradients and Product Separation Enabled by a Bipolar Membrane”. In: *Adv. Energy Mater* 6 (13 2016), pp. 1–7.

[37] M. Blommaert et al. “Electrochemical impedance spectroscopy as a performance indicator of water dissociation in bipolar membranes”. In: *J. Mater. Chem. A* 7 (32 2019), pp. 19060–19069.

[38] R. Moussaoui et al. “Co-ion leakage through bipolar membranes Influence on I-V responses and water-splitting efficiency”. In: *J* ().

[39] H. Strathmann et al. “Limiting current density and water dissociation in bipolar membranes.pdf”. In: *J. Memb. Sci* 125 (1997), pp. 123–142.

[40] F. Wilhelm et al. “Current-voltage behaviour of bipolar membranes in concentrated salt solutions investigated with chronopotentiometry”. In: *J. Appl. Electrochem* 32 (4 2002), pp. 455–465.

[41] S. Z. Oener et al. “Thin Cation-Exchange Layers Enable High-Current-Density Bipolar Membrane Electrolyzers via Improved Water Transport”. In: *ACS Energy Lett* (2020), pp. 1–8.

[42] A. Alcaraz et al. “Ion selectivity and water dissociation in polymer bipolar membranes studied by membrane potential and current-voltage measurements”. In: *Polymer (Guildf)* 41 (17 2000), pp. 6627–6634.

[43] M. Eisaman et al. “CO 2 desorption using high-pressure bipolar membrane electrodialysis”. In: *Energy Environ. Sci* 4 (10 2011), pp. 4031–4037.

[44] F. Wilhelm et al. “Chronopotentiometry for advanced current-voltage characterization of bipolar membranes”. In: *J. Electroanal. Chem* 502 (Apr. 2001), pp. 152–166.

[45] E. Al-Dhubhani et al. “Entanglement-Enhanced Water Dissociation in Bipolar Membranes with 3D Electrospun Junction and Polymeric Catalyst”. In: *ACS Appl. Energy Mater* (Mar. 2021).

4

in-situ MINERALIZATION: OCEANIC CARBON CAPTURE USING BIPOLAR MEMBRANE

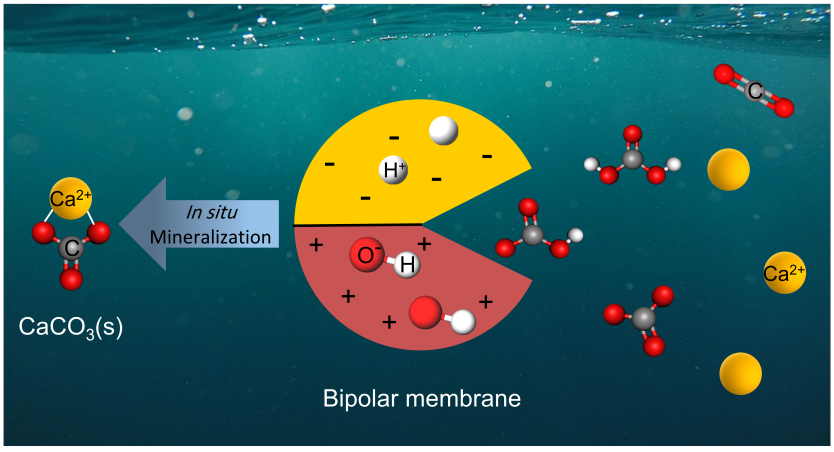

This chapter has been published as "Electrochemical oceanic carbon capture through *in-situ* carbonate mineralization using bipolar membrane" by R. Sharifian, L.Boer, R.M. Wagterveld, D.A. Vermaas. Chemical engineering journal **438**, 135326 (2022) [1].

Bipolar membrane electrodialysis (BPMED) can provide a sustainable route to capture the oceanic-dissolved inorganic carbon (DIC) using an electrochemical pH-swing concept. Previous works demonstrated how gaseous CO_2 (through acidification) can be obtained from ocean water, and how carbonate minerals can be provided via ex-situ alkalinization. In this work, we present, for the first time, the in-situ mineralization via the alkalinization route using both real and synthetic seawater. An in-situ pH-swing can be applied inside of the BPMED cell to allow reducing the energy consumption of the oceanic-DIC capture. We demonstrate that, by accurately controlling the applied current density and cell residence time, the energy required for the process can be indeed lowered through facilitating an optimized pH in the cell (i.e., base-pH 9.6 - 10). Within this alkaline pH-window, we can capture between 60% (for real seawater) up to 85% (for synthetic seawater) of the DIC from the feed together with minor $Mg(OH)_2$ precipitates. The maximum theoretical extraction of $CaCO_3$ is 97 %, below which the production increases linearly with the applied current density (and pH). The $CaCO_3$(s) production-current density proportionality is dependent on the cell design, while the energy consumption is dominated by the ohmic losses and BPM-overpotential. Through tuning the current density and flow rate, we obtained an energy consumption by applying a mild in-situ pH-swing of ca. pH 3.2 - 9.8 (for real seawater). As a result, Aragonite was extracted by using of 318 ± 29 kJmol^{-1} $CaCO_3$(s) (i.e., ca. 0.88 $\mathrm{kWh\,kg^{-1}}$ $CaCO_3$) from real seawater in a cell containing ten bipolar - cation exchange membrane cell pairs, which is less than half of the previously lowest energy consumption for carbonate mineralization from (synthetic) seawater.

4.1. INTRODUCTION

The damaging impacts of CO_2 on the climate encourages emission control and carbon capture to reduce the carbon footprint of all sectors [2]. In addition to capture from source points, CO_2(g) can be captured from its sinks including the atmosphere [3, 4], and ocean [5, 6], effectively addressing decentralized emissions. To ensure the carbon neutrality, this CO_2 capture should be able to be driven by renewable energy, which is most abundantly available as electricity. Thankfully, electrochemical methods can be used to achieve a circular carbon economy using (renewable) electricity [7] with no or minimal chemicals and at ambient temperature and pressure, as opposed to the conventional heat-driven CO_2 capture e.g., amine-based absorption or calcium looping. Electrochemical capture can be done via e.g., organic redox [8], pH-swing (via a e.g., bipolar membrane electrodialysis, electrolysis, capacitive deionization, H^+ (de)intercalation, and proton-coupled electron transfer (PCET) of organic molecules), high-temperature molten carbonate cells, and hybrid methods (including electrochemical CO_2 capture and conversion combinations and battery systems) [7].

In particular, electrochemical cells containing a bipolar membrane (BPM) has shown promise for CO_2 capture, thanks to their simplicity to make acids and bases for releasing inorganic carbon from the water, their small footprint, and facile upscaling [7]. The bipolar membrane generates acidic and alkaline pH on its sides (i.e., pH-swing), through the water dissociation reaction (WDR) upon application of an electrical field in the reverse bias mode [9]. This pH-swing leverages the carbonate equilibrium, making it suitable for direct air capture (DAC), oceanic capture, and even flue gas capture [7, 10]. Upon the pH-swing, the dissolved CO_2 in an aqueous solution can be captured in its gaseous form (at acidic pH) or as mineral carbonate (at alkaline pH) [5, 7].

Approximately 23 % of the global CO_2 emission ends up in the ocean [7], making oceanic CO_2 capture advantageous as it eliminates the use of any additional aqueous absorbent (e.g., alkaline and amines in direct air capture) by leveraging the vast atmosphere-ocean contact area. Extracting 1 Gton-CO_2 per year (~ 2.7 % of the total global CO_2 emission) from the ocean surface layer (i.e., the upper 50 m) requires processing only a fraction of 0.0005 of this layer volume [5]. Furthermore, ocean decarbonization combined with desalination plants (e.g., reverse osmosis), as a pre-treatment step, can potentially decrease the chance of carbonate scaling in the plant by reducing the DIC concentration below calcium carbonate solubility product.

The product of oceanic capture can be CO_2(g) or solid carbonate minerals, depending on the operating pH [9]. Extracting CO_2 in the gaseous form (from the acidic stream, Figure 4.1) has been demonstrated [5, 11], but requires the use of additional gas-liquid membrane contactors for CO_2(aq) to CO_2(g) exchange. Additionally, purification of the produced CO_2(g) is required before it can be considered as feedstock [6], while the challenges concerning gas transportation and storage arise, accordingly.

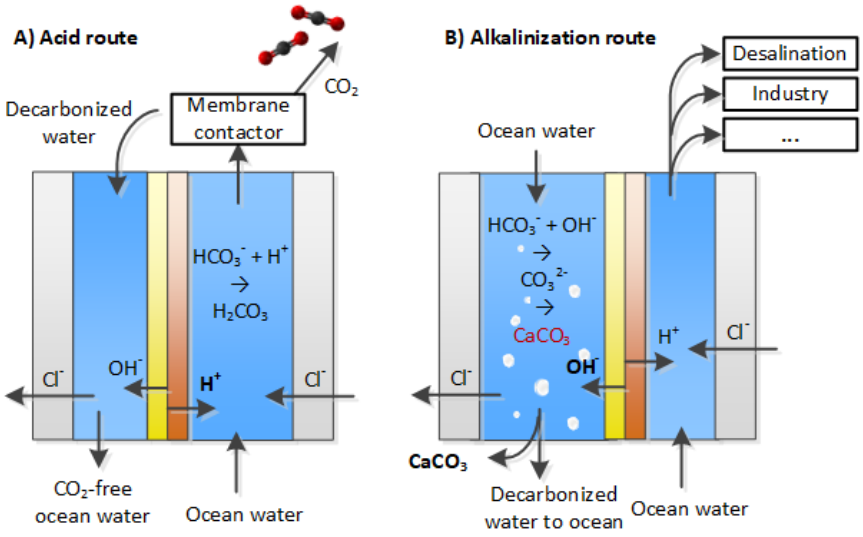

Figure 4.1: Concept of CO_2 capture from the ocean water via electrochemical pH-swing. A) CO_2 release using an acid route. B) CO_2 mineralization using alkalinization route.

On the other hand, for extraction of solid carbonate minerals via alkalinization of ocean water, no membrane contractors are required (Figure 4.1 (B)). Although the acid-route is more straightforward as negative emission technology (using the alkaline product to allow capturing CO_2 from the atmosphere again), the "alkalinization-route" could act also as circular oceanic CO_2 capture technology when the acid is used for other purposes. Possible combinations are using the slightly acidic stream for desalination (where the acidification prevents scaling [12]) or concentrating the acid further for industrial purposes. Returning only the alkaline, decarbonized stream, which has a pH between 9 and 10, brings net alkalinization to the ocean and allows further extraction of CO_2 from the atmosphere. A potential advantage of this "alkalinization-route" is that calcium carbonate is easy to transport, use, and store, and has a global market size of ~ 116 million ton $CaCO_3$ (i.e., ~ USD 43 billion in 2020, with annual growth rate of ~ 2.8 % [13]). Calcium carbonate applications include the paper industry (> 50 % of the market [13], where it is used as filler), coating, plastics, paints, adhesive/sealants, rubber, cement and construction materials [14–16].

BPMED based oceanic-CO_2 capture through the alkalinization-route has been performed *ex-situ* using synthetic seawater, where concentrated NaOH is first produced (from pure NaCl in BPMED) and then is gradually added to external storage tanks containing seawater, enabling the desired alkaline pH for carbonate mineralization [5]. Alternatively, during an *in-situ* process, seawater is pumped directly into the electrochemical cell [17]. The *in-situ* capture can eliminate the step of NaCl purification from the seawater, and avoids the necessity of making highly concentrated acid and base (i.e., large pH-swing), making the process more energy effective [18]. In fact, a mild pH-swing in the range of ~ pH 4 - 10 is adequate for CO_2 capture [19]. In addition, such mild pH-swing can preserve the lifetime and permselectivity of charged membranes better than

a harsher pH-swing. However, although an *in-situ* process might require less energy, it increases the chance of fouling within the cell.

In this work, we study the feasibility of the *in-situ* bipolar membrane electrodialysis (BPMED) for capturing oceanic-dissolved inorganic carbon (DIC) as carbonate minerals via alkalinization route. Special attention is given to minimizing the electrical energy consumption of the process. First, the thermodynamic optimum alkaline pH-window for the capture and the minimum electrical energy required for the pH-swing is simulated using Visual MINTEQ 3.1. Subsequently, using a six-compartment cell with a single BPM, the effect of the (local) pH on the carbonate mineralization and membrane fouling is demonstrated. We perform experiments using both synthetic seawater and real seawater (from Wadden Sea in the Netherlands). Finally, we validated the concept in an upscaled BPMED cell, containing 10 bipolar - cation exchange membrane (BPM-CEM) cell pairs, providing insight towards industrialization of the carbon capture from seawater via mineralization.

4.2. THEORY

4.2.1. EFFECT OF PH-SWING ON THE CARBONATE EQUILIBRIUM

The atmospheric CO_2(g) is in equilibrium with the dissolved inorganic carbon (DIC) species in the ocean [20–24].Oceanic-DIC has a concentration of ~ 2.3 - 2.5 mmolL^{-1}, and includes CO_2(aq)/ H_2CO_3, HCO_3^-, and CO_3^{2-} containing species [20]. At the typical surface seawater of pH ~ 8.2, these species contributions are 0.5 %, 89 %, and 10.5 %, respectively. Furthermore, calcium (and magnesium) ions are abundant in the ocean with concentrations ~ 4× (and ~ 20×) higher than that of DIC, respectively [24]. Upon ocean alkalinization, the carbonate equilibrium shifts from the bicarbonate to carbonate ion [24, 25]:

$$CO_2(aq) + OH^-(aq) \leftrightarrow HCO_3^-(aq) \tag{4.1}$$

$$HCO_3^-(aq) + OH^-(aq) \leftrightarrow H_2O + CO_3^{2-}(aq) \tag{4.2}$$

$$Ca^{2+}(aq) + CO_3^{2-}(aq) \leftrightarrow CaCO_3(s) \tag{4.3}$$

Theoretically, more than 97 % of the DIC can be extracted in the form of ~ 2.13 mM CO_2 (g) when bringing the seawater pH to 4.5, or in the form of ~ 2.13 mM $CaCO_3$(s) at a pH of ~ 10.0 (Table S1-S3). Upon CO_3^{2-} consumption in Equation 4.3, HCO_3^- will be dissociated to restore the equilibrium in Equation 4.2, accompanied by the consumption of OH^- ions, that in turn, decreases the solution pH.

The kinetics of above set of reactions are affected by the pH, temperature, and pressure [20]. In a well-mixed system with low mass transport resistances (at 25 ^oC, 1 atm, and pH 6), the carbonate-mineral precipitation step (Equation 4.3) is the rate limiting step (with a time scale of 10^3 s, which is much slower than Equation 4.1 and 4.2 [18, 26]).

Calcium carbonate ($CaCO_3$) precipitates in three anhydrous polymorphs including, in the order of thermodynamic stability, calcite (rhombohedral) > aragonite (orthorhombic) > vaterite (hexagonal) [25], [26], in addition to its hydrated form. The thermodynamically favorable state is indicated by the saturation index (see Equation S2); a positive saturation index allows precipitation [27], [28].Figure 4.2 maps the saturation index for the pH of typical seawater composition. To selectively precipitate carbonate minerals but

avoid hydroxides precipitation (especially brucite $Mg(OH)_2$ that can precipitate with a much faster rate than $CaCO_3$), a base-pH < 10 should be maintained. On the other hand, within the pH range of 9.3 - 10, since the saturation index of $CaCO_3$ polymorphs still increases slightly with pH (Figure 4.2, black curves), the higher limit (i.e., pH 9.6 - 10) is more desired, and is therefore chosen in this work as the optimum alkaline-pH window. See the supporting information 4.6 for more details on the precipitation prediction.

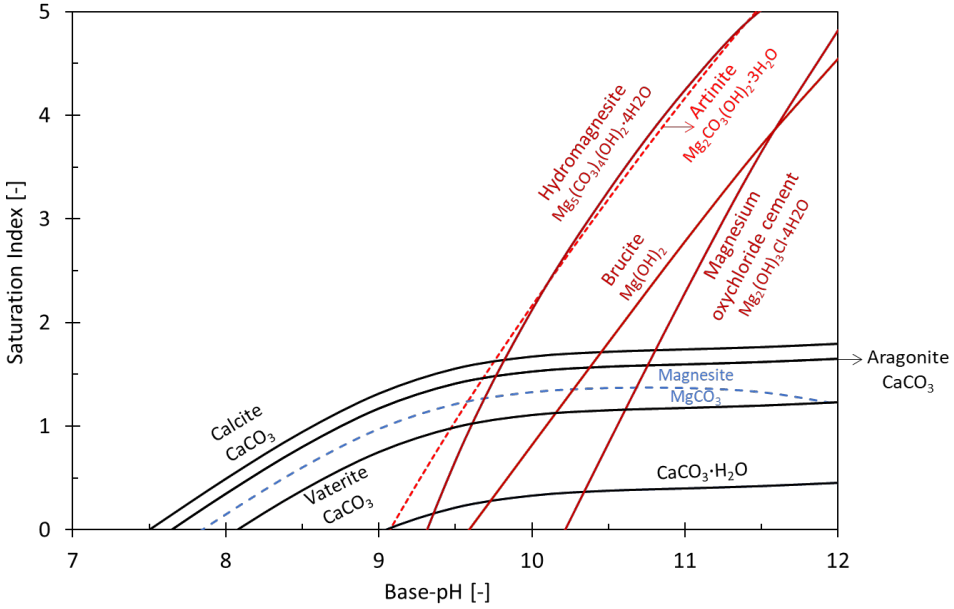

Figure 4.2: The saturation index (SI) of all thermodynamically possible minerals in synthetic seawater vs. the base-pH, determined by Visual MINTEQ at 25, based on the synthetic seawater compositions (Table 4.1) and assuming a closed system with no precipitation allowed during the pH-sweep. Minerals containing hydroxide ion (red), calcium carbonate (black), and magnesium carbonate (blue) are shown. Dolomite $CaMg(CO_3)_2$ [29] and Huntite $Mg_3Ca(CO_3)_4$ [30] are excluded from the graph due to their extremely slow kinetics at ambient temperature and pressure (in absence of any microbial activities). Calcium hydroxide $Ca(OH)_2$ does not occur as it stays under saturated in the demonstrated pH range < 12 [31].

4.2.2. BPM-INDUCED pH-SWING

The alkaline pH is the key parameter for facilitating the oceanic CO_2 capture through carbonate mineralization; a high pH increases the concentration of CO_3^{2-} ion (among other DIC forms), the $CaCO_3$ saturation index and kinetics of Equation 4.1-4.3. Using a bipolar membrane, the total concentration of the produced OH^- ions in the base compartment (determining pH_{Base}), assuming a Coulombic efficiency of 100 % and ideally selective membranes can be calculated via [32]:

$$\left[OH^-_{produced}\right] = \left[H^+_{produced}\right] = \frac{(i - i_{\lim})}{F}\left(\frac{t_r}{d}\right) \tag{4.4}$$

Table 4.1: Ion composition of the synthetic seawater as used in simulations and experiments. See the supporting information 4.6 for the underlying calculations (Table S4, S5). The simulated feed pH is 8.104 (for a closed system).

Ion	mol/L	Ion	mol/L
Chloride (Cl^-)	0.5363	Calcium (Ca^{2+})	0.0102
Sodium (Na^+)	0.4593	Magnesium (Mg^{2+})	0.0521
Sulphate (SO_4^{2-})	0.0275	DIC	0.00215
Potassium (K^+)	0.0097	Proton (H^+)	0.002

Where [OH^-] is the hydroxide ion concentration ($mol\,m^{-3}$), t_r the cell residence time (s), d the cell compartment thickness (m), i the applied electrical current density ($A\,m^{-2}$), i_{lim} the BPM-limiting current density ($A\,m^{-2}$), and F the Faraday constant 96485 ($C\,mol^{-1}$). The term $\frac{t_r}{d}$ is interchangeable with $\frac{A_m}{q}$, with A_m the membrane active area (m^2) and q the flow rate ($m^3\ s^{-1}$) [32].

For current densities lower than the limiting current density i_{lim}, the water dissociation reaction (WDR) in the bipolar membrane is not dominant yet, decreasing the Coulombic efficiency of the process due to the salt ion crossover through the BPM [9], [33]. In other words, due to the non-ideal selectivity of the BPM and slow WDR kinetics at the low current density regime, the ion crossover dominates the water dissociation at low current densities [33]. For simplicity, we assume that the first ($\sim i_{lim}$) part of the applied current ($< i_{lim}$) is not contributing to a pH-swing. By manufacturing BPM with high selectivity (to decrease the salt ions crossover), and high WDR-catalysts activity (i.e., fast WDR kinetics) one can reduce the limiting current density [34].

To remove carbonate ions efficiently, the produced OH^- ions (Equation 4.4) must only be used to convert the bicarbonate ions in the seawater feed stream to CO_3^{2-} ions rather than forming hydroxide precipitates. Therefore, the process parameters e.g., the current density and cell residence time must be carefully tuned in such a way that the precipitation of hydroxide minerals, e.g., $Ca(OH)_2$ and $Mg(OH)_2$, are avoided.

4.3. EXPERIMENTAL SECTION

4.3.1. REAGENTS AND MATERIALS

Synthetic seawater was made with ionic compositions shown in Table 4.1. For simplicity, minor present ions such as strontium (Sr^{2+}) and bromide (Br^-) were excluded from the synthetic seawater mix, while the difference in the total salinity was made up for by adding NaCl salt instead. All reagents were of analytical grade acquired from VWR or Sigma Aldrich. During the experiments, all solutions were kept at ambient temperature of 23°C ± 2°C. To avoid pre-precipitation (of e.g., $CaCO_3$), two separate feed tanks were used with their content mixed using T-connections right before entering the electrochemical cell, and not any sooner. Feed tank 1 contain ~ 47 gL^{-1} NaCl, 0.385 gL^{-1} $NaHCO_3$, 1.45 gL^{-1} KCl, and 7.8 gL^{-1} Na_2SO_4 salt while feed tank 2 contain 3 gL^{-1} $CaCl_2 \cdot 2H_2O$ plus 21.2 gL^{-1} $MgCl_2 \cdot 6H_2O$. When each feed tank reaches equilibrium with the atmospheric CO_2 (420 ppm) and upon mixing the two feed streams, the corresponding synthetic seawater ion concentrations, which is also the starting point for all

Table 4.2: Summary of the properties of electrochemical cells used in this work.

Stack	A_m [cm^2]	Compartment volume [cm^3]
Figure 4.3 (A)	22	$11 \times 2 \times 1 = 22$
Figure 4.3 (B)	11	$10 \times 10 \times 0.04 = 4$

simulations, will become as shown in Table 4.1 (see Visual MINTEQ calculations procedure in Table S4, S5). Note that, upon equilibration with the atmospheric CO_2, part of the initially added DIC (in the form of sodium bicarbonate salt) leaves the solution as CO_2(g), increasing the feed pH and lowering the remaining net DIC-concentration to ~ 2.15 mM (instead of initially added 2.3 mM). Since adding more $NaHCO_3$ in tank 1 (to make up for the lost DIC to the air) would come with the cost of a higher $CaCO_3$ pre-precipitation when tank 1 and tank 2 are mixed, it is avoided in our work.

Similar to the synthetic seawater, the real seawater is supersaturated with respect to calcite and aragonite even before entering the BPMED cell, with thermodynamic calculations predicting a subsequent aragonite precipitation [35]. However, in real seawater, as opposed to the synthetic seawater, due to the presence of soluble organic matter interacting onto surface of crystals such inorganic precipitation is limited and almost absent [36], [37].

In this work, in addition to the synthetic seawater, experiments using real seawater from the Wadden Sea, pre-treated with a 10 μm filter, was also conducted. In comparison with the synthetic seawater, the real seawater had a lower conductivity (35 mScm^{-1} vs. 50 mScm^{-1}), but a higher initial DIC-concentration (2.7 mM vs. 2.1 mM), see Table S7 for full ion composition.

4.3.2. EXPERIMENTAL SETUP

Two different electrochemical cells were used, Table 4.2 and Figure 4.3:

- (A) a six-compartment cell with a (single) BPM, with d = 1 cm thick compartment and no spacers between the membranes for *In-situ* observation of the electrochemical mineralization, plus BPM fouling studies.
- (B) an up-scaled BPMED cell containing 10 BPM-CEM cell pairs (REDstack B.V.), with integrated gasket mesh spacers of 400 ± 5 μm (AquaBattery B.V.) in between the membranes for energy consumption measurement.

All solutions were pumped through the stack by peristaltic pumps (Cole-Parmer, Masterflex L/S Digital drive, USA), through 6.0 mm PTFE tubing (EmTechnik). The pH of the feed and outflow streams of the BPMED cell were measured every 2 s, using Orbisit CPS11D-7BA21 pH probes connected to a Liquiline CM444 digital multiparameter transmitter, both from EndressHauser, with an accuracy of ± 0.2 pH-units. All membranes used in the BPMED cells were provided by FuMATech B.V. The FBM-130, FKB-PK-130 and FAB-PK-130 were used as bipolar membranes (BPM), cation exchange membranes (CEM) and anion exchange membranes (AEM), respectively. Electrodes of titanium mesh coated with platinum, provided by MAGNETO Special Anodes B.V. were used in both cells.

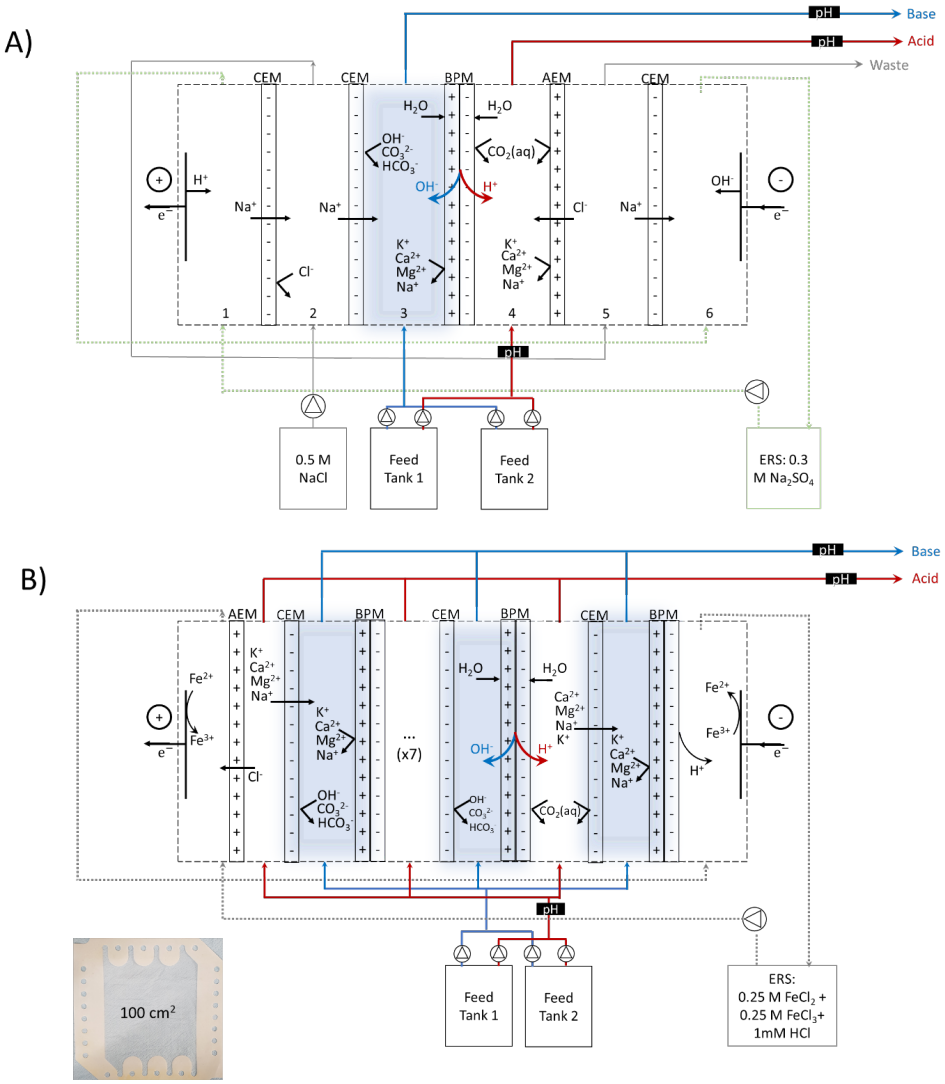

Figure 4.3: Graphical representation of the (A) six-compartment BPM cell demonstrating the compartment numbers, and (B) the BPM-CEM stacked upscaled cell (with 10 cell pairs) with the integrated 400 μm gasket-mesh spacer and blue cell-unit shown. Feed tank 2 contains $CaCl_2$ and $MgCl_2$ and Feed tank 1 contains remaining salts from Table 4.1. ERS is the electrode rinsing solution. For the tests with the real seawater, tanks 1 and 2 were replaced with a single seawater feed tank accompanied with 10 μm filter. In (B), a shielding AEM is used next to the anode, to avoid $Fe(OH)_2$ precipitation.

4.3.3. EXPERIMENTAL PROCEDURE

The experiments were conducted under ambient temperature and pressure, in a one-way single pass continuous mode. To determine the required optimum alkaline-pH, five constant current densities of 10, 20, 30, 40 and 50 $mA\,cm^{-2}$ were applied for 15 minutes to the thick six-compartment cell with a (single) BPM (Figure 4.3 (A)). A constant flow rate of 120 $ml\,min^{-1}$ (i.e., t_r = 11 s) was applied for those cases. After observing the *in-situ* mineralization in the short experiments, longer experiments of 120 min were conducted at i = 10 and 40 $mA\,cm^{-2}$ to determine membrane fouling and energy consumption of the process. For those samples, the BPM was prepared (see Membrane fouling and crystal analysis) for the Scanning Electron Microscopy (SEM) coupled with energy dispersive X-ray spectroscopy (EDS) (JEOL-6480LV, JEOL Ltd., Japan) analysis.

In the thin upscaled BPM-CEM stack (Figure 4.3 (B)), constant current density of 5 $mA\,cm^{-2}$ and a liquid flow rate of 68 $ml\,min^{-1}$ per compartment (i.e., t_r = 3.53 s) were applied for 30 minutes. This combination of the current density and flow rate in the upscaled stack was chosen based on the earlier results obtained from the six-compartment cell with a (single) BPM.

After each experiment, the stack was rinsed thoroughly with 1mM HCl solution followed by demineralized water to remove any fouling. Each experiment was performed at least three times.

4.3.4. PRECIPITATION COLLECTION INCL. SEEDING

Seed addition enhances the kinetics of carbonate crystallization [28, 38]. In the six-compartment cell with a (single) BPM, when the pH in the acid compartment was stable, ca. 200 mL sample was taken directly from the output of the base compartment. This content was divided over three bottles (50 mL each): where in one, 0.5 g solid calcite seeds (AquaMinerals B.V., particle size of 0.2 - 0.4 μm) where added (resulting in 10 $g\,L^{-1}$), one where 0.5 g solid lime pellets (AquaMinerals B.V., particle size ≤ 3 mm) where added (i.e., to get 10 $g\,L^{-1}$) and the last one with no seeding. The bottles were closed to avoid contact with the atmospheric CO_2 and left undisturbed for at least 72 hours. In the upscaled cell, the total produced base-volume was gathered in storage tank, left undisturbed for ≥ 72 h.

4.3.5. MEMBRANE FOULING AND CRYSTAL ANALYSIS

In the six-compartment cell with a (single) BPM, after applying current densities of 10 and 40 $mA\,cm^{-2}$, the AEL surface of the BPM was analyzed by the Scanning Electron Microscopy (SEM) coupled with energy dispersive X-ray spectroscopy (EDS) (JEOL-6480LV, JEOL Ltd., Japan) to determine the fouling of the membrane. After disassembling the cell, the BPM was washed with demineralized water and left at ambient temperature to be dried before SEM/EDS analysis. The samples were coated with gold using a JEOL JFC-1200 Fine coater at 10 Pa for 30 s.

The solid precipitate within the "alkaline gathering tanks" (obtained after carefully decanting the liquid and air-dried) were scraped on a microscope slide glass for Raman spectroscopy analysis. Raman spectroscopy (Horiba Jobin-Yvon LabRAM HR) was done using 532.13 nm laser within 10-100 s time spots.

4.3.6. DATA ANALYSIS

DIC, CALCIUM AND MAGNESIUM REMOVAL RATES

The DIC concentration of the feed and alkaline streams were determined via titration with 0.1 M HCl (see Figure S1 and Table S8). However, this method is sensitive to atmospheric CO_2, meaning that the DIC concentration can be slightly over- or underestimated depending on the sample pH. Therefore, in addition to the DIC removal, Ca^{2+} and Mg^{2+} ions removal was also measured, using Inductively Coupled Plasma (ICP). For both analyses, the liquid samples were first filtered through a MF-Millipore^{TM} Filter with a pore size of 0.22 μm to remove any formed minerals.

ENERGY CONSUMPTION

The total electrical energy consumption E kJ mol^{-1}DIC required for the *in-situ* mineralization is:

$$E = \frac{\int_{t_0}^{t_{end}} UIdt}{m_{DIC}} \approx \frac{UI\Delta t}{q\Delta t R_{DIC}[DIC_i]} \tag{4.5}$$

Where I is the applied current density (A), U the total cell voltage (V), and Δt = t_{end} - t_0 the experiment duration (s). m_{DIC} is the extracted carbonate mineral (mol) that is calculated using q the total liquid flow rate considering all base compartments L s^{-1}, $[DIC_i]$ the initial dissolved inorganic carbon concentration in the feed (mol L^{-1}), and R_{DIC} the DIC removal (%) measured via acid titration with $R_{DIC}[\%] = \frac{[DIC_i]-[DIC_e]}{[DIC_i]}$), and $[DIC_e]$ (mol L^{-1}) the remaining end DIC concentration after precipitation (> 72 h). The simplification of the integration in left-hand side of Equation 4.5 is possible when a constant voltage, current, flow rate and R_{DIC} is assumed throughout the whole duration of the experiment.

4.4. RESULTS AND DISCUSSION

4.4.1. EFFECT OF THE CURRENT DENSITY AND PH

To validate the pH range that is most effective for carbonate precipitate removal, we demonstrate the effect of applied current density, while keeping the residence time (t_r) constant, using the six compartment cell with a single BPM. Figure 4.2 compares the experimental and simulated values. The simulation assumptions and procedures are shown in the supporting information (Table S9).

The experimentally obtained acid-pH agrees well with the simulated-pH line without CO_2(g) extraction (Figure 4.4 (A)-red circles and red lines), supporting our assumption of a high Coulombic efficiency of the bipolar membrane at the tested current densities; when using Equation 4.4, if the Coulombic efficiency is low, the amount of the produced acid will be less than expected, which is not the case here. Similarly, the experimental feed-pH is constant at pH 7.9 and in close agreement with simulations which was pH 7.7 - 8.1 (Figure 4.4 (A)-grey line). The acid data point at 20 mA cm^{-2} also demonstrates that the experiments are better predicted by the solid line (representing no *in-situ* CO_2(g) extraction) than by the dashed curve (simulation where CO_2(g) is extracted during the BPMED process) in Figure 4.4 (A). This corresponds to our approach in this work, where no attempt for gaseous CO_2(g) extraction is taken (and no spontaneous CO_2 gas bubbles are extracted *in-situ*).

The experimental base-pH are 1.2 - 1.4 pH-units lower than that simulated without considering any DIC-extraction (Figure 4.4 (A)-blue bullets vs. lines). However, for the base compartment, the simulation when including *in-situ* precipitation (dotted blue lines in Figure 4.4 (A)) is close to the experimental value. This can also be expected from theory: while the acid compartment does not exceed the solubility of CO_2 in seawater surface (33 mM at 3.5 % salinity, 1 atm and 20 ^{o}C) [39], the solubility of carbonate CO_3^{2-} is far exceeded (i.e., more than 47 times of 2.15 mM) in the base stream, which causes *in-situ* mineral formation. The carbonate solubility in seawater is ca. 0.0451 mM, calculated assuming seawater-$K_{sp}^{CaCO3} = 4.39 \times 10^{-7}$ (mol per kg SW)^2 at salinity of 3.5 % at 1 atm, 25 ^{o}C [40], and Ca^{2+} concentration based on Table 4.1.

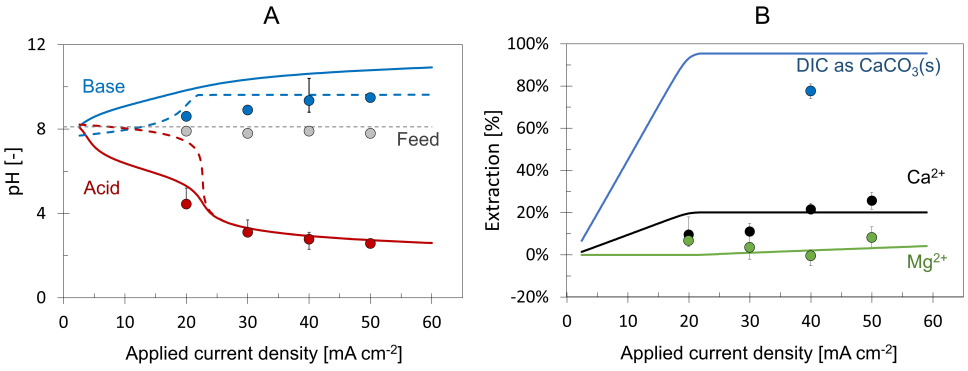

Figure 4.4: Comparison of the simulated (lines) and experimentally obtained values (bullets) at each applied current density in the six-compartment cell with a (single) BPM, averaged over the experiment duration and (four) repetitions (for simulation data see Table S9). In (A) Dashed lines show the (simulated) pH-change after DIC-extraction as CO_2(g) (red) and $CaCO_3$(s) (blue). Error bars show the margin between the minimum and maximum experimental data points to include all data. The error bars that are not shown are smaller than the data points. For all cases, flow rate q = 120 ml min^{-1}, resulting in a cell residence time and flow velocity of t_r = 11s and v = 1 cm s^{-1} is assumed (which is calculated excluding the effect of spacer-netting porosity ε = 0.48 in t_r and v, see Chapter 5). (A) outflow-pH and feed-pH from the cell vs. the applied current density, (B) species removal at each applied current density where the single measured DIC-removal point is shown (blue bullet) as an indication.

Even after correcting for the effect of precipitation on the base-pH, a small difference of ≤ 0.5 pH-unit exists between the measured and calculated values at current densities ≤ 30 mA cm^{-2}. The origin of this remaining 0.5 pH-unit difference can be because of

the local spots of high carbonate or OH^- concentrations within the cell. Although in the simulations a uniform pH and ions distribution are assumed, the OH^- ion concentration is higher next to the BPM surface than the bulk. As a result of this locally high concentration spots, if the produced OH^- ions partly precipitate at $Mg(OH)_2$, the end-pH lowers. Subsequently, such precipitation increases the resulted Mg^{2+} ions removal while decreasing the Ca^{2+} removal compared to the simulations. This is also confirmed from the ion removal analysis (Figure 4.4 (B)), which shows more Mg^{2+} and less Ca^{2+} removal (in the experiments) compared to simulations at $i \leq 30\ mA\,cm^{-2}$. Improving the mixing inside of the cell, using e.g., mesh spacers enhance the uniformity of ionic distributions.

Theoretically, for $i \geq 20\ mA\,cm^{-2}$, ≥ 94 % of the DIC can be extracted as $CaCO_3$ (Figure 4.4 (B) and Table S9). Similarly, if we calculate the DIC extraction from the experimentally measured Ca^{2+} ion removal at $i = 40\ mA\,cm^{-2}$ (i.e., removal of 2.079 mM Ca^{2+} ion), assuming all Ca^{2+} is removed as $CaCO_3$(s), ca. 97 % of the DIC is extracted. However, at $i = 40\ mA\,cm^{-2}$, the extracted DIC is measured to be between 74 - 81 % through HCl titration (Figure 4.4 (B)-blue circle). Such deviation is partly due to the inaccuracy of the titration method to determine the DIC concentration (hence, we deem estimation via Ca^{2+} and Mg^{2+} removal by ICP more accurate than direct DIC removal measurement through HCL titration), and partly due to the side-precipitations taking place due to a non-uniform ionic distribution, as explained above.

4.4.2. TOWARDS INDUSTRIAL SCALES: DECREASING THE ENERGY CONSUMPTION

To decrease the process electrical energy consumption, the total cell voltage must be reduced while the $CaCO_3$ production is unchanged/ improved. Furthermore, for mineralization, the optimum base-pH must be facilitated by accurate controlling the applied current density and flow rate (Equation 4.4). Prior to the upscaling, the theoretical relation between $CaCO_3$ production rate (i.e., extracted $CaCO_3$ in $kg\ h^{-1}\ m^{-2}$ which is normalized for the membrane area) and applied current density was studied for the BPM-CEM cell to find the optimum combination that provide the lowest electrical energy consumption (Figure 4.5). The calculation model is given in the supporting information (4.6, see Equation S4-S7). For estimating the thermodynamic energy required in BPMED based capture, the voltage of the bipolar membrane (V_{BPM}) is calculated via Nernstian voltage of $0.059\Delta pH$ [41].

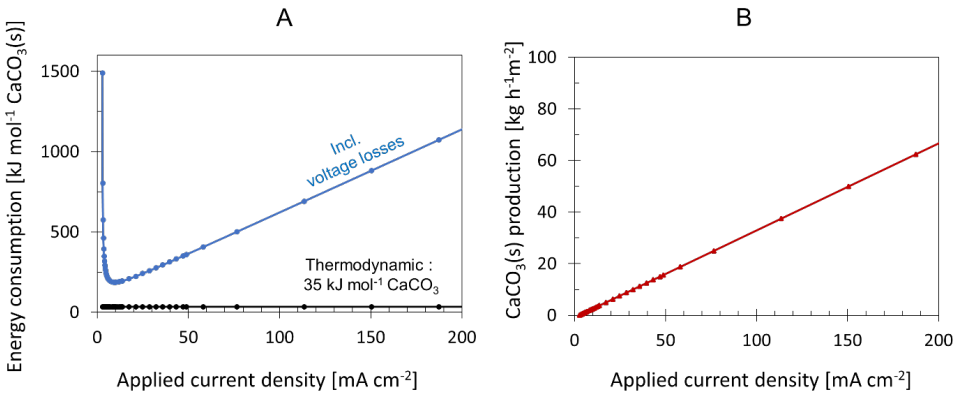

Figure 4.5: Relation between the applied current density vs. (A) electrical energy consumption and (B) calcium carbonate normalized production rate. Simulations are done assuming a 10×10 cm^2 BPM-CEM cell containing 10 cell pairs and base-pH 10.0 (i.e., produced OH^- ions of 0.0023 M, see Table S1). The value of the thermodynamic limit is obtained using the Nernstian membrane voltage for required ΔpH = 5.5; see Equation S4.

Figure 4.5 (B) shows that at a fixed base pH 10.0, the $CaCO_3$ production increases with the current density. Given the limited DIC, a maximum of ca. 2.078 mM $CaCO_3$ (= 208 mg per L) is extractable from seawater. Therefore, the increase in the production is merely the result of a higher flow rate (i.e., lower cell residence time) at higher current densities; to maintain a constant base-pH (in this case, pH 10.0), a linear relation between the current density and flow rate exists (Equation 4.4). However, the electrical energy consumption also increases upon increasing the current density due to ohmic losses of ΔV = IR (Figure 4.5 (A)-blue line).

The thermodynamic electrical energy consumption for $CaCO_3$ production is 35 kJ mol^{-1} $CaCO_3$ (i.e., 0.097 kWh kg^{-1} $CaCO_3$, Equation S4), Figure 4.5 (A). Since an *in-situ* process enables CO_2 capture and recovery in a mild pH-swing, it can perform theoretically at the Nernstian voltage of $V_{BPM} = 0.059 \times (10.0 - 4.5) \sim 0.3245$ V, while 0.83 V is thermodynamically required for extreme ΔpH = 14 in *ex-situ* cases, decreasing the required energy for the pH-swing by a factor of almost three. Although the membrane voltage is in reality higher than its theoretical voltage for mild pH gradients, the reversible BPM voltages are still < 0.83 V for an *in-situ* process, even at 25 mA cm^{-2} [32]. Moreover, as opposed to the *ex-situ* process, in an *in-situ* capture, no highly concentrated chemicals (i.e., NaCl, NaOH) are needed in the process.

Unfortunately, currently available BPM are not developed to take full advantage of

a mild-pH environment yet and, therefore, dissociate water at $V_{BPM} \geq 0.6$ V in practice for current densities > 5 mA cm^{-2}. In addition, the charged membranes and electrolyte compartments suffer from significant ohmic losses, which increase with the current density (i.e., $\Delta V = IR$). The practical energy consumption of the carbonate mineralization via *in-situ* pH-swing, including these voltage losses, is more than 5x higher than the thermodynamic value. Aiming for the lowest energy consumption, ohmic losses should be limited, marking the optimum current density for the BPM-CEM cell somewhere between i = 5 - 10 mAcm^{-2} in our system (Figure 4.5 (A)).

For reducing the process energy consumption, the cell design and membrane configuration are also crucial. Figure 4.6 shows the voltage and energy required for each component within the electrochemical cell, obtained from our experiments. To allow comparison between the cases, the measured base-pH is kept identical (9.6 - 9.8) for all four cases. The energy consumption normalized to the produced moles of $CaCO_3$ is shown in Figure 4.6 (B).

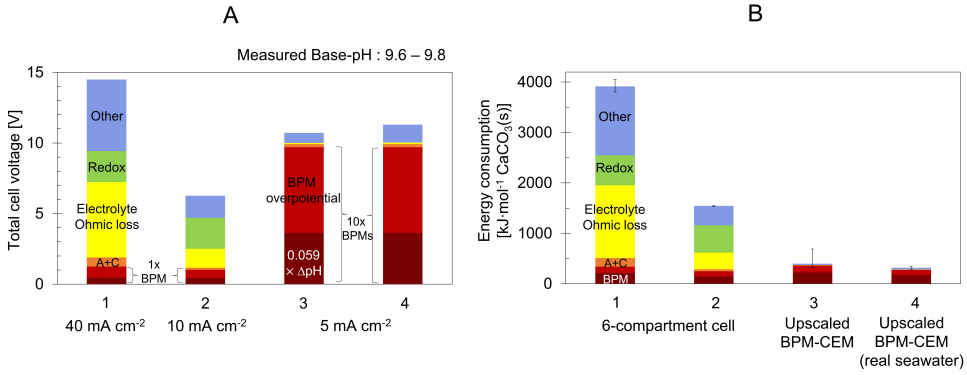

Figure 4.6: A) Total cell voltage and its components, from bottom to top : BPM thermodynamic voltage (0.059ΔpH, dark red), BPM-overpotential (red), monopolar membrane (AEM and CEM) ohmic loss (orange : A+C), electrolyte ohmic loss (yellow), the redox reactions (green), and other losses (blue) in the six-compartment cell with a single BPM. Case 1 and 2 both include 1 BPM while the upscaled BPM-CEM cell (case 3, 4) include 10 BPM's. B) The energy consumption and its components (from bottom to top same as A). In all the cases, the amount of charge added per volume via the BPM is ~ 220-413 CL^{-1} . Case 4 is tested via real seawater (Table S7), while other cases are done using synthetic seawater (Table 4.1). Error bars in B mark the minimum and maximum values among repetitions.

Ideally, all electricity input is used to dissociate water into H^+ and OH^- production

at the BPM (creating the ΔpH over the BPM) at a thermodynamic reversible potential (i.e., 0.059ΔpH), while the irreversible losses are nullified. This implies that the dark red segment (showing the thermodynamic BPM-voltage) in Figure 4.6 should be the only/highest portion of the cell voltage. Although the 10-cell BPMED stacks are more effectively using the cell voltage for water dissociation (i.e., relatively large dark red segment), irreversible losses still occur. Most notably, the BPM overpotential (light red contribution) exceeds the thermodynamic BPM voltage. This BPM overpotential is the difference between the measured BPM-voltage and the thermodynamic-BPM voltage and reveals the overpotential including ohmic losses and WDR overpotential of the BPM. "Other" involved losses (blue) are defined here as the difference between the measured and theoretically expected cell voltage. These losses include e.g., H_2/O_2 gas bubbles /covering the electrodes (for case 1, 2), possible CO_2(g) bubbles/ trapping in the acidic compartment of the BPMED [26], membrane/spacer fouling, and mesh spacers reducing the active membranes area (for case 3, 4).

In the six-compartment cell with a (single) BPM, reducing the current density from 40 to 10 mA cm^{-2} (case 1 to 2, charge added per volume 413 to 330 C L^{-1}), already decreases the cell voltage contributions of the electrolyte compartments and the "other" portion. However, to keep the base-pH identical, a four times lower flow rate was used in case 2 compared to case 1. While a lower flow rate increases the cell residence time (t_r), allowing more time for *in-situ* precipitation, it is less effective in "cleaning away" the formed minerals within the cell compartments, increasing the risks of fouling. Furthermore, the $CaCO_3$ production rate is lower when using a lower flow rate (Figure 4.7 (C), case 2). Case 3 and 4 (Figure 4.6 (B)) achieve a lower energy consumption by decreasing the compartment thickness (25x), increasing the number of cells, changing the redox couple from water to $FeCl_2$/ $FeCl_3$, and eliminating the AEM from the cell design with only BPM-CEM cell pairs remaining.

The achieved energy consumption of 318 ± 29 kJ mol^{-1} $CaCO_3$ (i.e., ca. 0.88 kWh kg^{-1} $CaCO_3$) for the real seawater case in this work is the lowest achieved using an electrochemical cell for carbonate removal, ever [7]; in other works, the lowest electrical energy required for (*ex-situ*) BPM-based oceanic calcium carbonate removal is calculated to be ≥ 640 kJ mol^{-1} $CaCO_3$ [5], [11], with experimental reported values of 1080-2880 kJ mol^{-1} $CaCO_3$ [17] and 1009-2162 kJ mol^{-1} $CaCO_3$ [42]. On a broader context, the energy consumption range for electrochemical captures is demonstrated at 56 - 6940 kJ_e mol^{-1} CO_2 [7]. This is while, assuming an average worldwide carbon emission for electricity of ca. 0.46 kg CO_2-eq kWh_e^{-1} (= 0.0029 mol CO_2-eq kJ_e^{-1}), the required energy for capturing must not exceed 344 kJ_e mol^{-1} CO_2 or electricity from renewable sources (i.e., zero electricity-emission sources) must be used.

However, the electric energy consumption of electrochemical CO_2 capture is still high, especially compared to the fossil fuel combustion energy which is 300- 700 kJ mol^{-1} of emitted-CO_2(g) [7]. Considering the thermodynamic electrical energy consumption (35 kJmol^{-1} $CaCO_3$), there is room left for improvements. In BPMED-capture (in the lab scale), approximately 90 % of the electrical energy is used in the BPM (Figure 4.6-case 3, assuming a WDR-voltage of 0.9 V and BPM-area resistivity of 8 Ω cm^2). Decreasing the WDR-voltage to its thermodynamic value of 0.059ΔpH, decreases the energy consumption by a factor of three. Utilizing a properly catalyzed BPM (i.e., fast WDR kinetics), with

highly perm selective ion-exchange layers to exclude co-ions, and with optimum thickness of the layers and the catalyst is therefore most effective way to minimize energy losses [33]. Furthermore, increasing the DIC-removal (from measured 65 % to 95 %) can decrease the total energy consumption by 59 %, but might come at the expense of lower Coulombic efficiency for $CaCO_3$ production.

The extraction rate of the dissolved inorganic carbon (DIC), calcium (Ca^{2+}), and magnesium (Mg^{2+}) ions, and the normalized calcium carbonate production for the four tested cases are shown in Figure 4.7. In all cases, the product of the seawater alkalinization with base- pH between pH 9.6 - 10 is mainly aragonite ($CaCO_3$), as expected [43] and confirmed with Raman spectroscopy (Figure S2). The simulations data for case 1-4 are shown in Table S10-S11.

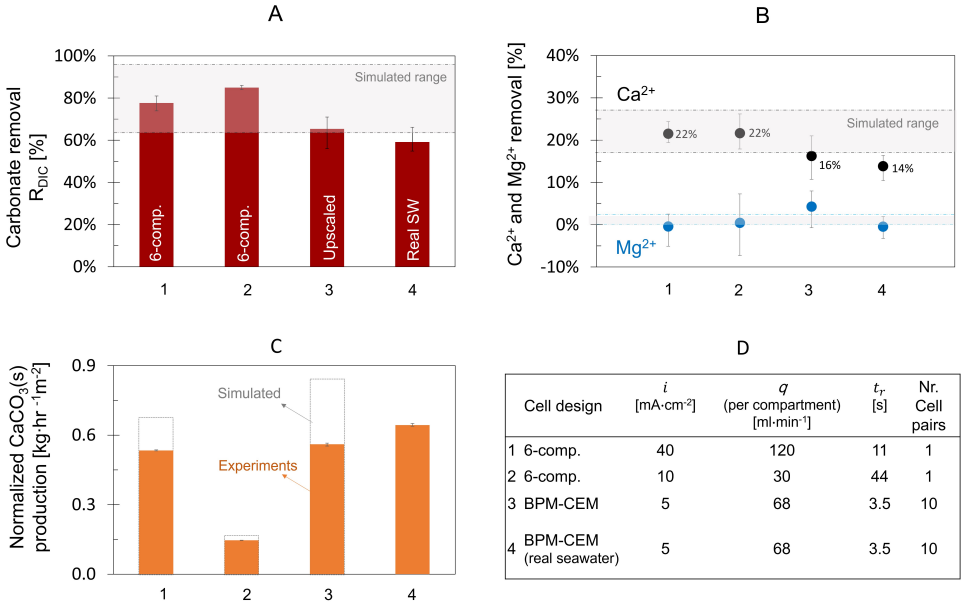

Figure 4.7: Comparison of the six-compartment cell with a (single) BPM (case 1 and 2) and upscaled BPM-CEM cell (case 3 and 4) performance with regards to (A) carbonate (i.e., DIC) removal, (B) Ca^{2+} and Mg^{2+} ions removal, and (C) normalized calcium carbonate production. Process properties are shown in D, in which q is the flow rate in each compartment. Error bars show the margin between the minimum and maximum data points. For simplicity, all simulations are based on the synthetic seawater compositions (Table 4.1) and not the real seawater (i.e., case 4). The simulation data is shown in Table S10-S11.

The measured carbonate removal (R_{DIC}) for all cases is within the expected range of 63 - 97 % (grey box in Figure 4.7 (A)), confirming our model and its underlying assumptions. The lower margin of 63 % corresponds to simulations assuming an open system, where the alkaline solutions keep absorbing CO_2(g) from the atmosphere until it reaches equilibrium. The 97 % margin is for a fully closed system. In an open system, the end-pH

after precipitation and the total DIC-extraction are lower compared to a closed system. In the experiments, the electrochemical cell and crystallization tanks are kept closed to avoid the contact with the atmospheric CO_2(g). However, such contact during sampling and titration (to determine DIC-concentration) cannot be avoided, making the system somewhere between fully closed and fully open.

In general, it was expected that adding calcite/ lime seeds in the gathering tanks increase the carbonate removal slightly, but although the seed may have sped up the precipitation process, the chosen settling time (≥ 72 h) was apparently long enough to reach equilibrium in all cases in this work. The upper margins of the error-bars in Figure 4.7 (A) show the R_{DIC} values obtained using seeding, which is slightly higher compared to without seeding. In Figure 4.7 (A), case 2 has the highest carbonate removal, with values slightly higher than case 1, but the Ca^{2+} and Mg^{2+} removal for both cases are identical (Figure 4.7 (B), 1 and 2). Therefore, as both cases produced mainly Aragonite (confirmed with Raman spectroscopy), the slight difference in R_{DIC} between case 1 and 2 is probably resulted from imprecision of the titration method to quantify carbonate removal.

For the real seawater (case 4), R_{DIC} is the lowest, probably due to the difference in ion composition and concentration between real and synthetic seawater (i.e., initial DIC concentration in seawater was 0.6 mM higher than that of the synthetic seawater). Moreover, in the real seawater, presence of elements such as Boron, Silicon, Sulphur, Nitrate (Table S7), and anti-scaling effects of organic substances can also influence the co-precipitation. This also justifies why Ca^{2+} removal is the lowest for case 4 in Figure 4.7 (B).

The Ca^{2+} removal for case 3 (i.e., BPM-CEM cell) is ca. 16 %, which is lower than case 1 and 2 (Figure 4.7 (B)), but all values are still close to the simulated 20 % (for closed systems) and in the range of 17 - 27 % (for open systems) as shown in Table S10-S11. Furthermore, it seems that the lower Ca^{2+} removal in case 3 is compensated with a higher removal of Mg^{2+} for this case (Figure 4.7 (B)-blue marks). This is while the simulated Mg^{2+} removal for case 1 to 3 shows a decreasing trend (from 2 % to 0 % since the simulated pH decreases). Since the observed discrepancy between the cases is not expected in the simulations, it must originate from the experimental condition including the different cell design and flow pattern inside of the compartments in case 3; the latter creating non-uniform flow and thus non-uniform local pH. As for the cell design, in the six-compartment cell with a (single) BPM, only Na^+ ions pass through the CEM into the base-compartment, carrying the charge (Figure 4.3 (A)-from comp.2 to 3). However, in the up-scaled cell containing BPM-CEM cell pairs (case 3), considering the concentration and mobility ratio of all five present cations, only 83 % of the current is carried via Na^+ ions transfer, while the contribution of H^+, K^+, Mg^{2+}, and Ca^{2+} are 2.5 %, 2.5 %, 10 % and 2 %, respectively, based on the Nernst-Planck equation (Table S12). We hypothesize that this additional Mg^{2+} ions present in the base compartment hinders $CaCO_3$ mineralization (i.e., decreasing both Ca^{2+} and DIC removal), promoting $Mg(OH)_2$ precipitation instead. Even though this additional Mg^{2+} concentration is only 0.2 mM in the bulk, it can still promote $Mg(OH)_2$ mineralization near the membrane surface due to the concentration polarization on the CEM surface. The influence of the magnesium ion is well documented and is known to reduce calcite growth rates [44–47].

Comparing Figure 4.7 (A) and 4.7 (B), if we assume all Ca^{2+} ions are extracted as

$CaCO_3$, a Ca^{2+}-removal of 20 % translates into 97 % DIC-extraction, which is higher than what was measured. This proves that part of Ca^{2+} is removed as other solids e.g., as hydroxides (e.g., at BPM local-pH ≥ 12 [31]), even though this was not seen in Raman spectroscopy analysis (Figure S2). Furthermore, the accuracy of the titration method can play a role in justifying this discrepancy.

Despite the slightly lower DIC (i.e., carbonate) and Ca^{2+} ion removal in case 3 and 4 compared to the six-compartment cell with a (single) BPM, the energy consumption per removed $CaCO_3$ is still lower for the upscaled cell (Figure 4.6 (B)). In case 1 and 2, the energy consumption is high due to the voltage losses (i.e., thick compartments + water redox) and the fact that only one base-compartment exists (with ratio of base-compartment to rest-compartments 1:6), decreasing the $CaCO_3$ production rate significantly (Figure 4.7 (C)). Between case 3 and 4, real seawater had a smaller conductivity compared to the synthetic seawater (i.e., 35 $mScm^{-1}$ vs. 50 $mScm^{-1}$) but higher initial DIC (i.e., 2.7 mM vs. 2.3 mM). Therefore, due to this higher initial DIC, despite of the lower relative DIC-removal (Figure 4.7 (A)), the absolute $CaCO_3$ production is still the highest for the real seawater case (Figure 4.7 (C)), making it also the most energy efficient case (Figure 4.6 (B)).

4.4.3. FOULING

While our *in-situ* mineralization process shows a clear benefit for the energy consumption compared to the *ex-situ* bipolar membrane electrodialysis (BPMED) (318 ± 29 kJ mol^{-1} $CaCO_3$, which is less than half of the lowest value in literature), the feasibility of the *in-situ* process is strongly affected by the cell design and fouling. The fouling at the membrane and spacers: (1) increases the pressure drop along the cell, increasing the pumping energy and causing non-uniform flow, and (2) increases the total cell voltage and hence the electrical energy consumption. Furthermore, the membrane lifetime and $CaCO_3$ harvesting rate are negatively affected by fouling. To determine the membrane fouling, SEM and EDS analysis have been done for the six-compartment cell with a (single) BPM by opening the cell (right) after finishing the 15 min constant current (40 $mA\,cm^{-2}$) experiments (Figure S3, S4) and after the 2 h experiment (Figure 4.8).

After opening the cell right after the 15 min constant current, only few minerals were seen on the membrane (Figure S4), which is logical considering the time scale of 10^3 s required for establishing the $CaCO_3$ precipitation equilibrium [18, 26]. We observed that the amount of deposition is increased with current and the time of experiment. After 120 min experiments, the surface of the BPM is decorated with a layer of minerals (Figure 4.8), even though the fouling does not increase the total cell voltage. The SEM analysis emphasizes the importance of fouling removal strategies for *in-situ* mineralization.

Furthermore, when a low current density, in combination with a low flow rate, is applied for the 120 min constant current experiments, although the output pH remained the same, there is a clear difference in the shape of the minerals (Figure 4.8) D-F vs. A-C). At 10 $mA\,cm^{-2}$, the minerals have a more defined "broccoli" shape that is the defined shape of Aragonite which is in accordance with Raman spectroscopy findings, while at 40 $mA\,cm^{-2}$ the membrane surface is covered with polydisperse, polymorph particles. However, the effect of the cell residence time (i.e., flow rate) in the *in-situ* bipolar membrane electrodialysis cell needs to be studied in more detail to draw a solid conclusion

on the precipitation kinetics and type of the scaling. In addition to adjusting the flow rate to wash out the fouling, fouling removal strategies such as, gas sparging and acid wash can be employed in future works.

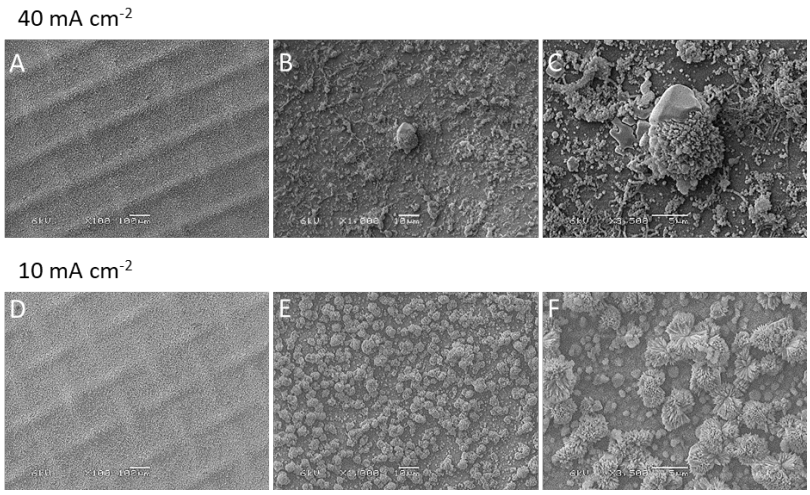

Figure 4.8: SEM images of the AEL of the BPM opened directly after applying the current for 120 minutes. (A), (B) and (C) concern the AEL of the BPM after applying a current density of 40 mA cm^{-2} and a flowrate of 120 ml min^{-1} (v=1 cm s^{-1}), resulting in a measured base-pH of ~ pH 9.8. (D), (E) and (F) concern the AEL of the BPM after applying a current density of 10 mA cm^{-2} and a flowrate of 30 ml min^{-1} (v= 0.25 cm s^{-1}), resulting also in a base-pH of 9.8.

4.5. CONCLUSION

Through *in-situ* mineralization enabled using bipolar membranes, Aragonite (polymorph of $CaCO_3$) was extracted from (real and synthetic) seawater as an ocean carbon removal strategy. By controlling the current density and cell residence time, more than 60 % of the dissolved inorganic carbon (DIC) and ≥ 16 % of the Ca^{2+} ion is extracted, without the need for any additional chemicals. An energy consumption of 318 ± 29 kJmol^{-1} $CaCO_3$ (i.e., ca. 0.88 kWh kg^{-1} $CaCO_3$) is obtained for DIC-capture from real seawater with $CaCO_3$ production rate of 0.64 kg$CaCO_3$(s) h^{-1}m^{-2}. Theoretically, at a mild pH-swing (e.g., base pH 10.0 and acid pH 4.5, thus ΔpH = 5.5) the thermodynamic energy required to capture $CaCO_3$ though *in-situ* mineralization is ~ 35 kJmol^{-1} $CaCO_3$ which is 10 - 12 % of that experimentally achieved. However, the irreversible BPM-overpotential is responsible for > 55 % of the required electrical energy. Focusing on membrane engineering to achieve fast WDR kinetics in the BPM, with highly perm selective ion-exchange layers to

exclude co-ions, and with optimum thickness of the layers is the most effective way to minimize energy losses. Despite the promising energy consumption, membrane fouling is a challenge that *in-situ* mineralization process faces. In the future, fouling removal strategies such as gas sparging and acid wash can be employed for interval cell cleaning.

4.6. SUPPORTING INFORMATION

4.6.1. SEAWATER CAPACITY FOR DIC-REMOVAL

Theoretically, (using ionic compositions of Table 4.1) upon a pH-swing of 5.5 (e.g., acid-pH 4.5 and base-pH 10.0), more than 97 % of DIC can be extracted in the form of ~ 2.13 mM CO_2(g) or ~ 2.078 mM $CaCO_3$ (s) per 1 L of seawater, respectively. Thermodynamically, a positive saturation index enables the precipitation [27], [28]:

$$\text{Saturation index} = \log_{10}\left(\frac{IAP}{K_{sp}}\right) \tag{S1}$$

Where IAP is the ion activity product, and K_{sp} the thermodynamic equilibrium solubility product [20].

In addition to carbonates, upon seawater alkalinization, saturation indexes (SI) of several minerals become positive, marking their oversaturation and thus possible precipitation (Figure 4.1, Table S6). Our aim in this work is to remove carbonate species while avoiding hydroxide precipitation, to make sure the BPM-produced OH^- ions only are used in converting bicarbonate to carbonate ions. To carefully define the pH-window that enables carbonate precipitation, but still circumvents hydroxide minerals precipitation, the co-precipitation is simulated via the total H^+ concentration-sweep function in Visual MINTEQ 3.1 (Figure 4.1). Visual MINTEQ is a free equilibrium speciation model, which calculates the chemical equilibria in the aqueous systems at a low ionic strength ($I < 1$). From bulk thermodynamics, the least soluble, most stable crystalline phase precipitates first from a supersaturated solution [43]. However, in reality, this rule of thumb does not always apply; one of the oldest examples is the precipitation of aragonite instead of calcite in seawater; even though aragonite is less stable than calcite and has a slightly higher solubility [43]. Furthermore, kinetically, magnesite $MgCO_3$ formation is reported unlikely at temperatures < 75 °C [48–50], and artinite $Mg_2CO_3(OH)_2{\cdot}3H_2O$ is expected to form only at temperatures < 15 °C [51]. However, as the kinetics of mineral precipitation is not well understood in low-temperature conditions [48], the exact sequence of precipitation as well as the dominant mineral at each pH-window needs to be studied experimentally.

In practice, the carbonate precipitation in seawater is reported to start at pH 9.3 - 9.5 and end at pH 10.0 [52]. In another study, $CaCO_3$ is reported to precipitate upon *ex-situ* seawater alkalinization between 9.3 < base-pH < 9.6, while $Mg(OH)_2$ precipitation starts at > pH 9.6 [5].

Using the starting values according to Table 4.1, if we assume addition of 0.0023 M H^+ ions (to simulate the acid side), and reduction of 0.0023 M H^+ ions (i.e., which is the MINTEQ equivalent of OH^- ions addition to simulate the base route), and use Na^+ ion concentration to balance the charge difference in both cases, (in a closed system) a base-pH of 10 and acid-pH of 4.49 are obtained, with ionic compositions shown in Table S1. Opening the acidic stream to 420 ppm CO_2(g) and allowing the precipitation of all possible solids (using the function of specify possible solid phases), delivers a decarbonized acidic stream with pH = 5.583, and a base stream (kept as a closed system) with pH = 9.618 with ionic concentrations shown in Table S2. Comparing the $CO_3{}^{-2}$ concentrations (which in MINTEQ shows the "total" dissolved inorganic carbon concentration, DIC) in Table S2 with that of Table 4.1, shows the *removed* DIC in the acidic and alkaline

Table S1: Simulated enabled pH-swing, upon addition of ca. 0.0023 M H^+ ions and the same amount of OH^- ions.

Component	**Total dissolved,** $molL^{-1}$	
	Base stream	**Acid stream**
	pH = 10	**pH = 4.49**
Ca^{2+}	1.02E-02	1.02E-02
Cl^-	5.36E-01	5.36E-01
CO_3^{2-}	2.15E-03	2.15E-03
H^+	-3.00E-04	4.30E-03
K^+	9.70E-03	9.70E-03
Mg^{2+}	5.21E-02	5.21E-02
Na^+	4.62E-01	4.57E-01
SO_4^{2-}	2.75E-02	2.75E-02

Table S2: The pH-change after decarbonization.

Component	**Total dissolved,** $molL^{-1}$	
	Base stream	**Acid stream**
	pH = 9.618	**pH = 5.583**
Ca^{2+}	8.12E-03	1.02E-02
Cl^-	5.36E-01	5.36E-01
CO_3^{2-}	7.19E-05	1.80E-05
H^+	-2.21E-04	3.61E-05
K^+	9.70E-03	9.70E-03
Mg^{2+}	5.21E-02	5.21E-02
Na^+	4.62E-01	4.57E-01
SO_4^{2-}	2.75E-02	2.75E-02

Table S3: Ionic composition of the (synthetic) seawater after decarbonisation of both the acidic and basic streams and mixing them.

Component	**Total dissolved,** $\mathrm{mol\,L^{-1}}$
Ca^{2+}	9.16E-03
Cl^{-}	5.36E-01
CO_3^{2-}	1.94E-04
H^{+}	2.05E-04
K^{+}	9.70E-03
Mg^{2+}	5.21E-02
Na^{+}	4.59E-01
SO_4^{2-}	2.75E-02

Table S4: The salt composition of the two used feed tanks.

Tank 1	**g/mol**	**g/L**	**mol/L**	**Tank 2**	**g/mol**	**g/L**	**mol/L**
NaCl	58.44	47.00	0.804244	$CaCl_2 \cdot 2H_2O$	147.02	3.00	0.0204
KCl	74.55	1.45	0.01945	$MgCl_2 \cdot 6H_2O$	203.30	21.20	0.1043
Na_2SO_4	142.04	7.80	0.054914				
$NaHCO_3$	84.01	0.385	0.004583				

stream. After mixing the two decarbonized streams (averaging for each ion in Table S2), a stream with pH = 9.28 will be obtained. Opening this stream to 420 ppm atmospheric CO_2(g) creates a pH = 7.188 (which is lower than the initial 8.104) with concentrations shown in Table S3. Comparing the $CO_3{}^{-2}$-concentration in Table S3 with the initial [DIC] = 2.15 mM, shows that in the total process ca. 91 % DIC (and 10 % Ca^{2+}) is extractable. Note that, initially, from each stream ≥ 97 % DIC is extractable, but after mixing, some CO_2(g) will be sucked into the solution from the atmosphere, decreasing the net DIC-removal, and lowering the mixture pH to 7.188.

4.6.2. SEAWATER COMPOSITION USED IN VISUAL MINTEQ SIMULATIONS

To achieve the values shown in Table 4.1 that we used as synthetic seawater, first, two feed tanks are assumed as shown in Table S4. The salt concentrations in each tank are double of the seawater, so that after combination, the correct concentrations for the feed are achieved upon a dilution (i.e., dilution factor: 2). In the experiments, the pH of tank 1 and tank 2 (after allowing equilibration with the atmosphere overnight) were measured to be 8.1-8.2 and 6-6.05, respectively. In Visual MINTEQ, these pH for individual tanks were reached by tuning the partial pressure of CO_2(g), manually. The pH and ionic compositions of the closed and open systems are demonstrated in Table S5. Subsequently, the average of the two equilibrated tanks are taken (under a closed system), providing Table 4.1 that is used as the input for all the simulations. Note that, in Visual MINTEQ, both options of "mass balance" and "mass and charge balance" must provide the same results, if the correct concentrations of anions and cations are used. In the case that a rounded concentration value is used (e.g., [Ca^{2+}] of 2.04E-02 instead of 2.04050E-02), the result will differ as MINTEQ will automatically add to [H^{+}] concentration to make

Table S5: The ionic composition of each tank in a closed and open system (assuming CO2(g) partial pressure of 420 ppm).

Tank 1		**Tank 2**	
Component	Total dissolved in mol L^{-1}	Component	Total dissolved in mol L^{-1}
Cl^-	8.2369E-01	Ca_2^+	2.04050E-02
CO_3^{2-}	4.2325E-03	Cl^-	2.49370E-01
H^+	3.8829E-03	CO_3^{2-}	2.45280E-06
K^+	1.9450E-02	H^+	4.90550E-06
Na^+	9.1865E-01	Mg_2^+	1.04280E-01
SO_4^{2-}	5.4914E-02		

Table S6: The solubility product of minerals shown in Figure 4.1, from high to low values.

Mineral	K_{sp}
$Mg_2(OH)_3Cl \cdot 4H_2O$(s)	1.0E+26
Brucite	1.3E+17
Artinite	4.0E+09
$CaCO_3 \cdot H_2O$(s)	7.2E-08
Magnesite ($MgCO_3$)	3.5E-08
Vaterite ($CaCO_3$)	1.2E-08
Aragonite ($CaCO_3$)	4.6E-09
Calcite ($CaCO_3$)	3.3E-09
Hydromagnesite	1.7E-09
Dolomite (disordered)	2.9E-17
Dolomite (ordered)	8.1E-18
Huntite	1.1E-30

up for the total charge difference. To ensure accuracy, either the full numbers should be inserted or the option of “mass balance" must be used. Table S6 shows the (simulated) solubility product of thermodynamically possible minerals in synthetic seawater upon alkalinization.

4.6.3. WADDEN SEA IONIC COMPOSITION AND INITIAL DIC CONCENTRATION

Table S7 summarizes the ionic composition and concentration of the real seawater used, which is slightly different than the synthetic seawater. The dissolved inorganic carbon (DIC) concentration was calculated via Equation S2, using the titration values in Table S8. According to Table S8, between pH 7.7 and 6.1, about (680 - 20 =) 660 μL HCl is added.

Table S7: Wadden Sea measured ionic and dissolved inorganic carbon (DIC) concentration.

Input seawater	**concentration,** $\mathrm{mol\,L^{-1}}$
Calcium	0.0077
Potassium	0.0095
Magnesium	0.0349
Sodium	0.3184
Boron	0.0010
Silicon	0.0009
Chloride	0.3815
Nitrate	0.0010
Sulphate	0.0198
DIC	0.0026

4.6.4. ACIDIC TITRATION FOR DETERMINING DISSOLVED INORGANIC CARBON (DIC) CONCENTRATION

The DIC concentration of 50 mL (synthetic) seawater sample was determined based on open titration with 0.1 M HCl. The pK_a and equivalence point of the solution were first determined with use of Visual MINTEQ simulations; At 25°C, the pK_a of synthetic seawater was 6.1 and 9.3. The equivalence point is 7.7. Between the equivalence point (pH = 7.7) and the pK_a (pH = 6.1), half of the DIC present is converted from bicarbonate ion (HCO_3^-) into dissolved CO_2/ carbonic acid. Therefore, through titration with HCl between pH 7.7 and pH 6.1, the concentration of DIC can be approximated according to:

$$[DIC] = \frac{2V_{acid}.[acid]}{V_{sample}} \tag{S2}$$

In which [DIC] is the approximate concentration of DIC ($\mathrm{mol\,L^{-1}}$), V_{acid} the volume of acid added between pH 7.7 and pH 6.1 (in L), [acid] the concentration of the used HCl acid (in $\mathrm{mol\,L^{-1}}$), and V_{sample} the volume of the seawater sample to be titrated (in L). The following steps were taken to estimate the DIC concentration in input and output samples:

1. After > 72 hrs of settling time, 50 mL sample was filtered through 0.20 μm filter,
2. The sample pH was measured,
3. Known amounts of 0.1M HCl (in μL steps) were added to the sample, gradually,
4. Step 3 was repeated until a sample-pH < 4 is reached,
5. The acid volume addition between 7.7 and 6.1 was calculated (Figure S1),
6. DIC concentration (in mol/L) was calculated using Equation S2.

For example, the DIC concentration of synthetic seawater (Table 4.1) was determined to be ~ 2.1 mM (Figure S1). This value is in accordance with the performed MINTEQ simulations (open system, using concentrations of Table 4.1).

Table S8: pH values upon the acidic titration, used to determine DIC concentration of the input real seawater from Wadden Sea, according to Equation S2 and Figure S1.

Volume of 0.1 M HCl added in μL	Sample pH
0	7.819
100	7.267
200	7.003
300	6.647
400	6.43
500	6.317
600	6.219
700	6.075
800	5.943
900	5.834
1000	5.662
1200	5.153
1400	3.767

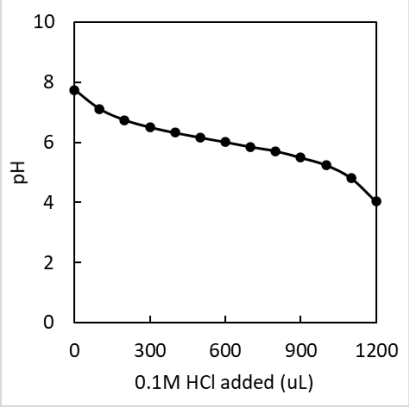

Figure S1: Titration curve of input synthetic seawater. With a pK_a of 7.7 and an equivalence point of 6.1. The DIC concentration was determined to be ~ 2.1 using Equation S2.

Table S9: MINTEQ simulation results for the base (top) and acid (bottom) routes, using the H^+ total concentration sweep function.

Base compartment								
i	q	Produced OH^- or H^+	Tot. H^+ concentration	pH		Removal [%]		
$mA\,cm^{-2}$	$ml\,min^{-1}$	mM	mM	Before precipitation	After precipitation	DIC	Ca^{2+}	Mg^{2+}
5	120	0.3	1.7	8.6	7.6	21	4	0
10	120	0.9	1.1	9.1	7.8	47	10	0
15	120	1.4	0.06	9.4	8.1	70	15	0
20	120	2	0	9.8	9.1	94	20	0
30	120	3.1	-1.1	10.3	9.6	97	20	1
40	120	4.3	-2.3	10.6	9.6	97	20	2
50	120	5.4	-3.4	10.8	9.6	97	20	3
60	120	6.6	-4.6	10.9	9.6	97	20	4
Acid compartment								
$mA\,cm^{-2}$	$ml\,min^{-1}$	mM	mM	Before degassing	After degassing	DIC removal [%]		
5	120	0.3	2.3	8.1	8.2	2		
10	120	0.9	2.9	6.6	8.1	26		
15	120	1.4	3.4	6.2	8	47		
20	120	2	4	5.7	7.7	72		
30	120	3.1	5.1	3.4	3.5	99		
40	120	4.3	6.3	3	3	99		
50	120	5.4	7.4	2.8	2.8	99		
60	120	6.6	8.6	2.6	2.6	99		

Table S10: Simulation results for Figure 4.7, using the H^+ total concentration sweep function (assuming a closes system). The first column shows the case number.

	i	q	Produced OH^- = Produced H^+	Total H^+ concentration	Base-pH		Removal [%]		
	$mA\,cm^{-2}$	$ml\,min^{-1}$	mM	mM	Before precipitation	After precipitation	DIC	Ca^{2+}	Mg^{2+}
1	40	120	4.3	2.3	10.6	9.6	97	20	2
2	10	30	3.4	1.4	10.4	9.6	97	20	1
3	5	68	2.3	0.3	10	9.6	97	20	0
4	5	68	2.3	No simulations for the real seawater case					

4.6.5. SWEEP VIA VISUAL MINTEQ

To obtain the theoretical values in Figure 4.4 and 4.7, a stepwise total H^+ concentration-sweep in a closed system (using the mass balance option) was applied. At each step, knowing the current density (i), flow rate (q), membrane area (A_m), and the limiting current density (i_{lim} = 2.5 $mA\,cm^{-2}$), first, the produced amount of OH^- ions via the BPM was calculated in $mol\,L^{1-}$. By applying the sweep, the base-pH (and acid-pH in the opposite direction) and Ca^{2+}, Mg^{2+}, and $CO_3{}^{2-}$ removal were obtainable. Such calculations assume fast mineralization kinetics and a 100 % Coulombic efficiency. The total H^+ concentrations are achieved by substituting the starting concentration (Table 4.1) with the produced OH^- concentration at each step.

Similarly, for the upscaled BPM-CEM cell, a H^+ concentration sweep can be applied which is used in Figure 4.4 and Figure 4.7. Table S10 shows the simulations assuming a closed system. In case the system be "open" to the atmospheric CO_2(g), more CO_2(g) will dissolve in the (alkaline) solution. As a result, more Ca^{2+} ion will be removed, but the DIC removal (in percentage) will decrease as the DIC concentration increase in the solution. Table S11 shows the simulation results for Figure 4.7, using the H^+ total concentration sweep function assuming an open system.

Table S11: Simulation results for Figure 4.7, using the H^+ total concentration sweep function assuming an open system.

	Base-pH if the system is open [-]	**Removal in** [%]	
	After precipitation	DIC	Ca^{2+}
Case 1	7.946	71.5	26.8
Case 2	7.934	68.5	22.54
Case 3	7.919	63.32	17.33

4.6.6. THEORETICAL ENERGY CONSUMPTION CALCULATIONS

The theoretical values are calculated assuming 100 % Coulombic efficiency, 100 % selective membranes, fast kinetics, uniform pH and ion distribution, and a limiting current density of 2.5 mA cm^{-2} for the BPM (which is reported for the used Fumatech BPM [32]).

For the simulations regarding the extraction, through the function of "specify possible solid phases" in Visual MINTEQ, precipitation of all possible minerals (shown in Figure 4.1) is allowed. However, in the software simulation eventually Brucite ($Mg(OH)_2$) and calcite ($CaCO_3$) dominates as the main precipitations (because of their high thermodynamic stability among other minerals).

THERMODYNAMIC ENERGY CONSUMPTION (FIGURE 4.5)

The thermodynamic energy to achieve the pH-swing using the BPM that enables the $CaCO_3$ extraction is calculated here. For these calculations, the limiting current density, as well as all voltage losses are excluded.

As established before, at base-pH of 10, according to Visual MINTEQ calculations, 2.078 mmol $CaCO_3$ can be extracted from 1 L seawater. On the acid side of the BPM, same amount of H^+ ions as OH^- ions are produced (0.0023 M), bringing the acid-pH down to ~ 4.49, creating a pH-swing of : ΔpH = 10 - 4.49 = 5.5 For a base-flow rate of 68 ml min^{-1}, the required current density at each BPM to create the pH-swing is (according to Equation 4.4, excluding i_{lim} is:

$$i = 0.0023\left(\frac{mol}{L}\right) \times 96485\left(\frac{C}{mol}\right) \times \left(\frac{68}{60000}\right)\left(\frac{L}{s}\right) \div 100(cm^2) = 0.002515\left(\frac{A}{cm^2}\right) \quad \text{(S3)}$$

The thermodynamic BPM-voltage for this pH-swing is

$$V_{BPM} = 0.059 \times \Delta pH = 0.059 \times 5.5 = 0.3245V$$

Assuming 10 BPM-CEM cell pair and thus a total Base-flow rate of 10 × 68 ml min^{-1} (= 0.01133 L s^{-1}), the required energy consumption according to Equation 4.5 (i.e., $\frac{IAV}{qn_{CaCO3}}$) is:

$$E = 0.001\left(\frac{0.002515\left(\frac{A}{cm^2}\right) \times 100\left(cm^2\right) \times 10 \times 0.3245\,(V)}{\left(\frac{68\times10}{60000}\right)\left(\frac{L}{s}\right) \times 0.002078(mol)}\right) \sim 35\left(\frac{kJ}{molCaCO_3}\right) \quad \text{(S4)}$$

MINIMUM PRACTICAL ENERGY CONSUMPTION

Calculations below involve the limiting current density effect (2.5 $mA\,cm^{-2}$) as well as the membrane voltage losses. First, the total cell resistivity is approximated using the measured voltage:

- Cell resistivity approximation:

Assuming the Ohm law in the BPM-CEM:

$$R = \frac{V - V_{cal}}{I} = \frac{10.72 - 8.3}{0.5} \sim 4.85\,(\Omega) \tag{S5}$$

Where R is the approximate total cell resistivity (Ω), which corresponds to 484 Ω cm^2 area resistivity. I is the applied current (A), and V is the total measured cell voltage (V). V_{cal} (V) is the *calculated* = estimated voltage for the water dissociation reaction of 10 BPM as $V_{cal} = 10 \times 0.83 = 8.3V$. The 0.83 V is assumed when the BPM creates a pH-swing of 14 (i.e., 0.059×14 ~ 0.83 V). For all calculations, a current (i.e., Coulombic) efficiency of 100 % is assumed. Assuming a limiting current density of 2.5 $mA\,cm^{-2}$ and a current (= Coulombic) efficiency of 100 %, the required current for a flow rate of 68 $ml\,min^{-1}$ in the BPM-CEM upscaled stack to reach a Base-pH ~ 10 is as represented in Equation S4 and S7. Equation S4 and S7 show the grey and blue lines in Figure 4.4, respectively.

$$i = 0.0025\left(\frac{A}{cm^2}\right) + 0.0023\left(\frac{mol}{L}\right) \times 96485\left(\frac{C}{mol}\right) \times \left(\frac{68}{60000}\right)\left(\frac{L}{s}\right) \div 100(cm^2) \sim 0.005\left(\frac{A}{cm^2}\right), \tag{S6}$$

$$E = 0.001\left(\frac{0.005\left(\frac{A}{cm^2}\right) \times 100\left(cm^2\right) \times (8.3 + 0.5 \times 4.85)\,(V)}{\left(\frac{68\times10}{60000}\right)\left(\frac{L}{s}\right) \times 0.002078(mol)}\right) \sim 229\left(\frac{kJ}{molCaCO_3}\right) \tag{S7}$$

4.6.7. DEFINING THE MAIN CHARGE CARRIER OVER THE CEM USING THE NERNST-PLANCK EQUATION

According to the Nernst-Planck equation [53], under an identical electrical potential gradient, the ionic fluxes depend on the magnitude of the species concentration (C_i), ion valence (z_i), and mass transfer diffusion coefficient (D_i). These data for the five present cations are listed in Table S12. To maintain the electroneutrality, the total concentration of cations in the base compartment increases (to make up for the increase of the OH^- ions, produced by the BPM). This increase is equal to 0.0023 mM under conditions of the case 3 in Figure 4.7 (see page 1 of the supporting information 4.6 for clarification on the total BPM-based OH- ions production = 0.0023 M).

Table S12: the contribution of each cation to carrying the charge through the CEM. All D_i values are in the order of 10^{-9} $m^2\,s^{-1}$ and are therefore simplified for the sake of comparison [54].

Cations	$D_i \times z_i \times C_i$	**Of the total**	**Increase in concentration in the base compartment,** $mol\,L^{-1}$
Na^+	$1.33 \times 1 \times 0.4593 = 0.613$	82.8%	$82.8\% \times 0.0023 = 0.0019$
H^+	$9.31 \times 1 \times 0.002 = 0.016$	2.5%	$2.5\% \times 0.0023 = 0.00006$
K^+	$1.96 \times 1 \times 0.0097 = 0.019$	2.6%	$2.6\% \times 0.0023 = 0.0001$
Ca^{2+}	$0.792 \times 2 \times .0102 = 0.016$	2.2%	$2.2\% \times 0.0023 = 0.0001$
Mg^{2+}	$0.706 \times 2 \times 0.0521 = 0.074$	9.9%	$9.9\% \times 0.0023 = 0.0002$

4.6.8. BIPOLAR MEMBRANE FOULING AND RAMAN SPECTROSCOPY RESULTS

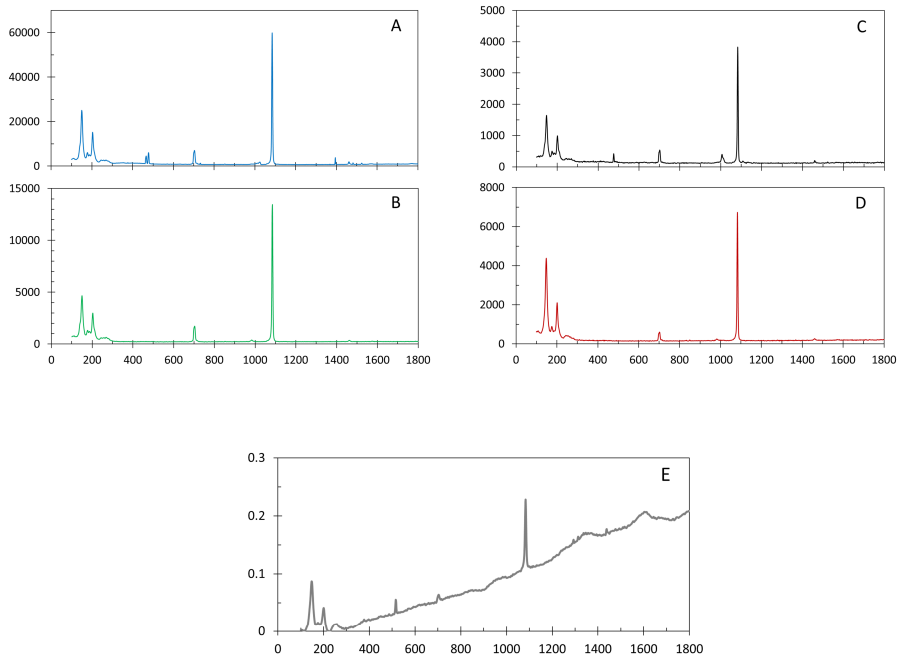

Figure S2: Raman spectra of the obtained precipitates from experiments (A) six-compartment BPMED with a (single) BPM, 40 $mA\,cm^{-2}$, 120 $ml\,min^{-1}$, 2 hours (B) six-compartment BPMED with a (single) BPM, 40 $mA\,cm^{-2}$, 30 $ml\,min^{-1}$, 2 hours, (C) upscaled BPMED, 5 $mA\,cm^{-2}$, 68 $ml\,min^{-1}$ per compartment, 30 minutes, (D) upscaled BPMED, 5 $mA\,cm^{-2}$, 50 $ml\,min^{-1}$ per compartment, 30 minutes, (E) real seawater (Wadden Sea), upscaled BPMED, 5 $mA\,cm^{-2}$, 68 $ml\,min^{-1}$ per compartment. All spectra show predominantly aragonite ($CaCO_3$) formation (characteristic peaks, at : 155, 205, 705, 1085 cm^{-1} [55]).

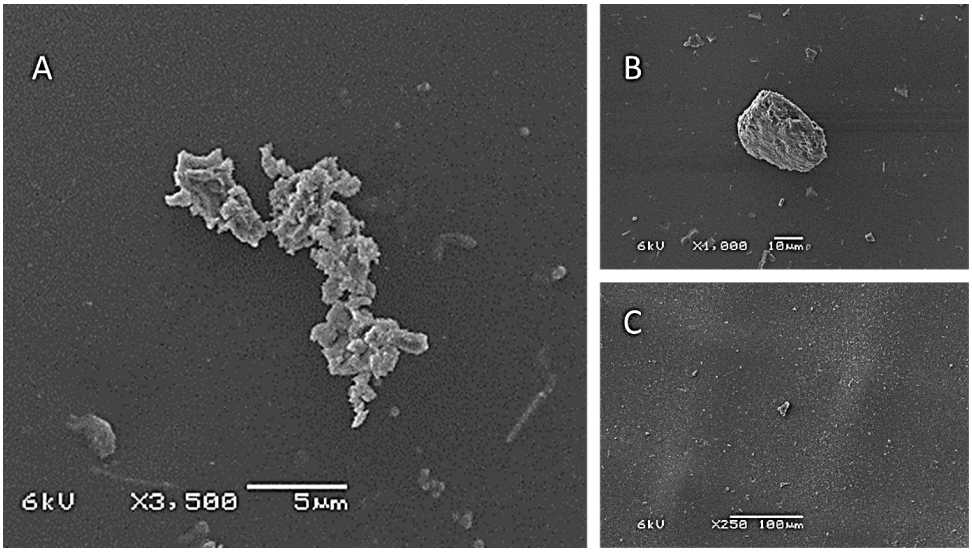

Figure S3: SEM images of the side of the BPM in contact with the alkaline pH in the six-compartment cell with a (single) BPM, when cell is opened right after applying 40 mAcm^{-2} for 15 minutes resulting in a base-pH of ca. 9.9. (A) and (B) Mg^{2+} and Ca^{2+} containing minerals, (C) BPM surface.

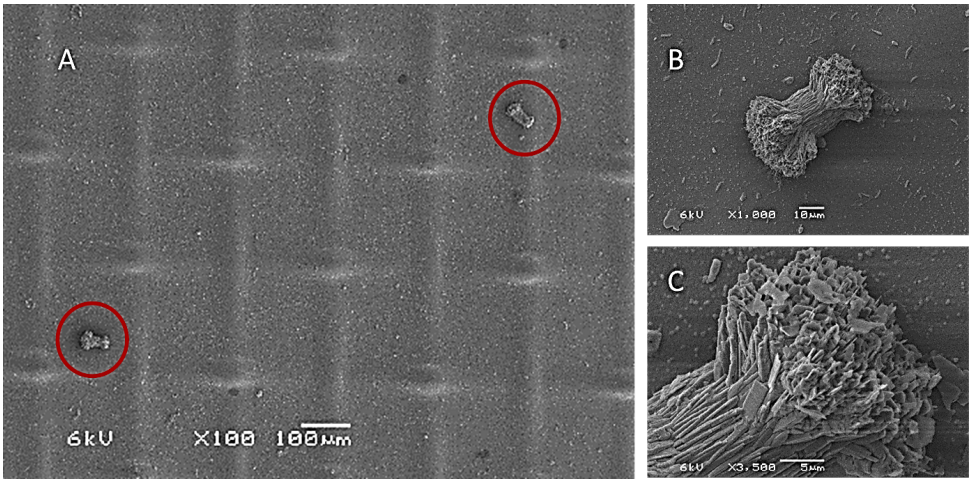

Figure S4: SEM images of the side of the BPM in contact with the alkaline pH in the six-compartment cell with a (single) BPM, after applying 40 mA cm^{-2} for 15 minutes resulting in a base-pH of ca. 9.9. (A) Anion exchange layer (AEL) of the membrane, (B) zoomed in on crystal containing Mg^{2+} and Ca^{2+}, (C) zoomed in on B. To allow time for precipitation, SEM here is done on the BPM where the cell has been opened 72 hours after the end of the experiment (with the alkaline compartment left undisturbed during the waiting time).

BIBLIOGRAPHY

[1] R. Sharifian et al. “Oceanic carbon capture through electrochemically induced in situ carbonate mineralization using bipolar membrane”. In: *Chemical Engineering Journal* 438 (2022), p. 135326.

[2] A. T. Fane. “A grand challenge for membrane desalination: More water, less carbon”. In: *Desalination* 426 (Sept. 2017), pp. 155–163.

[3] M. Eisaman et al. “Energy-efficient electrochemical CO2 capture from the atmosphere”. In: *Proc. 2009 Clean Technol. Conf. Trade Show* (2009), pp. 5–8.

[4] F. Sabatino et al. “Evaluation of a Direct Air Capture Process Combining Wet Scrubbing and Bipolar Membrane Electrodialysis”. In: *Ind. Eng. Chem. Res* 59 (15 Apr. 2020), pp. 7007–7020.

[5] C. F. de Lannoy et al. “Indirect ocean capture of atmospheric CO2: Part I. Prototype of a negative emissions technology”. In: *Int. J. Greenh. Gas Control* 70 (May 2018), pp. 243–253.

[6] I. A. Digdaya et al. “A direct coupled electrochemical system for capture and conversion of CO2 from oceanwater”. In: *Nat. Commun* 11 (1 2020), pp. 1–10.

[7] R. Sharifian et al. “Electrochemical carbon dioxide capture to close the carbon cycle”. In: *Energy Environ. Sci* (2021).

[8] J. H. Rheinhardt et al. “Electrochemical capture and release of carbon dioxide”. In: *ACS Energy Lett* 2 (2 2017), pp. 454–461.

[9] R. Parnamae et al. “Bipolar membranes: A review on principles, latest developments, and applications”. In: *J. Memb. Sci* 617 (2021), p. 118538.

[10] M. Eisaman. “Negative Emissions Technologies: The Tradeoffs of Air-Capture Economics”. In: *Joule* 4 (3 2020), pp. 516–520.

[11] M. D. Eisaman et al. “Indirect ocean capture of atmospheric CO2: Part II”. In: *Int. J. Greenh. Gas Control* 70 (2018), pp. 254–261.

[12] N. Prihasto et al. “Pre-treatment strategies for seawater desalination by reverse osmosis system”. In: *Desalination* 249 (1 2009), pp. 308–316.

[13] C. Bjg et al. “Calcium Carbonate MARKET ANALYSIS”. In: (2016).

[14] C. Woodall et al. “Utilization of mineral carbonation products: current state and potential”. In: *Greenh. Gases Sci. Technol* 9 (6 Dec. 2019), pp. 1096–1113.

[15] J. Van Heek et al. “Reduce, reuse, recycle: Acceptance of CO2-utilization for plastic products”. In: *Energy Policy* 105 (2017), pp. 53–66.

[16] R. Chang et al. “Calcium Carbonate Precipitation for CO2 Storage and Utilization: A Review of the Carbonate Crystallization and Polymorphism”. In: *Frontiers in Energy Research* 5 (2017), p. 17.

[17] Y. Zhao et al. “A novel technology of carbon dioxide adsorption and mineralization via seawater decalcification by bipolar membrane electrodialysis system with a crystallizer”. In: *Chem. Eng. J* 381 (8 2020), p. 122542.

[18] E. C. La Plante et al. “Saline Water-Based Mineralization Pathway for Gigatonne-Scale CO2Management”. In: *ACS Sustain. Chem. Eng* 9 (3 2021), pp. 1073–1089.

[19] S. Datta et al. “Electrochemical CO2 Capture Using Resin-Wafer Electrodeionization”. In: *Ind. Eng. Chem. Res* 52 (43 2013), pp. 15177–15186.

[20] R. E. Zeebe et al. *CO2 in seawater: equilibrium, kinetics, isotopes*. 65. Gulf Professional Publishing, 2001.

[21] A. Dickson. “The carbon dioxide system in sea water: equilibrium chemistry and measurements”. In: *Guid. Best Pract. Ocean Acidif. Res. Data Report* (Jan. 2010), p. 260.

[22] J. Butler. “Carbon dioxide equilibria and their applications”. In: (1991).

[23] V. L. Snoeyink et al. *Water chemistry*. John Wiley & Sons, Ltd, 1980.

[24] S. Emerson et al. “Chemical oceanography and the marine carbon cycle”. In: (2008).

[25] J.-H. Bang et al. “Sequential carbonate mineralization of desalination brine for CO2 emission reduction”. In: *J. CO2 Util* 33 (2019), pp. 427–433.

[26] M. Mitchell et al. “A model of carbon dioxide dissolution and mineral carbonation kinetics”. In: *Proc. R. Soc. A Math. Phys. Eng. Sci* 466 (2117 2010), pp. 1265–1290.

[27] Y. Lei et al. “Electrochemical Induced Calcium Phosphate Precipitation: Importance of Local pH”. In: *Environ. Sci. Technol* 51 (19 Oct. 2017), pp. 11156–11164.

[28] L. Boels et al. “Seeded calcite sonocrystallization”. In: *J. Cryst. Growth* 312 (7 2010), pp. 961–966.

[29] A. Banerjee. “Estimation of dolomite formation: Dolomite precipitation and dolomitization”. In: *J. Geol. Soc. India* 87 (5 2016), pp. 561–572.

[30] L. Zaitseva et al. “The role of cyanobacteria in crystallization of magnesium calcites”. In: *Paleontol. J* 40 (2 2006), pp. 125–133.

[31] B. Kutus et al. “A comprehensive study on the dominant formation of the dissolved Ca(OH)2(aq) in strongly alkaline solutions”. In: *RSC Adv* 6 (51 2016), pp. 45231–45240.

[32] R. Sharifian et al. “Intrinsic bipolar membrane characteristics dominate the effects of flow orientation and external pH-profile on the membrane voltage”. In: *J. Memb. Sci* (2021), p. 119686.

[33] J. Bui et al. “Understanding Multi-Ion Transport Mechanisms in Bipolar Membranes”. In: *ACS Appl. Mater. Interfaces* 12 (47 Nov. 2020), pp. 52509–52526.

[34] M. A. Blommaert et al. “Insights and Challenges for Applying Bipolar Membranes in Advanced Electrochemical Energy Systems”. In: *ACS Energy Letters* 6.7 (2021). PMID: 34277948, pp. 2539–2548.

[35] R. Berner et al. “Inhibition of aragonite precipitation from supersaturated seawater; a laboratory and field study”. In: *Am. J. Sci* 278 (6 June 1978), pp. 816–837.

[36] D. Buhmann et al. “Calcite dissolution kinetics in the system of watercarbon dioxide-calcium carbonate with participation of foreign ions”. In: *Chem. Geol* 64 (1 1987), pp. 89–102.

[37] G. Falini et al. “Calcium Carbonate Morphology and Structure in the Presence of Seawater Ions and Humic Acids”. In: *Cryst. Growth Des* 9 (5 May 2009), pp. 2065–2072.

[38] N. Spanos et al. “Kinetics of Precipitation of Calcium Carbonate in Alkaline pH at Constant Supersaturation. Spontaneous and Seeded Growth”. In: *J. Phys. Chem. B* 102 (34 Aug. 1998), pp. 6679–6684.

[39] H. Teng et al. “Solubility of CO2 in the ocean and its effect on CO2 dissolution”. In: *Energy Convers. Manag* 37 (6-8 1996), pp. 1029–1038.

[40] S. Zhong et al. “Calcite precipitation in seawatre using a constant addtion technique”. In: *Geochim. Cosmochim. Acta* 57 (1993), pp. 1409–1417.

[41] D. A. Vermaas et al. “Ion transport mechanisms in bipolar membranes for (photo) electrochemical water splitting”. In: *Sustain. Energy Fuels* 2 (9 2018), pp. 2006–2015.

[42] I. Zaslavschi et al. “Electrochemical CaCO3 scale removal with a bipolar membrane system”. In: *J. Memb. Sci* 445 (2013), pp. 88–95.

[43] W. Sun et al. “Correction: Nucleation of metastable aragonite CaCO3in seawater”. In: *Proc. Natl. Acad. Sci. U. S. A* 112 (20 2015), E2735.

[44] K. Davis et al. “The role of Mg2+ as an impurity in calcite growth”. In: 290 (2000), pp. 1134–1137.

[45] T. Ostvold et al. “Kinetics of CaCO3 scale formation. The influence of temperature, supersaturation and ionic composition”. In: *International Symposium on Oilfield Scale* (2001).

[46] K. Davis et al. “Morphological consequences of differential Mg2+ incorporation at structurally distinct steps on calcite”. In: *Am. Mineral* 89 (5-6 2004), pp. 714–720.

[47] V. Choudens-Sanchez et al. “Calcite and aragonite precipitation under controlled instantaneous supersaturation: elucidating the role of CaCO3 saturation state and Mg/Ca ratio on calcium carbonate polymorphism”. In: *J. Sediment. Res* 79 (6 2009), pp. 363–376.

[48] G. Saldi et al. “Magnesite growth rates as a function of temperature and saturation state”. In: *Geochim. Cosmochim. Acta* 73 (19 2009), pp. 5646–5657.

[49] Q. Gautier et al. “Hydromagnesite solubility product and growth kinetics in aqueous solution from 25 to 75 degree C”. In: *Geochim. Cosmochim. Acta* 138 (2014), pp. 1–20.

[50] M. Hanchen et al. “Precipitation in the Mgcarbonate system-effects of temperature and CO2 pressure”. In: *Chem. Eng. Sci* 63 (4 2008), pp. 1012–1028.

[51] E. Konigsberger et al. “Low-temperature thermodynamic model for the system Na2CO3, MgCO3, CaCO3, H2O”. In: *Geochim. Cosmochim. Acta* 63 (19 1999), pp. 3105–3119.

[52] S. El-Manharawy et al. “Study of seawater alkalization as a promising RO pretreatment method”. In: *Desalination* 153 (1 2003), pp. 109–120.

[53] B. Van Der Bruggen. “Chapter 7 -Ion-exchange membrane systems-Electrodialysis and other electromembrane processes”. In: (2018), pp. 251–300.

[54] P. Vanysek. “Ionic conductivity and diffusion at infinite dilution”. In: *CRC Hand B. Chem. Phys* (1993), pp. 5–92.

[55] U. Wehrmeister et al. “Raman spectroscopy of synthetic, geological and biological vaterite: a Raman spectroscopic study”. In: *Journal of Raman Spectroscopy* 41.2 (2010), pp. 193–201.

5

FOULING MANAGEMENT IN OCEANIC CARBON CAPTURE VIA *in-situ* ELECTROCHEMICAL BIPOLAR MEMBRANE ELECTRODIALYSIS

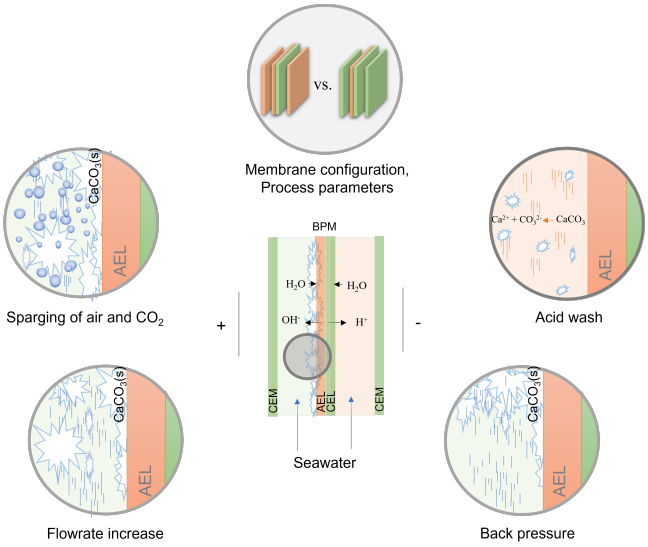

To reach a circular carbon economy within the context of climate change mitigation, the oceanic-dissolved inorganic carbon (DIC) can be extracted to enable an indirect air capture. The product of oceanic carbon capture is gaseous CO_2(g) and/ or carbonate minerals e.g., $CaCO_3$(s). An electrochemical bipolar membrane electrodialysis (BPMED) method provides a sustainable scalable route for such carbon capture by enabling a pH-swing that shifts the carbonate equilibrium. For the carbonate mineralization route, an in-situ seawater alkalinization offers a lower energy consumption compared to ex-situ processing, but suffers from inorganic fouling. This fouling occurs in the alkaline compartment adjacent to the bipolar membranes, where carbonate- and hydroxide minerals are formed. Such fouling increases the cell voltage and stack pressure drop, increasing the electrochemical and pumping energy consumption, respectively. In the current work, we investigate fouling management strategies including fouling control (i.e., via cell configuration and current density-flow rate optimization) and fouling removal methods, specifically targeting inorganic fouling. Fouling removal methods including air sparging, CO_2(g) sparging, dissolved CO_2(aq) cleaning, back-pressure, flow rate increase, and acid wash (dosed HCl and BPMED-based produced acid) are investigated under accelerated fouling conditions. The cell configuration containing the BPM-AEM pairs shows 4x lower fouling than the BPM-CEM stack, while the DIC-extraction and faradaic efficiency are similar for both cells. The BPM-AEM cell voltage remains constant for 2 h even under accelerated fouling conditions. From the fouling removal methods, only the acid wash combined with the back-pressure removed all the inorganic fouling, recovering both the cell voltage and pressure drop to its initial values. Upon the air sparging, the total cell voltage and pressure drop increased even more due to the trapped gas inside the netted spacers. Cleaning via dissolved and gaseous CO_2 decreases the cell pH, dissolving hydroxide- and carbonate-based fouling and thus removing scaling, but decreases the DIC-removal significantly, and is thus not preferred. Applying the back-pressure and higher flow rates decelerated the scaling buildup but was not enough to remove the fouling. A BPM-AEM membrane configuration in combination with periodic acid cleaning has potential as resilient oceanic carbon removal.

This chapter has been submitted as "Fouling management in oceanic carbon capture via *in-situ* electrochemical bipolar membrane electrodialysis." by R. Sharifian, H. C. van der Wal, R. M. Wagterveld, D. A. Vermaas.

5.1. INTRODUCTION

To mitigate the climate change [1], a circular carbon economy must be established where decarbonisation over all sectors is required, including the water sector [2]. Closing the carbon cycle and decreasing the carbon footprint of the water sector (e.g., desalination plants) are possible through extraction of the oceanic dissolved inorganic carbon (DIC), see Chapter 2 and 4. An additional benefit is that eliminating the carbonic species prior to membrane-based desalination (e.g., reverse osmosis (RO) or electrodialysis (ED)), as a pre-treatment step, can reduce the risk of carbonate-based scaling [3]. Particularly, a pH-gradient based decarbonisation step (see Chapter 2) is advantageous prior to seawater reverse osmosis (SWRO) as low-pH brine stream is ideal for further brine concentration processes [4, 5], while the high-pH stream can be returned into the sea, enhancing the atmospheric-carbon absorption in the ocean, facilitating the indirect air capture. Another benefit of the oceanic-DIC capture is its ability to address decentralised carbon emissions (i.e., ca. 42 % of the total emission), as these emissions (partly) end up in the ocean, see Chapter 2.

Oceanic (inorganic) carbon capture is possible through a pH-swing, providing products as gaseous CO_2(g) (in acidic pH) or carbonate minerals (in alkaline pH), see Chapter 2. In Chapter 4, we have shown the feasibility of the bipolar membrane electrodialysis (BPMED) for electrochemical oceanic carbon capture through *in-situ* alkaline mineralization. The BPM inside the BPMED cell consists of an anion exchange layer laminated or electro-spun to a cation exchange layer, with a water dissociation-catalyst inside the junction layer to enhance the kinetics of the water dissociation [6–8]. The bipolar membrane (BPM) uses (renewable) electricity to generate acid and base through the water dissociation reaction, enabling a sustainable pH-swing. No further chemicals, heat or steam are required for such carbon capture, see Chapter 2.

Previous work demonstrated a BPMED cell containing 10 bipolar-cation membrane (BPM-CEM) cell units to remove the oceanic dissolved inorganic carbon (DIC) in the form of calcium carbonate $CaCO_3$(s) through the *in-situ* alkaline route, see Chapter 4. The $CaCO_3$ (i.e., mainly aragonite) production rate of 0.64 $kgCaCO_3(s)\,h^{-1}m^{-2}$ using relatively low stack-electrical energy consumption of 0.88 $kWh\,kg^{-1}CaCO_3(s)$ was accomplished, see Chapter 4. The *in-situ* operation is essential to achieve this low energy consumption, as only a mild pH gradient is required in this process. However, the fouling inside of the electrochemical cell, particularly the scaling resulting from the alkaline-pH > 9, poses challenges to the technology. To mitigate the fouling and assess the technology's practical feasibility, this chapter discusses various strategies to control and remove the (inorganic) fouling.

5.1.1. MEMBRANE FOULING

There are four types of ion-exchange membrane fouling including (1) colloidal fouling (e.g., clay, precipitated iron, aluminium oxides, and silicates) [9], (2) organic fouling (e.g., humic acids) [10–15], (3) inorganic fouling known as scaling (i.e., insoluble compounds e.g., calcium carbonate ($CaCO_3$) and silica (SiO_2)), and (4) biofouling (e.g., micro-organisms, extracellular polymeric substances (EPS), and algae) [16–20]. Membrane fouling shortens the lifetime of membranes [21] and decreases the available membrane surface area. Furthermore, fouling increases the electrical resistance of the mem-

branes, thereby raising the voltage loss and energy required for the process [16–18, 22, 23]. Lastly, fouling increases pumping energy needed to maintain a water flow rate in the cell, by blocking the spacers/ compartments, increasing the pressure drop between the inlet and outlet of the electrochemical cell.

Fouling depends on the interaction between feed-compounds and the (chemical charged groups on the) membrane surface [16]. It is shown in previous studies (on reverse electrodialysis, RED), the chance of scaling is increased in seawater compartment in the vicinity of the CEM, due to the high concentration of multivalent ions in the seawater (e.g., Ca^{2+} and Mg^{2+}) [18]. On the other hand, AEM did not show mineral scaling, but is known to be more prone to organic and colloidal fouling (since these compounds are mostly negatively charged), especially when combined with fresh water [18, 19, 24, 25]. In another study on electrodialysis (ED) it was reported that the membrane scaling formed by Ca^{2+} and Mg^{2+} minerals on AEM surface mostly takes place at neutral pH values, while the CEM was scaled at more alkaline pH [26]. In RED and ED processes, the mineral scaling is always combined with a concentration gradient, thereby inducing uphill transport (i.e., transport from low to high concentrations) of multivalent ions [27, 28]. However, the lack of such substantial concentration gradient in the BPMED-based carbon capture cell generates a different case, where the impact of the membrane type needs to be studied.

In the BPMED-based *in-situ* mineralization method, when using real seawater as feed, the inorganic fouling in the alkaline pH (≥ 9) increases the cell voltage drastically, see Chapter 4. Therefore, this work focuses on controlling the inorganic fouling (i.e., scaling), in particular, the carbonates and hydroxide minerals that form at pH between 9 and 12. Considering the low pH in the acidic channels ($pH \leq 4$), no mineral scaling is assumed to develop in acidic compartments.

As the fouling is dependent on the cell configuration and the choice of membrane, we first compare the performance of CEM-BPM and AEM-BPM stacks when subjected to a fouling scenario, rating the $CaCO_3$(s) production and electrical energy consumption. Other cell configurations including BPM-AEM-AEM [29] or *ex-situ* AEM-BPM-CEM [30] are also possible. However, eliminating the third membrane in the cell-units reduces the ohmic resistance in the cell, increasing the $CaCO_3$(s) production per number of membranes, and thus reducing the total stack electrical energy consumption, see Chapter 4. In addition, we tune the ratio in applied current density and residence time combinations to mitigate fouling via process control, and to induce accelerated fouling conditions.

Unfortunately, even by applying scaling control strategies, fouling is inevitable and must be removed physically or chemically. Fouling management strategies include (1) membrane modification, (2) feed pre-treatment, (3) membrane cleaning, and (4) changes in the process regime [19]. This work investigates membrane cleaning and changes in the process regime. Various methods for cleaning of different membranes are reported in literature including, polarity-reversal [31], reverse flow [32, 33], gas sparging [22], cleaning using CO_2-saturated water [17], chemical wash [21], and flow rate increase [34]. However, data on fouling control/ removal for *in-situ* CO_2 capture via BPMED is missing. The membrane fouling cleaning methods in this work include air sparging, gaseous CO_2(g) sparging, cleaning using dissolved CO_2(aq), flow rate increase, back-pressure applica-

tion, and acid wash (using pure HCl acid or using the produced acid from the BPMED). All cleaning strategies are compared using *in-situ* seawater decarbonization in BPMED under accelerated scaling conditions.

5.2. MATERIALS AND METHODS

Prior to the experiments, the expected feed and outlet pH, possible minerals, and carbonate removal rate are simulated with Visual MINTEQ Ver. 3.1 at each current density (i) and cell residence time (t_r), following the calculation method presented in Chapter 4. Subsequently, experiments for fouling management are conducted.

5.2.1. REAGENTS AND MATERIALS

Synthetic seawater was made by dissolving pure salts in demineralized water, following the procedure in Chapter 4, resulting in the same ionic composition shown in Table 4.1. All reagents were of analytical grade acquired from VWR or Sigma Aldrich. During the experiments, all solutions were kept at ambient lab temperature of 23 °C ± 2°C. To avoid pre-precipitation (of e.g., $CaCO_3$(s)) in the feed tank, two separate feed tanks were used with their content mixed using T-connections just right before entering the electrochemical cell, and not any sooner, see Chapter 4.

Solutions were pumped through the stack by peristaltic pumps (Cole-Parmer, Masterflex L/S Digital drive, USA), through 6.0 mm OD PTFE tubing (EmTechnik). The pH of the feed and outflow streams of the BPMED cell were measured every second, using Orbisit CPS11D-7BA21 pH probes connected to a Liquiline CM444 digital multiparameter transmitter, both from Endress + Hauser, with an accuracy of ± 0.2 pH-units. The pH meters were calibrated weekly. The pressure drop (Δp) between the inlets and outlets of the acidic and alkaline compartments of the cell were measured using two pressure difference transmitters (Endress + Hauser). All membranes used in the BPMED cells were provided by FuMATech B.V. The FBM-130, FKB-PK-130 and FAB-PK-130 were used as bipolar membranes (BPM), cation exchange membranes (CEM) and anion exchange membranes (AEM), respectively. Electrodes of titanium mesh coated with platinum, provided by MAGNETO Special Anodes B.V. (Schiedam, The Netherlands) were used in both cells. The 10× 10 cm^2 cell is provided by REDstack B.V., with integrated gasket mesh spacers of 400 ± 5 μm (Sefar 07-500/48 PETP netting with an open area of 48 % supplied by Aqua-Battery B.V.) inserted in between the membranes to act as flow channels. In between each tests, the stack (including the membranes and spacers) were cleaned with recirculating HCl acid for several hours, followed by deminerlized water and 0.5 M NaCl flush. The stack was opened weekly for inspection.

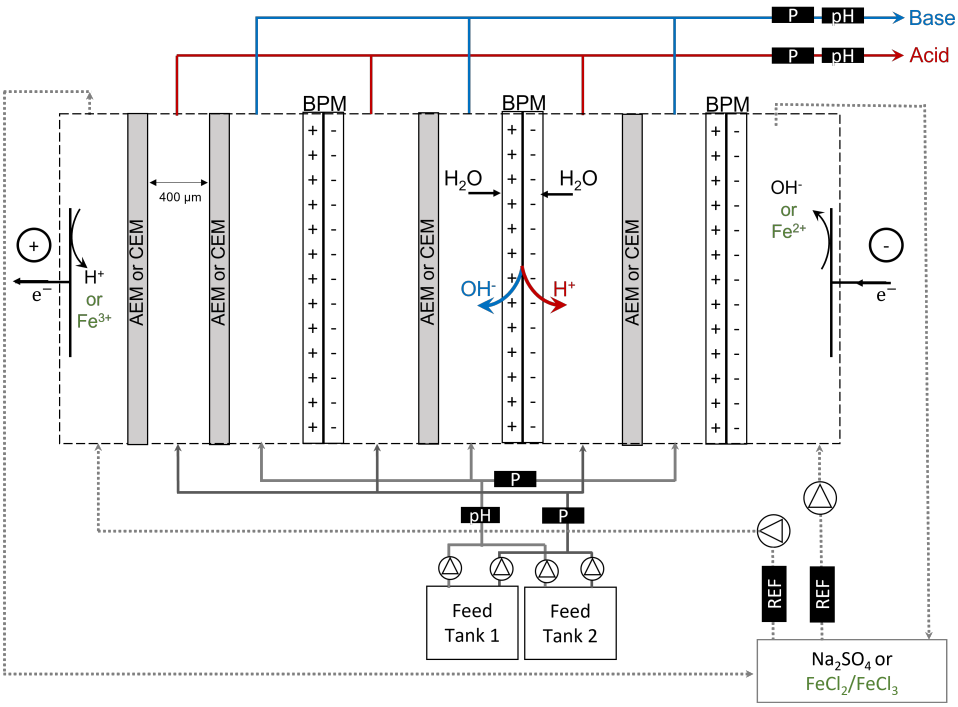

Figure 5.1: Schematic representation of the BPMED cell. In case of the AEM-BPM configuration, all three internal grey membranes (adjacent to the BPM's) are AEM's while for the CEM-BPM, they are all CEM's. A cation-exchange membrane (CEM) was used as a shielding membrane on the anode side, to avoid chlorine leakage to the electrode rinsing solution (ERS). In case of using iron chloride as ERS, this shielding membrane on the anode needs to be an AEM to avoid iron transfer towards the cell, and the 0.3 M Na_2SO_4 is replaced by 0.25 M $FeCl_2$ + 0.25 M $FeCl_3$ + 1 mM HCl solution. The symbols P, pH, and REF show the pressure difference transmitters, pH sensors, and the Ag/AgCl reference electrode for cell voltage measurement. Feed tank 2 contains $CaCl_2$ and $MgCl_2$ and Feed tank 1 contains remaining salts from Table (4.1). Two separate feed tanks are used to avoid precipitation of the synthetic seawater prior to entering the cell as explained in Chapter 4.

Depending on the cell configuration (Figure (5.1)) and the shielding membranes adjacent to the electrodes, two different electrode rinsing solutions (ERS) were used: (1) 0.25 M $FeCl_2$ + 0.25 M $FeCl_3$ + 1 mM HCl with a conductivity of 71 mS cm^{-1} and pH 1-1.5, and (2) 0.3 M Na_2SO_4 (to allow the water redox reaction), with a conductivity of 38.3 mS cm^{-1} and initial pH of 5-6. While the water electrolysis requires at least 1.23 V, the iron couple is a reversible ERS, requiring 0 V of standard potential thus minimizing the total cell voltage and energy consumption of the process [35]. To exclude the (water) redox voltage from the measurements, two Ag/ AgCl reference electrodes were submerged inside of the electrode rinsing solution (ERS) compartments (unless stated); where the potentiostat (Ivium Technologies B.V.) measured voltage between the two reference electrodes, excluding the reactions on the electrodes (i.e., the four-electrode connection).

5.2.2. EXPERIMENTAL PROCEDURE

The scaling buildup was measured by inline measurements through monitoring the:

1. Pressure difference (Δp_{Base}) development over time, between the inlet and outlet of the base compartments,
2. Development of the total cell-voltage over time,
3. The stack resistance, measured via current interruption (supporting information 5.5).

The development of pressure difference (Δp) between the inlet and outlet of the acid compartments over time was also monitored, but stayed constant during all experiments, confirming that no scaling builds up in the acidic compartments. For simplicity, summary of the applied fouling management strategies is given in Table 5.1, while the supporting information 5.5 provides a detailed description of each method.

Table 5.1: Summary of the applied strategies for fouling control (blue) and fouling removal, showing the applied current density i, flow rate per compartment q, and the cell residence time t_r parameters. The reference case and accelerated fouling conditions are also shown. The detailed description of each strategy is given in the supporting information 5.5.

Strategy	Configuration	i mA cm^{-2}	q ml min^{-1}	t_r [s]	Remarks
Reference case	BPM-CEM, BPM-AEM	5	72	2.4	$CaCO_3$(s) is formed but scaling buildup rate is slow
Accelerated fouling	BPM-CEM, BPM-AEM	12.5, 15	24, 72	7.3, 2.4	Scaling buildup rate is fast due to the high charge density
Membrane configuration	BPM-CEM, BPM-AEM	5, 10, 12.5, 15	24,72	7.3, 2.4	Effect of cell-configuration and $i - t_r$ were studied

Air sparging	BPM-CEM	12.5	72	2.4	Air pressure: 1-4 barg, every 10 min (for 5 s), with the first sparge starting 5 min after the start of the experiment
CO_2(g) sparging	BPM-CEM	12.5, 15	72, 24	2.4, 7.3	CO_2(g) pressure: 2 bar or 3 bar, every 5 min, for 5 s or for 3× 2s (combined with back-pressure)
Saturated CO_2(aq)	BPM-AEM	12.5	72	2.4	60 s cleaning after 1 h of experiment (Table S1)
Purge flow	BPM-CEM	12.5	72	2.4	Purge flow (5× and 15× q) every 10 min (for ca. 5 s), starting 5 min after the start of the experiment
Back-pressure	BPM-CEM, BPM-AEM	12.5	72	2.4	Separately or combined with gas sparging and acid-wash, applied by momentarily closing the base-outlet valve
Acid wash	BPM-CEM, BPM-AEM	12.5	72	2.4	Diluted HCl (pH 1.5-2) and BPMED-made acid (pH 2.4-2.6) was used. The effect of acid flow rate was also studied (q = 0, 72, 144 ml min^{-1}).

ACCELERATED FOULING CONDITIONS

The accelerated fouling condition is developed by applying high current density i, at each cell residence time t_r, in the single-pass continuous process. Theoretically, at a fixed t_r, the concentration of the BPM-produced OH^- ions increase linearly with i, Figure S5. Subsequently, the increase in the OH^- ions concentration, convert more and more bicarbonate ions HCO_3^- to carbonate ions CO_3^{2-}. After all carbonates are formed and precipitated, increasing the OH^- ions concentration (i.e., increasing i) increases the brucite ($Mg(OH)_2$) precipitation linearly, while carbonates precipitation remains constant, Figure S5. Assuming the linear relationship between the concentration of BPM-produced OH^- ions and applied current desnity i and the produced brucite $Mg(OH)_2$(s) vs. i, shown in Figure S5, and assuming the crystallization kinetics remain unchanged with a higher current density (after the minimal pH-threshold as shown in Figure 4.2 is reached), the accelerated fouling conditions suggests that (under the same t_r) running the experiment for 1 hr under i = 15 mA cm^{-2} results in the same exposure to mineral precipitation as that of 3 hr under i = 5 mA cm^{-2}. To show the relation between the normal and accelerated fouling condition, the voltage buildup graph for the two cases (i.e., flow rates of q = 24 and 72 ml min^{-1}) vs. the charge desnity are compared in section 5.5.11.

Furthermore, after measurements of the removal of DIC, Ca^{2+}, and Mg^{2+} ions and

SEM/ EDS analysis in Chapter 4, it is concluded that carbonate and hydroxide minerals are the main precipitation that take place, validating Figure S5.

However, in order to ensure if equal exposure to mineral precipitation results in the same fouling rate and to ensure findings under the accelerated fouling conditions can be considered as the final solution against scaling in *in-situ* BPMED-based carbon capture, the method of accelerated fouling needs to be validated with data from pilots, using real seawater for extended period of time. A combination of redesigned stacks, pretreatment, additional operational measures, and cleaning procedures might be the way to restrict fouling at minimum cost [33].

5.2.3. DATA ANALYSIS

All the output from the base compartments was captured and stored in sealed storage tanks/ bottles for at least 72 hours to allow mineral precipitation without the interference of the atmospheric CO_2(g). Thereafter, the sample was filtered through a 0.22 μm (MF-Millipore^{TM}) filter and analysed on Ca^{2+} and Mg^{2+} concentrations using inductively coupled plasma analysis (ICP). The carbonate concentration in the filtered sample was determined via titration with 0.1 M hydrochloric acid HCl conform procedure of section 4.6.

ELECTRICAL AND PUMPING ENERGY CONSUMPTION

The total energy consumption E in kJ mol^{-1} $CaCO_3$(s) required for the *in-situ* mineralization was determined using:

$$E = \frac{\int_{t_0}^{t_{end}} VIdt}{m_{DIC}} + \frac{\int_{t_0}^{t_{end}} (\Delta p_{Acid} + \Delta p_{Base}) q dt}{m_{DIC}} \tag{5.1}$$

The first part of the equation describes the stack-electrical energy consumption, in which V represents the total cell voltage (V), I the applied current density (A), t the experimental duration between t_0 and t_{end} (s). The second part of the equation describes the pumping energy in which Δp_{Acid} and Δp_{Base} are the pressure drop over the acid- and base compartments (Pa), respectively and q is the flow rate (m^3 s^{-1}), integrated over duration of the experiment. The values are divided by the amount of moles $CaCO_3$ captured during the running time of the experiment (m_{DIC}), see Chapter 4. The cell-voltage (V) includes the voltage required for the redox reaction, BPM-water dissociation, and the stack losses including the ohmic and non-ohmic losses, see Chapter 3. Fouling increases both the ohmic and non-ohmic resistances [18, 36].

FLOW VELOCITY AND CELL RESIDENCE TIME

The average flow velocity v (cm s^{-1}) inside the stack is calculated as [37]:

$$v = \frac{q}{60 \times A_{eff}} = \frac{q}{60 \times W \times d \times \varepsilon} \tag{5.2}$$

where A_{eff} in cm^2 is the cross-section area of the feed channel involving the spacer porosity ($\varepsilon \simeq 73$ %, [-]), q the flow rate in the compartment in ml min^{-1}, W width of feed

channel (= 10 cm for the used electrochemical cell), and d the spacer thickness ≃ 0.04 cm. The cell residence time t_r in s is defined as:

$$t_r = \frac{l}{v} \tag{5.3}$$

where l is the length of feed channel (parallel to the flow direction) = 10 cm and v the average flow velocity v ($\mathrm{cm\,s^{-1}}$) inside the stack. The used flow rate of q = 72 and 24 $\mathrm{ml\,min^{-1}}$ in this work, create flow velocities of (rounded up) v 4.1 and 1.4 $\mathrm{cm\,s^{-1}}$, and t_r of 2.4 s and 7.3 s, respectively.

The hydraulic Reynolds number Re_h as a function of the average velocity of the spacer-filled channel (Equation 5.2 but in SI unit of $\mathrm{m\,s^{-1}}$), hydraulic diameter d_h (in m), and W width of feed (in m) can be calculated via [37]:

$$Re_h = \frac{\rho.v.d_h}{\mu}, \text{ where } d_h = \frac{4 \times \varepsilon}{\frac{2}{w} + (1+\varepsilon) \times S_{v,SP}} \tag{5.4}$$

where ρ and μ are the density and viscosity of the feed (synthetic)seawater, respectively (i.e., assumed to be ρ = 1021.57 $\mathrm{kg\,m^{-3}}$ and μ = 0.000943661 $\mathrm{kg\,m^{-1}\,s^{-1}}$). $S_{v,SP}$ is assumed to be ≃ 18182 $\mathrm{m^{-1}}$ and is the specific surface of the feed spacer [38] (= feed spacer surface divided by its volume, in this work roughly approximated by $\frac{4}{d_F}$ [39], with d_F the spacer filament thickness of 220 μm). Given the above inputs, the Re_h in all experiments stays $Re_h < 1000$ indicating a laminar flow.

5.3. RESULTS AND DISCUSSION

5.3.1. EFFECT OF THE CELL CONFIGURATION

The AEM-BPM works remarkably better than the CEM-BPM cell with regards to the magnitude of the scaling buildup (Figure 5.2). The cell voltage for the AEM-BPM cell does not increase with time, while that of the CEM-BPM increases 4× within the same 1.5 h, Figure 5.2 (A). Also, the pressure drop curve shows a substantially better performance of the AEM-BPM configuration compared to CEM-BPM (Figure 5.2 (B)), although some increase in pressure is observed even for the AEM-BPM case. Some fouling still does occur which results in partially blocking the flow path and thus increasing the pressure drop, observed after opening the cell in both cases, and visually seeing the white precipitation on the membranes and spacers surfaces (results not shown). The AEM-BPM initially shows a slightly lower pressure drop, which is probably due to a stack-to-stack variability.

As for the DIC removal, both cells show comparable carbonate removal performances; ca. 79 % ± 8 % for the AEM-BPM and ca. 66 % ± 15 % for the CEM-BPM (at the end of a 2 h experiments). As the removed carbonate is similar for both cases, and because the CEM-BPM has much higher increase in the voltage and pressure drop compared to AEM-BPM, it is obvious that the AEM-BPM is the preferred setup with regards to its lower energy consumption (Equation 5.1). The reason is probably that in CEM-BPM cell, the fluxes of Mg^{2+} and Ca^{2+} ions towards the base compartment through the CEM (under migration force) create a high concentration of these divalent ions on the CEM boundary layer (i.e., concentration polarisation), increasing the saturation index of the carbonate (and

hydroxide) minerals close to the surface of the CEM, increasing the (inorganic) fouling rate. Such a scenario does not occur in the AEM-BPM cell, as the AEM suppresses the cation transfer. We hypothesize that this concentration polarization causes inorganic fouling at the CEM surface, in addition to fouling in the spacer channels. This also explains why both the cell voltage and pressure drop increase in the CEM-BPM case, and only the pressure drop increases in the AEM-BPM case.

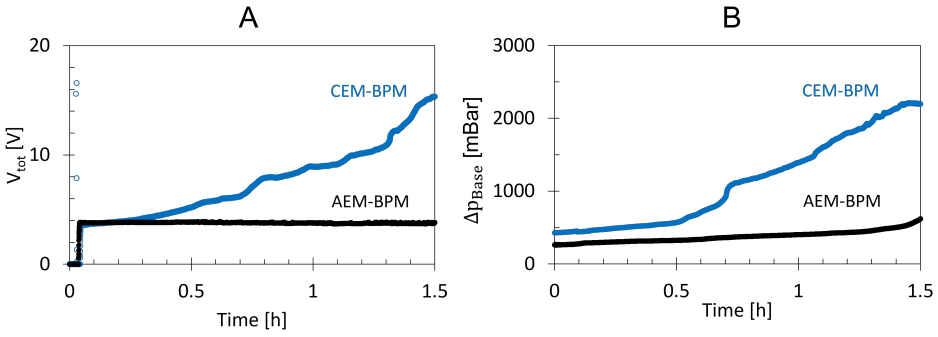

Figure 5.2: Comparison of the 3-pair CEM-BPM (+ACBCBCB-) and 3-pair AEM-BPM (+AABABAB-) cells with regards to the total cell voltage (A) and the pressure drop over the base compartment (B). In both cases, the iron couple was used as the electrode rinsing solution (ERS) with AEM as a shielding membrane next to the anode (ERS flow rate q = 200 ml min^{-1}). (A) shows the total cell voltage including the redox- reactions (i.e., V_{redox} is theoretically zero due to the redox reversibility of the iron couple). Current density of i = 12.5 mA cm^{-2} and flow rate of q = 72 ml min^{-1} were used for both configurations. Note that for DIC-removal, a i = 5 mA cm^{-2} under q = 68 ml min^{-1} is adequate, see Chapter 4. Therefore, the used i = 12.5 mA cm^{-2} here shows an accelerated fouling conditions.

5.3.2. EFFECT OF THE CELL RESIDENCE TIME AND APPLIED CURRENT DENSITY ON SCALING BUILDUP

Assuming the thermodynamic equilibrium in the bulk, at base-pH ≥ 9.9, using Visual MINTEQ simulations, more than 97 % of the dissolved inorganic carbon (DIC) can be removed as calcium carbonate, see Chapter 4. After that point, any further increase in the charge density (= $\frac{I}{qF} = \frac{It_r}{V_{eff}F}$, see section 5.5.11), only increases the OH^- ions concentration further, accelerating hydroxide containing minerals precipitation, Figure S5.

In the experiments, the total cell voltage (Figure 5.3) and pressure drop Figure S6,

thus the scaling buildup, indeed increase with cell residence time t_r and current density i. The increase of the cell voltage by scaling buildup is due to the increase of the membrane ohmic- (Figure S2) and non-ohmic resistances (e.g., explained under section 5.3.5). In this work, the change in the stack ohmic resistances where much more significant compared to that of non-ohmic resistances, Figure S2 and S3.

Comparing the scaling buildup under accelerated fouling conditions (i.e., q = 24 ml min^{-1}) to that of normal conditions (i.e., q = 72 ml min^{-1}) vs. "charge density × time" show a similar growth rate for the later within the same time frame, Figure S7 and S8.

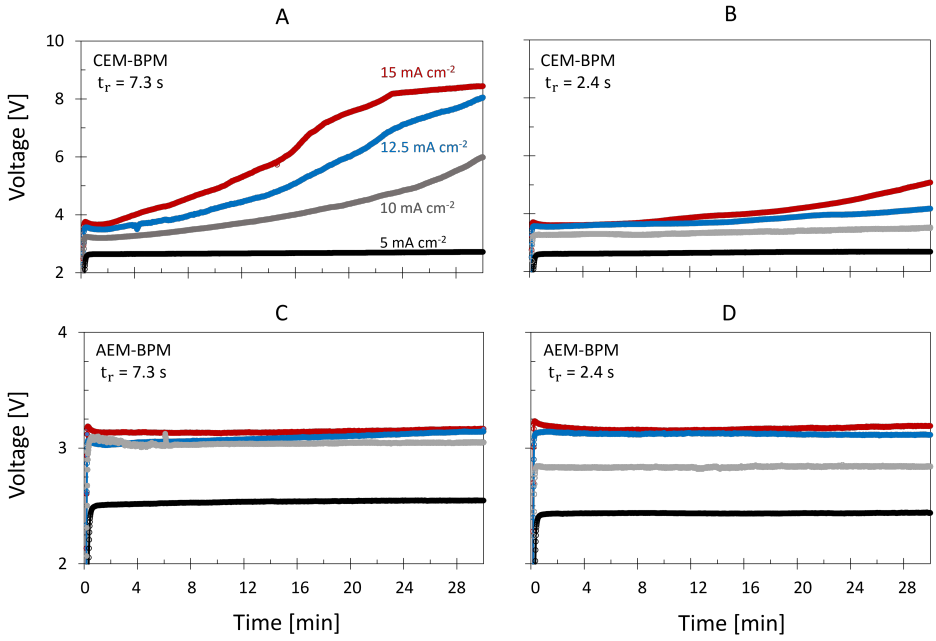

Figure 5.3: The measured experimental cell voltage (excluding the redox reaction voltage) vs. experiment duration time for two cell configurations (A, B: CEM-BPM, and C, D: AEM-BPM), four current densities (red 15, blue 12.5, grey 10, and black 5 mA cm^{-2}) and two cell residence time (t_r = 2.4 and 7.3 s, corresponding to flow rates of 72 and 24 ml min^{-1} per compartment, respectively).

The cell voltage increases with current density, due to the increase in the ohmic resistances (Figure 5.3, voltage of red > blue > grey > black); this can already be seen in the differences in initial voltages between the cases. Furthermore, the cell voltage increases with time due to the mineral precipitations that take place inside of the cell. The increase in the cell voltage vs. time due to this scaling buildup is the highest for the CEM-BPM cell (Figure 5.3 (A, B)) due to the concentration polarisation of divalent cations close to the surface of the CEM as explained under Figure 5.2.

In general, as the cell residence time t_r decreases, the scaling buildup rate decreases (Figure 5.3 (B, D) vs (A, C)), probably because the higher shear force associated with the higher flow rate, mechanically, removes the fouling particles better [40–43] and/ or

because a lower base-pH decelerates scaling buildup. A lower t_r is thus preferred (as long as the base-pH requirement is met for the bicarbonate ion to carbonate ion conversion and the subsequent carbonate mineral precipitation, see Chapter 4). The measured/ simulated bas-pH for each experiment shown in Figure 5.3 is very comparable and all at pH > 9.9. The charge density associated with each $i - t_r$ is shown in Table S3.

Higher current density creates a higher base-pH, promoting the mineral precipitation inside of the cell (including a higher hydroxide/ magnesium containing minerals precipitation, Figure S5), and thus increasing the scaling buildup (Figure 5.3 from red to black lines); which is undesired. The lowest current density of 5 $mA\,cm^{-2}$ does not create much fouling regardless of t_r and cell configuration (Figure 5.3, black lines). A low current density also has the added benefit of causing lower ohmic losses (iR), decreasing the total cell voltage and eventually the electrical energy consumption (Equation 5.1).

From Figure 5.2 to Figure 5.3 it becomes evident that the AEM-BPM cell configuration, in combination with high flow rate and current density of 5 - 10 $mA\,cm^{-2}$ (i.e., charge density < 0.01 $mol\,L^{-1}$, Table S3) provides the best process setting to decelerate scaling buildup for oceanic carbon capture. However, despite the decelerated scaling-buildup explained above, fouling is inevitable when *in-situ* mineralization is initiated. The stack pressure drop-increase vs. time graphs clearly reveals the presence of scaling in all cases, Figure S6. As the fouling is inevitable even under controlled fouling strategies, fouling removal techniques are required. The performance of each cleaning method is discussed below.

5.3.3. AIR SPARGING

Air sparging under 1 barg injection pressure was not sufficient as gas bubbles got trapped inside of the stack, not exiting the cell, Figure 5.4. The air sparging experiments show a similar trend for voltage and Δp_{Base}, increasing with time, just as the reference experiment (Figure 5.4), suggesting that the air sparging did not clean the BPMED stack-base compartments. Not only does the air sparging not recover the cell voltage/ pressure drop, it even increases them slightly after each injection (Figure 5.4 (A,B)-spikes and the slightly higher value after each spike). Such increase is probably due to presence of stagnant bubbles remaining trapped in the stack after every air injection, which is reported to increase the stack resistance in prior studies [17] as air has much lower electrical conductivity that the feed synthetic seawater (i.e., ca. 10^{-14} [44] vs. ca. 5 $S\,m^{-1}$). At the end of each air injection, an effort was made to remove stagnant bubbles from the stack by applying back-pressure through closing a valve located on the outflow of the base compartments (creating pressure buildup of 2-3 bar), but no decrease in the voltage nor Δp_{Base} was achieved.

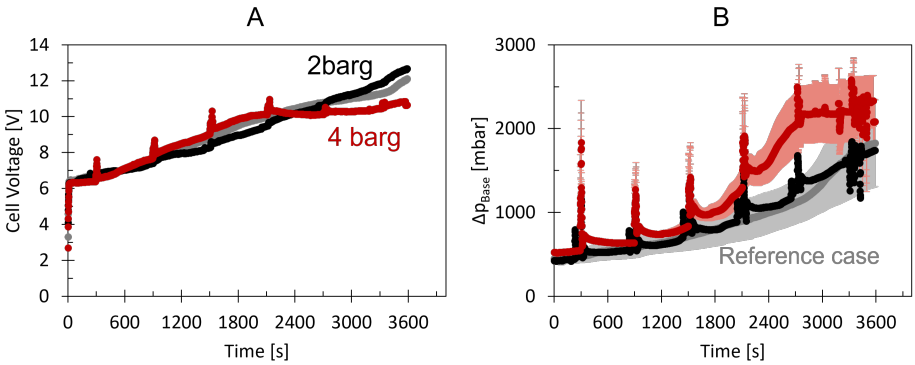

Figure 5.4: Air sparging under 2 (black) and 4 barg (red) done for the BPM-CEM configuration (i = 12.5 mA cm^{-2} q = 72 ml min^{-1}), done every 10 min for 5 s, with the reference experiment (i.e., no sparging applied) shown in grey. (A) cell total voltage and (B) pressure drop over the base compartments vs. time. Each set experiment is done three times. The graphs show the average of three repetitions. In (B), the standard error (= standard deviation/square root of 3) for the reference experiment (light grey) and the 4 barg experiment (in pink) are shown, the case of 2 barg (black) has a standard error of ca. 42 mbar. For (A), the standard error are ca. 0.7-0.9 V for all lines.

Furthermore, increasing the air pressure from 2 to 4 barg does not improve the cleaning efficiency (Figure 5.4), probably due to the formation of channels between the spacer material (figure S13); if channels are formed, the air chooses the 'way of least resistance' and only sparges the channels but not the rest of the compartment, particularly the edges and corners, being ineffective in scaling removal. However, air sparging has been shown effective in reverse electrodialysis (RED) where the use of profiled membranes made spacers obsolete [18], suggesting the important role of the spacers in fouling removal strategies.

As a final attempt for sparging in the spacer-filled channels, a pulsed injection was applied, as literature suggests an extra shear force can push out the deposited fouling [17]. Therefore, sparging 3× 2s (i.e., pulse injection) instead of 1× 5s (Figure 5.4) was applied. However, still no improvement in the efficiency of the cleaning removal is seen, Figure S10.

5.3.4. CLEANING WITH CARBON DIOXIDE

Sparging of gaseous carbon dioxide is reported to be more effective in scaling removal compared to the air sparging [17]; the CO_2(g) has the benefit of lowering feed-pH (upon CO_2 dissolution) and thus dissolving carbonate and hydroxide minerals, chemically. The effectiveness of gaseous CO_2(g) sparging in fouling removal is evaluated for 1× 30s (Figure S9) and 3× 2s sparging modes, Figure 5.5.

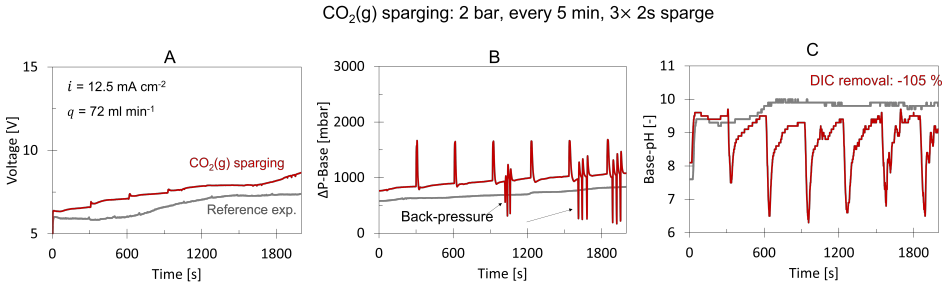

Figure 5.5: Gaseous CO_2 sparging regimes for fouling removal in the CEM-BPM cell. (A) The total cell voltage increase, (B) pressure drop increase over the base compartments, and (C) bulk-pH in the outlet from the base compartment versus time with regards to the reference experiment (i.e., no cleaning method, grey line) are shown. The dissolved inorganic carbon (DIC) removal is measured at the end of experiment via HCl acid titration method.

The total cell voltage and Δp_{Base} increase for the reference experiment as expected, Figure 5.5, grey line. Logically, this increase is higher under the accelerated fouling condition of Figure S9 compared to Figure 5.5; the higher scaling buildup is a result of 3.75× higher concentration of the BPM-produced OH^- ions in the base compartment, which increases the precipitation rate of hydroxide containing minerals (particularly $Mg(OH)_2$). For the reference experiment, the base-pH remains around pH 10 (Figure 5.5 (C)) due to the *in-situ* mineralization that takes place inside of the base compartments of the cell, reducing and stabilizing the bulk-pH, see Chapter 4.

CO_2(g) sparging increases the cell voltage and Δp_{Base} compared to the reference experiment, probably due to the trapped gases in the stack, Figure 5.5 (A, B)-red line. Upon each sparging, a spike in the voltage and Δp_{Base} curves and a sudden drop in the base-

pH are seen, Figure 5.5 and S9. The three downward spikes in Figure 5.5 (B), at ca. 1050 s and 1500-2000 s, are due to application of a back-pressure in an attempt to release possible trapped gas. As a result, part of the trapped gas probably does leave the cell as can be confirmed by a flattened curve at the same time in the voltage buildup, Figure 5.5 (A)-red. The pH lowers after each 'sparge' as CO_2 lowers the pH when it is dissolved into the feed, subsequently dissolving part of the previously formed scaling, Figure 5.5 (C).

However, the gaseous CO_2 sparging under the setting of Figure 5.5 does not remove the scaling and even results in higher voltage and pressure-drop values. On the bright side, increasing the CO_2(g) concentration in the stack, by applying a longer sparging time of 30 s (instead of 3× 2s) and a 3 bar-CO_2(g) pressure (instead of 2 bar), cleans the stack significantly even under accelerated scaling condition, Figure S9. It must be noted that in practice, applying longer sparging times and higher gas pressures are less economical due to the higher amount of CO_2(g) that is needed.

5

The CO_2(g) sparging does not (fully) recover the initial BPMED-performance and it even results in a negative DIC removal. When using CO_2(g)-sparging, the scaling buildup rate is equal or worse compared to the reference case. Furthermore, as the negative DIC removal goes against the main function of the BPMED-based oceanic carbon reduction (OCDR), and because CO_2(g) sparging does not recover the stack conditions to its initial state anyways, it is ruled out for scaling removal for this technology.

As for other methods of cleaning with carbon dioxide, CO_2(aq) saturated water cleaning for fouling mitigation has been shown effective for microfiltration (MF), ultrafiltration (UF), nanofiltration (NF), reverse osmosis (RO), electrodialysis (ED), and reverse electrodialysis (RED) [17, 18, 45]. However, in the BPMED stack, the injection of the demi-water saturated with (dissolved) CO_2(aq) as fouling removal still does not recover the pressure drop of the AEM-BPM cell nor decreases the irreversible voltage drops, Figure S11.

5.3.5. TEMPORARY INCREASE OF THE FLOW RATE: PURGE FLOW

Higher flow rates lead to higher velocity gradients which leads to higher wall shear stresses [46, 47], often cleaning the surface fouling through physical cleaning in membrane stacks [40–43]. In general, places in the stack compartments were the flow velocity is low (e.g., in spacer knits) are also reported to be more prone to fouling [36, 48]. Furthermore, a higher flow velocity enhances mixing in the compartments, reducing the thickness of the diffusion boundary layer (proportional to the flow velocity ($v^{1/3}$) if Reynolds number < 1000), possibly lowering voltage-losses [49, 50]. However, A sudden temporary increase in the flow rate of the BPMED-stack does not recover the cell voltage and Δp_{Base} compared to the reference experiment, Figure 5.6.

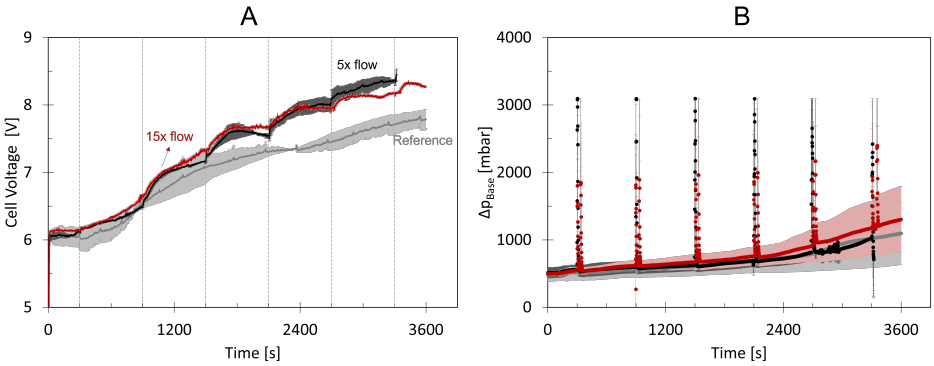

Figure 5.6: Development of the (A) cell voltage and (B) Δp_{Base} with time vs. the reference experiment (i.e., no cleaning method applied, grey line). All experiments were conducted for BPM-CEM cell, under i = 12.5 mA cm^{-2} and flow rate of q = 72 ml min^{-1} per compartment. Sudden short flow rate increase of 5× (black) and 15× (red), applied every 10 min (for 3-5 s using the pump "prime" option), are compared (vertical grid lines in (A) indicate the purging intervals). The error bars show the standard error between two repetitions with the dark lines showing the average of two repetitions. The standard errors for the reference experiment, 5× flow, and 15 × flow are shown in light grey, dark grey and pink, respectively.

In the first half of the experiments, application of the sudden-flow rate-increase does not change the cell voltage-time development compared to that of the reference experiment with no cleaning. For the second half (as the scaling inside the cell increases), the pump "priming" seems to even increase the cell-voltage slightly (ca. 10 %), Figure 5.6 (A). This difference is possibly resulted from various factors working against or in favour of increasing the cell voltage. With fouling present in the stack, random flow channels can form (Figure S13), resulting in a non-uniform flow velocity throughout the compartment; in reverse electrodialysis (RED), such nonuniform distribution (of feed water), increases the non-ohmic resistance due to depletion of ions in zones where the velocity is lower [36], which subsequently can increase the cell voltage. In the BPMED case, channel formation can speed up inorganic fouling deposition because in zones with low velocity, OH^- ions concentrations can increase (given the current density is uniform), causing locally high base-pH. Such higher base-pH accelerates (the thermodynamic and kinetics of) precipitation of hydroxide/ carbonate containing minerals, see Chapter 4. Upon such initial precipitation, the energy barrier for further deposition of e.g., Ca^{2+}, Mg^{2+}, CO_3^{2-} or OH^- ions lowers, enhancing the growth of the precipitates even more [51], ac-

celerating the fouling in whole. We hypothesize the latter to be the cause of increase in the cell voltage upon "priming" the pumps. As for Δp_{Base}, no significant differences between the cases exist, except that the higher flow rates create momentary spikes of high Δp_{Base} which is expected (as mathematically, Δp increases with linear velocity v in laminar flow regime $Re_h < 1000$ [39, 52]). Finally, at the end of the experiment, it seems like Δp_{Base} for 15× flow rate is slightly higher than the other two cases (ca. 150-200 mbar vs. the reference case), which can confirm the above hypothesise of the accelerated fouling in high base-pH under a temporary high flow rate.

5.3.6. APPLICATION OF BACK-PRESSURE

During application of a back-pressure, the outflow is temporarily interrupted, which causes a pressure buildup in the cell. Applying such back-pressure can decelerate fouling buildup because the flow rate is suddenly increased (more sudden than when priming) upon re-opening the outlet. Indeed, applying a back-pressure decelerates the rising rate of both voltage and pressure drop slightly (by 20 % and 100 % , respectively), Figure 5.7 (A-B).

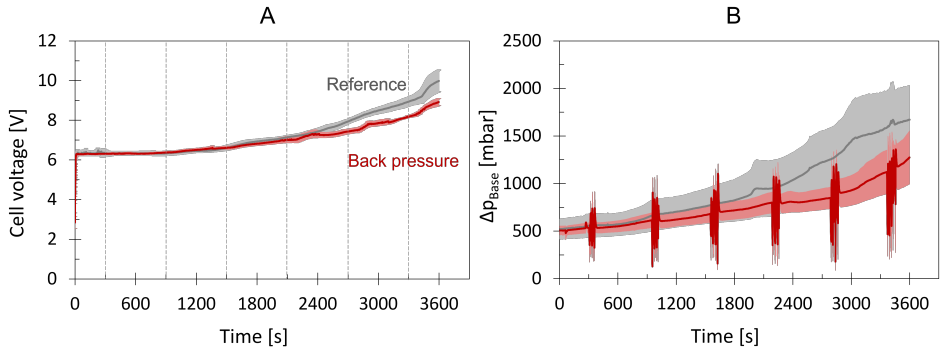

Figure 5.7: Comparison of (A) the cell total voltage and (B) pressure drop vs. time with the reference experiment (i.e., no cleaning method, grey line). All lines are averaged for two repetitions with back-pressure (i.e., red lines) being applied every 10 min for 3× 5s (with stack maximum pressure of ca. 3 bar reached upon closing the valve). A stack with cell configuration of +CCBCBCBC-, under i = 12.5 mA cm^{-2} and flow rate of q = 72 ml min^{-1} per compartment is used. The spikes in (B) show the sudden outburst of flow upon opening the valve. The error bars show the standard error of the two repetitions.

Upon closing the valve, Δp_{Base} becomes almost zero as the flow is temporarily stopped, Figure 5.7 (B). After re-opening the valve, Δp_{Base} increases substantially due to the temporarily high flow flushing out of the stack (spikes in Figure 5.7 (B)). The application of the back-pressure partially removes the scaling probably by mechanically removing the inorganic fouling due to the (temporary) very high flow rate (and thus high shear force [43]) that it induces upon reopening the valve. However, cleaning via applying a back-pressure does not fully restore the stack performance (i.e., cell-voltage and Δp_{Base} increase with time regardless), and hence is not sufficient as a method to remove inorganic fouling, fully. However, it may be combined with other inorganic fouling removal methods to increase their effectiveness.

5.3.7. ACID WASH: HCL VS. BPMED-PRODUCED ACID

Acid wash for fouling removal was applied in several modes (e.g., synthetic HCl solution vs. acid produced by the BPMED, and its flow rate ranging between 0 - 200 $\mathrm{ml\,min^{-1}}$). In all acid wash cleaning experiments, the base-pH and the pressure drop in the base compartment decrease upon the wash, Figure 5.8 and S12. Upon the acid wash, base-pH decreases, enabling the scaling dissolution and thus fouling removal. As a result, Δp_{Base} recovers to its initial value; in Figure 5.8 (A), the initial Δp_{Base} at the beginning of the experiment is 500 mbar, while after the acid wash (of ca. 15 min) Δp_{Base} becomes 590 mbar, showing > 80 % recovery, suggesting a very effective cleaning.

As for the reproducibility of data over multiple cycles, it must be noted that even under the same base-pH, cell configuration, and process parameters i and q, the location and amount of scaling, and thus the development of Δp_{Base} are not identical (Figure S12 vs. 5.8), but all show almost full recovery upon a HCl-acid wash. It can also be seen that the Δp_{Base} increases much more steeply in Figure S12 compared to 5.2 (B), even though the process parameters are identical. Such a difference might be due to e.g., the spacers aging which can alter their physical form, affecting the scaling rate. To ensure optimal cleaning, the cleaning time needs to be adjusted for each case individually. The required time for the acid wash and the amount of moles of H^+ ions needed vs. the pressure-recovery are compared for both cells AEM-BPM and CEM-BPM stacks, Figure 5.9.

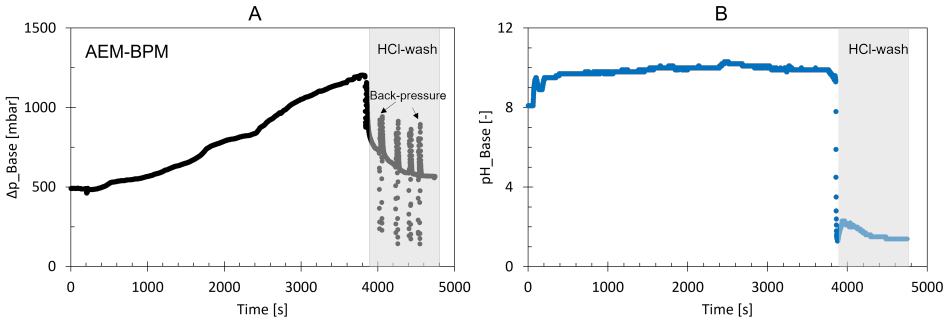

Figure 5.8: The development of the pressure drop (A) and base-pH (B) prior and during an acid wash for AEM-BPM configuration, using hydrochloric acid HCl with pH 1.5 and a flow rate of q = 72 ml min^{-1} per compartment for the scaling removal. The cell was 'scaled' the first hour under i = 12.5 mA cm^{-2} applied current density and q = 72 ml min^{-1} per compartment. After 3600 s, the current is turned off (thus, no voltage curve is measured/ shown during the cleaning). The acid wash starts (at 3864 s). Spikes during the acid wash show application of an (optional) back-pressure.

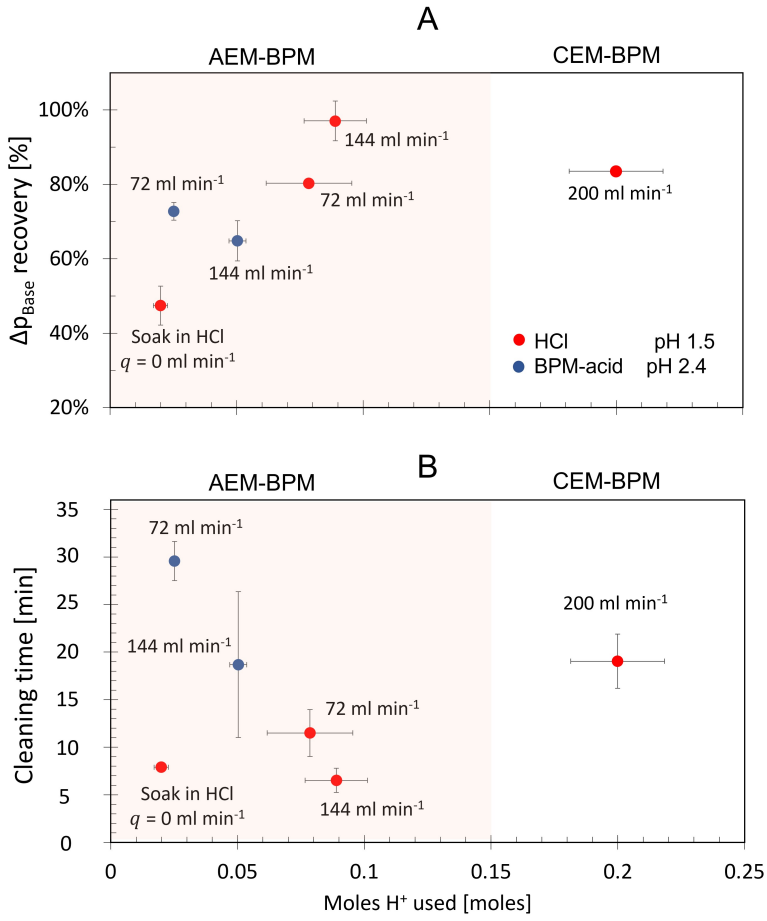

Figure 5.9: (A) Recovery of the stack pressure drop and (B) cleaning time required to achieve the shown pressure recovery upon acid wash vs. the amount of moles H^+ needed during the cleaning for the AEM-BPM cell (orange area) and BPM-CEM stack (white area). The cleaning time was noted when the pressure drop stabilized and would not decrease with time any further. Results are the average of two repetitions and the error bars show the standard errors between the repetitions.

In general, the pressure drop recovery for the AEM-BPM cell increases with the moles H^+ ions used (Figure 5.9 (A)-orange area); this is logical as "more H^+ used" reduces the base-pH more, enhancing the scaling dissolution. "Moles of H^+ ions used" is calculated via:

cleaning time× acid flow rate× H^+ ions concentration of the used acid.

The fouling removal with HCl acid delivers a higher Δp_{Base} recovery (by 20 – 40 % difference) in a 2-3× shorter time scale compared to the BPM-produced acid, Figure 5.9 (A, B)-red vs. blue bullets. These differences are probably due to the presence of various ions (e.g., Ca^{2+} and Mg^{2+} and DIC) in the BPM-produced acid that hinders the mineral dissolution and creates spots of high concentration (i.e., high mineral saturation index). Such higher ionic composition/ concentration increases the cleaning time and decreases the removal efficiency. Furthermore, the slightly higher efficiency of the HCl acid in scaling removal compared to the BPMED-acid can (also) be due to its lower pH (pH 1.5 vs. 2.4), which translates into ca. 8× higher H^+ ions concentration in the HCl acid.

Both used acids enable a chemical cleaning by dissolving the scaling. Increasing the acid flow should also contribute to an enhanced physical cleaning [40–43]; this can be seen as q = 144 ml min^{-1} HCl wash delivers 20 %-higher Δp_{Base}-recovery compared to the q 72 ml min^{-1} HCl-wash, Figure 5.9 (A)-orange area. However, for the BPMED-acid, the opposite holds as a higher flow velocity υ (i.e., flow rate) worsens the cleaning slightly compared to the 2× lower υ. As for the reason, it must be noted that scale formation is a multi-step complex process that involves nucleation, adhesion, and growth [53, 54]:

When removing the scaling mechanically, understanding the nucleation and crystal growth combined with hydrodynamics of the fouling-removal method is complex [55]. This complexity is reflected in different studies where contradictory results of higher scaling rates have been observed both in systems with increased [56–58] and reduced [59–63] fluid velocities and shear stresses. Theoretically, the flow velocity (υ) has a double effect on surface fouling [64], affecting the fouling deposition rate (i.e., proportional with the flow velocity) and its removal rate [64]. The fouling factor (in heat exchangers) is reported to be more sensitive to the flow velocity at low flow velocities with the sensitivity decreasing by increasing the flow velocity [64], this is observed in BPMED, as well [65]. From another point, in many membrane bio-film studies, a high hydrodynamic shear stresses makes the bio-film denser and thus more difficult to remove [66–70], which could also be the case for scaling here. We hypothesize that the effect of higher DIC, Ca^{2+}, Mg^{2+} ions concentration of BPMED-produced-acid on hindering the mineral dissolution (or even mineral compacting) overshadows the positive effect of a higher shear force for cleaning the scaling (i.e, detaching from the surface of the membrane/ mesh-spacer) [55]; explaining why a higher flow rate in the case of the BPM-acid lowers Δp_{Base} recovery instead of improving it, Figure 5.9, blue markers.

When comparing the HCl with BPM-acid for the AEM-BPM cell (Figure 5.9 (A)-red vs. blue markers), the gain in Δp_{Base} recovery in case of the HCl is not much higher than the latter. However, more than 2× the amount of H^+ ions is needed for cleaning with HCl compared to the BPM-acid. This can be clearly seen for q 72 ml min^{-1}, where 80 % Δp_{Base}-recovery using HCl vs. 73 % using BPM-produced-acid are obtained, while the amount of moles of H^+ ions used are 0.08 vs. 0.025, respectively. Furthermore, while no external chemicals/ costs are associated with using the BPM-produced acid, the HCl solution needs to be either bought separately or be produced with an additional BPMED cell, increasing the costs. An alternative for minimizing HCl use is “soaking the cell in HCl”, which is filling the base compartments with HCl and leaving the pumps off, allowing time for mineral dissolution; if so, ca. 50 % of the scaling buildup is cleaned using the

minimum amount of H^+ ions (Figure 5.9 (A)), which lowers the cleaning-chemical costs compared to the other cases.

As for the CEM-BPM cell, to achieve the same Δp_{Base}-recovery, more than twice higher H^+ ions are needed compared to the AEM-BPM cell. This is due to the (much) higher scaling buildup in the CEM-BPM stack (Figure 5.9 (A)-white area), as explained under Figure 5.2.

To put the required H^+ moles for scaling cleaning in perspective, both cell configurations extract ca. 81 ± 1 % of the input DIC, resulting in production of ca. 0.023 moles $CaCO_3$(s) after 60 min of experiment (based on three base compartments), which is unfortunately the same number of moles as the amount of H^+ required for cleaning via e.g., the "soak HCl" or BPM-acid 72 ml min^{-1} in Figure 5.9 (A). Hence, a more efficient use of the acid-wash should be studied in future work. On the bright side, it must be noted that the cleaning here is done for the stack under accelerated scaling conditions (section 5.5.9) of high current density of 12.5 mA cm^{-2} (with q = 72 ml min^{-1}). This is while using similar flow rate, but a lower current density of e.g., 5 mA cm^{-2} is already shown adequate for creating the required base-pH for DIC-extraction, see Chapter 4. We expect that, using the same flow rate, the experiment under 5 mA cm^{-2} should be able to be executed for at least $\frac{12.5}{5}$ = 2.5× longer than that of 12.5 mA cm^{-2}, before fouling removal is needed.

Furthermore, as the electrical energy consumption (thus voltage) has a much higher contribution to the final energy consumption than the pressure losses (Equation 5.1 and Figure S4), the cleaning is required mainly when the cell voltage is increased (and not necessarily the pressure drop). It is shown in Figure 5.2, that the cell voltage does not increase for the AEM-BPM for ca. 2 hrs even under the accelerated scaling condition of 15 mA cm^{-2}. In the worst-case scenario that the AEM-BPM cell voltage does increase drastically after $\left[\frac{15}{5} = 3\right]$ ×120 min = 6 hr of experiment under 5 mA cm^{-2} calling for an acid-wash, the required H^+ moles needed for cleaning is ≤ 17 % of the produced $CaCO_3$(s), making the cleaning step much more feasible.

5.4. CONCLUSION

This work investigates the fouling management scenarios to remove the mineral scaling in the alkaline compartments of the *in-situ* bipolar membrane electrodialysis (BPMED) - based oceanic carbon capture. The scaling buildup is measured indirectly through monitoring the increase in the total stack voltage and pressure-drop (in the alkaline compartments; Δp_{Base}). The rate of scaling buildup slows down by a (continuously) higher feed flow rate in combination with lower current density, due to the lower base-pH that lowers the hydroxide precipitation kinetics. Controlling the $i - t_r$ combination in such a way that the required base-pH for carbonate extraction is reached, but hydroxide containing minerals are avoided, is an efficient fouling control strategy. As for the membrane configuration, the stack voltage for the CEM-BPM configuration increases to 130 % within 30 min, while that of AEM-BPM remains constant for longer time, revealing beneficially lower scaling potential for the AEM. As for cleaning methods, air sparging, CO_2(g) sparging, CO_2(aq) saturated water cleaning, back- pressure, flow rate increase (5× and 15×), and acid wash (i.e., HCl solution and BPMED-based produced acid) are investigated. For both membrane configurations, the acid wash showed the highest recovery. The acid

wash using the BPM-produced acid (i.e., acidic seawater) needs no additional chemicals and is thus more sustainable than cleaning with HCl solution, even though cleaning with HCl results in a (slightly) higher recovery and shorter cleaning time. The back-pressure as a solo method is not effective enough for fouling removal, but helps decreasing the scaling rate. Air sparging increased the cell voltage and pressure drop even more because of stagnant bubbles that got trapped within the cell-spacers. CO_2(g) sparging does show suppression of the voltage and pressure drop increase (even though no full recovery is achieved), but causes negative DIC-removals, which is against the aim of the method (i.e., carbonate extraction). Based on our results, a combination of AEM-BPM based cell, operated under current density-flow rate combination that prevents $pH_{Base} > 10$ in the base compartment, followed by an acid wash-combined upon increase in the cell voltage, allows to control fouling in the *in-situ*-BPMED based carbonate mineralization from seawater.

5.5. SUPPORTING INFORMATION

5.5.1. FOULING CONTROL: EFFECT OF CELL CONFIGURATION AND PROCESS PARAMETERS

All experiments were carried out in a one-way single pass continuous mode. Four different current densities of i = 5, 10, 12.5 and 15 mA cm^{-2} in combination with two different flow rates of q = 24 and 72 ml min^{-1} per compartment (i.e., cell residence time of t_r = 7.3 and 2.4 s, respectively) were applied. These $i - t_r$ combinations were chosen in such a way that the (simulated) alkaline pH is between 9.6 < base-pH < 11.9. Higher base-pH was avoided to prevent precipitation of $Ca(OH)_2$, while lower base-pH was not desired due to the slow kinetics of mineral carbonate precipitation at pH < 9.5, see Chapter 4.

5.5.2. FOULING REMOVAL STRATEGIES

The effectiveness of fouling removal techniques was tested under accelerated scaling conditions to account for the worst-case scenario where the cell was 'pushed into scaling'. To do so, a current density of i = 12.5 and 15 mAcm^{-2}, cell residence time of t_r = 2.4 and 7.3 s(i.e., q = 72 and 24 ml min^{-1}) per compartment were used.

5.5.3. GAS SPARGING: AIR AND CARBON DIOXIDE

When using gas sparging, various factors including the gas type, sparging regime (i.e., duration/interval), presence of spacers, and gas pressure affect the cleaning performance [17, 22, 71–73]. In this work, gas sparging experiments were done with air and with CO_2(g), each in separate experiments. The gas was inserted into the feed using a T-joint. Only the base compartments were sparged with gas, Figure S1.

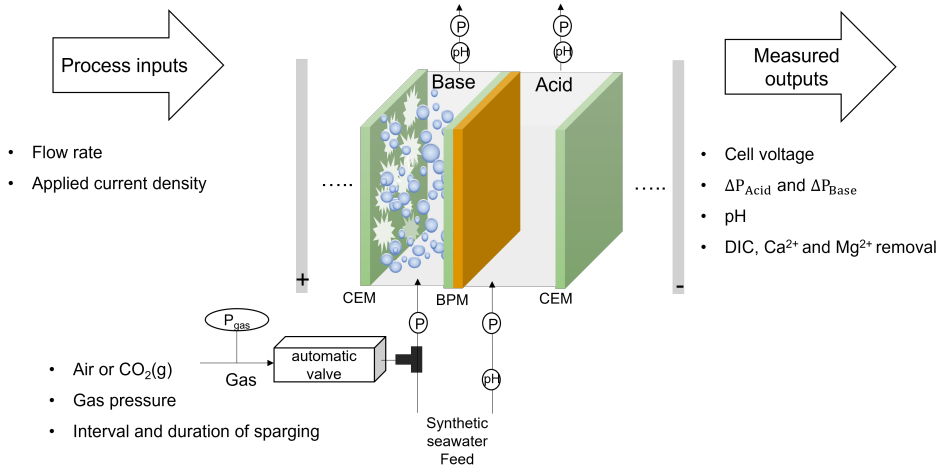

Figure S1: Illustration of the gas sparging in the base compartments (acid compartments were not sparged). The output refers to measured parameters during the experiment which are logged and saved every second. Gaseous CO_2(g) and air were supplied from gas pipes present in the lab. An automated valve was used for the gas which could be opened and closed according to defined interval and duration.

5.5.4. DISSOLVED CARBON DIOXIDE CLEANING

In addition to the gaseous CO_2(g) sparging, the performance of CO_2(a) saturated demi-water is investigated for the AEM-BPM cell. A 5 L water bottle filled with demi-water was purged with pure CO_2(g) (pressure ca. 1.2 atm) with flow rate of 500 ml min^{-1} for 10 min, to reach pH 3.9. Carbon dioxide has a solubility in water of ca. 1.27 g L^{-1} at 1 atm at 25°C [17], that is reached at this pH (based on our MINTEQ calculations). After one hour of experiments (under i = 12.5 mA cm^{-2} and q = 72 ml min^{-1} per compartment with +CABABAB- cell configuration), the current was turned off and the CO_2(aq) saturated water was injected into the base compartments with flow rate of q = 72 ml min^{-1} per compartment for 60 s. Using the potentiostat, the stack resistance before and after this "cleaning" was measured. The experiments were done at least for 2 cycles, based on the following current mode for each cycle (Table S1):

5.5.5. TEMPORARY INCREASE OF THE FLOW RATE IN THE BASE CHANNELS:PURGE FLOW

The feed flow rate of the base compartments was increased every 10 min, starting 5 min after the start of the experiment (for a 60 min experiment).

Table S1: The current interruption scheme done using the potentiostat to measure the performance of the cleaning method, by comparing the cell resistance before and after the cleaning.

Each cycle	Time [s]	Aim
open cell	60	To measure open circuit voltage (OCV)
12.5 mA cm^{-2}	3600	Using AEM-BPM cell
open cell	60	To measure cell resistance before cleaning
open cell	60	Cleaning with CO_2(aq) saturated water
12.5 mA cm^{-2}	60	Using AEM-BPM cell
open cell	60	To measure cell resistance after cleaning

5.5.6. BACK-PRESSURE

Back-pressure was applied by briefly closing the valve located at the outlet of the base channel while leaving the feed pumps on, causing pressure to build up in the base compartments (up to 3 bar measured with analog pressure gauge). By reopening the valve, this pressure is released suddenly, pushing scaling out of the cell. The back-pressure was applied every 10 min, for ca. 5 s, starting 5 min after the start of the experiment (for experiments of 60 min).

The back-pressure was tested on its own, as well as in combination with gas sparging and acid-wash methods to increase the cleaning performance.

5.5.7. CHEMICAL CLEANING: ACID WASH

A diluted hydrochloric acid HCl solution with a pH 1.5 - 2, as well as produced acid from the BPMED cell with pH 2.4 - 2.6 (and thus including all ions present in synthetic seawater) were tested for the "acid wash". The advantage of the latter is that no external HCl chemical is needed in the process. However, the disadvantage is that the presence of Ca^{2+} and Mg^{2+} in the produced-acid can complicate the cleaning step by reacting with anions e.g., OH^- and $CO_3{}^{2-}$ ions. Before testing the effectiveness of the acid-wash, 60 min experiments with i = 12.5 mA cm^{-2} and flow rate of 72 ml min^{-1} per compartment (t_r = 2.4 s) were conducted first.

In addition to the CEM-BPM configuration, acid wash was also done for the AEM-BPM configuration. For the CEM-BPM configuration, acid wash was done at high flow rate of 200 ml min^{-1} per compartment with HCl (lower acid flow rates were not sufficient to clean the cell within 30 min).

For the AEM-BPM cell configuration, in addition to the type of acid used for cleaning, the effect of the acid flow rate q was also investigated; acid feed was flushed with q = 72 and 144 ml min^{-1} per compartment. Furthermore, back-pressure on the base channels was applied to ensure the channels were filled with acid and to help pushing out any undissolved scaling upon reopening the valve. The current was turned off during the acid cleaning. The cleaning was performed until the pressure drop of the base channel showed a stable value, not recovering any further. The efficiency of the cleaning method was studied by measuring the amount of needed H^+ ion moles and the required cleaning time.

Finally, experiments were done where the base compartments of the cell were “soaked”

in HCl for 5 min; meaning that the base compartments were filled with acid and then the pumps were turned off ($q = 0$) for 5 min.

5.5.8. THE OHMIC RESISTANCE OF THE STACK, MEASURED VIA CURRENT INTERRUPTION

Ohmic resistance is determined via the voltage-time curve; when the current is turned off the Ohmic loss becomes zero by its definition. By comparing the $i \times R_{Ohmic}$ values before and after the experiment, the Ohmic resistance increase was determined. As an example, in Figure S2, the CEM-BPM configuration is much more prone to scaling even under the same current and flow rate applications, as discussed in the main text (ΔR_{Ohmic} in Ω in Table S2). The initially higher resistance of the CEM-BPM is probably due to the aging of the charged membranes due to usage [74]. The remaining voltage (after the current is turned off) shows the non-ohmic voltage, which as can be seen in Figure S2, remains the same for AEM-BPM and CEM-BPM configurations.

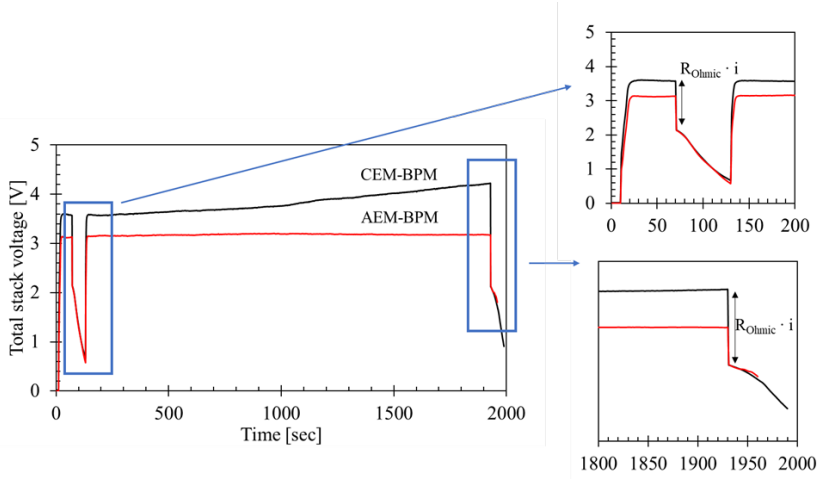

Figure S2: Ohmic resistance before and after a 30 min experiment, measured through current interruption. These experiments were done for 72 ml min^{-1} per compartment under 12.5 mA cm^{-2} applied current density.

Similarly, the difference in Ohmic resistance before and after the experiments for all 16 experiments of cell configuration $i - t_r$ comparison is shown in Figure S3.

Table S2: Increase in Ohmic resistance for Figure S2. The active membrane size is 100 cm^2.

Values [Ω]	For the AEM-BPM	For the CEM-BPM
R_{Ohmic} before scaling takes place [Ω]	0.8	1.18
R_{Ohmic} after the stack is scaled [Ω]	0.88	1.7
ΔR_{Ohmic} [Ω]	0.03	0.53

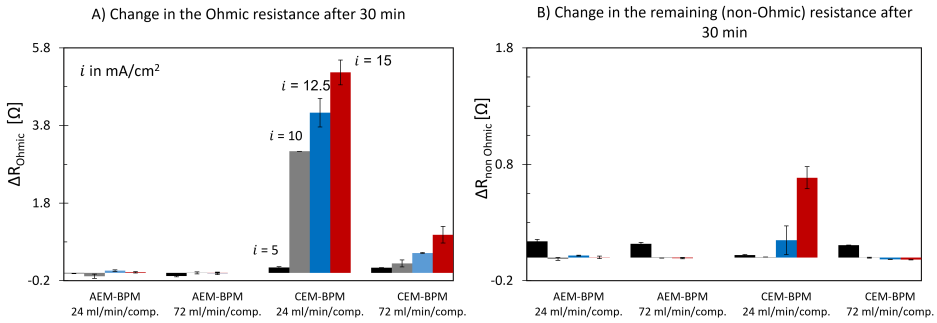

Figure S3: The difference in (A) Ohmic resistance (ΔR_{Ohmic}) and (B) remaining (non-Ohmic) resistances after 30 min experiment between the two tested cell configurations. The average of two repetitions (standard error included with error bars) are shown. Flow rates of q = 72 ml min^{-1} and 24 ml min^{-1} show a cell residence time t_r of 2.4 s and 7.3 s, respectively. Four different current density of 15 mA cm^{-2} (red), 12.5 (blue), 10 (grey), and 5 (black) are shown.

The higher Ohmic resistances (i.e., voltage loss), increases the electrical energy consumption while a higher scaling buildup increases Δp_{Base} and thus the pumping energy. However, the stack-electrical energy is much higher than the pumping energy, making the cell voltage a more important parameter to set the fouling strategies on compared to Δp_{Base}. In experiments shown in Figure S4, no attempt in decreasing the stack-electrical energy consumption is made and the values in kJ mol^{-1} $CaCO_3$ (s) should not be seen as an indication of an optimised process (see Chapter 4), but only to show the ratio of the stack-electrical energy consumption to that of pumping.

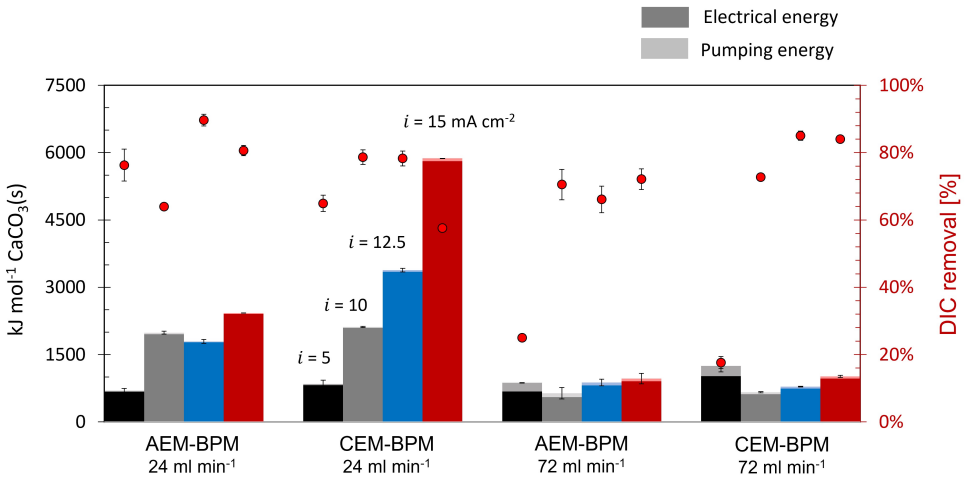

Figure S4: Total electrical energy consumption (Equation 5.1) for the AEM-BPM and CEM-BPM configuration for experiments of 30 min, under cell residence time of t_r 2.4 and 7.3 s (i.e., q = 72 and 24 ml min^{-1}, respectively) and applied current densities of i of 5, 10, 12.5 and 15 mA cm^{-2} (from left to right). Distinctions are made between stack-electrical energy (dark colour) and pumping energy (light colour). The red (right) y-axis shows the DIC-removal (%) measured via HCl-titration (see 4.6). The markers are the average of two repetitions with the standard errors included via the error bars. For the AEM-BPM configuration at i = 5 mA cm^{-2}, the measured DIC is very low at 20 - 30 %, even though longer experiment of ca. 60 min always enable a higher DIC-removal ca. 80 %, thus reducing the stack-electrical enegy consumption by a factor of 3.

5.5.9. ON THE ACCELERATED SCALING CONDITION

The water dissociation reaction (i.e., H^+ and OH^- ions production via the BPM) increases with current density and cell residence time, Figure S5. As a result of this increase of the OH^- ions concentration, the pH in the alkaline compartment increases, converting bicarbonate ions to carbonates, increasing the saturation index of carbonate ions and enabling its carbonate minerals precipitation, subsequently. The simulated alkaline pH (before any precipitation takes place) ranges between pH 9.9 - 11.9, increasing with current density and cell residence time. Thermodynamically, at pH ≥ 9.9, more than 97 % of the dissolved inorganic carbon (ca. 0.0021 mM $CaCO_3$(s)) can be removed as calcium carbonate (see Chapter 4). The excess OH^- will precipitate as hydroxide mineral, mainly as brucite $Mg(OH)_2$(s). For alkaline pH ≥ 9.9, the higher the current density and cell residence time (i.e., higher alkaline pH), the more brucite precipitates, while $CaCO_3$(s) precipitation remains constant, Figure S5 (B). Due to the fast kinetics of brucite $Mg(OH)_2$(s), it is thus expected that the $i - t_r$ combinations that establish higher alkaline pH, generate more scaling inside of the cell.

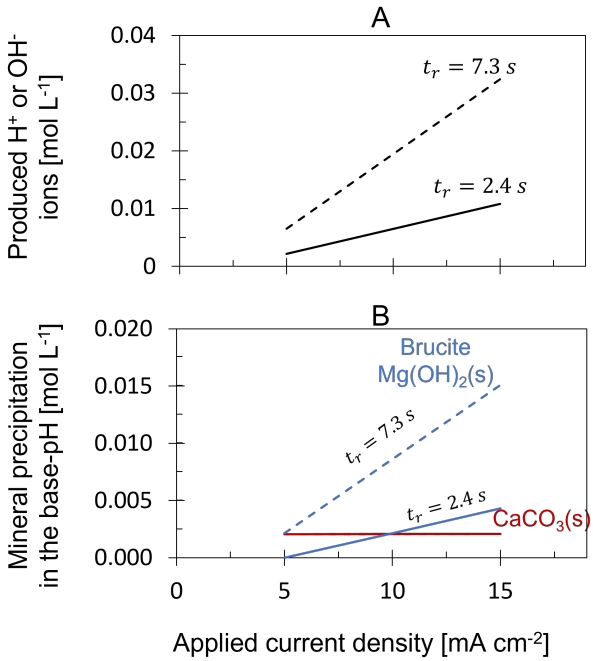

Figure S5: The simulated thermodynamic equilibrium in the bulk showing (A) OH^- and H^+ ions production via water dissociation and (B) mineral precipitation (in the base compartments) at each current density and cell residence time (t_r). The cell residence time t_r of 7.3 s and 2.4 s correspond to flow rates of $q = 24$ ml min^{-1} and 72 ml min^{-1} per compartment, respectively. Calculations are done assuming ionic compositions conform Table 4.1, 100 % BPM current efficiency, ideally selective membranes, Na^+ and Cl^- ions as main charge carriers (over the CEM and AEM, respectively), following procedure in Chapter 3 and 4).In (B), the calcium carbonate precipitation remains the same for both cell residence time. The simulations show an upper limit as the effect of kinetics and locally different pH inside the stack are not considered.

5.5.10. EFFECT OF PROCESS PARAMETERS ON THE PRESSURE DROP

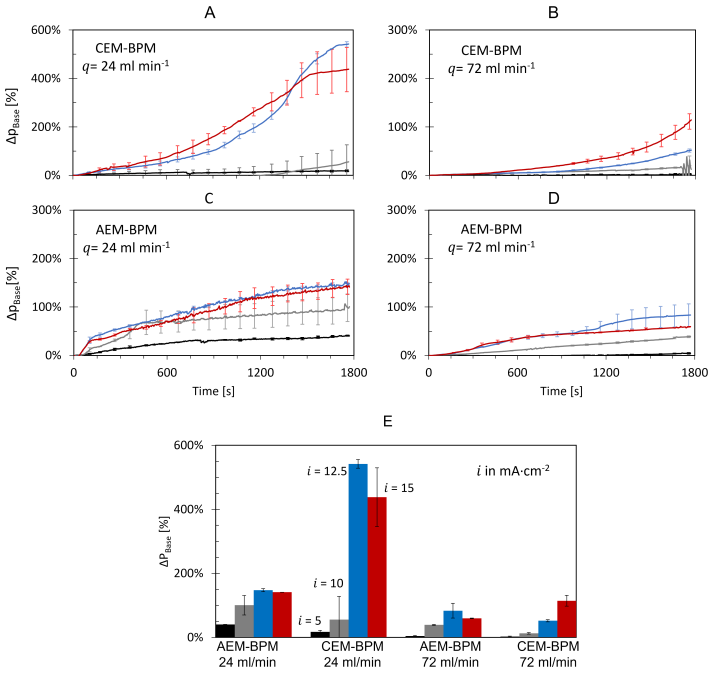

Figure S6: The measured experimental Δp_{Base} vs. time for two cell configurations (A, B: CEM-BPM, and C, D: AEM-BPM), four current densities (red 15, blue 12.5, grey 10, and black 5 mA cm^{-2}) and two flow rates (q = 72 and 24 ml min^{-1} per compartment). The error bars are the standard deviation between two repetitions. (E) shows the change in Δp_{Base} at the end of each experiments compared to its initial value.

Δp_{Base} increases with applied current density and t_r as the result of scaling in the base-compartments. The increase in % is calculated via:

$$\Delta p_{Base}[\%] = \frac{\Delta p_t - \Delta p_{t_0}}{\Delta p_{t_0}} \tag{S1}$$

Δp_{t_0} is the initial Δp_{Base} at the start of the experiment $t_0 = 0$.

5.5.11. CHARGE DENSITY

The charge density can be calculated via:

$$\text{Charge density} = \frac{I}{qF} = \frac{I \times t_r}{V_{eff} F} \tag{S2}$$

Where the charge density is in mol L^{-1}, I is the applied current in A, q the flow rate in L s^{-1}, F the Faraday constant of 96485 C mol^{-1}, t_r the cell residence time in s, V_{eff} the effective compartment volume in L. Here $V_{eff} = V_{tot} \times \varepsilon$, with ε the spacer porosity [-], and V_{tot} the total compartment volume in L $V_{tot} = l \times W \times d$ resulted from multiplying

the compartment length, width and thickness (see Table S3). The spacer porosity ε is calculated using the spacer's volume V_{sp} (through its weight 150 $g\,m^{-2}$, area 100 cm^2, and density 1.38 $g\,cm^{-3}$) via $\varepsilon = 1 - \frac{V_{sp}}{V_{tot}}$ [39], where V_{tot} is the total cell volume equal to 4 ml.

To compare the scaling buildup under accelerated fouling conditions (e.g., q = 24 $ml\,min^{-1}$), the graph of cell voltage (for the stack with BPM-CEM configurations) vs. the charge density×time is shown in Figure S7. The cell voltage is corrected for the ohmic voltage by subtracting the initial voltage (V_{ini}) at each step to account for the effect of the current density on voltage. For the AEM-BPM stack, the voltage values change within 10 mV range, not enabling a comparison between the different current density cases, but the pressure drop increase graph demonstrate the relation between the accelerated fouling conditions (A. C) and the normal conditions (B, D), Figure S8. The values of charge density are shown in Table S3.

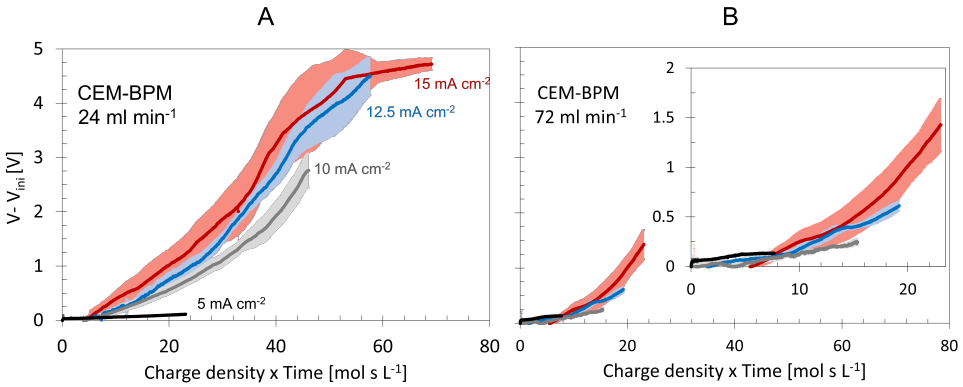

Figure S7: The cell total voltage minus the initial voltage V_{ini} (to correct for the effect of different current densities on voltage) vs. the charge density × time for the CEM-BPM stack for (A) the accelerated fouling condition under flow rate of q = 24 $ml\,min^{-1}$ and (B) the normal condition (with a zoomed in window shown). the error bars show the standard errors between repetitions. Four different current densities of 15 (red), 12.5 (blue), 10 (grey), and 5 (black) $mA\,cm^{-2}$ are used.

Table S3: The charge density (in mol L^{-1}) at each flow rate and current density combination (in mA cm^{-2}). Flow rates of q = 72 ml min^{-1} and 24 ml min^{-1} show a cell residence time t_r of 2.4 s and 7.3 s, respectively.

q [ml min^{-1}]	5 [mA cm^{-2}]	10	12.5	15
Charge density at q = 72	0.0043	0.0086	0.0108	0.0130
Charge density at q = 24	0.0130	0.0259	0.0324	0.0389

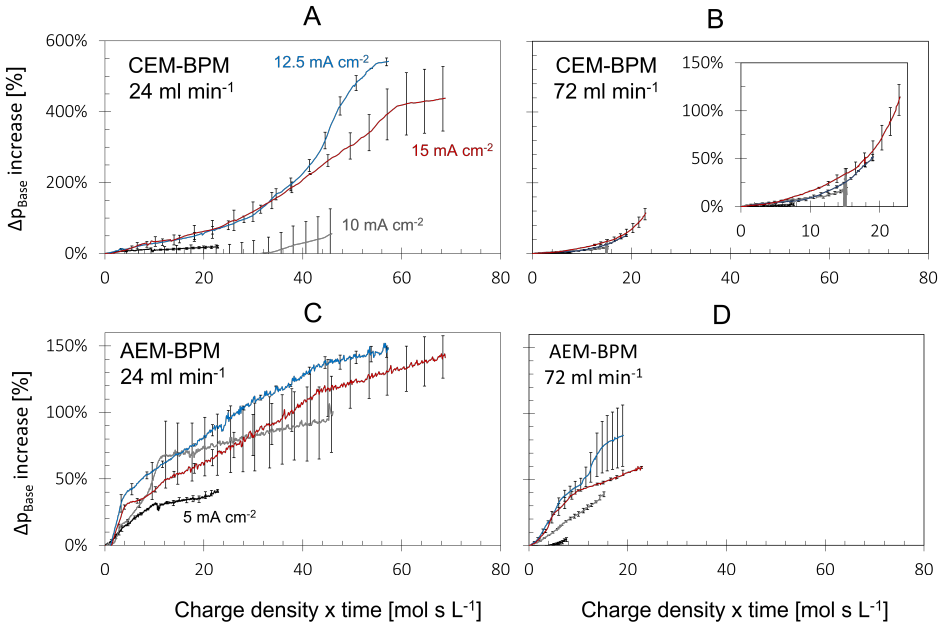

Figure S8: The increase in the Δp_{Base} vs. the charge density × time for the two configurations for (A, C) the accelerated fouling condition under flow rate of q = 24 ml min^{-1} and (B, D) the normal condition (with a zoomed in window shown for B). the error bars show the standard errors between repetitions. Four different current densities of 15 (red), 12.5 (blue), 10 (grey), and 5 (black) mA cm^{-2} are used.

5.5.12. RESULTS ON GAS SPARGING: AIR AND CARBON DIOXIDE

Gaseous CO_2(g) sparging does not always remove the scaling, but its performance depends on the sparge regime, Figure S9 vs. 5.5. However, for the oceanic carbon capture via BPMED, such CO_2(g) sparge results in negative DIC removals which goes against the goal of carbon capture. CO_2 sparging under 3 bar CO_2 can suppress the increase of voltage and pressure drop, Figure S9 (A,B). Voltage and Δp_{Base} increased ca. 50 % and 700 % less when CO_2(g) sparging-cleaning was used compared to the reference experiment where no cleaning was applied.

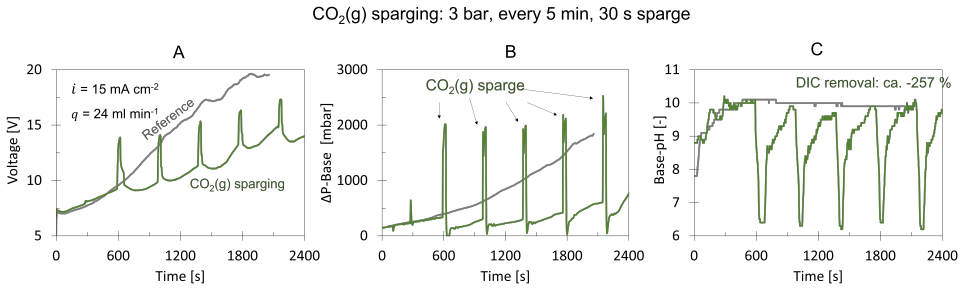

Figure S9: Gaseous CO_2 sparging regimes for fouling removal in the CEM-BPM cell. (A) The total cell voltage increase, (B) pressure drop increase over the base compartments, and (C) bulk pH in the outlet from the base compartment versus time (plus the DIC-removal) with regards to the reference experiment (i.e., no cleaning method, grey line).

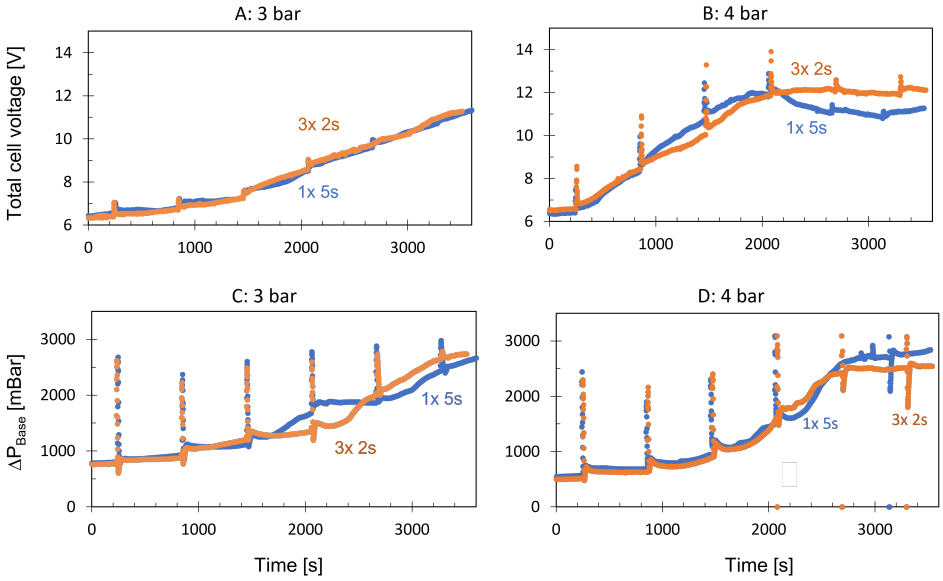

Figure S10: Comparison of a air sparging with 3× 2s regime with that of 1× 5s between 3 and 4 barg sparging pressure, for (A, B) voltage and (C, D) Base-pressure drop using a CEM-BPM configuration under i = 12.5 mA cm^{-2} and q = 72 ml min^{-1}.

5.5.13. RESULTS ON DISSOLVED CARBON DIOXIDE CLEANING

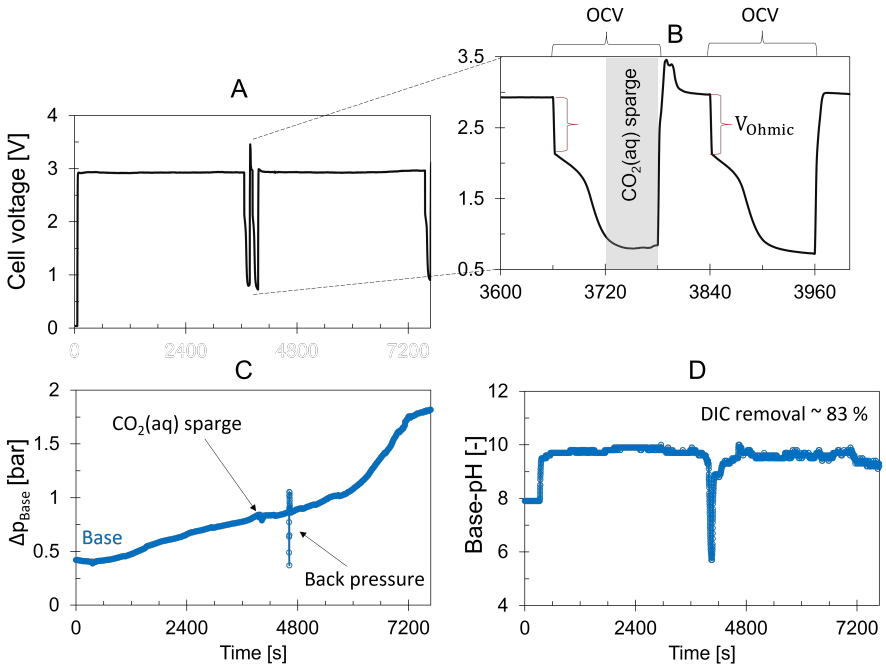

Figure S11: Comparison of (A, B) The total cell voltage (excluding the redox voltage), (C) pressure drop increase over the base compartments, and (D) bulk pH in the outlet from the base compartment (as well as the final measured averaged DIC-removal, with 5 % error) versus time for the 3 cell-unit stack with configuration of +CABABAB-. Scaling cleaning is done with dissolved CO_2(aq) in demi-water. The CO_2 saturated demi-water is injected with pH 3.9 and q = 72 ml min^{-1} per compartment (within the current turn-off period, Table S1), after 60 min of experiment under accelerated fouling condition of i = 12.5 mA cm^{-2} and q = 72ml min^{-1} per compartment (t_r = 2.4 s). (B) shows the zoomed in version of (A), with the cleaning time (60 s) and (irreversible) ohmic-voltage loss contribution (measured via current-interruption) shown. OCV stands for the open circuit voltage (i.e., the cell voltage when the current is turned off).

The cell voltage (Figure S11 (A, B)) using the AEM-BPM cell does not increase under process conditions of Figure S11. However, the increase in the pressure drop over the base compartment with time (Figure S11 (C)-blue) reveals scaling buildup in base-compartments. At 3720 s, for a duration of 60 s (> 37× the cell residence time t_r to ensure multiple times stack-refill), CO_2(aq)-saturated demi-water is pumped in the base compartments (instead of the synthetic seawater feed), which causes a small jump in the pressure drop curved (Figure S11 (C)) and a sudden decrease in pH of the base outlet (Figure S11 (D)). At 4800 s, back-pressure is applied to enhance the cleaning (upon valve release), which shows as a sudden spike in the Δp_{Base} graph, Figure S11 (C).

However, the CO_2(aq)-saturated demi-water flush does not recover the pressure buildup in the base compartments, Figure S11 (C). Therefore, even though it is shown to be a very effective fouling removal in RED [17], it does not clean the BPMED-stack. The reason probably is the high OH^- ions flux from each bipolar membrane into the base com-

partment (i.e., $\frac{(12.5-2.5)\,\mathrm{mA\,cm^{-2}} \times 100\,\mathrm{cm^2}}{96485\,\mathrm{C\,mol^{-1}}} \simeq 0.01\ \mathrm{mmol\,s^{-1}}$), which increases the Base-pH rapidly and promotes scaling precipitation. A longer cleaning interval might be able to remove part of the fouling but comes with the expense of a reduced DIC-removal rate (as explained under 5.3.4). Besides, for this cleaning method, demineralized water is needed which adds to the required chemicals and thus the final carbon capture costs. Under the setting of Figure S11, ca. 83 ± 5 % of the initial DIC was removed from the seawater which is acceptable for OCDR. The DIC-removal is measured indirectly via titration with HCl acid, according to the procedure in section 4.6.

5.5.14. RESULTS ON ACID-WASH

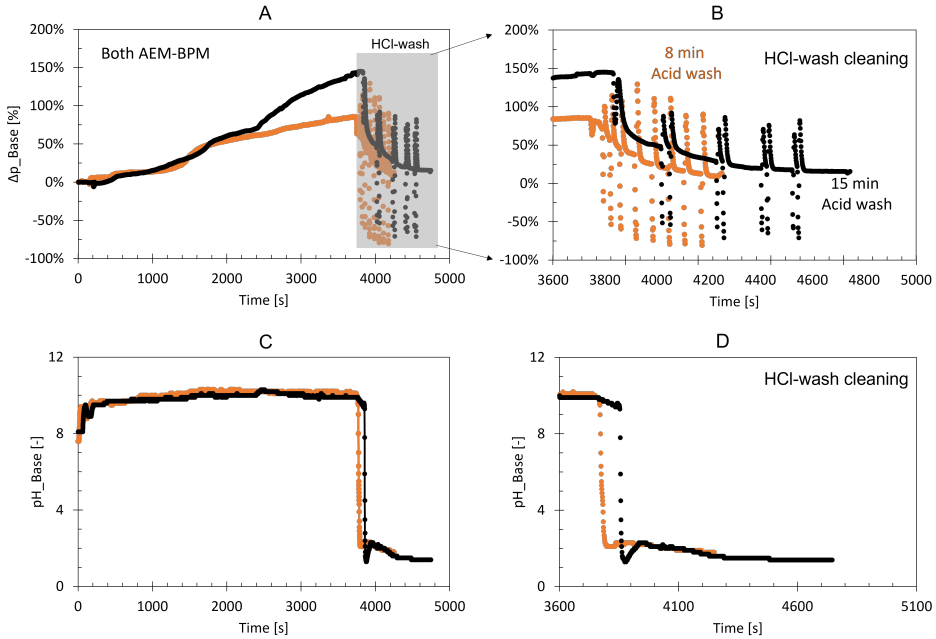

Figure S12: The development of the pressure drop (A, B) and base-pH (C,D) prior and during an acid wash for two experiments with AEM-BPM configuration, using hydrochloric acid HCl with pH 1.5 and a flow rate of 72 $\mathrm{ml\,min^{-1}}$ per compartment for the scaling removal. In both cases, the cell was 'scaled' the first hour under i = 12.5 $\mathrm{mA\,cm^{-2}}$ applied current density and q = 72 $\mathrm{ml\,min^{-1}}$ per compartment. After 3600 s, the current is turned off (thus, no voltage curve is measured/ shown during the cleaning) and acid wash starts (zoomed in B and D). Spikes during the acid wash show application of an (optional) back-pressure that can accelerate the cleaning rate, thus decreasing the cleaning time.

In all acid-wash experiments, the pressure drop in the base compartment and the base-pH decrease. The pH, cleaning time, and velocity of the acid determines the effectiveness of the cleaning. Even under the exact same process parameters (i.e., i and q), the amount and location of the scaling in the cell is not reproducible. This can be seen in the pressure drop developments in Figure S12 (A) where, even though both experiments

(shown in black and orange) are performed identically, one has a higher scaling buildup and thus require a longer cleaning time (15 min vs. 8 min), S12 (B). This is despite the fact that in both experiments similar base-pH is developed during the 3600 s of current application S12 (C, D).

5.5.15. CHANNEL FORMATION INSIDE THE SPACERS

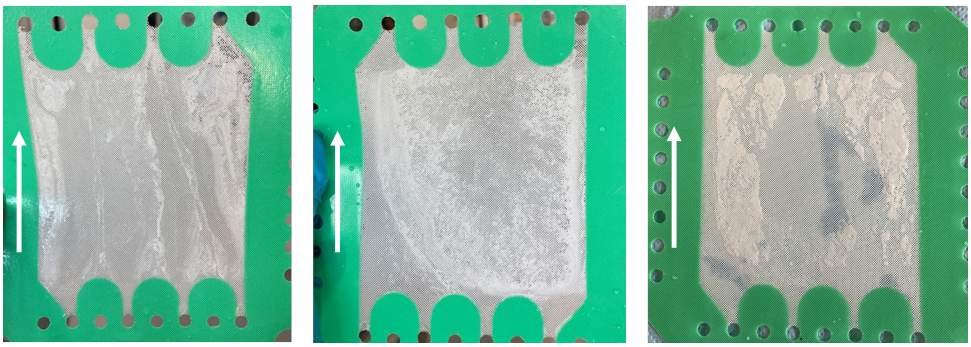

Figure S13: Channel formation on the alkaline compartments as result of scaling on spacers. The white arrow shows the flow direction. Photos were taken after an experiment with q = 72 ml min^{-1} flow rate and i 12.5 mA cm^{-2} applied current using a CEM-BPM configuration.

BIBLIOGRAPHY

[1] J. Rogelj et al. “Paris Agreement climate proposals need a boost to keep warming well below 2 degree C”. In: *Nature* 534.7609 (2016), pp. 631–639.

[2] A. T. Fane. “A grand challenge for membrane desalination: More water, less carbon”. In: *Desalination* 426 (2018), pp. 155–163.

[3] S. El-Manharawy et al. “Study of seawater alkalization as a promising RO pretreatment method”. In: *Desalination* 153.1-3 (2003), pp. 109–120.

[4] T. Altmann et al. “Process improvement of sea water reverse osmosis (SWRO) and subsequent decarbonization”. In: *Desalination* 499 (2021), p. 114791.

[5] N. Harlev et al. “Acidification and decarbonization in seawater: Potential pretreatment steps for biofouling control in SWRO membranes”. In: *Desalination* 467 (2019), pp. 86–94.

[6] E. Al-Dhubhani et al. “Entanglement-Enhanced Water Dissociation in Bipolar Membranes with 3D Electrospun Junction and Polymeric Catalyst”. In: *ACS Appl. Energy Mater* (Mar. 2021).

[7] E. Al-Dhubhani et al. “Performance of five commercial bipolar membranes under forward and reverse bias conditions for acid-base flow battery applications”. In: *Journal of Membrane Science* 640 (2021), p. 119748.

[8] R. Parnamae et al. “Bipolar membranes: A review on principles, latest developments, and applications”. In: *Journal of Membrane Science* 617 (2021), p. 118538.

[9] C. Y. Tang et al. “Colloidal interactions and fouling of NF and RO membranes: A review”. In: *Advances in Colloid and Interface Science* 164.1 (2011). Membrane Separation and Colloid Science, pp. 126–143.

[10] C. Bellona et al. “The effect of organic membrane fouling on the properties and rejection characteristics of nanofiltration membranes”. In: *Separation and Purification Technology* 74.1 (2010), pp. 44–54.

[11] B. Mi et al. “Organic fouling of forward osmosis membranes: Fouling reversibility and cleaning without chemical reagents”. In: *Journal of Membrane Science* 348.1 (2010), pp. 337–345.

[12] V. Parida et al. “Forward osmosis organic fouling: Effects of organic loading, calcium and membrane orientation”. In: *Desalination* 312 (2013). Recent Advances in Forward Osmosis, pp. 88–98.

[13] K. O. Agenson et al. “Change in membrane performance due to organic fouling in nanofiltration (NF) and reverse osmosis (RO) applications”. In: *Separation and Purification Technology* 55.2 (2007), pp. 147–156.

[14] E. Bodner et al. “The RED Fouling Monitor: A novel tool for fouling analysis”. In: *Journal of Membrane Science* 570-571 (2019), pp. 294–302.

[15] G. Amy. “Fundamental understanding of organic matter fouling of membranes”. In: *Desalination* 231.1 (2008), pp. 44–51.

[16] B. Vital et al. “Fouling fractionation in reverse electrodialysis with natural feed waters demonstrates dual media rapid filtration as an effective pre-treatment for fresh water”. In: *Desalination* 518 (2021), p. 115277.

[17] J. Moreno et al. “CO2 saturated water as two-phase flow for fouling control in reverse electrodialysis”. In: *Water research* 125 (2017), pp. 23–31.

[18] D. A. Vermaas et al. “Fouling in reverse electrodialysis under natural conditions”. In: *Water research* 47.3 (2013), pp. 1289–1298.

[19] S. Mikhaylin et al. “Fouling on ion-exchange membranes: Classification, characterization and strategies of prevention and control”. In: *Advances in colloid and interface science* 229 (2016), pp. 34–56.

[20] Z. Wang et al. “Extracellular polymeric substances (EPS) properties and their effects on membrane fouling in a submerged membrane bioreactor”. In: *Water Research* 43.9 (2009), pp. 2504–2512.

[21] H. Guo et al. “Mechanisms of chemical cleaning of ion exchange membranes: A case study of plant-scale electrodialysis for oily wastewater treatment”. In: *Journal of Membrane Science* 496 (2015), pp. 310–317.

[22] D. A. Vermaas et al. “Periodic feedwater reversal and air sparging as antifouling strategies in reverse electrodialysis”. In: *Environmental science & technology* 48.5 (2014), pp. 3065–3073.

[23] D. Pintossi et al. “Electrochemical impedance spectroscopy of a reverse electrodialysis stack: A new approach to monitoring fouling and cleaning”. In: *Journal of Power Sources* 444 (2019), p. 227302.

[24] R. Kingsbury et al. “Impact of natural organic matter and inorganic solutes on energy recovery from five real salinity gradients using reverse electrodialysis”. In: *Journal of Membrane Science* 541 (2017), pp. 621–632.

[25] T. Rijnaarts et al. “Role of anion exchange membrane fouling in reverse electrodialysis using natural feed waters”. In: *Colloids and surfaces A: Physicochemical and engineering aspects* 560 (2019), pp. 198–204.

[26] C. Casademont et al. “Impact of electrodialytic parameters on cation migration kinetics and fouling nature of ion-exchange membranes during treatment of solutions with different magnesium/calcium ratios”. In: *Journal of membrane Science* 325.2 (2008), pp. 570–579.

[27] A. Moya. “Uphill transport in improved reverse electrodialysis by removal of divalent cations in the dilute solution: A Nernst-Planck based study”. In: *Journal of Membrane Science* 598 (2020), p. 117784.

[28] J. Moreno et al. “Mitigation of the effects of multivalent ion transport in reverse electrodialysis”. In: *Journal of membrane science* 550 (2018), pp. 155–162.

[29] Y. Zhao et al. “A novel technology of carbon dioxide adsorption and mineralization via seawater decalcification by bipolar membrane electrodialysis system with a crystallizer”. In: *Chem. Eng. J* 381 (8 2020), p. 122542.

[30] C. F. de Lannoy et al. “Indirect ocean capture of atmospheric CO2: Part I. Prototype of a negative emissions technology”. In: *International Journal of Greenhouse Gas Control* 70 (2018), pp. 243–253.

[31] M. Hansima et al. “Fouling of ion exchange membranes used in the electrodialysis reversal advanced water treatment: A review”. In: *Chemosphere* 263 (2021), p. 127951.

[32] J. Gilron et al. “Prevention of precipitation fouling in NF/RO by reverse flow operation”. In: *Desalination* 199.1 (2006), pp. 29–30.

[33] J. W. Post. *Blue Energy: electricity production from salinity gradients by reverse electrodialysis*. Wageningen University and Research, 2009.

[34] D. Potts et al. “A critical review of fouling of reverse osmosis membranes”. In: *Desalination* 36.3 (1981), pp. 235–264.

[35] J. Veerman et al. “Reverse electrodialysis: evaluation of suitable electrode systems”. In: *Journal of Applied Electrochemistry* 40.8 (2010), pp. 1461–1474.

[36] D. A. Vermaas et al. “Early detection of preferential channeling in reverse electrodialysis”. In: *Electrochimica acta* 117 (2014), pp. 9–17.

[37] A. Haidari et al. “Effect of spacer configuration on hydraulic conditions using PIV”. In: *Separation and purification technology* 199 (2018), pp. 9–19.

[38] J. Vrouwenvelder et al. “Biofouling in spiral wound membrane systems: Three dimensional CFD model based evaluation of experimental data”. In: *Journal of Membrane Science* 346.1 (2010), pp. 71–85.

[39] G. Schock et al. “Mass transfer and pressure loss in spiral wound modules”. In: *Desalination* 64 (1987), pp. 339–352.

[40] O. Le Berre et al. “Skimmilk crossflow microfiltration performance versus permeation flux to wall shear stress ratio”. In: *Journal of Membrane Science* 117.1-2 (1996), pp. 261–270.

[41] K. R. Goode et al. “Fouling and cleaning studies in the food and beverage industry classified by cleaning type”. In: *Comprehensive Reviews in Food Science and Food Safety* 12.2 (2013), pp. 121–143.

[42] Y. Wibisono. “Two-phase flow for fouling control in membranes”. In: (2014).

[43] W. Zhang et al. “Membrane cleaning assisted by high shear stress for restoring ultrafiltration membranes fouled by dairy wastewater”. In: *Chemical Engineering Journal* 325 (2017), pp. 457–465.

[44] E. Seran et al. “What we can learn from measurements of air electric conductivity in 222Rn-rich atmosphere”. In: *Earth and Space Science* 4.2 (2017), pp. 91–106.

[45] E. Cornelissen et al. “Periodic air/water cleaning for control of biofouling in spiral wound membrane elements”. In: *Journal of Membrane Science* 287.1 (2007), pp. 94–101.

[46] D. F. Elger et al. *Engineering fluid mechanics*. John Wiley & Sons, 2020.

[47] Y. Son. "Determination of shear viscosity and shear rate from pressure drop and flow rate relationship in a rectangular channel". In: *Polymer* 48.2 (2007), pp. 632–637.

[48] J. Vrouwenvelder et al. "Biofouling of spiral-wound nanofiltration and reverse osmosis membranes: a feed spacer problem". In: *water research* 43.3 (2009), pp. 583–594.

[49] D. A. Vermaas et al. "Enhanced mixing in the diffusive boundary layer for energy generation in reverse electrodialysis". In: *Journal of membrane science* 453 (2014), pp. 312–319.

[50] D. A. Vermaas et al. "Ion transport mechanisms in bipolar membranes for (photo) electrochemical water splitting". In: *Sustain. Energy Fuels* 2 (9 2018), pp. 2006–2015.

[51] K. L. Mercer et al. "Enhancing calcium carbonate precipitation by heterogeneous nucleation during chemical softening". In: *Journal-American Water Works Association* 97.12 (2005), pp. 116–125.

[52] M. Brian S. Freeman. "Flow and Velocity". In: *Anesthesiology Core Review: Part One Basic Exam*. Ed. by B. S. Freeman et al. New York, NY: McGraw-Hill Education, 2014.

[53] A. Alabi et al. "Advances in anti-scale magnetic water treatment". In: *Environmental Science: Water Research & Technology* 1.4 (2015), pp. 408–425.

[54] A. Yi-Tsung Lu et al. "Nucleation and crystallization kinetics of barium sulfate in the hydrodynamic boundary layer: An explanation of mineral deposition". In: *Crystal Growth & Design* 21.3 (2021), pp. 1443–1450.

[55] I. A. Løge et al. "Scale attachment and detachment: The role of hydrodynamics and surface morphology". In: *Chemical Engineering Journal* 430 (2022), p. 132583.

[56] A. Quddus et al. "BaSO4 scale deposition on stainless steel". In: *Desalination* 127.3 (2000), pp. 219–224.

[57] M. M. Vazirian et al. "Surface inorganic scale formation in oil and gas industry: As adhesion and deposition processes". In: *Journal of Petroleum Science and Engineering* 137 (2016), pp. 22–32.

[58] X. Xing et al. "Mechanism of calcium carbonate scale deposition under subcooled flow boiling conditions". In: *Chinese Journal of Chemical Engineering* 13.4 (2005), p. 464.

[59] A. Janzen et al. "Understanding and analysis of fouling behavior of bare-wire heating elements in electric water heating". In: *Heat Exchanger Fouling and Cleaning*. 2019, pp. 1–8.

[60] M. Pourbozorg et al. "Effect of turbulence on fouling control of submerged hollow fibre membrane filtration". In: *Water research* 99 (2016), pp. 101–111.

[61] G. M. Graham et al. “Examination of the effect of generically different scale inhibitor species (PPCA and DETPMP) on the adherence and growth of barium sulphate scale on metal surfaces”. In: *International Symposium on Oilfield Scale*. OnePetro. 2001.

[62] D. Yang et al. “Model for seawater fouling and effects of temperature, flow velocity and surface free energy on seawater fouling”. In: *Chinese Journal of Chemical Engineering* 24.5 (2016), pp. 658–664.

[63] Z. Han et al. “CFD modeling for prediction of particulate fouling of heat transfer surface in turbulent flow”. In: *International Journal of Heat and Mass Transfer* 144 (2019), p. 118428.

[64] M. M. Awad. “Impact of flow velocity on surface particulate fouling-theoretical approach”. In: *Journal of American Science* 8.9 (2012), pp. 442–449.

[65] V. S. Nichka et al. “Fouling mitigation by optimizing flow rate and pulsed electric field during bipolar membrane electroacidification of caseinate solution”. In: *Membranes* 11.7 (2021), p. 534.

[66] M. Van Loosdrecht et al. “Biofilm structures”. In: *Water Science and Technology* 32.8 (1995), pp. 35–43.

[67] W. Kwok et al. “Influence of biomass production and detachment forces on biofilm structures in a biofilm airlift suspension reactor”. In: *Biotechnology and bioengineering* 58.4 (1998), pp. 400–407.

[68] M. O. Pereira et al. “Effect of flow regime on the architecture of a Pseudomonas fluorescens biofilm”. In: *Biotechnology and bioengineering* 78.2 (2002), pp. 164–171.

[69] S. Wasche et al. “Influence of growth conditions on biofilm development and mass transfer at the bulk/biofilm interface”. In: *Water Research* 36.19 (2002), pp. 4775–4784.

[70] J. Vrouwenvelder et al. *Biofouling of spiral wound membrane systems*. Iwa Publishing, 2011.

[71] C. Psoch et al. “Anti-fouling application of air sparging and backflushing for MBR”. In: *Journal of Membrane Science* 283.1 (2006), pp. 273–280.

[72] I. S. Ngene et al. “CO2 Nucleation in Membrane Spacer Channels Remove Biofilms and Fouling Deposits”. In: *Industrial & Engineering Chemistry Research* 49.20 (2010), pp. 10034–10039.

[73] P. Willems et al. “Bubbles in spacers: Direct observation of bubble behavior in spacer filled membrane channels”. In: *Journal of Membrane Science* 333.1 (2009), pp. 38–44.

[74] M. Blommaert et al. “Electrochemical impedance spectroscopy as a performance indicator of water dissociation in bipolar membranes”. In: *J. Mater. Chem. A* 7 (32 2019), pp. 19060–19069.

6

Outlook

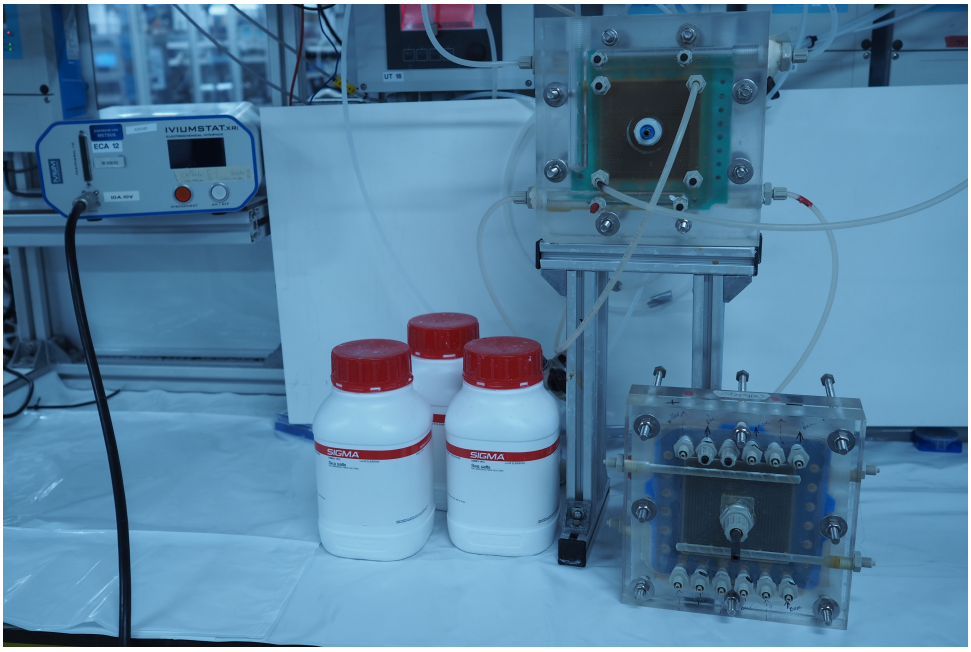

6.1. CARBON DIOXIDE CAPTURE DEMANDS

To close the carbon cycle, sustainable CO_2 capture and utilization are indispensable. Current technologies for CO_2 capture rely dominantly on absorption of CO_2 from point sources, where the absorbent is subsequently regenerated via energy intensive temperature swings, which imply a huge energy consumption when expanding capture towards a net zero CO_2 emission. When realizing that at least 35 % of CO_2 emissions are decentralized, we are facing a massive challenge for closing the carbon cycle. In that framework, electrochemical technologies for CO_2 capture, from the atmosphere and ocean, can play an important role. Thankfully, globally, renewable electricity capacity is estimated to increase by over 60 % between 2020 and 2026, reaching more than 4800 GW [1]. Currently, most electrochemical methods are at early stages of development (i.e., TRL < 5) and are still energy intensive. In this chapter, a broad context including carbon dioxide removal (CDR) needs, economics and scaling considerations is given.

Despite the necessity of carbon capture, utilization, and storage (CCUS, Figure 6.1) for climate change mitigation, implementation of CCUS has been very slow; the annual global CO_2 capture capacity in 2021 was ca. 40 $MtCO_2\,yr^{-1}$, with majority (ca. 28.5 $MtCO_2\,yr^{-1}$) resulting from natural gas processing [2]. However, for emissions that cannot be avoided or reduced directly, direct air capture (DAC) or indirect ocean capture (IOC [3]) must be implemented. Currently, the 19 operating DAC plants worldwide (in 2021) only enable a capture capacity of ca. 0.01 $MtCO_2\,yr^{-1}$ [4]. This is while to reach carbon neutrality by 2050, CCUS must increase to at least 4 $GtCO_2\,yr^{-1}$ already by 2030 (see Chapter 1), and DAC needs to increase to ca. 86.5 $MtCO_2\,yr^{-1}$ [4]; that is at least 100× more than the current global capacity.

The slow CCUS take off is mainly due to the high cost involved with available technologies [5]. Unfortunately, current climate policies like carbon pricing are not enough to make CCUS economically attractive. However, in the pursuit of carbon neutrality, we cannot afford to dismiss CCUS technologies only on cost grounds. Since the current energy transition lacks a "market pull" for making this transition fast enough, an additional technology "push" is needed. Developing CCUS technologies, even if they are currently too expensive, can act as that required "push", in addition to the market pull. Thankfully, experience shows that CCUS can become cheaper as the technology develops; for example, the cost of CO_2 capture from large-scale coal-fired power plants has decreased from 110 $\$\,t^{-1}CO_2$ in 2014 (Boundary Dam) to 65 $\$\,t^{-1}CO_2$ in 2017 (Petra Nova) [5]; future capture cost is estimated close to 45 $\$\,t^{-1}CO_2$ in 2025-2027 [5].

The CO_2 capture step is the most expensive step in the overall CCS cost; depending on the capture source, the higher the CO_2 concentration, the lower the capture costs. For instance, the carbon capture cost varies from 15-25 $\$\,t^{-1}CO_2$ for highly concentrated flue gas streams (e.g., ethanol production or natural gas processing) to 40-120 $\$\,t^{-1}CO_2$ for more dilute flue gas (e.g., cement production and power generation) [5]. However, to address decentralized emissions, or to obtain negative emissions, CO_2 needs to be removed from the environment: i.e., from ocean/ sea/ rivers or atmosphere. Direct air capture (DAC) is currently the most expensive approach estimated to be anywhere between 100-1000 $\$\,t^{-1}CO_2$ (see Chapter 2). Data on oceanic carbon capture is limited but estimations show that it can be cheaper or more expensive than DAC, depending on the plant location and design [6].

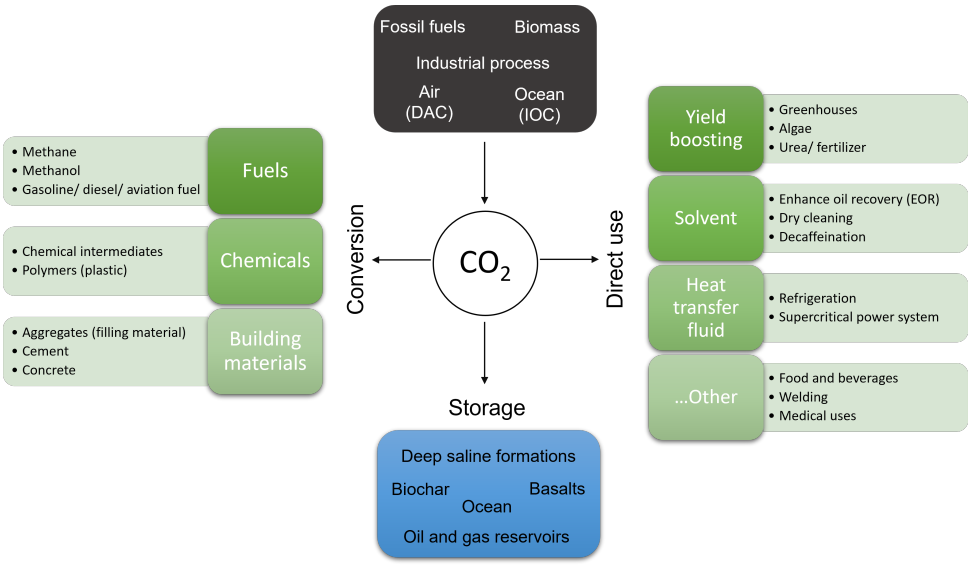

Figure 6.1: Simple classification of pathways for CO_2 capture, use and storage (CCUS). Adapted from [2]. Around 230 $MtCO_2\,yr^{-1}$ of CO_2 are used globally, primarily to produce fertilizers (around 125 $MtCO_2\,yr^{-1}$) and for enhanced oil recovery (around 70-80 $MtCO_2\,yr^{-1}$) [2].

6.2. THE *in-situ* VS. *ex-situ* PROCESS

The oceanic dissolved inorganic carbon can be extracted electrochemically by applying a bipolar membrane-based pH-swing; gaseous CO_2(g) can be recovered from the acidic stream (i.e., pH < 5) by e.g., use of a membrane gas-liquid contactor while solid carbonate minerals can be recovered from the base stream (i.e., pH > 9.5). The process can be done *ex-situ* [3] or *in-situ* [7] (see Chapter 4), as shown in Figure 6.2 (A) and (B), respectively.

In an *ex-situ* process, mixers assembled in seawater-tanks or separated parts of the ocean ensure gradual addition of concentrated HCl acid or NaOH base to the ocean to change its pH (Figure 6.2 (A)). Alternatively, the *ex-situ* process can be performed using separate pumping units and mixers to allow seawater mixing with acid or base within pipelines; both options increase the CAPEX and geographical footprint of the plant. Furthermore, in the *ex-situ* process, a pure NaCl solution stream (obtained from e.g., an electrodialysis step) is needed to produce the required HCl and NaOH solutions, meaning that a severe pH-swing is desired to minimize the required amount of pure NaCl solution. However, to achieve that wide pH-swing (e.g., pH = 0 vs. pH = 14), a high thermodynamic voltage (and thus higher electrical energy consumption) is required for the water dissociation reaction in the BPM (i.e., $V_{BPM} = 0.059\Delta pH = 0.059(14-0) = 0.826V$, see Chapter 3). Moreover, the charged anion and cation exchange membranes that are

needed in the stack are known to be less selective in harsh pH environments, leading to a lower Coulombic efficiency in the BPMED cell and a possibly lower membrane lifetime due to degradation [8].

To mitigate the crossover of protons and hydroxides (i.e., to enhance the acid and base purity in the *ex-situ* method) typically a third compartment is introduced in the membrane configuration inside the BPMED-stack. Such a desalination compartment with neutral pH in between the acid and base [9] requires an additional membrane in each repeating cell unit (i.e., AEM-BPM-CEM instead of AEM-BPM or BPM-CEM pairs). The addition of a third membrane at each cell unit, increases the CAPEX (i.e., membrane costs) and OPEX (i.e., higher cell resistance and thus voltage loss and electrical energy consumption) of the *ex-situ* process.

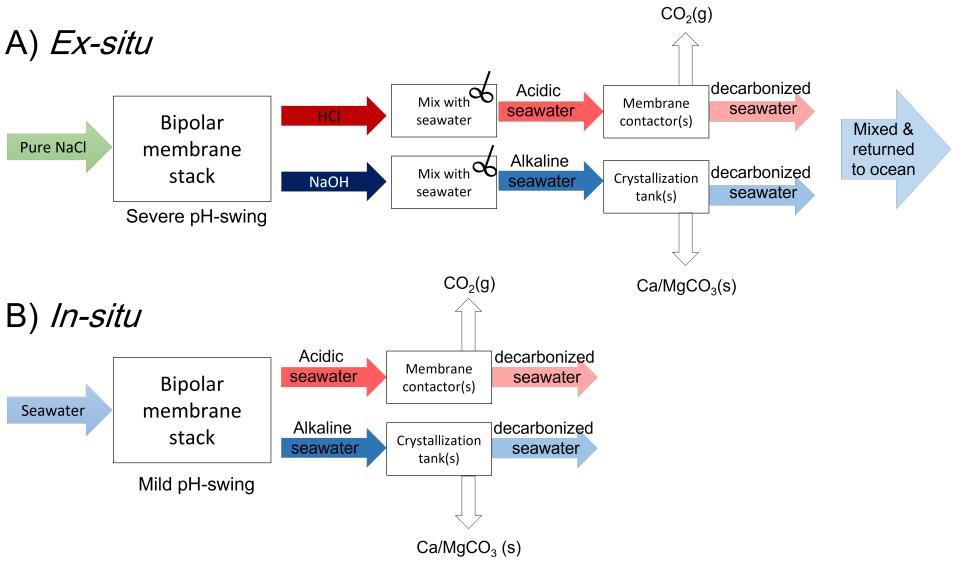

Figure 6.2: The electrochemical oceanic carbon capture based on pH-swing concept applied (A) *ex-situ* and (B) *in-situ*, respectively.

Theoretically, all above mentioned disadvantages for the *ex-situ* method can be eliminated by applying an *in-situ* process where seawater will be pumped inside of the BPMED cell, directly (Figure 6.2 (B)). To start with, a milder pH-swing compared to the *ex-situ* process is adequate for shifting the carbonate equilibrium because the gradual mixing takes place within the stack compartments. Thermodynamically, a pH difference between pH 5 and pH 10 across the BPM requires only $V_{BPM} = 0.059\Delta pH = 0.059(10-5) = 0.295V$ per BPM for water dissociation (see Chapter 3). Furthermore, the *in-situ* process enables the simultaneous acid and base routes more easily. The added advantage of a

simultaneous acid/base *in-situ* capture is that, even if DIC crosses over the membranes, it would not decrease the product efficiency as it will still be captured in the adjacent compartment, thanks to the two-membrane cell configuration.

The *in-situ* acid route has been investigated in previous works where gaseous CO_2 from synthetic seawater is extracted via AEM-BPM stack, using 285 kJ mol^{-1} CO_2 at acidic pH of ca. 3.7 with a CO_2 extraction efficiency of 68 % [7]. However, the *in-situ* alkaline route is more challenging due to the complexity of controlling the precipitation (and thus undesired membrane fouling) inside of the stack. We have successfully shown $CaCO_3$(s) extraction via the *in-situ* mineralization route with an electrical energy consumption of ca. 350 kJ mol^{-1} $CaCO_3$(s) (= 350 kJ mol^{-1} CO_2) for the BPMED cell (see Chapter 4). Theoretically, more than 90 % of DIC can be extracted as CO_2(g) from the acidic compartments simultaneously, without additional electrical energy required in the cell, which probably halves the stack-energy consumption for recovered carbon species (i.e., 175 kJ mol^{-1} CO_2, excluding the energy required in membrane contactors). Indeed, for mineralization via the *in-situ* process, separating tanks are still required for the crystallization process, but the tank volumes can be minimized through enhancing the mineralization kinetics inside of them (e.g., calcite seeds addition or heating the tanks using waste heat from nearby industries). Unfortunately, using the *in-situ* alkaline route, the membrane scaling is a disadvantage (see Chapter 5). Thankfully, membrane scaling inside of the cell can be slowed down by optimizing the current density-flow rate combination. However, fouling is inevitable in *in-situ* mineralization, complicating the operation and increasing the CAPEX (i.e., reduced membrane life time) and OPEX (i.e., pumping energy and membrane resistance). The fouling can be removed through chemical cleaning via an acid wash, but that comes at the price of a decreased production time (see Chapter 5).

Last but not least, when performing the alkaline route (regardless of *in-situ* or *ex-situ*), $CaCO_3$(s) precipitation (and subsequent extraction) will reduce ocean alkalinity. Thus, for the base-route to be a viable method of ocean CDR, after $CaCO_3$(s) precipitation, additional alkalinity (e.g., in the form of OH^- ions) would need to be added to the post-precipitation base stream before returning it to the ocean or the acid (from the acid-compartment) would need to be prevented from returning to the ocean.

Alternatively, only the acid-route can be applied (see Figure 4.1 (A)): first, by using the seawater for the acid compartment, then removing the CO_2 as gas, followed by recirculating the decarbonized acidic stream through the base compartment back in the stack. If so, the DIC removal in the first step and the lowered pH eliminate the risk of carbonates precipitation upon the return to the alkaline compartment. While there can still be fouling from biological or colloidal origin, probably much less scaling takes place compared to the *in-situ* base-route shown in Chapter 4. Additionally, using this recirculation route, the pH difference over the BPM is even further decreased when using counter-flow (see Chapter 3).

Even though the thermodynamic electrical energy consumption in a mild pH-swing via the *in-situ* route is ca. 3× lower than the *ex-situ*, in practice we still measured BPM-voltage > 0.7 V even at mild pH (see Chapter 3) as a counter-flow mode did not have significant impact on the voltage compared to the co-flow or recirculation modes. Such high voltage seems to be due to the intrinsic properties of the bipolar membrane itself

(e.g., layers and catalyst); current BPM's are developed for the traditional use of the BPM for high purity strong acid/base generation, and are not yet customized for more recent BPM applications e.g., in resource recovery and carbon capture. Therefore, current BPM's cannot yet benefit from the advantage of a milder pH-swing that is particularly interesting for such applications [10]. When a mild pH-swing is desired (i.e., in oceanic carbon capture), the membrane resistances need to be minimized to decrease voltage losses while the membrane selectivity is not as important compared to a large pH-swing applications. Such properties can be achieved e.g., through decreasing the membrane thickness of both the mono- and bipolar membrane. In addition to a lower membrane resistance (accompanied with sacrificed selectivity), a fast BPM-water dissociation catalyst that is active in mild pH is needed.

An alternative way to decrease the cost of capture is to combine (i.e., co-plant) the oceanic carbon capture units with that of desalination plants such as reverse osmosis (RO) and electrodialysis (ED) [11]. A pH-swing based decarbonisation step is particularly advantageous prior to seawater reverse osmosis (SWRO) because low-pH brine stream is ideal for further brine concentration processes due to reducing (1) membrane fouling and (2) the need for anti-scalant chemicals [12, 13].

6.3. THE REQUIRED OCEAN VOLUME

In order to capture 1 $MtCO_2\,yr^{-1}$, the upper layer of 365 $km^2\,yr^{-1}$ oceanic area must be treated, assuming carbon extraction from the surface layer (i.e., up to a depth of 100 m i.e., the so-called ocean surface/ mixed layer), an average oceanic dissolved inorganic carbon (DIC) concentration of 2.5 mM [14], a carbon capture efficiency of 50 %, and an ocean surface of 361 million km^2. In other words, an ocean volume of 36.5 $km^3\,yr^{-1}$ (i.e., equal to 0.1 $km^3\,d^{-1}$), assuming 100 m depth, must be treated. To put this in perspective, the annual Dutch CO_2 emission is ca. 135 $MtCO_2\,yr^{-1}$ (2020) [15], requiring the treatment of at least 49000 $km^2\,yr^{-1}$ of seawater, whereas the surface area of the North Sea is 575000 km^2 (with an average depth of ca. 90 m [16]).

As for the combination of oceanic BPMED-CDR with desalination units, currently, the highest worldwide reverse osmosis plant capacity is ca. 0.365 $km^3\,d^{-1}$, with a total global desalination capacity of ca. 100 million $m^3\,d^{-1}$ (i.e., 36.5 $km^3\,d^{-1}$, dominated by RO, but including other desalination methods e.g., multistage flash), revealing the scale limitation of such BPMED-RO co-planting. From another perspective, seawater is widely used for cooling in many areas of the world; approximately 927 million $m^3\,d^{-1}$ (i.e., ca. 338 $km^3\,yr^{-1}$) of seawater was used globally for power plants in the year 2000 [17], corresponding to a capacity of more than 9 $MtCO_2\,yr^{-1}$, under above assumptions, if the capture unit is combined with seawater cooling plants [11]. The combination of ocean CDR with seawater-desalination is only as early adopter that can help develop and bring down the CDR-cost.

6.4. UP-SCALING THE BPMED-BASED OCEANIC CARBON CAPTURE TECHNOLOGY

The current BPMED-based oceanic carbon capture is at TRL 4-5, with medium scale lab setups. In the presented work, an electrochemical 10 × 10 cm^2-BPMED-stack consisting of 10 BPM-CEM cell pairs have been shown to extract solid Aragonite (> 60 % extraction), achieving 0.64 $kgCaCO_3(s)\,h^{-1}\,m^{-2}$ production, experimentally using $i = 5\ mA \cdot cm^{-2}$ applied current density (see Chapter 4). To enable carbon capture in $ktCO_2 \cdot yr^{-1}$ scale, up-scaling in (1) the stack size, (2) number of cell units (i.e., number of membranes within the stack), and (3) applied current density is needed (Figure 6.3).

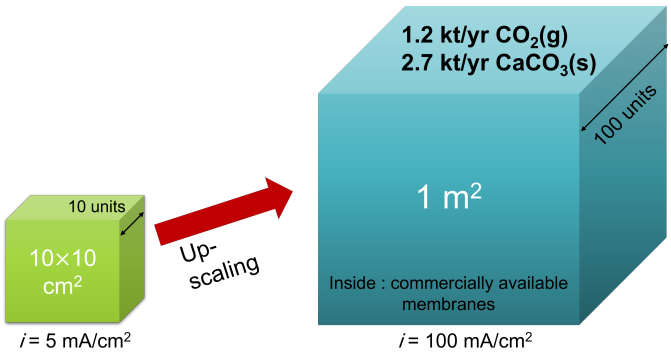

Figure 6.3: Up-scaling towards $ktC\,yr^{-1}$, assuming 100 % faradaic efficiency (i.e., 1 mol electron turning in to 1 mol H^+ and 1 mol OH^- ions and subsequently delivering 1 mol CO_2(aq) and 1 mol CO_3^{2-} on the acid and base compartment, respectively), DIC extraction efficiency of 85 %, limiting current density of 2.5 $mA \cdot cm^{-2}$ (see Chapter 3), applied current density of 100 $mA \cdot cm^{-2}$ (instead of the 5 $mA \cdot cm^{-2}$), 100-cell units with a cell size of 1 m^2 (instead of the current 10-cell units with a cell size of 0.01 m^2 used in Chapter 4), see the supporting information 6.7.1 for detailed calculations.

Upon an up-scaling such as shown in Figure 6.3, simultaneous ocean CDR of ca. 1.2 $ktCO_2\,yr^{-1}$ and ca. 2.7 $ktCaCO_3(s)\,yr^{-1}$ from the acid and alkaline compartments, respectively, is possible. Increasing the capture potential further can be done through e.g., increasing the number of cell-units, number of BPMED-stacks, and expanding capture locations worldwide.

6.5. COST OF OCEANIC CARBON CAPTURE USING BPMED

We have estimated the cost of *in-situ* based BPMED capture to be ca. 407 $\$\,t^{-1}CO_2$ for 1 $ktCO_2\,yr^{-1}$ scale, while for $MtCO_2\,yr^{-1}$ scale, the costs can reduce to 223 $\$\,t^{-1}CO_2$ (see the supporting information 6.7.2). According to the sensitivity analysis, the estimated costs are most sensitive to the price of (renewable) electricity (i.e., 78.33 $\$\,MWh^{-1}$ assumed for west Europe) and charged membranes (i.e., 1000 $\$\,m^{-2}$ BPM and 500 $\$\,m^{-2}$ AEM and

CEM are assumed), Figure S1. Thankfully, the price of (avoided) carbon is increasing by time, with the current sequestration/ Offsets CO_2 credit price slightly more than 80 $\$\,t^{-1}CO_2$ [18]. As for the costs of capture, in another study, the *ex-situ* cost of the oceanic carbon capture via electrochemical bipolar membrane electrodialysis (BPMED) is estimated to be 373-2355 $\$\,t^{-1}CO_2$, assuming a plant that extracts 20 $kmolCO_2\,h^{-1}$ (i.e., ca. 7.71 $ktCO_2\,yr^{-1}$) [11]. The difference in the costs estimations depend on (1) the plant location (i.e., stand alone, co-locate with desalination plant, or co-locate with power-plant using seawater cooling), (2) chosen acid-base routes, (3) plant capacity, and (4) *in-situ* vs. *ex-situ* [11].

In order to decrease the carbon capture costs, in addition to further process optimizations, there are two solutions when using electrochemical BPMED-based oceanic carbon capture:

1. The capture plant can be combined with an existing desalination plant (e.g., reverse osmosis (RO) or electrodialysis (ED)) as explained above. Such an arrangement decreases the CAPEX of the capture drastically (i.e., pumps, reservoirs, pretreatment facilities), but it also creates a good business case because a decarbonisation step prior to the desalination can increase the desalination efficiency due to possible membrane fouling reduction.

2. Both products of the capture (i.e., CO_2(g) and $CaCO_3$(s)(s)) can be sold and reused, Figure 6.1.

In addition to the above points, future reduction in the price and carbon-emission of electricity (i.e., currently ca. 0.42 $kgCO_2\,kWh^{-1}$) improves the future of electrochemical BPMED-based capture, drastically. In addition to the amount of required energy, the source of the electricity for our process is important; CDR technology is most effective as negative emission technology when driven by renewable energy. Thankfully, the installed renewable electricity generation capacity is increasing each year. In the pathway to net zero carbon, almost 90 % of global electricity generation in 2050 is to come from renewable sources, with solar PV and wind together accounting for nearly 70 %, reducing the CO_2 emissions by ca. 40 % [19].

The carbon market is growing fast, as well. In April 2022, an advance market commitment was formed to accelerate carbon removal; "Frontier" is the advance market commitment to buy an initial $ 925 million of permanent carbon removal (through purchasing carbon credits) between year 2022 and 2030 [20]. It's funded by Stripe, Alphabet, Shopify, Meta, McKinsey, and tens of thousands of businesses using Stripe Climate. Under this program, carbon capture startups may charge as high as 2000 $\$\,t^{-1}CO_2$, depending on the footprint, sustainability, and permanency of the capture. So far, Stripes and Shopify have each run a similar Frontier like fund with $7 million and $30 million, supporting 14 and 22 carbon capture startups, respectively [21].

6.6. CAPTURE AND ITS REQUIRED ENERGY FOOTPRINT

In addition to the amount of the required energy, the source of power, and plant locations are important; the facility area required for $GtCO_2\,yr^{-1}$ scale capture (that can actually tackle the climate change) is rather large; As an example, capturing 1 Gton CO_2(g)

per year from the atmosphere requires ca. 7612 km^3 air to pass through the fans, on a daily basis (assuming air density of 1.184 $kg\,m^{-3}$ that contains 0.608 $gCO_2\,kg^{-1}$ air and a capture efficiency of 50 % [22]). To put this in perspective, extracting ca. 1 GtC from the ocean surface layer (i.e., the upper 100 m) would require processing less than 100 km^3 of the ocean surface volume per day (assuming 50 % extraction efficiency and DIC = 2.5 mM).

As for the footprint of renewable electricity, as an example, area needed to produce the solar energy is as follow. Assuming an electrical energy consumption for CO_2 capture of 60 – 350 $kJ\,mol^{-1}CO_2$, to capture 1 $GtCO_2$ per year, a minimum of 1789 - 10435 km^2 solar panels is required (assuming average annual solar irradiation of 2.9 $kWh\,m^{-2}\,d^{-1}$ and solar panel efficiency of 20 %, for the Netherlands), which translates to 4 – 25 % of the size of the Netherlands. To reduce the required area of solar panels for CO_2 capture, wind farms can be combined, but above calculations already show the location restrains with regards to the capture facilities and energy generation.

In the Netherlands, the annual Dutch CO_2 emission is ca. 135 $MtCO_2\,yr^{-1}$ (2020) [15]. As an attempt to achieve carbon neutrality by 2050, if within five years, $MtCO_2$ per year scale capture is achieved via the presented method, we can significantly offset the Dutch GHG emission, and even enable negative emissions. However, as the worldwide emission ends up in the environment (air and ocean), to effectively keep global warming below 2°C (i.e., Paris agreement [23]), capture in $GtCO_2$ scale must be realized as soon as possible and in various spots in the world to balance the atmospheric CO_2 concentration, effectively. The presented electrochemical oceanic carbon capture technology does have the ability to capture Gt scale carbon.

6.7. SUPPORTING INFORMATION

6.7.1. UP-SCALING CALCULATIONS

The total molar flux of extracted carbon, dn in $mol\,s^{-1}$, can be estimated as

$$dn = \text{Nr. cell units} \times \frac{I}{F} \tag{S1}$$

where F is the Faraday constant of 96485 $C\,mol^{-1}$, I the net applied current in A, and Nr. cell units the number of membrane pair (or triplet) units inside the BPMED-stack. Assuming a membrane area of A_m =1 m^2, a limiting current density of i_{lim} = 2.5 $mA\,cm^{-2}$ for the BPM (see Chapter 3), an applied current density of i = 100 $mA\,cm^2$ (i.e., I = (100 − 2.5) × 10000/1000 = 975 A), for a stack containing Nr. cell units of 100 membrane cell-pairs (i.e., assuming a BPM-AEM configuration, this means 100 acid compartments and 100 base compartments), and assuming daily production of 24 $h\,d^{-1}$ and 365 $d\,yr^{-1}$ and a 100 % capture efficiency, CO_2(g) and $CaCO_3$(s) production values of 1402 $tCO_2\,yr^{-1}$ and 3190 $tCaCO_3(s)\,yr^{-1}$ are obtained respectively (production rate = $M_W.dn$, with molecular weight $CaCO_3$ and CO_2 of 100 $g\,mol^{-1}$ and 44 $g\,mol^{-1}$, respectively). Multiplying the production values by 0.85 (to account for 85 % carbon extraction instead of 100 %) results in 2.71 $tCaCO_3(s)\,yr^{-1}$ and 1.19 $tCO_2\,yr^{-1}$ extraction, respectively (Figure 6.3).

6.7.2. COST-WORKSHEET

Template cost worksheets provided by Xprize carbon removal foundation [24] is used for cost estimations of a plant with 1 $MtCO_2\,yr^{-1}$ capacity, Figure S1 (A). For the revenue calculations, it is assumed that all the "net tonnes CO_2 removed per year" can be sold, either directly or through conversion for a price of $100\$t^{-1}CO_2$. If no product is sold, the revenues decrease to zero, bringing the net costs to 223 $\$t^{-1}CO_2$, Figure S1 (B).

A

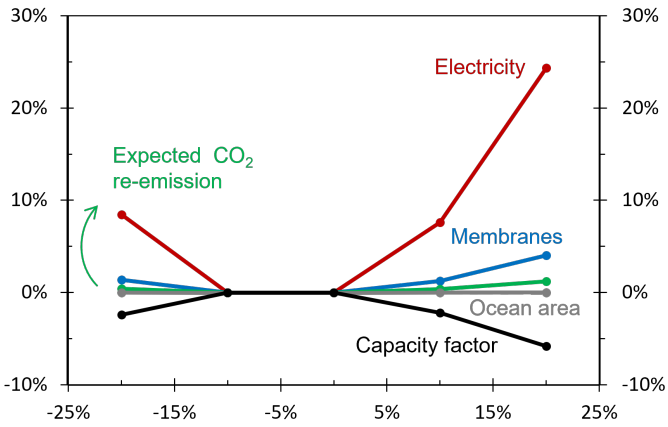

B

Project Location (Country)	Netherlands
Project Region	West Europe
CDR Category (Primary)	Oceanic carbon capture
Gross tCO_2 Removed (per year)	1,000,000
Emitted $tCO_{2\text{-eq}}$, per year	100
Expected CO_2 Re-Emission over 100 years (%)	5%
Capacity Factor (%)	85%
Net Tonnes Removed (per year)	808
Cost ($/$tCO_2$)	223
Revenue ($/$tCO_2$)	85
Net Cost ($/$tCO_2$)	138

Figure S1: (A) Spider diagram demonstrating the sensitivity/ uncertainty of the estimated carbon capture cost (for the $MtCO_2\,yr^{-1}$ capacity) against five key variables of required electricity (red), membranes (blue), ocean area (grey), capacity factor (black), and expected re-emission of CO_2 (green). Inputs are shown in (B) and in "data table functions" in reference excel file [24]. The electricity is assumed to be generated from solar sources and to be supplied by industrial grid. (B) General project information summarizing the final costs and potential revenues. The capacity factor is the production time the system can be expected to operate in a given year. Expected re-emission indicates the amount of the removed CO_2 which may be re-emitted to the atmosphere within 100 years. The chosen values for the "expected re-emission" and "capacity factor" are rough estimations and thus their effect is analysed separately in the sensitivity analysis shown in (A).

BIBLIOGRAPHY

[1] *IEA: Renewables 2021*. https://www.iea.org/reports/renewables-2021.

[2] *IEA: About CCUS 2021*. https://www.iea.org/reports/about-ccus.

[3] C. F. de Lannoy et al. "Indirect ocean capture of atmospheric CO2: Part I. Prototype of a negative emissions technology". In: *Int. J. Greenh. Gas Control* 70 (May 2018), pp. 243–253.

[4] *IEA: Direct Air Capture 2021*. https://www.iea.org/reports/direct-air-capture.

[5] *IEA: Is carbon capture too expensive? 2021*. https://www.iea.org/commentaries/is-carbon-capture-too-expensive.

[6] M. D. Eisaman. "Negative Emissions Technologies: The Tradeoffs of Air-Capture Economics". In: *Joule* 4.3 (2020), pp. 516–520.

[7] M. D. Eisaman et al. "CO2 extraction from seawater using bipolar membrane electrodialysis". In: *Energy Environ. Sci.* 5 (6 2012), pp. 7346–7352.

[8] D. Li et al. "Durability of anion exchange membrane water electrolyzers". In: *Energy Environ. Sci.* 14 (6 2021), pp. 3393–3419.

[9] H. Nagasawa et al. "A New Recovery Process of Carbon Dioxide from Alkaline Carbonate Solution via Electrodialysis". In: *AIChE Journal* 55 (Dec. 2009), pp. 3286–3293.

[10] M. A. Blommaert et al. "Insights and Challenges for Applying Bipolar Membranes in Advanced Electrochemical Energy Systems". In: *ACS Energy Letters* 6.7 (2021). PMID: 34277948, pp. 2539–2548.

[11] M. D. Eisaman et al. "Indirect ocean capture of atmospheric CO2: Part II. Understanding the cost of negative emissions". In: *International Journal of Greenhouse Gas Control* 70 (2018), pp. 254–261.

[12] T. Altmann et al. "Process improvement of sea water reverse osmosis (SWRO) and subsequent decarbonization". In: *Desalination* 499 (2021), p. 114791.

[13] N. Harlev et al. "Acidification and decarbonization in seawater: Potential pretreatment steps for biofouling control in SWRO membranes". In: *Desalination* 467 (2019), pp. 86–94.

[14] R. E. Zeebe et al. *CO2 in seawater: equilibrium, kinetics, isotopes*. 65. Gulf Professional Publishing, 2001.

[15] *IEA: The Netherlands 2020*. https://www.iea.org/countries/the-netherlands.

[16] *The European Maritime Spatial Planning Platform: North Sea*. https://maritime-spatial-planning.ec.europa.eu/sea-basins/north-sea-0.

[17] S. S. Hutson. *Estimated use of water in the United States in 2000*. 1268. Geological Survey (USGS), 2004.

[18] *EU Carbon Permits data*. https://tradingeconomics.com/commodity/carbon.

[19] S. Bouckaert et al. “Net Zero by 2050: A Roadmap for the Global Energy Sector”. In: (2021).

[20] *An advance market commitment to accelerate carbon removal*. https://frontierclimate.com/.

[21] *Stripe, Alphabet and Others to Spend Nearly $1 Billion on Carbon Removal*. https://financialpost.com/pmn/business-pmn/stripe-alphabet-and-others-to-spend-nearly-1-billion-on-carbon-removal.

[22] W. A. Smith et al. “Pathways to Industrial-Scale Fuel Out of Thin Air from CO2 Electrolysis”. In: *Joule* 3.8 (2019), pp. 1822–1834.

[23] J. Rogelj et al. “Paris Agreement climate proposals need a boost to keep warming well below 2 degree C”. In: *Nature* 534.7609 (2016), pp. 631–639.

[24] *XPRIZE carbon removal cost worksheet 1Mt 2022*. https://docs.google.com/spreadsheets/d/1-cVnVX2x8yvoB_iI5xorH4zcf3Hl7iGW/edit?usp=sharing&ouid=108216637628046395874&rtpof=true&sd=true.

SUMMARY

To mitigate climate change, carbon capture is necessary. In addition to the energy transition towards renewable sources and green house gasses emission reduction, CO_2 capture from flue gas and its sinks, including air and the ocean, must be promoted. By 2030, in less than 8 years, the global carbon capture capacity must increase 100 × (from the current ca. 40 $MtCO_2\,yr^{-1}$ to 4 $GtCO_2\,yr^{-1}$). To meet the net zero carbon goals of 2050, sustainable, scalable, inexpensive technologies that fit in an electrified industry and have a small footprint are needed for carbon capture. Currently, such technologies do not exist. In the framework of the necessary carbon capture, and the opportunities for electrochemical (ocean) CO_2 capture, five research questions are defined and addressed in this thesis.

In this thesis, we first introduce and evaluate electrochemical carbon capture methods while focusing on the pH-swing approach. We establish the current state of the art, describe the major technical barriers and R&D needs, and discuss opportunities for improving electrochemical CO_2 capture **(Chapter 2)**. This thesis focuses on the pH-swing method applied via a bipolar membrane electrodialysis (BPMED) cell for oceanic carbon capture. The BPMED cell consists of two end electrodes, charged membranes, and in-between-membranes flow paths. The desired chemical reaction in the case of oceanic carbon capture is the conversion of bicarbonate ions to gaseous CO_2 or carbonate ion (and subsequently e.g., calcium carbonate $CaCO_3$(s)) using the water dissociation reaction (WDR) facilitated by the bipolar membrane (BPM). The BPM consists of a cation- and an anion-exchange membrane laminated/ electro-spun together with a water dissociation catalyst in between.

Electrochemical carbon capture methods are still energy intensive in spite of their higher energy efficiency, flexibility and sustainability compared to the conventional approaches. To better understand the reason for this high energy consumption, this work investigates the possible (voltage) losses in the bipolar membrane electrodialysis technology (BPMED) method for carbon capture. The main energy component of the BPMED cell is the bipolar membrane itself as the voltage it needs to dissociate water into acid and base is > 60 % of the required input energy consumption. With the aim of decreasing the energy consumption of bipolar membrane (BPM) based applications, the effect of pH gradient (ΔpH_{BPM}) on the reversible and irreversible voltage components associated with the BPM is investigated **(Chapter 3)**. The BPM-voltage pH dependency is studied through an analytical model and is also measured experimentally, for four flow orientations using buffered and unbuffered electrolytes. First, using the analytical model, the pH profile along the BPM (i.e., in the flow direction) is obtained for each flow orientation. The simulated results fit the experimentally obtained ΔpH_{BPM} at the outflow very well. Second, based on the simulated pH profile, for each flow orientations, the reversible voltage (V_{rev}) is modeled. Surprisingly, except for the co-flow mode, the experimentally measured V_{rev} were higher (up to six times) than what was simulated. The

origin of this discrepancy is the difference between the bulk and local pH; The local pH at the BPM-electrolyte interface and BPM junction layer (JL) determines the measured reversible voltage of the BPM V_{rev}. However, the (measured) bulk pH is not representative of this local pH. Our results show that, although changing the flow orientations alters ΔpH_{BPM}, it does not affect V_{rev}, V_{irr}, and thus V_{BPM}. It seems that, when the water dissociation reaction (WDR) dominates, the membrane internal properties overshadow the effect of the bulk ΔpH_{BPM}. Therefore, to decrease the BPM-voltage (thus its energy consumption) under WDR regime, focus must be shifted towards tuning the membrane properties through membrane engineering (e.g., WDR catalyst, its thickness, and the BPM layers-thickness) rather than the external pH profile along the membrane **(Chapter 3)**.

In further attempts to decrease the process electrical energy consumption through process optimization, oceanic carbon capture through electrochemically induced *in-situ* carbonate mineralization using bipolar membrane was investigated **(Chapter 4)**. Using this method, aragonite (polymorph of $CaCO_3$(s)) was extracted from (real and synthetic) seawater as an ocean carbon removal strategy. By controlling the current density and cell residence time, > 60 % of the dissolved inorganic carbon (DIC) and ≥ 16 % of the Ca^{2+} ion is extracted, without the need for any additional chemicals. An energy consumption of 318 ± 29 kJ mol^{-1} $CaCO_3$(s) (i.e., ca. 0.88 kWh kg^{-1} $CaCO_3$(s)) is obtained for DIC-capture from real seawater. Theoretically, at a mild pH-swing (e.g., base pH 10.0 and acid pH 4.5, thus ΔpH = 5.5) the thermodynamic energy required to capture $CaCO_3$(s) though *in-situ* mineralization is ca. 35 kJ mol^{-1}$CaCO_3$(s) which is 10 - 12 % of that experimentally achieved. However, the irreversible BPM-overpotential is responsible for more than 55 % of the required electrical energy. Focusing on membrane engineering to achieve fast WDR kinetics in the BPM, with highly permselective ion-exchange layers to exclude co-ions, and with optimum thickness of the layers is the most effective way to minimize energy losses. Despite the promising energy consumption, membrane fouling is a challenge that *in-situ* mineralization process faces **(Chapter 4)**.

Chapter 5 investigates the fouling management scenarios to remove the mineral scaling in the alkaline compartments of the bipolar membrane based oceanic carbon capture. The scaling buildup is measured through increase in the cell voltage and increase in the stack pressure drop. The rate of scaling buildup slows down by a (continuously) higher flow rate in combination with lower current density, due to the lower base-pH that lowers the hydroxide precipitation kinetics. As for the membrane configuration, the stack voltage for the CEM-BPM configuration increases to 130 % within 30 min, while that of AEM-BPM remains constant, revealing its beneficial lower scaling over the CEM-BPM cell. As for cleaning methods, air sparging, CO_2(g) sparging, CO_2(aq), back pressure, flow rate increase (5× and 15×), and acid wash (i.e., pure HCl and BPMED-based produced acid) are investigated. For both membrane configurations, the acid wash showed the highest recovery. The acid wash using the BPM-produced acid needs no additional chemicals and is thus more sustainable than cleaning with pure HCl, though cleaning with HCl results in a higher recovery and shorter cleaning time. Combining the acid wash with back-pressure application reduces the cleaning time. However, the back-pressure as a solo method is not effective enough for fouling removal. Air sparging was done at pressures of 2, 3, and 4 bar, with sparging intervals of 10 min

for 5 s and 3× 2s. In all cases, air sparging increased the cell voltage and pressure drop even more because of stagnant bubbles that got trapped within the cell-spacers. CO_2 gas sparging does show suppression of the voltage and pressure drop increase (even though no full recovery is achieved), but causes negative DIC removal, which is against the aim of the method. Covering a large range of fouling management strategies, the findings in (Chapter 5) gives directions in cell design and process optimisation for further developing the BPMED technology for oceanic carbon capture. Based on our results, a combination of AEM-BPM based cell, operated under current density-flow rate combination that prevents pH-Base > 10 in the base compartment, followed by an acid wash-combined with back pressure upon an increase in the cell voltage, is the optimal setting for the fouling management **(Chapter 5)**.

Finally, in **Chapter 6**, an outlook on the cost of carbon capture, energy consumption, and up-scaling of the presented BPMED-cell is given. The oceanic carbon capture technology has the potential of a negative emission technology. The up-scaling is possible by (1) increasing the size of the electrochemical cell, (2) the applied current density, and (3) the number of the cell units (i.e., membrane units) inside of the stack. Through up-scaling the current prototype **(Chapter 4)** and using a simultaneous acid and base route, up-scaling from 0.01 m^2 to 1 m^2 cell size, from 5 to 100 $mA\,cm^{-2}$ applied current density, and from 10-cell units to 100-cell units (which is shown possible commercially for electrodialysis and BPMED cells), $ktCO_2\,yr^{-1}$ capture scale is possible. Increasing the faradaic efficiency to 100 % and enhancing the DIC-extraction rate from 60 % to 85 % (through further process optimization) enables production of 2.7 $ktCaCO_3\,yr^{-1}$, and 1.2 $ktCO_2(g)\,yr^{-1}$ from the cell. Further up-scaling can be done by increasing the stack numbers, cell units, and capturing locations **(Chapter 6)**.

SAMENVATTING

Om klimaatverandering tegen te gaan, is het afvangen van koolstof noodzakelijk. Naast de energietransitie naar hernieuwbare bronnen en de reductie van de uitstoot van broeikasgassen, moet de afvang van CO_2 uit rookgas, lucht en zelfs de oceaan, worden bevorderd. Tegen 2030, dus in minder dan 8 jaar, moet de wereldwijde koolstofafvangcapaciteit met 100 keer toenemen; dit betekent van de huidige koolstofafvangcapaciteit van 40 $MtCO_2$ per jaar naar 4000 $MtCO_2$ per jaar. Om de netto nul-koolstofdoelstellingen van 2050 te halen, zijn duurzame, schaalbare, goedkope technologieën nodig die passen in een geëlektrificeerde industrie en een kleine voetafdruk hebben voor het afvangen van koolstof. Momenteel bestaan dergelijke technologieën niet. In het kader van de noodzakelijke koolstofafvang en de mogelijkheden voor elektrochemische (oceaan) CO_2-afvang, worden in dit proefschrift vijf onderzoeksvragen gedefinieerd en beantwoord.

We introduceren en evalueren eerst de elektrochemische koolstofafvangmethoden, waarbij we ons concentreren op de pH-swing-benadering. We stellen de huidige stand van de techniek vast, beschrijven de belangrijkste technische barrières en R&D-behoeften, en bespreken mogelijkheden voor verbetering van de elektrochemische afvang van CO_2 **(Hoofdstuk 2)**. Dit proefschrift richt zich op de pH-swing methode die wordt toegepast via een bipolaire membraanelektrodialyse (BPMED) cel voor het opvangen van oceanische koolstof. De BPMED-cel bestaat uit twee eindelektroden en geladen membranen tussen de elektroden. De gewenste chemische reactie in het geval van oceanische koolstofafvang is de omzetting van bicarbonaationen HCO_3^- in gasvormige CO_2(g) of carbonaationen CO_3^{2-} (en vervolgens bijvoorbeeld calciumcarbonaat $CaCO_3$(s)) met behulp van de waterdissociatiereactie (WDR). De WDR is mogelijk gemaakt door het bipolaire membraan (BPM). Het BPM bestaat uit een kation- en een anionenuitwisselingsmembraan gelamineerd/elektrogesponnen samen met een waterdissociatiekatalysator ertussen.

Elektrochemische koolstofafvangmethoden zijn nog steeds energie-intensief ondanks hun hogere energie-efficiëntie, flexibiliteit en duurzaamheid in vergelijking met de conventionele benaderingen. Om de reden voor dit hoge energieverbruik beter te begrijpen, onderzoekt dit werk de mogelijke (spannings)verliezen in de bipolaire membraanelektrodialysetechnologie (BPMED) methode voor koolstofafvang. De meeste energieconsumptie van de BPMED-cel wordt veroorzaakt door het bipolaire membraan (BPM) zelf, aangezien de spanning die het BPM nodig heeft om water te scheiden in zuur en base > 60 % van het input-energieverbruik bedraagt. Met als doel het energieverbruik van op bipolair membraan (BPM) gebaseerde toepassingen te verminderen, wordt het effect van de pH-gradiënt (ΔpH_{BPM}) op de reversibele en irreversibele spanningscomponenten over het BPM onderzocht **(Hoofdstuk 3)**. De pH-afhankelijkheid wordt bestudeerd met behulp van een analytisch model en wordt ook experimenteel gemeten, voor vier stromingsoriëntaties met gebufferde en ongebufferde elektrolyten. Eerst wordt met behulp

van het analytische model het pH-profiel langs het BPM verkregen voor elke stroomoriëntatie. De gesimuleerde resultaten passen zeer goed bij de experimenteel verkregen ΔpH_{BPM} bij de uitstroom. Ten tweede wordt op basis van het gesimuleerde pH-profiel voor elke stromingsrichting de omkeerbare spanning (V_{rev}) gemodelleerd. Verrassend genoeg, behalve voor de co-flow mode, waren de experimenteel gemeten V_{rev} hoger (tot zes keer) dan wat was gesimuleerd. De oorzaak van deze discrepantie is het verschil tussen de bulk en de lokale pH; de lokale pH bij het BPM-elektrolyt grensvlak en de junctielaag (JL) van het BPM bepaalt de gemeten V_{rev}. De (gemeten) bulk pH is echter niet representatief voor deze lokale pH. Onze resultaten tonen aan dat, hoewel het veranderen van de stromingsoriëntaties ΔpH_{BPM} wijzigt, dit geen invloed heeft op V_{rev}, V_{irr} , en V_{BPM}. Het lijkt erop dat, wanneer de waterdissociatiereactie (WDR) domineert, de interne membraaneigenschappen het effect van de bulk ΔpH_{BPM} overschaduwen. Om de BPM-spanning (en dus het energieverbruik) onder het WDR-regime te verlagen, moet de aandacht dus verschoven worden naar het afstellen van de membraaneigenschappen (bv. WDR-katalysator en -dikte en membraandikte) in plaats van het externe pH-profiel langs het membraan **Hoofdstuk 3)**.

In een poging om het elektrische energieverbruik van het proces te verlagen, werd oceanische koolstofafvang door elektrochemisch geïnduceerde *in-situ* carbonaatmineralisatie met behulp van een bipolair membraan onderzocht **(Hoofdstuk 4)**. Met deze methode werd aragoniet (polymorf van $CaCO_3$(s)) uit (echt en synthetisch) zeewater geëxtraheerd als een strategie om koolstof uit de oceaan te verwijderen. Door de stroomdichtheid en de verblijftijd van de cel te regelen, wordt > 60 % van de opgeloste anorganische koolstof (DIC) en ≥ 16% van het Ca^{2+} ion geëxtraheerd, zonder dat er extra chemicaliën nodig zijn. Een energieverbruik van 318 ± 29 kJ mol^{-1} $CaCO_3$(s) wordt verkregen voor DIC-vangst uit echt zeewater. Theoretisch, bij een milde pH-swing (b.v. base pH 10.0 en zuur pH 4.5) is de thermodynamische energie die nodig is om $CaCO_3$(s) vast te leggen door *in-situ* mineralisatie, is ca. 35 kJ mol^{-1} $CaCO_3$(s), hetgeen 10 - 12 % is van de experimenteel bereikte waarde. De irreversibele BPM-overpotentiaal is echter verantwoordelijk voor > 55 % van de vereiste elektrische energie. De meest effectieve manier om energieverliezen te minimaliseren is om te focussen op membraantechnieken om een snelle WDR kinetiek in het BPM te bereiken, met zeer permselectieve ionenuitwisselingslagen om co-ionen uit te sluiten, en met optimale dikte van de lagen. Ondanks het veelbelovende energieverbruik is membraanvervuiling een uitdaging waarmee het *in-situ* mineralisatieproces wordt geconfronteerd **(Hoofdstuk 4)**.

In **hoofdstuk 5** worden de beheersscenario's onderzocht voor aangroeibeperking en verwijdering van minerale aanslag in de alkalische compartimenten van het bipolaire membraan voor het afvangen van oceanische koolstof. De opbouw van verkalking wordt gemeten door verhoging van de cel-spanning en toename van de drukval. De opbouw van verkalking wordt vertraagd door een (continu) hoger debiet in combinatie met een lagere stroomdichtheid, als gevolg van de lagere pH die de hydroxide precipitatie kinetiek verlaagt. Wat de membraanconfiguratie betreft, stijgt de cel-spanning voor de CEM-BPM-configuratie tot 130 % binnen 30 min, terwijl die van de AEM-BPM constant blijft, wat de gunstiger lagere scaling onthult ten opzichte van de CEM-BPM-cel. Wat de reinigingsmethoden betreft, zijn luchtsparging, CO_2(g) sparging, CO_2(aq), tegendruk, verhoging van het debiet (5 × en 15 ×), en zuurwassen (inclusief zuiver HCl en op BPMED ge-

baseerd geproduceerd zuur) onderzocht. Voor beide membraanconfiguraties vertoonde de zure spoeling het beste herstel. De zure wassing met het BPM-geproduceerde zuur vereist geen bijkomende chemicaliën en is dus duurzamer dan de reiniging met zuiver HCl, hoewel de reiniging met HCl resulteert in een hogere terugwinning en een kortere reinigingstijd. De combinatie van het wassen met zuur met tegendruk verkort de reinigingstijd. De tegendruk als solo methode is echter niet effectief genoeg voor de verwijdering van aangroei. Het spoelen met lucht werd uitgevoerd bij drukken van 2, 3 en 4 bar, met spoelintervallen van 10 min gedurende 5 s en 3× 2s. In alle gevallen verhoogde luchtsparging de cel-spanning en de drukval nog meer door stagnerende belletjes die in de celruimten vast kwamen te zitten. CO_2-gassparging geeft wel een onderdrukking van de spannings- en drukdalingstoename te zien (ook al wordt geen volledig herstel bereikt), maar veroorzaakt een negatieve DIC-verwijdering, wat tegen het doel van de methode ingaat. De bevindingen in dit werk bestrijken een breed scala van aangroeimanagementstrategieën en geven aanwijzingen voor celontwerp en procesoptimalisatie voor de verdere ontwikkeling van de BPMED-technologie voor het afvangen van oceanische koolstof. Op basis van onze resultaten is een combinatie van een AEM-BPM gebaseerde cel, bedreven onder een combinatie van stroomdichtheid-stroomsnelheid die voorkomt dat pH-Base > 10 in het basiscompartiment, gevolgd door een zure wasbeurt in combinatie met tegendruk bij een verhoging van de cel-spanning, de optimale instelling voor het foulingbeheer **(Hoofdstuk 5)**.

Ten slotte wordt in **Hoofdstuk 6** een vooruitblik gegeven op de kosten van koolstofafvang, energieverbruik en opschaling van de gepresenteerde BPMED-cel. De oceanische koolstofafvangtechnologie heeft het potentieel van een negatieve emissietechnologie. De opschaling is mogelijk door het vergroten van (1) het formaat van de elektrochemische cel, (2) de toegepaste stroomdichtheid, en (3) het aantal celeenheden in de cel. Door de huidige demo op te schalen **(Hoofdstuk 4)** en een gelijktijdige zuur- en baseroute te gebruiken, opschaling van 0.01 m^2 naar 1 m^2 celgrootte, van 5 tot 100 $mA\,cm^{-2}$ toegepaste stroomdichtheid, en van 10-celeenheden tot 100-celeenheden (wat commercieel mogelijk is voor elektrodialyse en BPMED-cellen), is afvangen op $ktCO_2\,jr^{-1}$ mogelijk. Het verhogen van de faraday-efficiëntie tot 100 % en het verhogen van de DIC-extractiesnelheid van 60 % naar 85 % (door verdere procesoptimalisatie) geeft een productie van 2.7 $ktCaCO_3(s)\,jr^{-1}$, en 1.2 $ktCO_2(g)\,jr^{-1}$ uit de cel. Verdere opschaling kan worden gedaan door de membraan-aantallen, celeenheden en het aantal locaties voor CO_2-afvang te vergroten **(Hoofdstuk 6)**.

ACKNOWLEDGEMENTS

The end of my PhD is here, but "END = Efforts Never Die". Hopefully, this book will remain as a proof of all the efforts that have been made to get here. It would certainly have not been possible to reach this milestone without the help and support of many people. I like to thank a few here.

The chair and members of the Doctoral Committee, the time and effort you put into reading this dissertation, critically evaluating it, and taking part to the defense is highly appreciated. Thank you very much.

My promoter **Prof.dr.ir. Chris Kleijn**, my TU Delft supervisor **Dr.ir. David A. Vermaas**, and my Wetsus daily supervisor **Dr.ir. Martijn Wagterveld**, thank you for guiding me in every step of my PhD path. None of this would have happened if you did not choose me for this PhD. I am grateful that you trusted me to deliver and granted me the freedom to take the research directions that I found most appealing. In addition to guiding me to become an independent researcher, you also helped me greatly to improve my scientific skills. **Chris**, you taught me how to plan a PhD and you were there anytime I needed extra guidance. Thank you. **David**, you taught me how to present my work for a broad audience, how to smartly answer questions, how to write scientifically, how to collaborate with other scientists to make impact, and many more things. Thank you. I am happy we continue working together in our next chapter: SeaO2. **Martijn**, you taught me to focus on one research question at a time and not to rush through experiments, to analyse data critically, and to work efficiently in the lab plus much more. Thank you.

Wetsus. The brainchild of **Cees Buisman, Bert Hamelers, and Johannes Boonstra**, Wetsus is an amazing place to do research. The concentration of expertise, resources, and support opens up possibilities that other researchers can only dream of. Thank you for making and keeping it possible. I am looking forward to continue our collaboration further, through SeaO2. Wetsus analytical and technical support teams, HR, PR, secretaries, talent team, ICT, and canteenees. Thank you for all the hard work you do in the background of the scientific research. In particular, I am very grateful to **Ernst** and **Jan** for all the help in building my experimental setup and keeping it running and big thank to **Jelmer, Marianne, Jan Willem, and Mieke** for SEM, and for analysing all those TOC, ICP, IC, samples. Thank you **Gerrit Visser** for doing the orders for anything I needed for the lab setup, and thank you **Rienk Smit** for all your ICT supports. **Wetsus** people. Thank you all for living the Wetsus values (innovation, partnership, cooperation, reliability, and joy) and creating a very nice, fun, and supporting environment. PV. Thank you to the PVs from 2018 to 2022 for all the activities they organized. Even though I missed 95 % of them, I immensely enjoyed the ones I did attend. **Office 1.10C**. I was lucky to have many amazing people as office mates: **Hector, Gosia, Diego, Emanuel, Rebeca, Kaustub, Emad, Bárbara, Marianne, Jolanda, Marco, João, Kestral and Sam** (never Kikko even though I love him). Thank you for the nice time together and good luck! **Jolanda**, Thank you for being my dear friend and paranymph. My students. Doing research can

be time consuming, so students can provide great help. I was lucky and had some of the best students. Thank you for all the help, **Max, Wybren, Lieneke, Hannah, and Nick**. I learned a lot while working with you. I hope I was half as good a supervisor as you were good as students. **Concentrates theme**. There is a sense of purpose and a desire to deliver in the theme that keeps us running. Contributing to this theme was a great experience. I am grateful for the financial support, the exchanges during the meetings, and the feedback on reports, manuscripts, and presentations.

I would also like to thank the TU Delft Applied Sciences faculty members, and specifically **Transport Phenomena (TP)** group for their openness and interest in my research. Particularly, the **Electrochemical Flow Systems (EFS)** group deserves a big thank you: David, Christiaan, Evert, Duco, Lorenz, **Marijn** (thank you for all of our nice talks and awesome collaborations), Kosta, Jorrit, Vojtech, Christel, Jan-Willem, Nathalie, Kaustub, Andrey and Minu. **Jorrit**, thank you for your enthusiasm and our cool patent. **Nathalie and Christel**, Thank you for taking care of all the social media and for being so kind and awesome. **Lorenz**, Thank you for teaching us what a true organised researcher works, and thank you for our fun times in Southampton for the electrochemical summer school. Your lecture on "how to get things done" has been an inspiration for me and helped me immensely. **Sandra** (TU Delft TP group secretary). You know all the details and helped me navigate forms, attachments, and deadlines. For that and all the work you do to keep the TP group running smoothly, thank you.

To the **faculty of impact** and **NWO**, thank you for funding our research after the PhD to bring our ocean carbon capture idea from the lab to the market. This is a great opportunity. Thank you **Hans** and **Frans** for coaching me to become a successful entrepreneur.

Ruben Brands, Thank you for finding us and gathering to start SeaO2. I am looking forward to working with you and David.

Hanna, Ruben, Marta, Roel. I know you since a long time ago when I was a newbie at TU Delft and in Europe! you taught me how to survive here and always checked up on me through my MSc, work, life, PhD and all. Thank you for being in my life and thank you for your awesome weddings that I was lucky enough to be part of.

Dr. Toering from MDL of MCL thank you for keeping me alive and well, literally. Good luck in Heerenveen.

Linda, thank you for all of our wonderful walks and talks in Froskepolle, thank you for teaching us how to handle a German pointer (Faya).

To may Family:

To my mom, **Fariba**. You taught me how to be a fierce, independent, and confident woman. Thank you for making me who I am today and helping me to live my ideal life even though it means us living so far away from each other. To my dad, **Mehdi**. You taught me to be humble and kind, to listen well, and to never give up no matter how long it takes. You also gave me the "academic blood" that led me into becoming a "doctor". Thank you. To my sister, **Zahra**. You have my back no matter what. I simply would not have made it so far without you. anytime I need help with anything, I know I can count on you. I love you. Thank you for being such an awesome big sister.

To **Tim**, my partner in crime, in good and bad days. I do not know how you manage to be so positive, supporting, calm, and caring every day. Thank you for helping me getting through the rough times and celebrating the good times. Thank you for always being

enthusiastic about any lab-results, articles, pitches, presentations, pictures, paragraphs etc that I showed you. Also, thank you for helping me compile this thesis latex file over and over again. Without you, I would have gone mad. I hope I can always be there for you the way you have been there for me. Thank you for being my Paranymph.

To family **Stadman** and **Drenthe**, thank you for all your love and support. **Ina, Dana, Bram, Wilma, Fokko**, thank you for taking interest in my work and your kindness.

To Nila and Faya. You cannot read, but I like to have your name in this thesis. You have been my co-workers during the pandemic and helped me keep an organized daily plan, in any circumstances. I love you.

To all the people I forgot to mention. Sorry about that. I might not have a good memory for names, but I never forget faces and the actions that have been taken. Thank you all.

CURRICULUM VITÆ

Rezvan SHARIFIAN

06-04-1992	Born in Hamedan, Iran
2010–2014	B.Sc. in petroleum engineering Sharif university of technology (Iran, Tehran)
2014–2016	M.Sc. in Applied Earth Science (petroleum engineering) TU Delft (the Netherlands, Delft)
2016–2018	Project manager Tebodin Bilfinger B.V.
2018–2022	PhD. Chemical engineering Faculty of Applied Sciences Delft University of Technology, the Netherlands *Thesis:* Electrochemical oceanic carbon capture *Promotor:* Prof. dr. ir. C. Kleijn *Co-promotor:* Dr. ir. D. A. Vermaas *Daily-supervisor:* Dr. ir. R. M. Wagterveld
2022–present	Co-founder SeaO2 B.V. Faculty of Impact (NWO) fellow

Photo by Bianca Sistermans

LIST OF PUBLICATIONS

6. K.M. Diederichsen*, **R. Sharifian***, J. Kang, Y. Liu, S. Kim, B. Gallant, D. A. Vermaas, T. A. Hatton, *Electrochemical methods for carbon dioxide separations*, Nat Rev Methods Primers **2**, 68 (2022) (* Shared co-first authorship).

5. **R. Sharifian**, L. Boer, R.M. Wagterveld, D.A. Vermaas, *Electrochemical oceanic carbon capture through in-situ carbonate mineralization using bipolar membrane*, Chemical Engineering Journal **438**, 135326 (2022).

4. **R. Sharifian**, M.A. Blommaert, M. Bremer, R.M. Wagterveld, D.A. Vermaas, *Intrinsic bipolar membrane characteristics dominate the effects of flow orientation and external pH-profile on the membrane voltage*, Journal of Membrane Science **638**, 119686 (2021).

3. M.A. Blommaert, **R. Sharifian**,N. Shah, N. T. Nesbitt, W.A. Smith, D.A. Vermaas, *Orientation of bipolar membrane determines the dominant ion and carbonic species transport in membrane electrode assemblies for CO_2 reduction*, J. Water. Chem. A **9**, 11179 (2021).

2. **R. Sharifian**, R.M. Wagterveld, I.A. Digdaya, C. Xiang, D.A. Vermaas, *Electrochemical carbon dioxide capture to close the carbon cycle*, Energy Environ. Sci. **14**, 781-814 (2021).

1. **R. Sharifian**, H. C. van der Wal, R.M. Wagterveld, D. A. Vermaas, *Fouling management in oceanic carbon capture via in-situ electrochemical bipolar membrane electrodialysis*, submitted to Chemical Engineering Journal in September 2022.